Tip Clearance Flows in Axial Compressors:
Stall Inception and Stability Enhancement

Stephanie April Weichert
Clare Hall

A dissertation submitted for the degree of
Doctor of Philosophy

September 2011

UNIVERSITY OF CAMBRIDGE
Department of Engineering

Tip Clearance Flows in Axial Compressors:
Stall Inception and Stability Enhancement

Stephanie April Weichert

Summary

The flow in the rotor tip clearance gap in an axial compressor influences the loss levels and the stall onset point. The role of tip clearance flows in the stall inception process is still debated, though. The aim of this thesis is to improve the fundamental understanding of the tip clearance flow field and its role in the stall inception process. The knowledge gained is used to develop a new casing treatment for an aero-engine core compressor.

Detailed static pressure, total pressure, and velocity measurements were made in the rotor tip clearance gap at design and near stall flow conditions. The resulting overtip flow maps showed the flow field in more detail than previously possible. Flow variations around the annulus and among blade passages were analyzed and found to increase as stall is approached. This increase was not uniform around the annulus or among passages; instead, some blade passages exhibited unique behaviour compared to all the other passages. The flow variations in the unique passages were linked to small physical irregularities in compressor blading.

Detailed overtip measurements were also made at stall inception to investigate the formation of the spike disturbance. These measurements, the first of their kind, showed that the disturbance which initiates the formation of the spike destabilizes the boundary between the reversed flow and incoming flow. After destabilization, reversed flow increasingly dominates the passage until the neighbouring passage is affected. The spike was found to originate most often from those regions in the compressor where the flow variations are highest and was not, as suggested by some research, associated with the forward movement of the tip leakage vortex.

A new casing treatment for axial compressors was proposed and tested. The casing treatment extracts air from over the rotor blade tips and re-injects it upstream of the rotor blade leading edges into the tip region through discrete re-circulation loops. The overtip location of air extraction is unique and enables self-regulation of the amount of flow re-circulated: a minimum amount of air is re-circulated at compressor design conditions (thus minimizing any loss of efficiency) and a maximum amount of air is re-circulated near the stability limit (thus maximizing stall margin). Modest stall margin improvements (2%) were achieved without any loss of compressor efficiency at design conditions.

Preface

The research presented in this dissertation was carried out at the Whittle Laboratory, University of Cambridge Engineering Department between October 2006 and August 2011. This dissertation is the result of my own work and includes nothing which is the outcome of work done in collaboration except where specifically indicated in the text. No parts of the work have been submitted to any other university or place of learning. This dissertation contains approximately 47,000 words and 91 figures.

Part of this dissertation has been presented in the following publication:

Weichert, S., Day, I. & Freeman, C. (2011) Self-Regulating Casing Treatment for Axial Compressor Stability Enhancement. *Proceedings of ASME Turbo Expo 2011, June 6-10, Vancouver, CA, GT2011-46042.*

This work was funded by the European Union Framework 6 Project NEWAC: NEW Aero engine Core concepts (FP6-030876). Additional support from Rolls-Royce is also gratefully acknowledged.

Stephanie Weichert
September 2011
Cambridge, United Kingdom

Acknowledgments

I am indebted to many people for enriching my experience in Cambridge. This completed work was made possible through their support and kindness.

My supervisor, Ivor Day, has been a true mentor. I am thankful for his tremendous dedication to quality research and for passing on his knowledge to me.

The skill and advice of the workshop staff and technicians were crucial to my experimental program. I am especially indebted to David Barlow and Mick Whibley for their technical expertise and attention to detail.

It is said that you only learn when you have to explain, so I would like to thank the Whittle lab staff and visitors who have encouraged me to discuss my work. In this regard I am grateful to John Longley, Chris Freeman, Nick Cumpsty, and John Adamczyk. I extend special thanks to the visitors from Rolls-Royce, in particular, Nick Baker, Mike Howard, John Bolger, and Simon Gallimore.

I acknowledge the kind support of students in the Whittle lab. I am especially indebted to Tony Dickens for sharing his knowledge and skills, even as he was writing his own dissertation. Simon Evans, Chris Wakelam and Kathryn Evans deserve special mention for their true and lasting friendship. Phil Athayde, Tim Houghton and Chia Hui Lim went out of their way to pass on useful information.

The dedication of Clare Hall staff to each of their students is remarkable. I am thankful for the opportunity to have met so many wonderful people there.

Without encouragement from a deep network of family and friends I wouldn't have made it here; I am grateful for each of you in my life. I am especially thankful to my parents and their spouses, who gave me everything and keep on giving. To Heinz and Erika, thank you for accepting me as your own daughter, it has meant the world to me.

Finally, I extend my most heartfelt appreciation to Matthias, for unwavering support every step of the way. You have made the past five years a joy.

Contents

Nomenclature **xi**

1 Introduction **1**

2 Literature Review **5**

2.1 Introduction to Compressor Performance 5

2.2 Tip Clearance Flow 7

2.3 Stall Inception 13

2.4 Stability Enhancement 21

2.5 Scope for present Research 30

3 Experimental Methods **33**

3.1 Introduction 33

3.2 Research Compressors 34

3.3 Data Acquisition 37

3.4 Rig Monitoring 38

3.5 Pressure Measurements 39

3.6 Hot-Wire Measurements 41

3.7 Compressor Performance 46

3.8 Procedure for Stalling the Compressor and Recording the Results 50

3.9 Processing Unsteady Data 50

3.10 Summary 51

4 Rotor Overtip Flow Maps 53

4.1 Introduction 53

4.2 Methodology for Rotor Overtip Ensemble Averaged Results . . . 55

4.3 The Ensemble Averaged Overtip Flow Field 59

4.4 Unsteady Overtip Passage Flow Variations 64

4.5 Conclusions 77

5 Stall Inception Investigation 79

5.1 Introduction 79

5.2 Statistical Preference in the Stall Inception Location 81

5.3 Study of Spike at the Stage of Traditional Detection 84

5.4 Study of Nascent Spike Propagation 89

5.5 Study of Embryonic Spike Formation 93

5.6 Discussion 102

5.7 Conclusions 107

6 Extraction/Re-Injection Casing Treatment **111**

6.1 Introduction 111

6.2 Simple Model based on Rotor Overtip Flow Field Results 114

6.3 Extraction Hole Optimization 116

6.4 Injection Nozzle Design Optimization 120

6.5 The Influence of Stalling Mechanism 126

6.6 Single Circumferential Groove 127

6.7 Re-Circulating Groove 128

6.8 Extraction/Re-injection Casing Treatment: Performance and Recommendations 129

6.9 Conclusions 131

7 Conclusions **133**

7.1 Tip Clearance Flow at Stable Conditions 133

7.2 Spike Stall Inception 135

7.3 Casing Treatment 137

7.4 Recommendations for Future Work 139

Figures **141**

References **213**

Nomenclature

Greek Symbols

α	Angle of velocity vector relative to axial reference
β	Angle of hot-wire relative to axial reference
ϕ	Flow Coefficient, V_x/U
η	Stage efficiency, Eqn. 3.10
ν	Kinematic Viscosity
ρ	Inlet Air Density
T	Rotor torque
ω	Rotational speed
ψ	Stage Loading, $(h_{03} - h_{01})/U^2$
Ψ	Pressure Rise Coefficient, $(p_3 - p_{01})/(\frac{1}{2}\rho U^2)$

0. NOMENCLATURE

Latin Symbols

a	Hot-wire calibration constant
b	Hot-wire calibration constant
BP_{uns}	Blade passage unsteadiness, Eqn. 4.1
E	Hot-wire raw voltage
h	Enthalpy
k	Bellmouth calibration constant for mass flow rate
K	Probe position
l	Rotor True Chord
$\dot{m}$	Mass Flow Rate, Eqn. 3.6
n	Hot-wire calibration constant
P	Pressure
$P2P_{var}$	Pressure to passage variation, Eqn. 4.2
R	Stage Reaction, $(h_2 - h_1)/(h_3 - h_1)$
Re	Reynolds Number based on mid-span chord, $W_1 * l/\nu$
s	Pitchwise spacing
U	Blade Velocity, mid-span if unspecified
V	Absolute Flow Velocity, mid-span if unspecified
W	Rotor Relative Flow Velocity, mid-span if unspecified

Superscripts and Subscripts

0	Stagnation condition
1	Rotor inlet conditions
2	Rotor exit, stator inlet conditions
3	Stator exit conditions
$a1$	Deverson compressor bellmouth inlet
$d2$	Deverson compressor bellmouth exit
D	Design condition
EX	Extraction (port location)
INJ	Injection (port location)
i	Injected (velocity)
m	Used to denote the effective magnitude measured by the hot-wire
mid	Rotor blade mid-height
NS	Near stall condition
s	Static condition (for pressure); stalling condition (for ϕ)
tip	Rotor blade tip
x	Axial component, positive pointing downstream

Abbreviations

CFD	Computational Fluid Dynamics
SMI	Stall Margin Improvement, Eqn. 3.9

Chapter 1

Introduction

Demands on aero-engine manufacturers to reduce emissions and cut costs ultimately rest on operation at improved efficiencies. One limit to these efforts is the flow range over which the compressor can operate. At the low-flow stability limit, operation is restricted by rotating stall and surge, aerodynamic instabilities which must be avoided at all costs. As a result, compressor operation is required to be kept safely away from the stability limit. This safety margin, or stall margin, requires design compromises which often increase the weight and lower the efficiency of the engine.

Despite the damaging consequences of an engine surge, the "stall inception process" which precedes the surge event is poorly understood. Some research suggests the stall inception process is linked to the behaviour of the tip clearance flow. The precise mechanism of stall inception and the role of tip clearance flows remain uncertain, however, due to the complexities of flow measurements in this region.

The present study focuses on the flow field in the rotor tip region with two research objectives. The first objective is to improve the fundamental understanding of the tip clearance flow field and its role in the stall inception process. The second objective is to use the knowledge gained to develop a new form of stability enhancing casing treatment for an aero-engine core compressor.

In order to achieve the first objective, measurements are made at stable conditions in the rotor tip clearance gap with new instrumentation and at a level of detail

not previously attained. In addition, extensive experimental observation from within the tip clearance gap was used to investigate the stall inception process, in particular, the formation of the spike disturbance. The detailed measurements show subtleties of the stall inception process which were previously unknown. This work contributes to a better fundamental understanding of tip clearance flows and the stall inception process which paves the way for improved predictions of the compressor stability limit.

In order to meet the second objective, a new form of re-circulating casing treatment is proposed and tested in a parametric study. Current re-circulation designs extract air from a downstream blade row or stage and re-inject it through discrete loops into the rotor tip region. Valves are usually required to control the re-circulated flow. The present work departs from this by using knowledge of the tip clearance flow field to seek a better air extraction location. In the new design, air extraction from over the rotor tips of the same blade row enables the system to self-regulate the amount of air re-circulated. A parametric study is conducted to produce a working design. This new form of overtip injection casing treatment for axial compressors is a low weight, low complexity design that has little or no impact on compressor efficiency.

Structure of Thesis

Chapter 2 provides a context for the present study in the form of a literature review that discusses the current understanding of tip clearance flows, stall inception and stability enhancement.

Chapter 3 discusses the facilities, data acquisition system and instrumentation used in these investigations. The methodology for the experimental investigations, performance monitoring, and data-processing is also outlined.

Results are presented in **Chapter 4** from a comprehensive experimental study of the rotor overtip flow field (at stable operating conditions) for design and near stall flow rates. These are the most detailed measurements yet obtained for the flow field in the tip clearance gap.

The overtip flow field is further investigated at the transient condition of stall inception. Presented in **Chapter 5**, these results show the formation and growth of the disturbance which eventually leads to stall.

Casing treatment is used to delay stall and thereby improve the operating range of compressors. A parametric study is presented in **Chapter 6** in which a new casing treatment concept is developed for a local extraction and re-injection of flow over the rotor tips. The extraction/re-injection system is self-regulating and optimized to provide the greatest improvement in stability and specific fuel consumption.

Chapter 7 summarizes the new ideas and findings presented in the previous chapters and highlights the gains made in the understanding of tip clearance flows, stall inception and casing treatment.

Chapter 2

Literature Review

This literature review provides an overview of the current understanding of the topics researched in this thesis: tip clearance flows, stall inception, and stability enhancement. Compressor performance is introduced first as a general background. Tip clearance flows are then reviewed as they are relevant to the subsequent discussions on stall inception and stability enhancement.

2.1 Introduction to Compressor Performance

High-speed compressors operate over a wide range of speeds and flow rates as seen in the performance map in Figure 2.1. At a fixed rotational speed, the compressor operating point follows a characteristic line of pressure rise versus mass flow rate. In steady operation, at varying rotational speeds, the aero-engine compressor ideally follows a working line as shown in Figure 2.1, where the solid lines depict the constant speed lines and the lower dashed line is the working line. For an aero-engine, the operating point moves away from the working line during speed transients; the amount by which it moves is controlled by shaft momentum and fuel flow rate. If the operating point moves away from the working line with decreasing mass flow rate or increasing pressure ratio, the stability limit, indicated by the surge line, is approached. If the compressor is pushed beyond this limit then a disastrous flow instability occurs in the form of rotating stall or

surge, the former marked by a drastic reduction in pressure rise and the latter by a violent oscillation of flow. Both instabilities compromise the structural integrity of the machine. The risk of these dangerous instabilities means that the working line must be kept a safe distance from the surge line, the difference being known as the stall margin.

The distance between the surge line and the working line is a stack-up of all uncertainties in the system. The exact locations of the surge line and working line are uncertain due in part to compressor degradation over time and speed transients. This often requires the working line to lie away from the peak efficiency, which increases fuel burn.

Aero-engine compressor research uses full scale high-speed rigs or scaled low-speed models. High-speed testing is, however, brief and expensive. Low-speed testing, on the other hand, is generally done at a constant speed and provides an inexpensive means for longer testing times and more extensive probe access. Fundamental differences between high-speed and low-speed tests exist in terms of Reynolds number and Mach number (e.g., the presence of shock waves). However, years of experience in compressor instability research has shown that low-speed test results are reasonably indicative of the stability behaviour of high-speed compressors, Day and Freeman (1994).

Low-speed machines generally operate at a fixed speed. A typical characteristic for a low-speed compressor is shown in Figure 2.2. As the compressor is throttled toward a lower flow rate (1), the pressure rise in the compressor increases. Compressor operation along this characteristic line is stable and the flow rate can be increased or decreased to follow this line. At the peak of the characteristic, i.e., at the stall inception point, however, rotating stall begins and there is a rapid decrease in pressure rise (2). Once the stall inception point has been crossed, opening the throttle will not immediately restore the pressure rise to the original characteristic line. Instead, the compressor operates in rotating stall as the throttle is opened (3), and then rapidly recovers to rejoin the characteristic line at a point below the maximum pressure rise (4).

Rotating stall is a compressor instability where stalled flow rotates around the circumference of the compressor propagating from passage to passage. Discrete

regions of stalled flow are called stall cells. The radial extent of a stall cell will depend on the individual compressor, the rotational speed, and the mass flow rate. If the stalled flow extends radially from the hub to the blade tip, this type of rotating stall is called "full span stall". If the stalled flow is confined to the tip region only, this is called "part span stall".

Surge, in contrast to rotating stall, is a system instability. It occurs when the pressure in any volume downstream of the compressor can no longer be supported by the stalling flow in the compressor, which initiates a full annulus oscillation of axial velocity. Figure 2.3 provides a simple schematic for rotating stall and for surge. Whereas rotating stall settles to a quasi-steady state, surge exhibits cyclic behaviour. The behaviour of developed stall cells and the performance of the compressor during rotating stall and surge is discussed in more detail in Day (1976), Wilson and Freeman (1994), and Day (1994).

Tip clearance flows are often implicated in stall inception, and will be discussed in the next part of this review.

2.2 Tip Clearance Flow

Interest in tip clearance flow research is significant due to the influence of tip flows in loss considerations and stall inception. A better understanding of this flow field may lead to more efficient designs and more accurate prediction methods.

This section on the tip clearance flow field is discussed in three parts. First, the main features of the tip clearance flow are discussed. This is followed by a discussion of the various approaches used to study tip clearance flows. Finally, the focus turns to what is known about how the tip clearance flow changes as stall is approached.

2.2.1 The Tip Clearance Gap and Local Flow Features

The tip clearance gap exists between the tips of the rotor blades and the outer casing to prevent rubbing. The tip clearance height (about 1-2% of span) is not

constant during operation of an aero-engine, though. The tip clearance height is influenced by rotor speed changes, internal temperature changes, and the varying thermal inertias of the machine components, Baghdadi (1996). Variations also occur over time due to wear and tear.

Due to the aerodynamic loading on the blade, there is a pressure difference across the blade tip (pressure side to suction side). This pressure difference drives air to leak from the pressure side to the suction side through the tip clearance gap. The magnitude of this leakage is strongly related to the aerodynamic loading of the blades, Storer and Cumpsty (1991).

The leakage flow creates a local flow pattern in the rotor tip region which is different from the mid-span flow field. This is illustrated in Figure 2.4, adapted from Inoue and Kuroumaru (1989). The rotor tips are viewed from outside of the compressor casing looking in toward the centre of the machine and the blade movement is from right to left. The leakage flow is illustrated over the blade tip on the left. As can be seen, the jet of leakage flow over the blade tip opposes the direction of the incoming through flow. The two flows meet in the "interference zone" labelled in the figure. As a result of this clash, a stagnation interface forms between the tip leakage flow and the through flow which then rolls up to form the tip leakage vortex.

The tip leakage flow and vortex are major sources of loss, Storer and Cumpsty (1994). Without a tip clearance gap between the rotor blade tips and the casing, however, a corner separation between the endwall and blade suction surface would form, Adamczyk et al. (1993), creating a different source of loss. An optimum tip clearance gap exists which will reduce, or even eliminate, this corner separation. Smaller than optimum tip clearance values increase loss due to the presence of the corner separation, while larger tip clearance values increase loss due to the leakage jet and decrease the operating range, Freeman (1985). Unfortunately, the optimum size of the tip clearance gap is normally too small to be maintained in an aero-engine compressor for mechanical reasons. Thus, a slightly larger than optimum clearance is maintained in practice, Cumpsty (2004).

The character of the leakage flow over the tip of the rotor blade depends on the blade thickness relative to the tip clearance height. The leakage flow separates

from the pressure side edge of square ended blades when entering the clearance gap between the blade and the wall. This is shown in Figure 2.5 for two scenarios. For relatively thick blades (top) the separated flow reattaches on the tip surface, creating a separation bubble on the tip. For thin blades (bottom) the separated flow forms a vena contracta. Storer (1991) found reattachment occurs if the blade aspect ratio (tip clearance height/maximum blade thickness) is lower than 0.4.

2.2.2 Approaches used to Investigate Tip Clearance Flows

The main features in the tip clearance flow field discussed in the previous section are based on decades of research. This section will give a brief overview of the experimental, analytical and computational approaches that have been used to build the current understanding of the tip clearance flow field.

Experimental Studies

The tip clearance gap flow field has been studied experimentally in cascades, low-speed and high-speed compressors.

The simplest and lowest cost model of a rotor blade row is a cascade. With stationary blades, the structure of the tip clearance flow and vortex within the blade passage can be easily investigated, e.g., Storer and Cumpsty (1991); Kang and Hirsch (1994); and Saathoff et al. (2003). Cascades have limitations, however. As the blades in the cascade do not rotate, their boundary layers are not centrifuged. This will change the flow entering the tip clearance gap. The relative motion between the blades and the casing is also important because the viscous force on any non-tangential flow near the casing wall has a relative component that is not simulated in a stationary cascade. This skews the inlet boundary layer, changes the incidence to the blade tip and alters the flow in the passage which is swept over the blade tip. Cascade results must be carefully considered in light of these limitations.

Experiments using low-speed or high-speed compressors are therefore preferable to cascade studies. Investigations in high-speed compressors would be closest to

the aero-engine environment; however, probe access is severely complicated and testing is limited by high cost and risk. Low-speed compressors, on the other hand, can be limited by having a lower Reynolds number and Mach number than found in a high-speed machine. In general, though, past experience indicates that trends and flow features in low-speed compressors are indicative of the behaviour in high-speed machines. This has been demonstrated for the role of tip clearance flows in compressor loss (Wisler (1985)), stall (Adamczyk et al. (1993) and Day and Freeman (1994)), and casing treatments (Hathaway (2006)). Low-speed compressors are therefore considered an economical and low-risk method to investigate flow phenomena relevant to high-speed machines.

The instrumentation used to obtain data in cascades and rotating machines is wide ranging. Much work on clearance flows is based on five hole pneumatic pressure probe and hot-wire anemometry measurements taken downstream of the rotor row, e.g., Hunter and Cumpsty (1982) and Lakshminarayana et al. (1995). These studies primarily discuss the roll-up of the tip leakage flow and its interaction with the casing wall boundary layer and rotor wake.

Investigations within the rotor passage in the tip region observe the roll-up of the leakage flow with the main flow and the trajectory of the tip leakage vortex. This has been achieved with a rotating five hole probe by Lakshminarayana et al. (1982a,b); with laser doppler anemometry (LDA) by Murthy and Lakshminarayana (1986) and Suder and Celestina (1996); and with particle image velocimetry (PIV) by Liu et al. (2003) and Wernet et al. (2005).

Experimental measurements in rotating rigs within the tip clearance height itself are very rare because probe placement is restricted by the physical constraint of the small tip clearance height and the moving blades. Inoue and Kuroumaru (1989) obtained hot-wire measurements in the tip clearance gap of an axial rotor. These results show the violent clash of the incoming flow with the leakage flow. The accuracy of the results is limited, unfortunately, by a sizable cavity in the casing wall surrounding the stem of the hot-wire probe.

Analytical and Computational Approaches

The difficulty of obtaining comprehensive measurements in the tip clearance gap has led to the development of analytical and computational methods to study tip clearance flows. In the study of rotor flow using computational fluid dynamics (CFD), the flow in the tip clearance gap is either modelled or fully simulating by gridding the space over the rotor tip.

Simple models of the tip clearance flow were developed to be used in conjunction with steady three-dimensional Navier-Stokes flow calculations, e.g., Chen et al. (1991). When computational resources were limited, this was an important method used to minimize gridding in the tip gap. These models have limitations, though. VanZante et al. (2000) found that the tip leakage mass flow differed by 30% between modelled and fully gridded simulations. They also found that increased grid resolution near the casing wall is necessary in order to accurately predict the tip leakage vortex trajectory and radial extent, and to improve the prediction of the stable operating range of the rotor. Since that time, ever increasing computer power and resources have seen the rise of CFD solutions which include full simulation of the tip clearance flow, Davis and Yao (2006); Gourdain et al. (2006); Houghton (2010). As a result, tip clearance flow models are now largely unnecessary.

The accuracy of CFD predictions has steadily increased, yet it is still not possible to predict the effect of tip clearance flows on compressor performance (efficiency, pressure rise capability and operating limit) based on first principles, Tan (2006). Predictions are particularly challenging at lower flow coefficients near stall. As the influence of unsteady effects becomes greater, it becomes necessary to perform more time intensive unsteady calculations of multiple blade passages, or even the entire annulus (rather than the steady single blade passage calculations which are adequate at higher flow rates), Hah et al. (1999) and Chen et al. (2008).

2.2.3 Changes in the Tip Clearance Flow Field as Stall is Approached

As a compressor is throttled toward stall, the pressure rise through the rotor row increases and the maximum pressure difference across the rotor blade tip (pressure side to suction side) increases and moves closer to the leading edge. The tip clearance flow is most vigorous at the location of the maximum pressure difference, and the tip leakage vortex originates from this location. Hence, it is understandable that changes to the tip clearance flow, and vortex behaviour, occur as the compressor is throttled. The changing behaviour will be introduced in this section.

Using three-dimensional particle image velocimetry (3D PIV) in a low-speed compressor, Wernet et al. (2005) found that the tip leakage vortex increases in size and moves upstream as the flow coefficient is reduced. The trajectory of the vortex turns further from the axial direction and assumes a more tangential direction. These observations are also found in other low-speed compressors, e.g., Furukawa et al. (1999) and Hoying et al. (1999).

As stall is approached, the forward movement of the vortex is accompanied by an increase in passage blockage. This blockage is comparatively small at design conditions. "Blockage" refers to a region of significant velocity deficit that reduces the core flow area. Khalid et al. (1999) present a method for quantifying compressor endwall blockage based on the magnitude of velocity component in the core flow direction relative to the total velocity magnitude. This quantitative parameter is useful when studying tip clearance flow changes at various operating conditions.

Results from transonic compressor tests by Suder and Celestina (1996) indicate a similar trend of passage blockage increase as the flow coefficient is reduced toward stall, but due to a different flow mechanism than in low-speed compressors. The main difference in the flow field of a transonic compressor is a shock front ahead of the rotor leading edge. The shock front is distorted by intersection with the tip leakage vortex in the passage. Upstream of the shock, the vortex trajectory is approximately the same for the design and near stall flow coefficients. However, since the pressure gradient of the shock is greatest at the near stall flow coefficient,

the vortex is diffused more as it crosses the shock boundary near stall than at design conditions. This increased diffusion following the vortex/shock interaction causes more blockage in both radial and circumferential extent near stall. The overall result is that as rotor back pressure is increased from design to near stall, the blockage becomes more severe and moves further upstream. This behaviour is also reported in other transonic compressors, e.g., Adamczyk et al. (1993) and Chen et al. (2008).

2.3 Stall Inception

Stall inception refers to the local onset of rotating stall, which, in an aero-engine, can rapidly develop into surge. Stall inception is irreversible in the sense that once the stability line has been crossed, the compressor behaviour cannot be symmetrically reversed to rejoin the unstalled characteristic. After stalling at the peak of the characteristic, the instantaneous operating point of the compressor tracks a hysteresis loop in an anti-clockwise direction, as shown in Figure 2.2.

There are multiple routes to stall. The two most common routes, initiated by "modal" or "spike" type disturbances, are briefly reviewed first. The mechanism of the spike type disturbance is still debated, and the various mechanisms proposed in the published literature are reviewed.

2.3.1 Routes to Stall Inception

This section will discuss the two main routes to rotating stall in axial compressors. Both were discussed hypothetically by Emmons as early as 1955. The first, "modal stall inception", is a long length scale oscillation which appears prior to the formation of a finite stall cell. The second, "spike-type stall inception", is a short length scale disturbance local to only a few blade passages. This disturbance is characterized by a sharp spike in a hot-wire signal measured near the rotor leading edge.

Modal waves are a low amplitude resonance of the flow in the compressor as stall

approaches. Stenning (1980) predicted oscillations near the peak of the total-to-static characteristic curve and suggested they might grow in amplitude until the compressor surges or settles into rotating stall. By coupling a system model of the inlet duct, compressor, plenum, and throttle with a two-dimensional compressor flow model, Moore and Greitzer (1986) and Greitzer and Moore (1986) showed numerical solutions of an oscillating disturbance developing into rotating stall or surge depending on the compressor system geometry. The first experimental evidence for this type of compression system instability was presented by McDougall (1988) and McDougall et al. (1990). This work confirmed the analytically predicted existence of rotating modal perturbations prior to stall in a low-speed compressor.

It is generally observed that modal waves propagate at 20 to 50% of rotor speed and can be detected 10 or even 100 rotor revolutions before stall onset. Modal oscillations are reversible by increasing the mass flow through the compressor, Day (1993a), and they do not always lead directly to rotating stall, Camp and Day (1998). Also, even when modal oscillations are present, the spike-type disturbance may appear and lead directly to the formation of a finite stall cell, Houghton (2010).

Spike stall inception is characterized by the development of a three-dimensional short length scale disturbance (on the order of a blade pitch), originating near the rotor tip leading edges, Day (1993a). The disturbance, commonly referred to as a spike, develops quickly and propagates at about 70 to 80% of rotor speed. The spike can lead directly to rotating stall, or surge, within only a few rotor revolutions. As the disturbance develops into a mature stall cell, the speed of propagation slows to about 20 to 50% of rotor speed.

Spike stall inception is the most common route to rotating stall and yet the least understood, Day (2006a). The mechanism for the formation of the spike disturbance is debated and this will be discussed in the section to follow.

It is important to note that other routes to stall exist, as recorded by Day et al. (1999) and Dickens (2008). A single compressor may exhibit more than one type depending on variations to the tip clearance gap, Day (1993a); rotor stagger,

Camp and Day (1998); rotor speed, Day et al. (1999); and inlet distortion, Longley et al. (1996). Although these studies indicate general trends, it is not yet possible to predict the type of stall inception, or the stability limit, of a compressor in advance of experimental observation, Houghton (2010).

2.3.2 Proposed Mechanisms of Spike Stall Inception

As discussed in the previous section, spike stall inception is the most common route to compressor instability. The earliest sign of the "spike" disturbance is first observed in the tip region, Day (1993a), and many of the proposed mechanisms for the onset of this disturbance are therefore associated with the tip clearance flow near the leading edge of the rotor blade tips. This section reviews the proposed mechanisms in three main groups: blockage growth, critical incidence, and forward spillage.

Blockage Growth

The possible link between blockage growth and stall inception was based on observations that stall initiates from regions of high blockage which increases noticeably near stall. In this context "blockage" refers to regions of significant velocity deficit that reduce the core flow area, Khalid et al. (1999).

One region of high blockage is where the tip clearance flow opposes the through flow to form a stagnation interface and the tip leakage vortex, Storer (1991). Research which supports the blockage growth model of stall inception suggests that the tip leakage vortex is the source of blockage associated with stall, Adamczyk et al. (1993), Suder and Celestina (1996) and Khalid et al. (1999). Suder and Celestina (1996) proposed that the blockage growth redirects incoming flow to increase the incidence on the rotor blade tips as stall is approached, and that this plays a roll in triggering stall in the tip region.

Other areas of blockage which have been implicated in the onset of stall are separations from the suction side of the rotor blade, Emmons et al. (1955); the

low momentum fluid near the casing wall, Freeman (1985); and breakdown of the tip leakage vortex, Furukawa et al. (1999) and Schrapp (2008).

In Section 2.2.3, blockage in both high-speed and low-speed compressors was shown to increase near the passage inlet as stall is approached. However, in each case this is due to different mechanisms. In high-speed compressors, the vortex/shock interaction causes the blockage to increase. In low-speed compressors, blockage near the passage inlet increases because the trajectory of the tip leakage vortex moves forward with decreasing flow coefficient.

The different blockage growth mechanisms in high-speed versus low-speed compressors could explain the rate of stall progression. Day et al. (1999) found that high-speed compressors operating at full speed progress from stall inception to surge much faster than when the same compressors operate at lower speeds. The blockage growth rate caused by the vortex/shock interaction as stall is approached is much greater than the blockage growth rate in the absence of shock waves at low speeds, as found by Suder and Celestina (1996). This higher blockage growth rate could be responsible for the much faster progression from stall inception to surge in high-speed compressors.

A direct link between blockage growth rate and spike stall inception is yet to be proven, however. The primary evidence for this link is based on two things: (1) trends in tip clearance flows as stall is approached (knowledge of which was shown to be limited) and (2) the observation that early stall cells resulting from spike stall inception appear to originate in the rotor tip region where blockage growth is high.

Critical Incidence

Critical incidence refers to research by Camp and Day (1998) which found spike stall inception to occur when a critical value of incidence onto the rotor blade tips was exceeded; this is referred to later as the "critical incidence hypothesis". In addition, they proposed a model based on the critical incidence concept to determine when to expect spikes or modes: as the compressor flow rate is reduced, if the critical value of rotor incidence is reached before the peak of the

total-to-static pressure rise characteristic, then spike stall inception will occur; otherwise, if the peak of the characteristic is reached before the critical value, modal oscillations will occur.

When the critical value of rotor incidence is reached, it was proposed that the development of the spike is due to a localized flow separation. A model for the propagation of a short length scale disturbance caused by a blade separation was proposed by Emmons et al. (1955). A schematic for this is shown in Figure 2.6. The stalled blade passage "B" restricts the flow through the blade row which causes the upstream flow to deflect, thereby increasing the incidence on blade "A" and decreasing the incidence on blade "C". The increased incidence will initiate stall on blade "A" and the decreased incidence will restore blade "B" to an unstalled state. A propagating disturbance is thus established. The number of blade passages affected by the disturbance will increase rapidly (within two or three rotations) as shown on the right hand side of the figure. An arrow indicates the direction of stall cell propagation relative to the blades.

The critical incidence model (in terms of where on the characteristic spikes and modes might be expected) is supported by many other studies, including Spakovsky et al. (1999b), Chen et al. (2008) and Simpson and Longley (2007). Simpson and Longley (2007) also supported the critical incidence hypothesis in so far as they agreed with Camp and Day (1998) that increasing rotor incidence is related to spike stall inception. However, Simpson and Longley (2007) found that critical incidence is not a fixed value, but rather depends on the flow environment in which the rotor operates (e.g. radial distribution of flow due to hub separations).

The critical incidence hypothesis, as a description for the spike stall inception mechanism, is also debated in the literature. The underlying assumption is that as the incidence increases, the likelihood of a localized flow separation increases, Suder and Celestina (1996) and Camp and Day (1998). This was supported in a computational study by Hah et al. (1999) whereby a suction side separation leading to rotating stall was found. Further support was produced in an experimental study by Inoue et al. (2000) which also found stall inception linked to a separation on the suction side of the rotor blade. In contrast, a CFD study by

Chen et al. (2008) ruled out separation from the suction side of the rotor blade at stall inception.

Whether separation occurs or not, changes in rotor incidence nevertheless influence stall inception. It is possible that increasing incidence may cause unsteady effects which could play an equally important role in stall inception as a separation might. This is one of the primary topics explored in the current work.

Forward Spillage

The "forward spillage" hypothesis is based on observations that the tip leakage vortex swings toward the rotor leading edge plane as stall is approached. This is illustrated in Figure 2.7. At design conditions, the schematic to the left in the figure shows the tip leakage vortex within the rotor passage. At stall conditions, the schematic to the right shows the tip leakage vortex forward of the leading edge plane and the "forward spillage" of tip clearance flow into the neighbouring passage. The forward spillage hypothesis suggests that the alignment of the tip leakage vortex with the rotor leading edge plane is the unstable flow condition which leads to spike stall inception.

Evidence for the forward spillage hypothesis is provided in an unsteady CFD study of eight blade passages by Hoying et al. (1999). At conditions just before stall inception (the lowest flow coefficient with steady convergence), the tip leakage vortex trajectory is aligned with the rotor leading edge plane. Unsteady flow solutions at a slightly lower flow coefficient after the formation of the spike then show spillage of the tip leakage vortex forward of the leading edge of the neighbouring blade. They conclude that a tangential tip leakage vortex trajectory (i.e., aligned with the rotor leading edge plane) is a criteria for spike stall inception.

In a similar computational study, Vo (2001) and Vo et al. (2008) extended this hypothesis and defined two events necessary for the onset of spike stall inception. One event is the forward spillage of the tip leakage flow; this is depicted in Figure 2.8. The other event is "tip clearance backflow". This is characterized by the tip clearance flow moving downstream, spilling behind the trailing edge of the next rotor blade, and then reversing its trajectory to impinge on the pressure

side surface of the neighbouring blade; see Figure 2.9. Either one of the events may occur first, however, they found stall inception only occurs when both flow patterns are present at the same time.

Full annulus computational studies by Chen et al. (2008) and Cameron et al. (2008) support the forward spillage hypothesis. These unsteady computations produce large amounts of data, so snapshots of data are extracted from the simulations at various time instances in order to present contour plots and streamlines. These studies showed the flow field at a few points in time: (1) just before a spike disturbance is observed at the last stable flow coefficient, (2) about one revolution after the pressure in the compressor has started to collapse, and (3) during the progression to fully developed rotating stall. These points in time are more than one rotor revolution apart. This is not high enough resolution to provide direct observation of spike formation, but rather supports the hypothesis based on the trends observed. The results show the trajectory of the tip leakage vortex swinging toward the rotor leading edge plane as stall is approached, and the forward spillage of tip leakage flow just after the onset of stall.

Some experimental investigations also supported the forward spillage hypothesis. Results from a low-speed compressor by Deppe et al. (2005) used two probes, one upstream and one downstream of the rotor blade row at the casing, to determine the flow direction at stall inception. The results showed continuously reversed flow upstream of the rotor leading edges. Reversed flow at the trailing edge was observed as the first spike passed over the circumferential location of the trailing edge probe. In order to determine if the reversed flow observed in the rotating rig was spilled from one passage to the next, Deppe et al. (2005) showed flow visualization results from a cascade model of the rotating rig at a flow coefficient just after stall inception. These results showed both the forward and rearward spillage of leakage flow. These cascade experiments are limited, however, as the flow near the leading edge does not agree with the experimental measurements obtained in the rotating rig. The rotating rig experiment shows continuously reversed flow at the leading edge, whereas the cascade shows regions of through flow and regions of reversed flow. It is likely that the absence of a moving wall over the rotor tips is one factor in this discrepancy. The viscous force on flow near the casing wall has a relative component that is not simulated in the stationary

cascade. This will alter the movement of the tip clearance flow relative to the blade.

Further experimental support for the hypothesis is offered by overtip casing flow visualizations in rotating rigs. Visualizations presented by Saathoff et al. (2003) and Bennington et al. (2007) showed a circumferential "separation line" over the rotor tips, which they attributed to the clash of the incoming through flow and the axially reversed leakage flow. This line is shown to move upstream of the leading edge plane as stall is approached. Bennington et al. (2007) concluded that the forward movement of this line supports the forward spillage criteria because stall is initiated after the separation line reaches the rotor leading edge plane.

These results must be interpreted with caution, though. The "separation line" indicated by the flow visualization is not a true separation line, but a pitchwise average of the shear stress as the instantaneous flow field in each blade pitch passes over the casing. The true lift-off line and any vigorous pressure gradients that influence the surface shear may be at an angle to the movement of the blades, or even unsteady. Separation regions and pressure gradients are a challenge for flow visualization in steady conditions, and even more difficult in an unsteady environment.

The experimental evidence discussed above that supports the forward spillage hypothesis is not adequate enough to provide a stand alone conclusion (i.e., without the computational studies, forward spillage of the tip leakage flow is not a forthcoming conclusion). Further doubt is cast by studies which show the flow field at conditions near stall (for compressors which exhibit spike stall inception) where the tip leakage vortex, or the interface of the reversed tip clearance flow with the inlet flow, are far from being aligned with the rotor blade leading edges, e.g., Suder and Celestina (1996), Furukawa et al. (1999) and Houghton (2010).

A unifying picture of stall inception remains to be drawn, and more research is needed into the spike stall inception mechanism. This particular problem is one of the prime considerations in the current work. The final part of this review will now discuss known methods of delaying stall.

2.4 Stability Enhancement

Restricting the operating point of a compressor to a safe distance from the stability limit is necessary for safety reasons. This precaution may rule out operation at flow rates where the compressor runs with a higher pressure ratio, or maximum efficiency, because these flow rates lie too close to the stability limit. Therefore, it is desirable to be able to extend the stable operating range of the compressor by moving the surge line further from the working line.

Casing treatment is one means of delaying stall onset. Casing treatment is applied by perforating the compressor casing wall in the region over the rotor tips. Various treatment geometries will be reviewed in this section. Other stability enhancement techniques exist (which will not be discussed further here), including improved blade design, variable stator vanes, and bleed slots.

The gain in surge margin provided by casing treatments may be used to allow engine operation at higher efficiencies (in the previously excluded range) or to reduce engine weight by removing a bulkier technology that provided the same stall margin improvement, such as variable stator blades. As a result, casing treatments are primarily evaluated on their ability to improve the operating range of the compressor with minimum efficiency penalty. In addition, the weight, cost, and reliability of the casing treatment system must be considered.

Overview of Casing Treatment Geometries

A historical survey of casing treatment designs is given by Hathaway (2006). Casing treatments often employ a pattern of shapes, holes or gaps cut out of the outer wall of the compressor annulus over the rotor tips. Many involve variations of slots, circumferential grooves, baffled slots, and honeycomb geometries, an assortment of which is shown in Figure 2.10. Osborn et al. (1971) showed that of these various geometries, casing grooves and slots perform best. These two treatments will be the focus of the following section.

Another form of casing treatment, illustrated in Figure 2.11, involves extracting high pressure air from a downstream location in the compressor and re-injecting

it just upstream of the blade row requiring stabilization. This re-circulating form of casing treatment is a topic of active research and will be discussed in greater detail in a later section.

The sections below review proven forms of casing treatment (e.g., circumferential grooves, slots and re-circulating designs) and possible mechanisms of stall suppression.

2.4.1 Circumferential Groove and Slot Casing Treatments

Much of the early development of circumferential grooves used multiple grooves placed over the rotor tips. Osborn et al. (1971) demonstrated stall margin improvement with seven grooves distributed over the rotor tips from the leading to the trailing edges. Using two to nine grooves, Bailey (1972) found that deep grooves provide greater stall margin improvement than shallow grooves, without an additional increase in efficiency penalty. Fujita and Takata (1984) applied two to five fixed width grooves and show stall margin improvement to increase with the number of grooves. They also found that partitioning the grooves increased stall margin. This early work influenced the design of circumferential grooves for some time to come. Shabbir and Adamczyk (2005), for example, used five grooves distributed from the leading to the trailing edges that are at least twice as deep as their width.

More recently, Houghton (2010) investigated the optimum axial location for a single circumferential groove and showed two maxima for stall margin improvement: at 8% and 50% axial chord. The groove near the leading edge incurs a higher efficiency penalty as a result of interacting with the tip leakage vortex. The mid-chord groove is much more efficient, and it was suggested that multiple grooves will provide good stall margin with minimum efficiency penalty if centred on mid-chord.

Slotted casing treatments are made up of a series of parallel cuts in the casing that are axial or aligned with the blade (see Figure 2.10, top left). The slots may protrude radially outward (Figure 2.10, top left) or be skewed in the direction

of blade rotation (Figure 2.10, top left). Slots skewed in the direction opposing blade rotation (not shown) decrease the stall margin, Takata and Tsukuda (1977).

Early slot designs extended from the leading to the trailing edges. Osborn et al. (1971) compared axial slots, axial skewed slots (skew in direction of blade rotation), and blade angle slots. Of these, the skewed slots provided the greatest stall margin improvement, but the lowest efficiency. Blade angle slots provided a slightly lower stall margin improvement with better efficiency. Prince et al. (1974) and Takata and Tsukuda (1977) also found that skewed slots provide the greatest stall margin.

In a departure from the traditional overtip location of the slot, Seitz (1999) reported an axial skewed slot design which extends from 75% axial chord length upstream of the leading edge of the blades to 25% axial chord length downstream of the leading edge plane. This position is reported to reduce the efficiency penalty whilst maintaining the same stall margin improvement as overtip axial skewed slots.

Although the above discussion focuses on the development of slots and grooves separately, in many ways, the two forms of treatment were developed in parallel by researchers who compared their performance on their own particular machine. This is important, as comparing results from different researchers and compressors is complicated by the unique set-up, geometry and stalling mechanism of each compressor, as well as by the particular laboratory conditions, methodology and instrumentation used. In general, direct comparison shows that slots provide greater stall margin improvement than circumferential grooves; however, this often comes at a higher efficiency penalty, Osborn et al. (1971), Prince et al. (1974), Fujita and Takata (1984), Wilke and Kau (2002), and Houghton (2010). On the other hand, circumferential grooves may provide a limited stall margin improvement, yet they have a greater mechanical integrity than the thin landing separating slots (which are vulnerable to breakage).

2.4.2 Re-circulating Casing Treatments

Traditionally, re-circulating designs have relied on air extracted from ports downstream of the rotor row in question, or from even further back in the compressor. In such cases, the downstream pressure driving the re-circulated flow is relatively constant, and hence flow is re-circulated at all operating flow rates - including at design where loss of efficiency can least be tolerated. A control valve could be used to shut off re-circulated air at design conditions, but this introduces additional weight and complexity.

The critical blade row requiring stabilization can change depending on engine speed as a result of changes in stage matching (Wilson and Freeman 1994; Day and Freeman, 1994), but flow injection ahead of the first blade row most consistently improves the stall margin across the speed range, Freeman et al. (1998).

The air may be injected toward the rotor tips either passively (steady injection as driven by the prevailing pressure difference) or actively (in a pulsed action based on continuous feedback signals from disturbances in the flow).

Pulsed (Active) Re-injection

Epstein et al. (1989) first proposed active control for stability enhancement. They observed that although rotating stall and surge are global nonlinear processes, the onset of stall is found in small disturbances which can be modelled using linear theory (based on Moore and Greitzer (1986)). Epstein et al. suggested a system which uses feedback from these small disturbances to control air injection aimed at eliminating the original disturbance. In this way, the proposed system would use small forces to suppress modal perturbations before they lead to stall.

The first systems to successfully employ this strategy to delay stall in axial compressors are reported by Paduano et al. (1993) and Day (1993b). Re-circulation systems using actively controlled re-injection are usually tailored to a specific stalling mechanism (e.g., Gysling and Greitzer (1995) and Weigl et al. (1998)) or applied to remedy a restricted operating range due to inlet distortion (Spakovsky et al. (1999a,b)).

The advantage of actively controlled re-injection compared to steady re-injection is that it has been shown in some cases to provide more stall margin improvement (Weigl et al. (1998)) and in others to provide the same stall margin improvement as steady injection, but with less re-circulated mass flow (Strazisar et al. (2004)).

Actively controlled re-injection has two major disadvantages, though: lack of durability and reliability. These factors are considered below.

Durability is important because a casing treatment integrated into an engine will be an important stall control device that must preserve the stall margin as the engine degrades. Freeman et al. (1998) found that the actuators needed for active control do not have the life span required for a flight worthy aero-engine. The cost and life cycle of the control system is therefore not compatible with the requirements of an aero-engine.

Research of a transonic single stage compressor by Weigl (1997) (published as Weigl et al. (1998)) achieved an increase in the stability margin using a feedback loop that analyzes harmonics in the flow. However, the author noted that this system is only effective when the mechanism of stall inception is modal in nature. As axial compressors often exhibit a wide range of stalling mechanisms (in addition to spikes and modes), Day et al. (1999) suggested that active control techniques are insufficiently reliable to suppress all possible forms of stall inception.

The above disadvantages have led to a decline in further research into the application of actively controlled re-injection systems. A general purpose passive treatment is a better option - provided, of course, that the problem of efficiency loss can be overcome.

Steady (Passive) Re-injection

Although the re-circulation studies focusing on active re-injection have been largely abandoned as unfeasible, some researchers (e.g., Weigl et al. (1998) and Spakovsky et al. (1999a,b)) demonstrated stall margin improvement with steady blowing systems. This section will discuss how the more recent passive re-injection

casing treatments reported in the literature have developed. The overall trend has been to gain more stall margin improvement for less flow re-injected.

Research on a transonic single stage compressor by Weigl et al. (1998) achieved an increase in the stability margin of 4.3% using steady injection of 3.6% of compressor mass flow at design speed.

A comprehensive numerical and experimental study on steady injection was published by Suder et al. (2001). They developed a system that injected 2% of annulus flow along the casing to increase the stability margin by 6% at design speed. This study correlated stall margin improvement with increased mass averaged axial velocity in the tip region. No correlation was found with injected momentum or injected mass flow.

Strazisar et al. (2004) demonstrated 4% to 6% stall margin improvement by injecting 0.7% to 1.3% of annulus flow in a highly loaded transonic rig.

In each of the above studies, the best stall margin improvement for the least injected mass flow is quoted.* A trend can be observed which shows each successive researcher has decreased the amount of air re-circulation required to affect the same stall margin improvement. Within each investigation, many configurations were tested. In each case, it was shown that the amount of re-injected flow could be reduced without affecting the stall margin improvement. This was achieved by reducing the radial extent of the jet (i.e., confining the injected air to the casing wall).

In particular, in the development process, Suder et al. (2001) showed that reducing the injector height (halving the injected mass flow and maintaining the same injected velocity) achieved nearly the same stall margin improvement. In the same compressor, Strazisar et al. (2004) improved on this; they confined the injected flow further to casing wall by using Coanda injectors (as opposed to sheet injectors, in which injected flow often separates from the casing wall). As a result, the improved system achieved the same stall margin improvement as Suder et al. (2001) for less flow re-circulated.

*Much higher stall margin improvements are found at part speeds in each case; however, the above comparisons are at design speed for consistency.

A large focus in the above research was on minimizing the amount of re-circulated mass flow required to achieve an adequate gain in stall margin. This is because, by entraining and re-circulating worked flow, casing treatments inevitably lead to a reduction in efficiency. Minimizing the re-circulated flow reduces the efficiency loss. In some axial compressors, a small stall margin improvement of 2 or 3% may be all that is required to correct a weak stage. However, even modest stall margin gains can lead to unacceptable losses, especially when the loss is incurred at design conditions. (A half percent loss of efficiency in an aero-engine compressor is totally unacceptable.)

Unfortunately, few studies in the open literature quote efficiencies for re-circulation systems. Those studies that do report efficiency have not performed extensive parametric studies to show what parameters of the re-circulation system effect the efficiency most, Hathaway (2002) and Dobrzynski et al. (2008).

Many avenues exist to develop the re-injection form of casing treatment further. The best axial location for the air extraction has not been investigated; past studies have set the extraction port downstream of the same rotor row as injection, or even one or more stages downstream. Parametric studies have instead largely focussed on the performance of isolated air injection. Clear recommendation for the parameters of the optimum injected jet cannot yet be made, though. Finally, the absence of consistent efficiency measurements means that the design trends affecting efficiency are unknown and therefore the viability of a re-circulation system is still an open question. These topics are investigated further in the current work.

2.4.3 Published Mechanisms of Stall Delay

This section reviews the various physical mechanisms attributed to the stall delay provided by casing treatments. Casing treatments were successfully applied well before the distinction of stall inception into modal and spike type patterns. It was, however, understood that casing treatments were most successful when applied to so-called "tip critical" compressors, i.e., compressors where stall initiated in the rotor tip region. It is now known that the maximum benefit of casing treatment is

only achieved if the compressor stalls by means of a spike type stalling mechanism (where inception occurs near the casing), Houghton and Day (2010).

Therefore, the following discussion is relevant to the physical mechanisms attributed to delaying spike type stall inception in particular. It was shown in Section 2.3.2 that there are three major mechanisms of stall inception discussed in the current literature: blockage growth (Khalid et al. (1999)), critical incidence (Camp and Day (1998)), or forward/backflow spillage (Vo (2001)). These stall inception mechanisms are reflected in the explanations of stall delay. The discussion in this section of the stall delay mechanisms is organized according to the most relevant proposed stall inception mechanism.

Shabbir and Adamczyk (2005) showed the blockage growth rate near stall is reduced in the presence of grooves. Assuming a link between blockage growth and stall inception, they concluded that the radial transport of axial momentum between the flow in the groove and near-casing region was the mechanism which allowed the compressor to operate at a lower flow coefficient. In a re-circulating system, Hathaway (2002) also linked stall delay to blockage reduction.

In an alternative view of the stall delay mechanism in a re-circulating system, Suder et al. (2001) found that flow injected upstream of the rotor tips increases stability by unloading the rotor tips. This follows the idea of critical incidence.

Seitz (1999) suggested that the mechanism for stall inception delay is entrainment by the slots of reversed flow in the tip region near the leading edges. Without entrainment, this fluid would spill forward of the blade and contribute to stall cell growth. This theory relies on the assumption that spike stall inception is due to flow spilling forward of the rotor leading edge.

This discussion is disjointed due to uncertainty in the stall inception process. Speculation can be made as to how dependent the various stall inception mechanisms are on each other and how casing treatments affect them. A unifying picture, however, remains to be drawn.

2.4.4 Casing Treatment Effectiveness

The review of casing treatments focused on stall margin improvement and the corresponding efficiency penalties. However, there are other benefits and challenges that casing treatments present.

As an aero-engine compressor degrades with age, the tip clearance gap increases. One valuable effect of casing treatment is the ability to desensitize the compressor to changes in tip clearance. This effect is reported for slots (Smith and Cumpsty (1984)), grooves (Fujita and Takata (1984)), and re-circulating designs (Strazisar et al. (2004)).

In the past, casing treatment has not been widely used in aero-engine compressors because the efficiency penalty often outweighs the benefits of stall margin improvement. In addition, designers have difficulty applying a suitable design for their situation, because the stall inception and delay mechanisms are not understood and nor can the stalling mechanism of a new machine be predicted computationally. Further difficulties arise, as Houghton (2010) found CFD simulations of the optimum location for a single circumferential groove predicted the opposite trend to that established experimentally.

As a result of this fundamental lack of understanding, the optimization of a casing treatment configuration to a given situation is still largely done by experimentation. This is carried out on both low-speed and high-speed machines, as past experience indicates that trends found in low-speed compressors apply to high-speed compressors, Greitzer et al. (1979) and Hathaway (2006).

The main difficulty of stability enhancement lies in the implementation of a design on a new compressor. The stability limit is unique to each compressor as is the flow mechanism leading to instability. Due to the highly unsteady and three-dimensional nature of the flow, CFD cannot reliably predict the stability limit of the compressor. The flow mechanism for stall delay remains as much a mystery as that for stall onset. In addition, experimental measurements characterizing the onset of compressor instability are usually not available at the design stage. Until these areas become more advanced, stability enhancement design remains largely an expensive and time consuming exercise in trial and error.

2.5 Scope for present Research

It has been shown that the present understanding of the tip clearance flow structure relies on experimental measurements near the tip region and computational predictions; direct measurement of the tip clearance flow field is rare and the accuracy limited.

In **Chapter 4**, new instrumentation and methodology are used to obtain detailed experimental flow field measurements in the tip clearance gap at design and near stall conditions. The examination of the unsteady behaviour of the flow field near stall is of particular interest; it has been shown in this review that the understanding of tip clearance flows near stall is limited by a lack of both experimental observation and accurate computational prediction.

It has also been shown that the mechanism of spike stall inception is poorly understood. There are multiple routes to stall and it is not yet known whether or how changes in the tip clearance flow prior to stall directly influence stall inception. The precise mechanisms of the blockage growth and critical incidence hypotheses are not clear, and the forward spillage criteria lends itself to muddled interpretation. It is not yet possible to create a unifying picture of the observations which have been made.

Current understanding of stall inception is based on the observation of trends leading up to stall, and the structure of the emerging stall cell. The greatest barrier to understanding spike stall inception is the lack of direct observation of the formation of the spike disturbance. Correcting this is one of the challenges of the present work.

In **Chapter 5**, the overtip flow field is investigated at the transient condition of stall inception. The initial growth of the disturbance which leads to stall is shown by direct observation for the first time. The methodology is outlined so that future experimental and computational studies might also study stall inception by direct observation.

Existing methods of stall delay were reviewed. Slot and groove casing treatments are relatively mature, while re-circulation systems pose an opportunity for ad-

vancement. The optimum parameters for both extraction and injection ports are in their infancy; no work has been done to examine their effects on the efficiency of the system. In addition, it has been shown that there is potential to re-circulate less mass flow (and thereby improve efficiency of the system) to achieve reasonable stall margin improvements.

Hence, **Chapter 6** investigates an advanced form of a re-circulation system. Improving stall margin while maintaining efficiency is the primary challenge a casing treatment must overcome. The new design approaches this by employing a passive means of regulating the re-circulated flow which takes advantage of knowledge gained from the overtip flow field results of Chapter 4.

The purpose of the work detailed in this dissertation is to improve the fundamental understanding of tip clearance flows and stall inception, and to develop an advanced form of casing treatment.

Chapter 3

Experimental Methods

3.1 Introduction

In the past, very little experimental data has been acquired in the rotor tip clearance gap because of complications posed by the close proximity of rotating blades and the casing wall. In the present work, a detailed experimental investigation is made of the flow field in the tip clearance gap. The purpose is to improve the understanding of the flow field in this region and to better understand the role of tip clearance flows in the stall inception process. Overtip static pressure contour maps have been acquired, as well as velocity and total pressure maps. The latter two are the first of their kind. An extensive array of instrumentation has also been used to observe the flow field during stall inception. Finally, these measurements were used in the development of a new form of casing treatment. A parametric study was carried out to optimize the casing treatment system, which included total-to-static pressure characteristics and efficiency measurements.

The aim of this chapter is to outline the facilities, instrumentation, and methodology used to acquire these results. Key instrumentation includes two new probes developed for this study: a miniature hot-wire and an unsteady total pressure probe. These probes were used to acquire the velocity and total pressure fields in the tip clearance gap. Of particular importance to the stall inception investigation are the procedures used to acquire many channels of data at high sampling

rates. The uncertainty of all measurements is estimated and shown to provide a high level of confidence in the results.

3.2 Research Compressors

This section is presented in two parts to describe the research compressors used in this work, the Deverson and Mini-Deverson compressors. The Deverson compressor is a 5 ft diameter single stage test rig. This large scale compressor was used to obtain detailed overtip pressure and velocity measurements and for preliminary optimization of the casing treatment. The Mini-Deverson compressor, as the name suggests, is a smaller scale version of the Deverson compressor. This smaller compressor was more practical for the full annular application of the casing treatment.

Both rigs model a low aspect ratio embedded stage as might be found in a high pressure compressor of an aero-engine. Fundamental differences between high-speed and low-speed tests exist in terms of Reynolds number and Mach number. However, years of experience in compressor stability research suggests that low-speed test results are reasonably indicative of the stability behaviour of high-speed compressors provided shock waves are not present, Day and Freeman (1994). Past experience also indicates that casing treatment function is not sensitive to compressibility effects; i.e., the function in a low-speed compressor is indicative of high-speed performance, Hathaway (2006).

3.2.1 Deverson Compressor

The Deverson compressor is a low-speed, single stage, axial flow compressor, as shown in Figure 3.1. The major features of the rig are listed in Table 3.1. The large diameter has many advantages. Of particular importance is the relatively large size of the rotor tip clearance gap at 1.4 mm from the casing to the rotor blade tips. This feature allows for adequate probe access and makes the Deverson compressor suitable for the detailed tip clearance gap measurements and stall

	Deverson	Mini-Deverson
IGV Blades	49	49
IGV Inlet Swirl	25°	25°
Rotor Blades	51	51
Stator Blades	49	49
Casing Diameter	5 ft, 1.524 m	0.45 m
Hub/Casing Ratio	0.8	0.8
Design Flow Coefficient, ϕ	0.510	0.510
Mid-span Stage Loading, ψ	0.456*	0.46†
Mid-span Stage Reaction, R	51.6%*	54.5%†
Rotor Tip Pitch/Chord Ratio	0.8	0.8
Rotor Tip Clearance	1.4 mm	0.5 mm
	0.9% Span	1.1% Span
	1.2% Tip Chord	1.4% Tip Chord
Reynolds Number, Re_{chord}	3.1 x 10^5	1.6 x 10^5

Table 3.1: Deverson Compressor Rig Features

inception investigations. In addition, this compressor was also useful in testing the initial casing treatment design concept.

A schematic of the rig from Bolger (1999) is shown in Figure 3.2 and described here. The bellmouth inlet is covered with a honeycomb supported gauze to filter dust and air-born particles from the incoming flow. The flow then passes through two further honeycomb sections to straighten the flow. The 9:1 passage area contraction leads to the 6 inch high parallel annulus where the blades are located. The inlet guide vanes are preceded upstream by a turbulence grid and followed downstream by hub and casing boundary layer blockage generators to simulate the boundary layer conditions found in an embedded stage.

The compressor may be opened just upstream of the rotor inlet plane as in Figure 3.1. The stator blades are fixed at the casing and sealed at the hub, positioned approximately 0.5 rotor axial chord lengths downstream of the rotor blade row. A pressure loss screen and honeycomb are used approximately 0.4 stator axial

*From Bolger (1999)
†From Dickens (2008)

chord lengths downstream of the stator blade row. This screen is intended to simulate the presence of a downstream stage. The parallel annulus continues approximately 15 stator axial chord lengths downstream where the flow is dumped into a small plenum chamber. A conical throttle valve and auxiliary fan allow the mass flow rate to be modified independently of rotor speed.

For more detailed information about the features necessary to model an embedded stage see Place (1997). Additional information about detailed steady flow measurements can be found in Bolger (1999) (see Build II).

3.2.2 Mini-Deverson Compressor

The Mini-Deverson compressor was used to optimize and evaluate the performance of the casing treatment in a full annular arrangement. The Mini-Deverson is a low-speed single stage scaled version of the Deverson compressor shown in Figure 3.3. As the two compressors are so similar, only their differences will be described briefly here.

Structurally, the most obvious difference is in the vertical build of the smaller compressor. Aside from this, the Mini-Deverson has a larger spacing between the rotor and stator blade rows (1.36 rotor axial chord lengths, compared to 0.51 in the Deverson). Also, the Mini-Deverson does not have an auxiliary fan, so it cannot support the pressure loss screen downstream of the stator blade row.

As seen in Table 3.1, the Mini-Deverson compressor is nearly identical to its counterpart in stage specifications and performance. The Reynolds number of the smaller rig is lower; however, this does not affect the similarities in performance of the two compressors. The pressure and efficiency characteristics of the two machines are nearly identical. Both machines exhibit spike type stall inception. It has also been shown that the radial profiles of axial velocity, stagnation pressure rise, and relative flow angle downstream of the rotor in the two compressors are nearly identical, Dickens (2008).

3.3 Data Acquisition

This section describes the system and procedures used to acquire, amplify, filter, and digitize data. The methods described in this section are relevant to all experiments conducted, but were most critical to the success of the stall inception investigation, where the acquisition of up to 48 channels required extra care to avoid ghosting and cross talk between channels.

Data was acquired through one of two systems. The first system consists of one 16 channel multiplexer connected to a 12 bit analogue to digital converter. This system was used for to acquire the pressure and velocity data for the flow maps presented in Chapter 4 and for the parametric study presented in Chapter 6. The second system consists of three 16 channel multiplexers connected to a 16 bit analogue to digital converter. This system was used to acquire the unsteady pressure data presented in Section 4.4 and for the stall inception investigation in Chapter 5.

For each configuration of instrumentation, data was sampled in an initial test run. Then, the following procedures were used to minimize uncertainty due to analogue to digital discretization, settling time and crosstalk, and aliasing.

To minimize uncertainty due to analogue to digital discretization, the gain settings on the instrumentation amplifiers were adjusted for each channel. The measured voltage range was set to be as close as possible to the voltage range of the analogue to digital conversion in order to maximize the number of discretization steps. This step is particularly important for the system with the 12 bit analogue to digital converter.

The sampling frequency and inter channel delay were adjusted to ensure that uncertainty due to settling time and crosstalk is negligible. This was done by exciting the probes on selected channels and increasing the inter channel delay and/or decreasing the sampling frequency until unexcited probes showed no response. The optimum set-up resulted in the following sampling frequencies. The detailed rotor overtip flow map measurements described in Chapter 4 were sampled at 40 kHz, equivalent to 94 samples per blade passing. The data for the unsteady flow variations presented in Section 4.4 and for the stall inception investigation in

Chapter 5 were sampled at 30 kHz, equivalent to 70 points per blade passing. The casing treatment measurements presented in Chapter 6 were sampled at 40 kHz, equivalent to 16 points per blade passing on the Mini-Deverson compressor. The lower resolution on the Mini-Deverson compressor is satisfactory for the pressure and efficiency characteristics measured.

In order to avoid aliasing, all unsteady measurements were low-pass filtered at 10 kHz. According to the Nyquist criteria, measurements sampled at 40 kHz and 30 kHz resolve frequencies up to 20 kHz and 15 kHz, respectively. Setting the low-pass filter below this level ensures that all signal content is either resolved or of negligible magnitude.

The above procedure ensures the maximum uncertainty in the data acquisition process is less than ±0.2% of the nominal signal voltage.

3.4 Rig Monitoring

This section describes how ambient and compressor conditions were monitored to ensure that measurements were conducted at consistent and repeatable conditions. The compressor mass flow rate, rotor speed, and lab conditions were monitored and recorded during testing.

Laboratory temperature and pressure were recorded before and after every test or at most every 15 minutes. The atmospheric pressure was read from a mercury barometer and the ambient temperature from thermocouples near the bellmouth inlet. The mass flow rate was maintained within ±0.3% of the target value for each test conducted at a constant mass flow rate. The uncertainty of nominal mass flow rate across test cases is ±0.7%. The measurement of the mass flow rate is discussed in Section 3.7.1.

A once per revolution signal on the rotor was used to obtain the speed of the rig. The speed of the rotor was set to within ±0.3% of the target value and monitored during each experimental run. The speed of the rotor did not vary more than ±0.03% within an experimental run.

3.5 Pressure Measurements

The instrumentation for pressure measurements is described in two parts: pneumatic probe measurements and fast response pressure transducer measurements. Each of these groups provides a description of the instrument and its use, the method of calibration, and its accuracy.

3.5.1 Pneumatic Probe Measurements

Steady pressure transducers were used to obtain measurements from static pressure tappings and Pitot probes to monitor the compressor performance. Static pressure at the compressor casing was measured with 1 mm bore tappings. In the case of monitoring the pressure upstream and downstream of the blade rows, six such tappings were distributed around the annulus at the same axial and circumferential position relative to the stator blades. Each set of tappings were connected to a manifold with equal lengths of tubing with 1 mm inner diameter.

Static pressure tappings were similarly used to monitor static pressure in calibration tunnels and Venturi probes as well. Pitot probes measuring total pressure were also connected to 1 mm tubing.

The pneumatic pressure lines were connected to digital manometers or pressure transducers calibrated against an inclined silicone manometer. The transducers used have a linear pressure to voltage response. The linear response is very robust over time, though the offset drifts slightly. The offset was recorded at no flow conditions before and after each experiment. The uncertainty due to drift is less than 0.1% of nominal measured values.

3.5.2 Fast Response Pressure Transducers

The fast response pressure transducers are manufactured by Kulite Semiconductor Products, Inc. The Kulite probes are often simply referred to as pressure transducers, or transducers, throughout this work. Unless noted, all fast response

pressure transducers used were 2.4 mm in diameter. The transducers were used both for static and total pressure measurements as described below.

Unsteady Static Pressure Measurements

For unsteady static pressure measurements, the pressure transducers were installed with the sensing screen flush with the surface of the casing. The analogue signal from the transducer passes through an amplifier and low-pass filter before being digitized, as described in Section 3.3. The voltage response of the pressure transducer varies linearly with pressure over the range of pressures measured. Each transducer was calibrated at four static pressure levels before and after every configuration set-up. The offset value was recorded at zero flow conditions before and after each experiment. Based on the manufacturer's data sheets, the maximum uncertainty of the probes is $\pm 0.7\%$ of inlet dynamic head.

Unsteady Total Pressure Measurements

A new probe was made to take unsteady total pressure measurements in the tip clearance gap. The probe is made up of a fast response pressure transducer embedded in a sheath with a low-profile stagnating head on it. The sensing diaphragm is placed as close to the stagnating Pitot head as possible. A profile view of the probe size relative to the tip clearance gap in the Deverson compressor is shown in Figure 3.4. The total pressure probe was rotated through 360° in 10° steps. The probe was calibrated and used similarly to a hot-wire, which will be described in the next section. The uncertainty of the measured total pressure when compared with a conventional boundary layer probe of similar proportions is $\pm 1.2\%$.

The major advantage of this probe is that it can fit in the tip clearance gap and the stagnation interface is at the centre of the axis of rotation. This probe resolves the flow direction in 360°, whereas a single hot-wire provides resolution in only 180°. Therefore, the flow angle results from the unsteady stagnation pressure probe were used to resolve the ambiguities in the flow angle results from the hot-wire.

3.6 Hot-Wire Measurements

This section describes a special miniature hot-wire probe developed in the Whittle Laboratory for tip clearance gap measurements. The new probe made experimental measurements possible that provide greater detail than previously available in this region. This section is described in four parts: (1) the hot-wire probe construction; (2) calibration procedures; (3) algorithm to determine velocity magnitude and direction; and (4) estimation of uncertainty.

3.6.1 Miniature Hot-Wire Construction

The new hot-wire probe has two distinguishing features. First, the stem, or body of the probe, fills the access hole and maintains a smooth surface with the casing wall; see Figure 3.5. When using a conventional hot-wire probe for near wall measurements, there is usually an air gap between the probe stem and the access hole. This leads to re-circulating flows and inaccurate measurements. Second, the prongs which support the sensing wire are adjustable in length during operation and so measurements at various heights from the casing wall are easily obtained.

The height of the hot-wire from the flat surface of the probe and the casing wall was traversed from 0.3 mm to over 1.5 mm. This feature was used to investigate the flow in the rotor tip clearance gap at three radial planes: 25%, 50% and 75% of the tip clearance gap.

Additional low profile hot-wire probes were also developed for tip clearance measurements which required multiple probes to be used at one time. The face of the probe stem was again flush with the casing wall. The only difference between these additional probes to the probe described above is the absence of the traverse capability. The height of the hot-wire prongs in these probes was set at various lengths from 0.5 mm to 5.5 mm.

3.6.2 Miniature Hot-Wire Calibration Procedures

The hot-wire was calibrated in a small wind tunnel with a known boundary layer profile. When calibrating, the flat surface of the probe perpendicular to the hot-wire prongs was always flush with the tunnel wall - as it would be in the compressor casing. The hot-wire was positioned perpendicular to the flow to get a voltage to velocity calibration. A curve fit adapted from King's Law as recommended by Bruun (1995) was used:

$$E^2 = a + bV^n \tag{3.1}$$

where E is the raw hot-wire voltage, a, b and n are constants, and V is the velocity at the position of the hot-wire from the wall. Calibration was carried out at each of the radial positions that would be used during the compressor tests, i.e., at 25%, 50% and 75% of tip clearance height. The ambient temperature was maintained to within $\pm 0.5^\circ$ of the calibrated temperature. The uncertainty in the velocity magnitude as a result of calibration was found to be less than $\pm 3\%$ of nominal velocity values for measurements at constant flow coefficients.

The response of the hot-wires to a square wave signal was between 12,000 and 16,000 Hz. According to Bruun (1995), the hot-wire frequency response sets the maximum cut-off value for the low-pass filter. The signal was therefore low-pass filtered at 10 kHz.

3.6.3 Hot-Wire Signal Processing

This section describes the procedure and algorithm used to resolve the flow velocity magnitude and angle from a single hot-wire. The algorithm applies to any number (2 or more) of hot-wire orientations and is similar to the least squares method described by Dambach and Hodson (1999).

First, the data for all hot-wire orientations was prepared (re-interpolated, calibrated, non-dimensionalized, and ensemble averaged) according to the procedures to be outlined in Section 3.9. For example, the hot-wire results of Chapter 4 are

based on 21 hot-wire orientations, each 10° apart. Fifty rotor revolutions were recorded for each hot-wire orientation. The data for each hot-wire orientation were first re-interpolated to 64 points per blade passage. After calibration and non-dimensionalization, they were then ensemble averaged (phase locked to the rotor). The result is 21 sets of ensemble averaged data for a rotor revolution (51 rotor blade passages, 64 points per blade passage). At each pitchwise location in the set, the data from all hot-wire orientations were used to obtain the magnitude and direction of the flow velocity as outlined below.

The method is based on the result presented by Bruun (1995) that the effective velocity measured by the hot-wire is approximately equal to the component of the velocity vector perpendicular to the sensing wire:

$$V_m = V cos(\alpha - \beta) \tag{3.2}$$

where V is the magnitude of the velocity vector, V_m is the effective velocity measured by the hot-wire, α is the flow angle, and β is the angle of the hot-wire. These definitions are illustrated in Figure 3.6 in the plane normal to the hot-wire prongs, which for this experiment is the "plane" of the casing near the probe.

It follows from Equation 3.2 that if the hot-wire is turned through 180°, the signals from each hot-wire orientation form a cosine curve. This is illustrated in Figure 3.7, left. When the flow aligns with the hot-wire the voltage is at a minimum, and when the flow is perpendicular to the hot-wire the voltage is at a maximum. This curve can be linearized by transforming the x and y axes (shown in Figure 3.7, right). The transformation is described below as well as the application of using it to extract the magnitude and direction of the flow velocity.

Equation 3.2 may be simplified with trigonometry:

$$V_m = V cos(\alpha) cos(\beta) + V sin(\alpha) sin(\beta) \tag{3.3}$$

Dividing by $cos(\beta)$ yields:

$$\frac{V_m}{cos(\beta)} = V cos(\alpha) + V sin(\alpha) tan(\beta) \tag{3.4}$$

Equation 3.4 is linear in the form:

$$y = c + mx \tag{3.5}$$

where

$$y = \frac{V_m}{cos(\beta)}$$
$$x = tan(\beta)$$
$$c = V cos(\alpha)$$
$$m = V sin(\alpha)$$

After the axes have been transformed, a straight line fit using the least squares method will yield the slope, m, and y-intercept, c. Using the definitions for m and c above, the flow angle, α, and magnitude of the flow velocity, V, can then be calculated. Ambiguity in the flow direction due to the symmetry of the hot-wire was removed with measurements from the unsteady total pressure probe described earlier.

As can be seen, this method assumes there is no radial component of velocity and no cooling from velocity components parallel to the hot-wire. The resulting error is an overestimation of V_m and therefore also an overestimation of the velocity magnitude, V. Measurements closest to the casing will have minimal uncertainty from the radial velocity component.

For the rotor over tip flow field investigation of Chapter 4 (where 21 hot-wire orientations were ensemble averaged over 50 rotor revolutions), the uncertainty in the calculation of the ensemble averaged angle is $\pm 0.2°$. This is based on a simulated signal tested in the algorithm, and on multiple angular calibration tests. The alignment of the hot-wire in the machine is accurate to $\pm 0.5°$. These sources of uncertainty are combined, and the maximum uncertainty is estimated to be $\pm 0.7°$.

The investigation described in Chapter 4 uses 21 hot-wire orientations, but it is possible to use as few as two to resolve the flow field. Using fewer hot-wire orientations to determine the flow vectors would be a considerable advantage in situations where acquiring sufficient data is a problem. Just such a situation arises when repeated stalling events are recorded for the purpose of deriving an instantaneous picture of the origins of a spike-type disturbance. It will be explained in Chapter 5 how selected samples from hundreds of stalling events are used to produce such a figure. For a time intensive process such as this, the use of fewer than 21 orientations is a great advantage. The section below discusses

the inevitable decline in measurement uncertainty that accompanies the use of data from fewer hot-wire orientations.

Flow Angle Uncertainty for Measurements at Stall Inception

Stall inception is a transitory event and so vectors created from ensemble averaged traces at multiple hot-wire orientations must be done very carefully. In order to obtain accurate vectors of the flow field in and around a spike disturbance, it is necessary to make repeated measurements of the spike at the same stage in its development. Suitably repeatable stall events were selected by comparing raw pressure and hot-wire traces as will be described in Chapter 5. This criteria necessarily limited the number of ensemble averages and hot-wire orientations available.

For the stall inception investigation of Chapter 5, four angular orientations were used for each axial and circumferential position of the hot-wire. At each angular orientations, two repeatable events were obtained to form the ensemble average. The uncertainty in the vector angle was found to be $\pm 9^\circ$ at the leading edge and $\pm 4.5^\circ$ at the trailing edge. Considering the flow vectors change by more than 180° within a blade pitch at the leading edge, the uncertainty, though much higher than for measurements at a constant flow coefficient, is within a reasonable range to make general observations of the flow field. The method used to estimate this uncertainty is described below, as well as additional steps to ensure confidence in the results.

In order to estimate the uncertainty in the calculation of the flow angle, data for the flow field near stall (at a stable condition) was used. At these conditions, data exists for 50 rotor revolutions at each of 21 hot-wire orientations. From the 21 hot-wire orientations available, data for 4 equidistant hot-wire orientations were selected to calculate the angle again (also using 50 ensemble averages). As the vectors derived from 21 hot-wire orientations were found to be robust, these vectors are used as a control set for comparison. It was found that the vectors using only 4 hot-wire orientations varied from the control set by $\pm 3.5^\circ$ at the leading edge and $\pm 1.5^\circ$ near the trailing edge.

Next, using the same 4 hot-wire orientations, the number of ensemble averages were steadily reduced to estimate the effect on uncertainty. At the leading edge, reducing the number of traces used in the ensemble average from 50 to 8 only increased the uncertainty to $\pm 5°$. Using 3 traces increases the uncertainty to $\pm 7.5°$, for two traces the uncertainty is $\pm 9°$, and for a single trace (no ensemble average), the uncertainty is $\pm 11°$. For every 10 stall events, it was found that the repeatable stall event was found in anywhere from 2 to 6 of the cases. While the uncertainty increases for fewer ensembles, it is not unreasonable and it was decided to use 2 traces for each hot-wire orientation to calculate the vectors.

The reliability of the velocity vectors was also ensured in the following way. When calculating the vectors for the stall inception event, the results of the algorithm were double checked in the following way. As was discussed above, the algorithm calculates the flow vectors for each pitchwise location. For the stall inception investigation, four values (from the ensembles at each of the four hot-wire orientations) were input. These four values theoretically lie on a cosine curve, as discussed above in Section 3.6.3 with Figure 3.7. In the region of the spike, the four values for selected pitchwise locations were checked by eye to ensure that they followed an approximate cosine pattern. (If they didn't, then this would imply that the algorithm was simply producing meaningless numbers). The raw hot-wire traces at the spike were also compared to the final vectors at the spike to ensure that the picture made sense, i.e., that appropriate dips and peaks were observed in the signal where the vectors showed changes in flow direction. In this way, a high level of confidence in the vectors and this method of analysis was established.

3.7 Compressor Performance

Total-to-static pressure rise characteristics were used to monitor and compare the compressor performance of both compressors used. The stall margin improvement, based on the stalling flow coefficient, was used to determine which casing treatment provided the greatest benefit near stall. Efficiency characteristics were used to determine which design imparted the lowest penalty to maximum efficiency.

3.7.1 Total-to-Static Pressure Rise Characteristics

Total-to-static pressure rise characteristics were measured by continuously recording the inlet and casing pressures as the flow rate was slowly reduced. The pressure rise across the stage increases as the mass flow decreases until the stability limit is reached. At this point the compressor stalls, leading to a collapse of the pressure rise across the stage. Once the stability limit is exceeded, the compressor will operate in rotating stall even when the throttle is opened again to increase the mass flow rate. As the flow rate increases, a point is reached at which the operating point will suddenly recover to the stable characteristic. The data points obtained for a typical total-to-static pressure rise characteristic in the Deverson compressor are shown in Figure 3.8. A curve fit through the stable range of continuously obtained points represents the characteristic. The non-dimensional parameters used for the mass flow rate and pressure rise are described below.

The mass flow rate, $\dot{m}$, is defined:

$$\dot{m} = \rho A V_x = k\sqrt{\rho \Delta P} \tag{3.6}$$

where ρ is density, A is the inlet flow area, V_x is the average axial velocity at inlet, ΔP is the change in pressure across the bellmouth, and k is a constant.

In the Deverson compressor, the bellmouth pressure difference $\Delta P = p_{a1} - p_{d2}$ was used to monitor the inlet mass flow using p_{a1} and p_{d2}, two casing static pressures at the bellmouth inlet and exit, respectively. The subscript letters are maintained to be consistent with past Deverson theses and the labelling on the rig. The change in pressure across the bellmouth was correlated with the area averaged flow rate by Place (1997) using $k = 0.9091$.

In the Mini-Deverson compressor, the inlet mass flow was monitored with the bellmouth pressure difference $\Delta P = P_{o,in} - p$. In this case $P_{o,in}$ is the total pressure at the bellmouth inlet (downstream of the inlet flow straightener) as measured by three Pitot probes equally spaced around the circumference. The static pressure at the exit of the bellmouth (in the parallel section of the annulus) was obtained from six equidistant circumferential static tappings. The change in

pressure across the bellmouth was correlated to the flow rate by Dickens (2008) using $k = 0.0794$.

The change in pressure across the bellmouth, ΔP, is measured as a differential pressure on a digital manometer. The same measuring instrument was used on both compressors.

When used to present a pressure rise characteristic, the mass flow rate is expressed in non-dimensional form by the flow coefficient, ϕ as

$$\phi = \frac{\dot{m}}{\rho A U_{mid}} = \frac{V_x}{U_{mid}} \tag{3.7}$$

where U_{mid} is the blade velocity at mid-span.

The total-to-static pressure rise across the compressor is expressed by the non-dimensional pressure rise coefficient, Ψ as

$$\Psi = \frac{p_3 - P_{0,in}}{\frac{1}{2}\rho U_{mid}^2} \tag{3.8}$$

where p_3 is the stator exit static pressure and $P_{0,in}$ is the inlet total pressure. The pressure rise across the stage is again measured as a differential pressure on a second digital manometer.

Using the Kline & McClintock uncertainty method, as described by Beckwith et al. (1995), the uncertainties of the flow coefficient, ϕ, and the pressure rise coefficient, Ψ, are both within $\pm 0.6\%$ of their nominal values.

3.7.2 Stall Margin Improvement

For each casing treatment arrangement evaluated, the stability limit of the compressor operating with the casing treatment was compared to the stability limit of the compressor without the treatment (the "smooth wall" case). The stall

margin improvement, SMI, is calculated as follows:

$$SMI = \frac{\phi_{s,datum} - \phi_s}{\phi_{s,datum}} \tag{3.9}$$

where ϕ_s is the stalling flow coefficient with casing treatment and $\phi_{s,datum}$ is the stalling flow coefficient of the smooth wall configuration.

In all cases to be presented in Chapter 6, the measurement of the characteristic curve was repeated several times to obtain the stalling flow coefficients. The coefficient values used to calculate the SMI were averaged values to ensure representative results.

3.7.3 Efficiency Characteristics for the Mini-Deverson Compressor

Efficiency characteristics were measured to compare the performance of the compressor with and without casing treatment. The efficiency, η, is calculated using the shaft torque, T, and the change in static pressure across the stage, ΔP:

$$\eta = \frac{\dot{m}\Delta P}{\rho T \omega} \tag{3.10}$$

As the absolute Mach number through the compressor is relatively low (< 0.1), the flow was assumed to have constant density which was calculated from laboratory temperature and pressure.

In each figure to be presented in Chapter 6, the efficiency characteristic for each casing treatment configuration has been tested back-to-back with the smooth wall case. By "back-to-back" testing is meant that the smooth wall case was measured at the beginning and end of each set of measurements. Any set with a significant change (greater than 0.2%) in the efficiency and mass flow measurements from beginning to end was discarded. The efficiency of the compressor with casing treatment installed is thus always relative to the efficiency of the smooth wall case. This minimizes uncertainty across compressor builds as the results do not depend on absolute efficiency values.

3.8 Procedure for Stalling the Compressor and Recording the Results

This section describes the procedures used to record a stall inception event and to distinguish spikes and modes. The following method was used to provide consistent and repeatable results.

The compressor is slowly throttled very near to stall. The compressor runs at this flow coefficient very near to stall for a limited amount of time before a naturally occurring random disturbance causes the machine to stall. Meanwhile, the instrumentation logs continuously to a buffer. When the stall occurs, the data logging system is tripped and the previous 100 revolution of data are saved.

3.9 Processing Unsteady Data

The unsteady data is presented in raw form as well as used to produce statistics, contour maps and velocity vectors of the overtip flow field. Preliminary processing was applied first to overcome the complexities of comparing data taken from different tests and on different days. This includes re-interpolation, calibration, and non-dimensionalization, which are used to process all data before it is processed further or presented. Calibration has been described for each instrument in the previous section, and non-dimensionalization parameters are displayed with the results. Re-interpolation is described below.

All data was recorded relative to a rotor revolution trip as described in Section 3.3. Due to the discrete nature of sampling and small fluctuations in rotor speed over time, there is a discrete variation in the number of samples per revolution (e.g., 4000 ± 1 samples per revolution). In order to compare data across rotor revolutions, and to compute statistical properties, the raw data points are re-interpolated so that each rotor revolution has the same number of points and each point occurs at the same physical location for subsequent revolutions. All sampled points were re-interpolated to 64 points per blade passing (3264 points

per revolution). This allows for more accurate ensemble averaging and statistical analysis of the signal.

3.10 Summary

This chapter outlined the methods used to obtain previously unavailable measurements in the tip clearance gap. The measurements were also used to develop a new casing treatment design. The facilities and new instrumentation which made this investigation possible have been described. A new miniature hot-wire probe and a new unsteady total pressure probe were shown to be of particular importance in achieving these delicate measurements. With these new probes, a large number of unsteady static pressure transducers, and a sophisticated data acquisition system, an advanced approach to investigating tip clearance flows and stall inception has been made possible.

Chapter 4

Rotor Overtip Flow Maps

4.1 Introduction

In the small space of the tip clearance gap, between the sweep of the compressor rotor blade tips and the outer casing wall, is a region of dynamic flow influenced by many factors. The incoming mainstream flow is opposed by flow driven in the opposite direction by the pressure difference across the blade tip (from the pressure side to the suction side) and by the pressure difference across the blade row (from the trailing edge to the leading edge). These flows interact in a viscous and highly turbulent manner to create a resistance to the mainstream flow. This resistance, or blockage, is in the form of velocity deficit to the mainstream flow and opposing momentum, a major source of loss affecting efficiency (Khalid et al. (1999); Storer and Cumpsty (1994)).

Blockage reducing the core flow area has far reaching effects. The diversion of flow reduces the possible work input and alters the radial loading distribution. As a consequence, the stage pressure rise and mass flow capacity are limited. Changes in the size of the tip clearance gap have also been shown to alter the stability limit of the machine (Freeman (1985)), and the tip clearance flow itself is often cited as having an influence on the stalling mechanism (Greitzer et al. (1979); Shabbir and Adamczyk (2005); Vo et al. (2008)). These effects contribute to the continued interest in tip clearance flow research.

Direct experimental measurements in the tip clearance region are extremely difficult: probe placement is restricted by the physical constraint of the small tip clearance height and the moving blades. The experiment also carries an increased risk, as the damage for a mistake may range from the ruin of a probe to a rotor blade-off and the resulting destruction of the entire stage.

As a result, much effort has been expended to study tip clearance flows and their effects through analytical and computational methods. Simple models of the tip clearance flow were developed to be used in conjunction with steady flow calculations (Chen et al. (1991); Storer and Cumpsty (1991)); ever increasing computer power and resources has seen the rise of CFD solutions which include the tip clearance flow (Gourdain et al. (2006)). The calculations often strive to study the influence of the tip clearance flow on loss mechanisms (including the formation, character and breakdown of the tip leakage vortex, such as Furukawa et al. (1999)) and stall inception (e.g., Vo et al. (2008)). Although computational methods have made great strides, experimental results remain the benchmark of stall inception research.

Past experimental work on clearance flows has mostly been based on measurements taken downstream of the rotor row or in cascades (Deppe et al. (2005); Lakshminarayana et al. (1995); Storer (1991)). Little experimental work has been done in the tip clearance gap itself because of the difficulties described above. This chapter describes the results of a detailed experimental investigation of the tip clearance flow. The purpose is to advance the fundamental knowledge of tip clearance flows, in particular as stall is approached. Three measurement techniques have been employed to build up a detailed map of the flow field in the tip clearance gap: static pressure measurements on the casing wall, total pressure measurements, and hot-wire surveys in the tip clearance gap. Overtip static pressure maps may be familiar measurements in the tip clearance gap (e.g., Seitz (1999)); however, hot-wire and total pressure measurements in this region have not been previously reported.

This chapter is set out as follows:

1) The novel measurement techniques are described which were used to obtain a complete set of pressure and velocity maps for the flow in the tip clearance gap

at two flow coefficients: design and near stall.

2) The ensemble averaged pressure and velocity flow maps are examined and changes in the tip clearance flow field that occur when the compressor is throttled from design to near stall conditions are discussed.

3) Unsteady and non-uniform effects are discussed by examining circumferential and passage to passage flow variations.

The results presented here increase the understanding of the fundamental flow physics in the tip clearance region, and are integral to the stall inception and casing treatment investigations presented in the chapters to follow. It will be shown in this chapter that as stall is approached, the trajectory of the tip leakage vortex (and the incoming/reversed flow interface) does not become parallel with the rotor leading edges. This indicates that forward spillage as a criteria for spike stall inception as proposed by Vo (see Section 2.3.2) is unlikely to be valid in this compressor. This will be explored further in the stall inception investigation presented in Chapter 5. The results in the present chapter also show an increase in flow irregularity as stall is approached, which will be related to the stall inception investigation as well.

The changes in the flow field observed between design and near stall conditions are also of interest to the the casing treatment investigation presented in Chapter 6. The changing flow field is exploited to enable a self-regulating re-circulation in the new casing treatment.

4.2 Methodology for Rotor Overtip Ensemble Averaged Results

The flow in the tip clearance gap is vigorous and the acquisition of reliable data is not straight forward. This section will discuss the experimental methodology and the new instrumentation which were used to achieve detailed pressure and velocity measurements in the rotor tip clearance gap. For the sake of brevity, only the most important information needed to understand the results is outlined

here; more details from the relevant sections of Chapter 3 will be referenced as appropriate.

The investigation was carried out on the Deverson compressor, a large single stage research compressor. The large size of the machine (5 ft in diameter) means that the tip clearance gap is also relatively large (1.4 mm), making it possible to take detailed measurements in the gap between the tips of the moving blades and the casing wall. A total-to-static pressure characteristic for the Deverson compressor is shown in Figure 3.8. The two specific flow coefficients are marked on the figure at which the detailed rotor overtip flow maps were obtained. Conditions near the compressor design were investigated at $\phi = 0.50$. Conditions were also investigated at the lowest stable flow coefficient, $\phi = 0.43$. The compressor is increasingly likely to stall at flow coefficients lower than this.

A schematic view of the blade tips projected on the casing wall is shown in Figure 4.1. Vectors show the axial direction, blade rotation, and the mainstream velocity vectors in the absolute and relative reference frame. All overtip flow map results are presented from this perspective. Thirteen axial probe positions were used to investigate the flow in this region; these are numbered in the figure. This axial array of probe access holes is located at circumferential position 1, as shown on the right hand side of Figure 4.1.

Three measurement probes were used: a fast response pressure transducer, an unsteady total pressure probe, and a miniature hot-wire (Section 3.5). The three probes were not installed simultaneously, but one at a time. Measurements were obtained by moving the probe to each of 13 positions distributed from the leading to the trailing edge of the blade shown in Figure 4.1. The unused probe access holes were plugged to maintain a smooth casing.

The specific procedures for each probe are described in turn below.

4.2.1 Static Pressure Measurements

The pressure measurements produce contour maps of casing wall static pressure as blades pass the measuring location.

The unsteady pressure is measured with a single pressure transducer mounted flush with the casing wall and inserted in each of 13 positions, as shown in Figure 4.1. At each of the 13 positions, the transducer was sampled at the design and near stall flow coefficients, making 26 test cases in total for this probe. Each test case was sampled for 50 rotor revolutions, at a rate providing 94 sample points per blade pitch.

The measurements from each test case were calibrated, non-dimensionalized, and re-interpolated to give 64 points per blade pitch (Section 3.9). The measurements were then ensemble averaged (phase-locked to the rotor) to give an ensemble result for each blade in the rotor. For each flow coefficient, the ensemble averaged pressure traces for each axial position were then used to produce two-dimensional contour maps of casing static pressure, i.e., Figures 4.2 and 4.3.

4.2.2 Total Pressure Measurements

Unsteady total pressure measurements were used to determine the flow direction and to produce contour maps of total pressure in the tip clearance gap at mid-height.

The unsteady total pressure is measured with a fast response pressure transducer embedded in a sheath with a Pitot head attached (Section 3.5). The opening is at tip clearance mid-height and at the centre of the probe's rotational axis.

At each of the 13 axial positions, and the two flow coefficients discussed above, the total pressure probe was rotated in 10° steps through 360° (36 probe orientations). Thus, there are 26 (2x13) "sets", each set consisting of 36 probe orientations. This makes 936 (36x26) test cases in total for this probe. Each test case was sampled for 50 rotor revolutions, at a rate providing 94 sample points per blade pitch.

The data for each test case were calibrated, non-dimensionalized, and re-interpolated to 64 points per blade pitch, then ensemble averaged (Section 3.9). Each data set (consisting of measurements from the 36 probe orientations) was then processed to determine the total pressure and flow angle (Section 3.6.3). This results in 26 pitchwise traces (each with 64 points per blade pitch) of total pressure and

flow angle. The total pressure traces were then used to produce two-dimensional contour maps of total pressure at both flow coefficients, i.e., Figures 4.4 and 4.5. The use of the flow angle data will be described below.

4.2.3 Miniature Hot-Wire Measurements

A special miniature hot-wire probe was used to obtain velocity vector maps at three radial positions in the tip clearance gap.

The angle of the flow in the rotor tip clearance gap varies considerably with the passing of each rotor blade. A special miniature hot-wire probe was designed for these measurements (Section 3.5). Parallel prongs (which the hot-wire spans) protrude from a flat surface which seals and remains flush with the casing during measurement. The prongs themselves are traversable, allowing measurements at varying radial positions while maintaining a smooth casing wall. This new probe design eliminates the cavity effect a standard hot-wire would have on the near casing flow field and eliminates the effect of stem blockage.

At each of the 13 axial positions, and the two flow coefficients discussed above, the hot-wire measurements were conducted at three radial positions, 25%, 50% and 75% of the tip clearance gap. This makes 78 (13x2x3) "sets". For each set, the hot-wire was rotated in 10° steps through 200° (21 probe orientations) to obtain the maximum accuracy in velocity magnitude and direction. Thus, there are 1638 (78x21) test cases in total for this probe. Each test case was sampled for 50 rotor revolutions, at a rate providing 94 sample points per blade pitch.

The data for each test case were calibrated, non-dimensionalized, and re-interpolated to 64 points per blade pitch, then ensemble averaged (Section 3.9). Each of the 78 data sets (each consisting of measurements from the 21 probe orientations) was then processed to determine the velocity magnitude and angle (Section 3.6.3). This results in 78 pitchwise traces (each with 64 points per blade pitch) of velocity magnitude and angle.

The flow angles obtained from the hot-wire probe are more accurate than those from the total pressure probe. However, the hot-wire angles are ambiguous by

180° due to the symmetry of the single hot-wire. All flow angles were therefore compared with those obtained from the total pressure probe and given the correct flow orientation.

The resulting traces were used to produce two-dimensional ensemble averaged vector maps of the flow at three radial planes in the tip clearance gap for two flow coefficients, i.e., Figures 4.6 to 4.11. These measurements are thought to be the first of their kind.

4.3 The Ensemble Averaged Overtip Flow Field

Ensemble averaged flow maps are presented in this section for the static pressure, total pressure, and velocity fields. The static pressure and total pressure contours are presented first. When the velocity measurements are presented, they are superimposed on the static pressure contours. This is done so that features from both fields can be compared directly. In all figures, a blade tip profile is superimposed on the maps for reference. A tip speed vector (U) is shown to indicate the direction of blade rotation and as a scaled reference for the velocity vectors. The perspective of the flow field maps is as if the casing surface is viewed radially outwards looking from the centre of the machine.

4.3.1 Static Pressure Maps

The static pressure contours at the design flow coefficient ($\phi = 0.50$) are shown in Figure 4.2. From the leading edge to the trailing edge, the pitchwise pressure increases on average as the flow passes through the rotor. The most apparent feature in the pressure topology is the steep pressure gradient from the pressure side of the blade (high pressure, red) to the suction side (low pressure, blue). The maximum pressure difference across the blade is seen to occur at about 20% axial chord downstream of the leading edge. In this and the following figures, the trajectory of the tip leakage vortex is recognized by a low pressure core that originates from the peak suction of the convex side of the blade and reaches

toward the pressure side of the next blade. In Figure 4.2 the trajectory of the tip leakage vortex is emphasized by a black arrow.

The flow field at the near stall coefficient ($\phi = 0.43$) is shown in Figure 4.3. The pressure scale is the same as in Figure 4.2 so that pressure magnitudes can be compared between the two figures. The overall pressure rise across the blade row is now higher as a result of the compressor operating point having moved up the pressure rise characteristic. In comparison with conditions at design, the near stall static pressure field in Figure 4.3 shows that the maximum pressure difference across the blade tip has increased and has moved toward the leading edge. It is now at about 10% axial chord. The trajectory of the tip leakage vortex has turned further from the axial direction by about 8°; however, it remains within the passage.

4.3.2 Total Pressure Maps

The total pressure contours at mid-height for design and near stall conditions are shown in Figures 4.4 and 4.5, respectively.

The overall total pressure increases from the leading to the trailing edge as the blades do work on the flow. A large region of low pressure (blue) is seen on the suction side of the blade. This indicates the loss of total pressure as flow diverts over the blade tip. The greatest losses in the tip clearance gap are indicated by the low total pressure region that extends from under the blade tip to the suction side of the blade, and along the trajectory of the tip leakage vortex. The trajectory of the vortex is again marked by a black arrow in both figures. As before, the trajectory at near stall conditions is turned about 8° more from the axial direction than at near design.

4.3.3 Velocity Flow Maps

The velocity flow maps are presented in two groups: "absolute" vectors referenced to the casing wall (Figures 4.6 to 4.11), and "relative" vectors referenced to the rotor blade tip (Figures 4.12 to 4.17). Six flow maps in each group represent

the flow field at three radial depths (25%, 50% and 75% tip gap height from the casing wall), each at two flow coefficients. In all figures, the flow vectors are superimposed on static pressure contours. The scale of the vectors is consistent across all figures.

Absolute Velocity Field

Skipping Figures 4.6 and 4.7 for the moment, Figure 4.8 shows the absolute velocity field near design conditions at 50% tip clearance. Three main regions labelled on the flow maps are of interest. Region A is the inlet flow penetrating into the passage relatively undisturbed. The flow is at an angle due to swirl introduced by the inlet guide vanes. In Region B, flow leaking over the blade tip from the pressure side to the suction side gives rise to reversed flow vectors that oppose the incoming flow. This jet of leakage flow is driven by the pressure difference across the blade. Approaching the rear of the blade the flow becomes more tangential (Region C). The tendency for the flow to leak forward from the high pressure at the rear of the passage is balanced by the through flow dragging it axially downstream.

As can be seen, the reversed leakage flow is strongest near the maximum pressure difference across the blade. This reversed flow from Region B directly opposes the incoming flow from Region A. A dashed line is marked where the two flows meet (where the flow direction changes abruptly). Where the two flows meet, the flow must separate away from the casing wall. This lift-off line is parallel to the tip leakage vortex core (the trajectory of which, as before, is marked with an arrow). As the flow separates away from the casing wall it is swept axially downstream by the main through flow, wrapping around to form the tip leakage vortex. Hence, the core of the vortex is parallel to, and downstream of, the lift-off line.

In contrast, the equivalent flow field at near stall conditions is shown in Figure 4.9. It is observed that the maximum pressure difference across the blade tip has intensified and moved toward the leading edge. The result is that the reverse flow vectors in Region B near stall are larger and extend further across the blade passage than at design conditions. As before, the leakage vortex trajectory has

shifted, but remains within the blade passage. Another important change between the conditions near design in Figure 4.8 and those near stall in Figure 4.9 is the tip clearance flow at the rear of the blade row. A significant amount of reversed flow is now indicated, dominating the aft portion of the blade passage (Region C). This flow may be driven by the pressure difference across the blade row, from the trailing edge to the leading edge. This reversed flow meets less resistance from the through flow which is now weaker as a result of throttling.

It is worth noting that the casing static pressure field reflects both the strong pressure field within the passage and the tip clearance flow. This is most apparent in Region B, where the low pressure in the blade tip region cannot be explained by the low pressure on the suction side of the blade. Rather, it is thought that the acceleration of the flow moving across the blade tips causes the low static pressure in this region.

Velocity Field at Three Radial Positions

The major features of the flow maps discussed above are also found at the other measurement planes. Flow maps at near design conditions at planes from 25% tip clearance (near casing wall), 50% tip clearance, and 75% tip clearance (near blade tips) are shown in Figures 4.6, 4.8, and 4.10. At near stall conditions, equivalent flow maps in the three planes are shown in Figures 4.7, 4.9, and 4.11. Examining the flow field from near the casing to near the blade tip reveals an increase in most velocity magnitudes, most marked in the reversed flow originating from the rear of the passage, Region C. The radial velocity gradient observed throughout most of the flow in the tip clearance gap indicates that much of the tip clearance flow is shear layer flow.

With increasing distance from the wall, it is increasingly likely that a component of the velocity is in the radial direction. This is especially true in regions where the flow changes directions suddenly such as along the pressure side of the blade and along the dashed lift-off line in Figures 4.8 and 4.9.

The tip clearance flow maps, discussed thus far from the perspective from the casing wall, show a very dynamic flow field driven by the continuous cycle of

passing blades and the vigorous pressure fields they create. The tip clearance flow field will now be discussed from the perspective of the rotor blades.

Relative Velocity Field

Figures 4.12 to 4.17 show the tip clearance flow field from the rotor frame of reference. As with the absolute reference frame figures, they are arranged according to radial position and mass flow conditions.

At near design conditions, relative frame flow maps for planes at 25% tip clearance (near casing wall), 50% tip clearance, and 75% tip clearance (near blade tips) are shown in Figures 4.12, 4.14, and 4.16. The flow fields at 25% and 50% tip clearance are very similar (Figures 4.12 and 4.14). The flow field at 75% tip clearance is slightly different; compare Figures 4.14 and 4.16. The extent of the reversed flow region over the blade tips is greater further from the wall (compare Region B in the two figures), as is the extent of the through flow (compare Region A). Both of these observations demonstrate the role of near wall viscous effects on the tip clearance flow and the increasing influence of the blade pressure field (driving the reverse flow) and the through flow as the distance from the wall increases.

Equivalent relative frame flow maps for conditions near stall conditions are shown in Figures 4.13, 4.15, and 4.17. At these conditions, axially reversed flow dominates the passage and the magnitude increases with distance from the wall. Nearest the blade tips (Figure 4.17), the reversed flow moves in the same direction as one might expect if it were being entrained into the tip leakage vortex. The origin of the (aft) axially reversed flow may be mainstream flow in the passage. Incoming through flow passing over the tip leakage vortex could be entrained and turned toward the wall as it passes over the aft portion of vortex.

4.3.4 Summary

These results show new detail of the flow field in the tip clearance gap. Most importantly, they reveal the dynamic nature of tip clearance flow. From blade to

blade, the flow direction often changes a full 360°. The most sudden changes in flow direction are observed at the interface between the through flow and axially reversed tip leakage flow, which is strongest near the leading edge and the suction side of the blade.

Two regions of reversed flow were observed. One is the tip leakage flow driven by the pressure difference across the blade tip. The other region of reversed flow originates from the back of the passage and is driven forward by the pressure difference across the blade row.

Another interesting result is that the tip leakage vortex and the incoming/reversed flow interface are still firmly in the blade passage. According to the hypothesis presented by Vo (2001), a criteria for spike stall inception is the forward spillage of the tip clearance flow over the adjacent blade. The present results suggest that this is far from the case in this compressor.

The analysis of the following section investigates the unsteady and non-uniform aspects of this dynamic flow field.

4.4 Unsteady Overtip Passage Flow Variations

The ensemble averaged flow maps in the previous section show details of the major features in the overtip flow field. The flow maps also show how these features change from design to near stall conditions. However, as a result of the ensemble averaging process, most of the unsteady, or instantaneous, features of the flow field are suppressed. This section uses two statistical parameters to examine how well the instantaneous flow field is represented by the ensemble average flow field. Further, this section explores how the instantaneous flow field changes around the compressor annulus, from passage to passage, and as stall is approached.

4.4.1 Methodology

This section will briefly discuss the experimental methodology and define the two aforementioned statistical parameters.

Additional measurements were made in the same compressor (Deverson) as was used for the overtip flow maps. In this case, the measuring configuration consisted of seven axial arrays of pressure transducers, each with four axial positions. The seven axial arrays of probes are distributed equally around the compressor annulus. The circumferential and axial positions are shown in Figure 4.18; the numbering of the axial positions is consistent with the axial positions used to produce the overtip flow maps in the previous section.

Unsteady static pressures from flush mounted pressure transducers were recorded simultaneously at all 28 (4 axial positions at 7 circumferential locations) measuring positions. One hundred rotor revolutions were sampled at a rate providing 70 sample points per blade passing. This was repeated for 13 flow coefficients from design to near stall conditions.

Preliminary Processing

The preliminary processing produces three types of traces. They are the *instantaneous*, *ensemble*, and *mean* traces of the overtip static pressure for one blade passing. The three types of traces were produced for each of the 28 pressure transducers, at each of the 13 flow coefficients. Described below, these traces are the building blocks of the statistical parameters to follow.

1. The *instantaneous* trace is the raw data. The data from each pressure transducer and each test case were calibrated, non-dimensionalized, and re-interpolated to 64 points per blade passing (Section 3.9). Since a trace represents the passage of a single blade passing, each trace consists of 64 pitchwise values of static pressure. There are 100 *instantaneous* traces for each of the 51 blade passages. (This represents the 100 revolutions of data recorded.)

2. The *ensemble* trace for a blade passage is the average (an ensemble average phase-locked to the rotor) of the 100 *instantaneous* traces for that same blade passage. There is one *ensemble* trace for each of the 51 blade passages. Each *ensemble* trace of static pressure consists of 64 pitchwise values of ensemble averaged static pressure. An *ensemble* trace for a particular blade passage represents the behaviour of that blade passage on average.

3. The *mean* trace is the average of each of the 51 *ensemble* traces (one for each blade passage). There is one *mean* trace which consists of 64 points. The *mean* trace represents the average behaviour of all blade passages in the rotor.

Blade Passage Unsteadiness

The first statistical parameter, the *passage unsteadiness*, quantifies the unsteadiness of a passage relative to its own average behaviour, each time the rotor passes the same circumferential position. Analysis of this parameter can answer the questions: How unsteady is each blade passage? How does that change with axial and circumferential positions? What changes occur as stall is approached?

The *blade passage unsteadiness*, BP_{uns}, is calculated for each of the 28 probe positions, K, and 13 flow coefficients, ϕ. The unsteadiness is defined for each blade passage as:

$$BP_{uns}(\phi, K, x) = \sum_{n=1}^{64} \sum_{rev=1}^{100} |instantaneous(\phi, K, x, n, rev) - ensemble(\phi, K, x, n)| \tag{4.1}$$

where x identifies each blade passage (from 1 to 51), n is the number of the data point in the blade passage, rev is the revolution number, and the *instantaneous* and *ensemble* traces are those defined above in the previous section. BP_{uns} for each blade passage, is, in other words, the difference between its instantaneous flow behaviour and its own average behaviour at the same flow coefficient and axial/circumferential position.

The BP_{uns} calculation results in one value for each blade passage. An increase in the *blade passage unsteadiness* value indicates that the behaviour of the flow is becoming more erratic in that blade passage.

A change in all 51 *passage unsteadiness* values would indicate a change in the unsteady behaviour of the rotor as a whole. This is characterized by the *mean passage unsteadiness*, $\overline{BP_{uns}}$, which is simply the arithmetic average of the 51 *passage unsteadiness* values, $BP_{uns}(x)$. Whereas $BP_{uns}(x)$ answers the question

"How unsteady is this blade passage?", $\overline{BP_{uns}}$ answers the question "How unsteady are all of the blade passages on average?"

When results are presented, the unsteadiness parameter is non-dimensionalized by $\overline{BP_{uns}}(\phi_{design}, 1)$. This is the mean passage unsteadiness value evaluated at the design flow coefficient, circumferential position 1, axial position 1 (leading edge). Non-dimensionalizing the results allows for easier quantitative comparison. By non-dimensionalizing in this way, any unsteadiness value greater than 1 indicates a higher unsteadiness value than at the leading edge at design conditions and vice versa.

Passage to Passage Variation

The *passage to passage variation* quantifies the flow variation for each of the 51 blade passages relative to the average flow behaviour in all of the passages. Analysis of this parameter can answer the questions: How much does the flow vary from passage to passage? How does this change axially, around the circumference, and as stall is approached?

The *passage to passage variation*, $P2P_{var}$, is calculated for each of the 28 probe positions, K, and 13 flow coefficients, ϕ. The parameter is defined for each blade passage as:

$$P2P_{var}(\phi, K, x) = \sum_{n=1}^{64} |ensemble(\phi, K, x, n) - mean(\phi, K, n)| \qquad (4.2)$$

where x identifies each blade passage (from 1 to 51), n is the number of the data point in the blade passage, and the *ensemble* and *mean* traces are those defined above in a previous section. For each blade passage, $P2P_{var}$ is, in other words, the difference between its average flow behaviour and the average flow behaviour of all 51 passages.

This parameter also provides a single value for each blade passage. A higher *passage to passage variation* value indicates that the behaviour of the flow in

that particular blade passage is more unusual than the average behaviour of all the rotor blade passages.

A change in all 51 *passage to passage variation* values would indicate a change in the variation to flow patterns around the entire rotor. This is characterized by the *mean passage to passage variation*, $\overline{P2P_{var}}$, which is the arithmetic average of the 51 *passage to passage variation* values, $P2P_{var}(x)$. Whereas $P2P_{var}(x)$ answers the question "How much does the flow in this blade passage vary from all the others?", $\overline{P2P_{var}}$ answers "How much does the flow vary among the blade passages on average?"

When results are presented, this parameter is also non-dimensionalized as discussed above for the passage unsteadiness parameter. The *passage to passage variation* parameter is non-dimensionalized by $\overline{P2P_{var}}(\phi_{design}, 1)$, the value at the design flow coefficient at circumferential position 1, axial position 1 (leading edge).

4.4.2 Passage Unsteadiness Results

The passage unsteadiness, BP_{uns} (Eqn. 4.1), looks at the unsteady behaviour of a blade passage relative to itself. This section will examine how the overall blade passage unsteadiness changes as the compressor is throttled toward stall. This is first done by examining $\overline{BP_{uns}}$ around the annulus and from the leading edge to the trailing edge of the blade row. Then, the unsteadiness of each individual passage is specifically examined using BP_{uns}.

Changes in blade passage unsteadiness as the compressor is throttled from design to near stall conditions is shown in Figure 4.19. $\overline{BP_{uns}}$ is evaluated at the leading edge position for seven positions equally spaced around the annulus. Following the lines from the right to the left tracks the passage unsteadiness as the compressor is throttled toward stall. For the most part, it is seen that the unsteadiness in the blade passages remains constant or decreases as the compressor is throttled from design ($\phi = 0.51$). Just before stall, however, the unsteadiness increases at all circumferential positions, with the greatest increase seen at circumferential position 1.

The spread in the unsteadiness values around the annulus in Figure 4.19 is remarkable. The maximum level of unsteadiness at circumferential position 7 (reached just before stall) is less than the minimum level of unsteadiness at circumferential position 4 (which occurs at design). There is also no trend in terms of the amount of ramp-up in unsteadiness that can be expected just before stall (based on either the value of unsteadiness preceding the ramp-up or the circumferential position).

The results in Figure 4.19 are for conditions at the leading edge, i.e., measuring position 1 in Figure 4.18. However, three other axial positions were measured. Figure 4.20 shows $\overline{BP_{uns}}$ evaluated at all four axial positions for circumferential location 1. In general, this figure shows that $\overline{BP_{uns}}$ is similar at different axial positions. The unsteadiness is highest at axial position 5 (35% axial chord downstream of the leading edge). At this position, about half the pitchwise flow is reversed and half is through flow; the two regions are separated by the tip leakage vortex. Momentary changes in the trajectory of the tip leakage vortex change the tip clearance flow dramatically, which is the source of the high unsteadiness at this axial position. The results for $\overline{BP_{uns}}$ at the four axial positions shown in Figure 4.20 are similar at the other six circumferential locations.

The unsteadiness parameter for each blade passage, BP_{uns}, will now be considered to determine if the results for mean passage unsteadiness discussed above are due to the action of all blades or only a few. In Figure 4.21, BP_{uns} is evaluated at the leading edge for all circumferential locations. Solid lines indicate results at near stall operating conditions, and dotted lines indicate the design condition. The most prominent aspect of the figure is that the variation of unsteadiness, from passage to passage, and around the circumference, is much higher near stall than near design. At design there is no obvious "most unsteady" blade passage, while near stall there are passages that have an unsteadiness significantly higher than the rest at most circumferential positions: in particular the passages surrounding blades 15 and 43.* That said, the unsteadiness of the blade passages at any one circumferential position is well distributed, i.e., the mean and median values are very close, differing by only about 1%.

*The blades are numbered from 1 to 51, which correspond to the labels on the rotor blades in the Deverson compressor. The value of BP_{uns} corresponds to the passage on the suction side of the blade labelled in the figure.

To summarize the results in this section, it has been shown that the unsteadiness in the tip clearance flow decreases or stays the same as the compressor is throttled from design conditions, but then rises sharply just before stall. The sudden increase just prior to stall is not predictable, and is due to a general increase in unsteadiness in most blade passages. The variation in unsteadiness from passage to passage, and around the circumference, is much higher near stall than near design. This behaviour is seen around the annulus and from the leading edge to the trailing edge of the rotor. The greatest absolute value of unsteadiness is seen where the tip clearance flow is most vigorous, i.e., at about 35% axial chord (axial position 5). Some passages are shown to have greater unsteadiness compared to the other blade passages at most circumferential locations, namely passages near blades 15 and 43. The possible physical causes for these variations will be discussed in more detail later in this chapter.

Clearly, the BP_{uns} unsteadiness parameter is not suitable for predicting stall. However, the parameter is useful for showing that unsteadiness in tip clearance flows around the circumference of the compressor is not uniform, nor is it uniform from passage to passage. This may have consequences on CFD performance predictions and may explain the inability to predict the stalling flow coefficient of a new machine; again, this will be discussed later.

4.4.3 Passage to Passage Flow Variation Results

This section presents the results from the second parameter, the passage to passage variation, ($P2P_{var}$, Eqn. 4.2), which looks at the flow behaviour of a particular blade passage relative to all the other blade passages. As in the previous section, the emphasis is on how the parameter changes as the compressor is throttled toward stall. This is first done by examining $\overline{P2P_{var}}$ around the annulus and from the leading edge to the trailing edge of the blade row. Then, the flow variation of each individual passage is specifically examined using $P2P_{var}$.

Changes in flow variation from passage to passage as the compressor is throttled from design to near stall conditions is shown in Figure 4.22. $\overline{P2P_{var}}$ is shown at the leading edge position for seven positions equally spaced around the annulus. Following the lines from the right to the left tracks the amount of flow variation as

the compressor is throttled toward stall. This figure shows that the flow variation among the passages generally increases as stall is approached. This means that as blade loading is increased, the blade passages become more unique from one another. This trend is not uniform at all circumferential positions, though. The passage to passage flow variation at circumferential position 2 increases very little. The flow variation at circumferential positions 3 to 5 increases almost constantly, and at positions 6, 7 and 1 it increases most just before stall. This appears to show something of a circumferential pattern to the results, which will be discussed later.

A higher value of $\overline{P2P_{var}}$ indicates the flow behaviour of the passages is less uniform, i.e., the blade passages are acting more uniquely from each other. Changes in $\overline{P2P_{var}}$ around the compressor annulus also indicate less uniform flow behaviour. In other words, the behaviour of the passages relative to each other depends on the individual passage and the circumferential location of the passage when the behaviour is observed. Figure 4.22 shows the behaviour of the tip clearance flow varies significantly among passages and around the circumference, and this variation increases as stall is approached.

Figure 4.23 shows $\overline{P2P_{var}}$ evaluated at all four axial positions for circumferential location 1. At each axial position, $\overline{P2P_{var}}$ increases just before stall, although this effect is less significant at axial position 8. This behaviour (at circumferential location 1) is very similar at circumferential locations 3, 6 and 7. The behaviour at circumferential positions 2, 4 and 5 is discussed below.

At circumferential position 2, $\overline{P2P_{var}}$ at all axial positions changes very little as the compressor is throttled (as is seen for axial position one in Figure 4.22).

$\overline{P2P_{var}}$ is very similar at circumferential positions 4 and 5, and is shown for position 4 in Figure 4.24. Axial position 5 (green line) demonstrates the most interesting behaviour. $\overline{P2P_{var}}$ at axial position 5 increases as the compressor is throttled from design and then decreases just before stall. The hump in $\overline{P2P_{var}}$ at axial position 5 can be explained by recalling that at this axial position (35% axial chord), the tip leakage vortex passes at about mid-pitch and shifts toward the neighbouring blade as the compressor is throttled. The results from the $\overline{P2P_{var}}$ parameter indicate that this change occurs in a non-uniform way among blade

passages. Because this hump is not observed at every circumferential position, the behaviour of a passage at one circumferential position is not necessarily indicative of its behaviour at other positions around the annulus.

To examine how the blade passages vary from one another, the passage to passage variation parameter for each blade passage, $P2P_{var}$, is examined at the seven circumferential locations. The results discussed above looked at the mean value of this parameter, and showed most generally that the leading edge position experiences the biggest change to passage to passage flow variations as the compressor approaches stall. For this reason, the following results will be presented for the leading edge position.

Figure 4.25 shows $P2P_{var}$ for each of the 51 blade passages at the leading edge and at seven circumferential locations. Solid lines indicate results at near stall operating conditions, and dotted lines indicate the design condition. High peaks in $P2P_{var}$ indicate the blade passages whose flow behaviour varies the most from the other passages. While $P2P_{var}$ of most blade passages near stall has increased modestly compared to that at design, about 20% of the blade passages have a variation 5-12 times higher near stall than at design. This shows that as the compressor is throttled, a minority of passages are behaving very differently from the rest. Blade 43 has the highest variation at any circumferential position, and passages surrounding blade 15 have the second highest variation.

This section showed as stall is approached, passages become more unique from each other. Passage to passage flow variations are not uniform around the annulus, but depend on passage geometry and the circumferential location of the passage when observed. About 20% of the blade passages experience the biggest change in passage to passage flow variations as the compressor approaches stall. These results indicate the behaviour of the tip clearance flow varies significantly from passage to passage around the circumference of the compressor. This is particularly true near stall. The passages surrounding two blades in particular, blades 43 and 15, vary the most from the other passages. These are the same two blades associated in the previous section with higher passage unsteadiness. The passages surrounding these blades vary the most from the norm and the variation itself is unsteady.

As with the BP_{uns} discussed in the previous section, the $P2P_{var}$ parameter highlights significant variation in the behaviour of tip clearance flows from passage to passage, and around the compressor annulus. The following section discusses physical causes of this behaviour.

4.4.4 Physical Origins of Non-Uniform Tip Clearance Flow and Unsteadiness

The previous two sections showed that the behaviour of the flow in the blade passages is not uniform - neither relative to each other nor around the circumference of the compressor. While it is unlikely to find all origins for this behaviour, the purpose of this section is to look at some of the possible physical causes of the observed variations. First, annulus and blade irregularities are discussed and compared to the unsteadiness and flow variation results. Then, the wider implications of these observations are considered.

The tip clearance gap height at the rotor leading edge was measured with a feeler gage around the compressor annulus. The clearance among the blades (at a fixed circumferential location) is uniform, i.e., the rotor is perfectly circular and the blades are all of the same height.

However, the clearance around the annulus varies as shown by the solid line in Figure 4.26. This varies in a roughly sinusoidal pattern with the maximum clearance at the bottom of the compressor (circumferential position 2) and the minimum clearance near the top of the compressor (circumferential position 6). The circumferential variation of the $\overline{BP_{uns}}$ and $\overline{P2P_{var}}$ parameters (evaluated here at the leading edge near stall) are shown in the same figures as dashed and dotted lines, respectively. The two parameters show similar trends to one another, and their values are high at the minimum clearance, and low at the maximum clearance. (The trends at other flow coefficients from design to near stall conditions are similar, with the pattern accentuated as stall is approached.)

It is well documented (Cumpsty (2004); Freeman (1985)) that the tip clearance height affects the behaviour of the tip leakage flow, so it is likely that the varying clearance height has had some influence in causing the observed non-uniform

behaviour of the tip clearance flows. The precise influence of eccentricity on unsteady flow behaviour is not yet clear, though. In a study on the effect of tip clearance and eccentricity on compressor flow irregularity, Young et al. (2011) found that maximum flow irregularity (similar to the $\overline{BP_{uns}}$ parameter) occurred near the maximum tip clearance. In contrast, Figure 4.26 shows the opposite trend: $\overline{BP_{uns}}$ is minimal at the maximum tip clearance. The contrast in these results indicates the complexity involved in relating the cause of unsteadiness. It is possible that different blade geometries alter the influence of eccentricity, and that other factors (e.g., inlet flow distortions) can also cause circumferential variations in unsteadiness.

Next, possible causes were explored for the increasingly irregular behaviour among individual blade passages. The rotor blades were inspected to determine if any physical irregularities could be found to account for the tip flow irregularity. Tip stagger was confirmed to be uniform. Most blades appear in good condition and no correlation was found between the physical appearance of the blade (presence of chips or varying surface roughness) and its unsteadiness or passage to passage flow variations.

The pitchwise spacing between all blades was measured and found to vary by up to $\pm 1.5\%$ of pitch at the blade tips. Neither of the BP_{uns} and $P2P_{var}$ parameters correlate strongly with the absolute pitchwise spacing. From this pitchwise spacing, however, a blade spacing parameter was derived to look at the relative spacing between neighbouring passages. The blade spacing parameter is a measure of the disparity between the spacing of neighbouring blade passages. Consider three blades numbered 1, 2 and 3. These three blades form two passages, 1-2 and 2-3. The pitchwise spacing of these passages is written as s_{1-2} and s_{2-3}. The blade spacing parameter for blade 2 in this example is

$$BladeSpacingParameter(2) = (s_{1-2} - s_{2-3})^2 \tag{4.3}$$

This is calculated for each blade. A high blade spacing parameter value indicates a greater disparity between the spacing of neighbouring blade passages.

Figure 4.27 shows the blade spacing parameter (red line with crosses), and the passage to passage variation parameter at the leading edge for circumferential positions 1 (black line with circles). There is a high correlation between $P2P_{var}$ and the blade spacing parameter. For most of the peaks in $P2P_{var}$, there is a matching peak in the blade spacing parameter. This shows slightly uneven blade spacing can give rise to significant variation in the passage to passage overtip flow field.

The blade spacing parameter does not distinguish between which side of the blade (pressure or suction side) has the wider or narrower spacing. For the two blades with the highest unsteadiness and flow variation values, 15 and 43, it is interesting to note that the spacing on the pressure side of blade 15 is slightly wider than average and the spacing on the suction side of blade 15 is narrower than average. The converse is true for blade 43. Although the statistical behaviour of the two passages is similar, it is likely that the physical cause is different.

The peaks in the $P2P_{var}$ parameter in Figure 4.27 indicate the passages near blades 15 and 43 vary significantly from the other passages (i.e., from the "mean" passage). By overlaying the ensemble pressure traces for all blade passages, it is possible to look at what physical variation in the passage flow is associated with this non-uniform behaviour. The ensemble traces for all 51 blades are shown in black in Figure 4.28. The mean trace is yellow and blades 15 and 43 are highlighted in red and green, respectively. The traces for blades 15 and 43 are the two most obvious outliers from the mean trace (yellow). This corresponds to these passages having the highest peaks in passage to passage variation in Figure 4.25. Figure 4.28 shows that the biggest variation among the passage flow patterns is in the suction side pressure. Blade 15 has the lowest suction side pressure, while blade 43 has the highest suction side pressure. This may explain why the passage unsteadiness is highest near blade 15 (Figure 4.21). A low suction side pressure, assuming a constant back pressure, faces a higher adverse pressure gradient than a higher suction side pressure, and is therefore more likely to be sensitive to fluctuations and small disturbances in the flow.

The non-uniform behaviour of the tip clearance flow, both around the annulus and among passages, has been shown to increase steadily as stall is approached, i.e., as the adverse pressure gradient encountered by the flow increases. Shear

layers are expected to be more sensitive to fluctuations under these conditions, Panton (1996). Any fluctuations in the flow (caused by physical irregularities, noise, or turbulence in the incoming flow field) may be amplified to a greater extent near stall than near design. The amplification of such flow irregularities in physically different passages may explain the increasingly non-uniform behaviour of the tip clearance flow as the rotor approaches stall.

4.4.5 Implications for Future Tip Clearance Flow Research

The increased sensitivity to physical irregularities of the tip clearance flow field near stall discussed above may explain the difficulty in modelling and predicting the flow field at near stall conditions. It may also explain the unreliability of computational methods when it comes to predicting the absolute stability limit. In CFD, blades are usually identical and the boundary conditions are uniform. In reality, every machine will have its own unique physical blade and annular irregularities. This work shows that small physical irregularities may cause significant variation to the tip clearance flow field. These variations are amplified as stall is approached.

Hence, while uniform blades and boundary conditions may be adequate for modelling the flow near design conditions, the present work suggests that more physical realism is needed for reliable CFD predictions near stall. Turbulence modelling may increasingly affect the accuracy of calculations at lower flow coefficients where viscous effects are shown to be most apparent. The accuracy of near stall calculations may be improved by introducing the unsteady boundary conditions and physical irregularities that are known to exist in a real machine.

It is not known if a better understanding of the non-uniform and unsteady effects of tip clearance flows near stall will shed light on the stall inception mechanism. A need thus exists for even more extensive unsteady measurements just before and during the stall event to understand the role of tip clearance flows in the inception process. The next chapter will look at this topic in greater detail.

4.5 Conclusions

1) The results from the overtip flow studies, in particular those from the new boundary layer hot-wire and unsteady total pressure probe, are thought to be the most detailed experimental measurements in the tip clearance gap of their kind.

2) The tip clearance flow field has been shown to be very dynamic. The flow direction at some axial locations was shown to change direction by a full 360° from blade to blade. Two distinct regions of axially reversed flow were shown, and these increase dramatically in magnitude and extent when the compressor is throttled from design to stall.

3) The trajectory of the overtip leakage vortex has been shown to change direction as stall is approached, but not by nearly as much as is required to bring the trajectory of the vortex to the rotor leading edge plane. It was suggested that forward spillage as a mechanism of spike stall inception is unlikely in this compressor. The following chapter will describe measurements carried out during the stall inception process and discuss this further.

4) A statistical analysis of unsteady pressure measurements indicates that the flow field around the annulus and among passages becomes increasingly non-uniform as stall is approached, in terms of both steady and unsteady flow variations.

5) The increase in passage unsteadiness and passage to passage flow variations as stall is approached was shown to depend on the axial and circumferential location of the measurements. The greatest unsteadiness is seen where the tip clearance flow is most vigorous, i.e., at about 35% axial chord. The greatest passage to passage flow variation is seen at the circumferential location where tip clearance is a minimum.

6) As the compressor is throttled toward stall, the tip clearance flows in a minority of blade passages were shown to behave differently from the norm. Static pressure traces show that the tip clearance flows in these blade passages are the most unique on average from all passages and the most unsteady. It was found that small variations in blade to blade spacing near the tips was correlated to

the variation observed in the tip clearance flow field of the most disturbed passages. The amplification of disturbances near small physical irregularities may be explained by the increased sensitivity of shear layers as the adverse pressure gradient encountered by the flow increases (which occurs as stall is approached).

7) These measurements highlight the level of flow irregularity near stall and suggest that CFD predictions of stall onset will improve with greater physical realism, e.g., by introducing the unsteady boundary conditions and machine imperfections which are known to be present in real compressors.

Chapter 5

Stall Inception Investigation

5.1 Introduction

The mechanism of stall inception, which leads to surge in a jet engine, remains a frontier in compressor research despite over half a century of investigation. Moreover, the stability limit of a new compressor is not accurately predicted by computational means. As a result, costly surge testing of a new aero-engine is carried out to determine its operating limits. While it is unlikely that surge testing will be eliminated, a better understanding of stall inception could eventually lead to the ability to predict the stability limit. Designers could then more accurately evaluate the influence of design changes on the stability limit.

Many stall inception patterns have been observed (Day et al. (1999)), and it is still not possible to predict which stalling pattern a given compressor will exhibit (Houghton (2010)). The goal of the present study is to improve the fundamental physical understanding of stall inception. In particular, "spike" stall inception is examined as this is the most commonly observed and least understood type.

Traditionally, stall inception is detected with six to eight probes (hot-wires or flush mounted pressure transducers) evenly distributed around the annulus near the rotor leading edge tips, Day (1993a). Fluctuations in pressure or velocity at stall inception are tracked as they propagate around the machine annulus. This method is commonly used to distinguish between different stalling patterns.

From this it is known that spike stall inception is characterized by the growth of a short length scale disturbance (a "spike" in the pressure or velocity signal on the order of a few blade pitches) propagating at about 70-80% of rotor speed. The transition from the onset of the spike disturbance to fully developed rotating stall usually happens within three rotor revolutions.

What is not well understood is the flow mechanism that initially gives rise to the spike disturbance. Published work on spike stall inception can generally be categorized into three distinct mechanisms: rotor critical incidence (Camp and Day (1998)), blockage growth (Khalid et al. (1999)), and forward/backflow spillage (Vo (2001)). It is unknown whether, or how, these mechanisms might be related.

The proposed stall inception mechanisms are based on the observation of trends leading up to stall, and the structure of the emerging stall cell. Experimental studies focus on how the flow field changes as stall is approached (e.g., Khalid et al. (1999)) or on the structure of the spike the first time it passed over special instrumentation (e.g., Deppe et al. (2005)). The scope of these approaches is limited, as the formation of the spike disturbance is not directly observed. In the latter case, the spike disturbance may occur at some other circumferential position where instrumentation is not available.

There is a clear need for a better understanding of stall inception. The aim of the present experimental investigation is to study the formation of the spike disturbance by direct observation. This requires a higher concentration of instrumentation than has been used in the past. It is not feasible, however, to place a high concentration of instrumentation around the entire annulus. The instrumentation only needs to cover a region of the annulus sufficient enough to observe the emergence of the spike disturbance. In this regard, the greatest difficulty lies in not knowing where the spike formation will occur around the annulus for any given stall event. To overcome this, the present study first seeks to establish if a preferred circumferential location exists where stall inception is most likely to occur. It is possible that the steady and unsteady flow variations discussed in the previous chapter give rise to such a preferred location. If the spike is observed to form most often at a certain annular position, then a concentration of probes set

at this location will increase the likelihood of consistently capturing the formation of the spike.

This chapter is set out as follows:

1) The traditional method of spike detection is used to investigate the idea of a statistically preferred location for stall inception.

2) Instrumentation is then concentrated where the spike is first detected. NB: the spike is already formed at this stage because it has grown to such a size as to be detected by instrumentation ahead of the blade row.

3) Additional instrumentation is then used to track the spike back in reverse chronological order to the earliest detectable origins of the disturbance.

4) Overtip instrumentation is then concentrated at this location to examine the emergence of the embryonic spike.

This is a new method of experimental investigation which allows more detail of the stall event to be captured than previously possible. This method is made possible by advances in computer power that allow simultaneous data acquisition of many channels at high processing speeds. As the experimental method is key to, and often inseparable from, the results, each section begins with an explanation of the relevant methodology before presenting the results.

5.2 Statistical Preference in the Stall Inception Location

For any particular stall inception event, it is unknown where the spike will form around the circumference of the compressor. In the past, the physical location of stall inception has sometimes been set by artificial means, such as by introducing an artificial flow blockage. This procedure is not favoured, as this might distort the very flow event that is being investigated. Instead, a circumferential location is sought where the compressor is "most likely" to stall naturally. The existence of such a location would be helpful in placing a concentration of instrumentation

at a location at which the likelihood of capturing the formation of the spike is increased. Although not every stall event would occur at this location, statistically, a larger number might occur in the region of highest instrument density.

5.2.1 Traditional Stall Inception Detection Methodology

The spike is a disturbance local to a few blade passages and it grows quickly to fully developed rotating stall in only a few rotor revolutions. Stall inception is traditionally detected with six to eight unsteady pressure transducers positioned upstream of the rotor leading edge, evenly distributed around the annulus. The traces are usually low pass filtered to remove the blade passing frequency. "Stall inception" is then deemed to have occurred at the instant when a small disturbance is seen propagating (at less than rotor speed) from one probe position to the next. This traditional way of locating stall inception is used here as the starting point in this investigation.

In the Deverson compressor, pressure transducers are placed flush with the outer casing wall at the leading edge (axial position 1) at each of seven equally spaced circumferential locations*. This configuration is shown at the top of Figure 5.1.

The compressor is stalled 100 times using the method described in Section 3.8; that is, the compressor is slowly brought near the stalling point and then left to stall naturally. The pressure transducers are recorded according to the procedures of Section 3.3; sampling frequencies are sufficiently high to resolve the flow details within the blade passage (sampling at 30 kHz, with low-pass filtering at 10 kHz to avoid aliasing). In order to produce the traditional stall inception traces, the signals are post-processed with a digital low-pass filter at half of blade frequency (200 Hz). The stall inception traces without the additional digital low-pass filter will be discussed in a later section.

The traces for a typical stall inception event are shown in Figure 5.1. Each trace

*As discussed earlier, seven locations are chosen as a multiple of the number of stator blades. Placing each probe at the same location relative to the corresponding downstream stator blade eliminates spurious variations caused by the potential effect of the stationary blade. The potential effect of the stator blades is clearly detectable upstream of the rotor blades.

corresponds to a transducer placed at the corresponding circumferential location. The first four revolutions shown in the figure are of relatively undisturbed flow prior to spike formation. The solid line labelled "blade" tracks the same physical blade at each circumferential location. The dashed line in the next revolution tracks the propagation of the emerging spike. It is observed that the dashed line tracking the spike is at a different angle than the solid line tracking a blade. The speed of the spike propagation is determined in this case to be 77% of rotor speed, which is representative of the propagation speed spikes exhibit in this compressor.

In Figure 5.1 the first sign of the spike is at circumferential location C. Each of the 100 stall inception events was similarly examined to record the circumferential location of the first sign of the spike.

5.2.2 Statistical Location of First Clearly Visible Sign of a Spike

The results indicate the first sign of the spike, as detected in the traditional way, occurs at circumferential location C in 73 out of 100 events. In a further 21 out of 100 events, the first sign of the spike was observed at circumferential locations A and G. In the remaining 6 stall inception cases, the first sign of the spike was observed at the remaining four locations B, D, E, and F.

These results establish that, in the Deverson compressor, the spike has a statistical preference to form at a certain circumferential location. This preference allows for the possibility of a statistically repeatable "stall event". It also means that the inception process can be studied in detail by stalling the compressor multiple times and only analyzing those stall events that form consistently at the same circumferential location.

The following section will describe a concentration of instrumentation which is placed near circumferential location C. Results will show what the spike looks like at the location where the disturbance is detected in the traditional way.

5.3 Study of Spike at the Stage of Traditional Detection

This section focuses on detailed tip clearance measurements of the spike at the phase of its development when it is traditionally detected and at the location in the present compressor where this is most likely to occur.

The section is presented in two parts. First, the distribution of measuring instruments is described, and second, the results are presented to show the spike at this stage in its development.

5.3.1 Probe Set-up at Circumferential Location C

The set-up described in this section consists of 40 fast response pressure transducers. The majority of transducers are arranged in four arrays at circumferential location C. A schematic of the complete set-up is shown in Figure 5.2 which will be explained below.

One pressure transducer is placed at each of the seven circumferential locations, A through G. These probes are used to confirm the location of spike formation using the traditional approach (as performed in the previous section). Only cases where the spike is first clearly observed at circumferential location C will be used in the present study.

In the compressor casing over the rotor blade tips, there are six arrays of probe holes between circumferential locations C and D, each array one rotor pitch apart. The first array of holes following C is identified as C.1, the second C.2, and so on. See Figure 5.2.

At four of the measuring stations (C.2, C.3, C.4, and C.5), seven pressure transducers have been installed extending from just upstream of the leading edge to the trailing edge. The measurements from these arrays of probes will be used to produce static pressure contour maps at stations C.2, C.3, C.4, and C.5. The contour maps will provide four progressive views of the spike as it passes from one station to the next.

At stations C.1 and C.6, there is a partial array of transducers. At station C.1, probes have been placed at axial locations +1 and 3. At station C.6, the probes are at axial locations +1, 3, and 5. These probes were used to help identify the spike and confirm its propagation beyond the narrow range of the central four stations.

The compressor is stalled using the method described in Section 3.8. Pressure measurements are recorded according to the procedures of Section 3.3 as before.

The results were examined and compared in detail to determine what features of the spike are consistently repeatable. One case has been chosen to represent the common features of a spike at this phase of its development.

5.3.2 Static Pressure Contours of an Established Spike

A representative spike at the phase of development when it is normally detected by the traditional approach is shown in Figure 5.3. Each of the four static pressure contour plots are from the arrays of transducers at stations C.2 to C.5 (Figure 5.2). The top contour plot represents the flow field at station C.2. The stations are spaced one pitch apart, so each subsequent contour plot represents the flow field after the rotor has turned by one blade pitch. All of the contour plots are on the same absolute scale of static pressure, with red being the highest pressure and blue the lowest. The blades travel from right to left in Figure 5.3, and the axial direction is downward. The blade numbers are marked in the vicinity of the spike. The passages are identified by their adjacent blades (so passage 13-14 is the passage between blades 13 and 14). Looking at the same blade passage from the top frame to the bottom shows the change in flow conditions in that blade passage over a time period of four rotor blade pitches. The following discussion will look at the flow field in sequence from station C.2 to C.5.

At station C.2, the spike, or stall cell, is located in passages 13-14 and 12-13. The stall cell is identified by the lower pressure pattern observed in these passages, which is not normal at stable operating conditions.

The size of the disturbance in passage 12-13 (the extent of depressed pressure) increases in size from station C.2 to C.3. At station C.3, a distinct low pressure

spot is observed just over midway in passage 12-13, as labelled. This low pressure spot is, in fact, the "spike", or sharp dip in the static pressure traces that is so characteristic of this form of stall inception; see Figure 5.1. Such a well defined low pressure spot could represent a radial vortex attached to the casing. Radial vortices of this type were first reported by Inoue et al. (2000) in an experimental and computational study of the propagation of stall cells. Inoue et al. proposed that the radial vortex is shed from the suction side when circulation is lost as a result of the blade stalling.

Moving to station C.4, the stall cell appears to have propagated to the right. The boundary of the stall cell on the left side appears to recede, i.e., pressure is recovering to a more normal level in passage 13-14. The stall cell has expanded on the right side; the space between blades 11 and 12 is now affected by a low pressure spot in mid-passage. The low pressure spot (radial vortex) travels slower than the blades, and has propagated to the neighbouring passage (11-12) by C.4. Inoue et al. (2000) also suggest that the propagation of the spike is driven by the tangential movement of the radial vortex, which increases incidence on the neighbouring blade, causing it to separate and so producing a new vortex.

Finally, at station C.5, the stall cell appears to have shifted completely to passages 12-13 and 11-12, thereby propagating relative to the rotor by 1 pitch movement over the observed region from station C.2 to C.5.

The right hand edge of the stall cell was observed to expand, or propagate, to the neighbouring passage, thus, the right hand edge of the stall cell is referred to as the "propagating edge" of the stall cell (as labelled at C.5). The flow in the passages to the left of the stall cell recover as the stall cell propagates, hence the left hand edge of the stall cell is referred to as the "receding edge" of the disturbance. Recalling from Figure 5.1 in the previous section, the spike was shown to propagate at 77% of rotor speed. At 77% rotational speed, the stall cell should move the space of three rotor pitch movements in the time the rotor moves four pitches (in the absolute reference frame). In the rotor reference frame, this means the stall cell would lag the rotor by one pitch after the rotor has moved four pitches, which is exactly what is observed in Figure 5.3.

The static pressure contours discussed above suggest the presence of a radial

vortex within the stall cell. As an aside, further evidence for this feature from hot-wire measurements is examined more closely below before moving on to the next section.

5.3.3 Radial Vortex in Stall Cell

A miniature hot-wire was used to investigate the radial vortex. The hot-wire is placed just upstream of the leading edges adjacent to the leading edge pressure transducer at station C.3. The hot-wire is oriented perpendicular to the incoming flow direction, and the prong height is 5.5 mm, just over three times the tip clearance gap height.

The hot-wire results to be presented here are part of the same stall event that was discussed in the previous section and shown in Figure 5.3. The static pressure contours from station C.3 in Figure 5.3 are reproduced in Figure 5.4. As before, the stall cell observed in the static pressure contours at station C.3 spans from blades 12 to 14, and the low pressure spot is observed in passage 12-13. A scaled view of the hot-wire relative to the blade and tip clearance gap is shown in the upper right hand corner.

The black line above the static pressure contours in Figure 5.4 represents the ensemble average of the hot-wire at stable conditions very near to stall. This is used as a reference for the red line, which is the instantaneous hot-wire signal at the stall event acquired simultaneously with the instantaneous static pressure measurements. It is to be expected that the instantaneous hot-wire signal (red) is very unsteady compared to the ensemble averaged trace (black). The instantaneous hot-wire signal at the center of blade passage 13-14 has an unusually low magnitude, though, indicating a redirection and/or reduction in flow through that passage.

At passage 12-13, there is a very distinct double trough/peak pattern in the instantaneous signal. The peaks are labelled “A” and “B”. The first two troughs (indicated by dashed lines) align with the low pressure spot observed in that passage. Based on the extensive experience of looking at raw hot-wire signals when analyzing the flow direction in the tip clearance gap for the previous chapter,

each sharp trough indicated by the dashed lines is indicative of a change in flow direction by about 180°. The magnitude decreases as the flow aligns with the hot-wire (making a trough in the signal), and increases to a peak as it crosses at right angles to the wire. The peak in the signal, marked A, is therefore most likely reversed flow. The peak marked B indicates the flow has turned to again cross the hot-wire, but in the through flow direction.

The sharp double trough/peak in the hot-wire signal observed here is therefore virtually assured of being caused by a vortex because the flow has turned by 180° twice in a very short physical space. This conclusion is congruent with the low pressure spot observed at the same position in the static pressure traces.

One may ask why the troughs in the hot-wire signal are not as low as the troughs that indicate the blade passing. At the blade passing, the trough is due to the flow velocity reaching a very low magnitude as a result of the flow directing around a physical obstruction. In the case of a vortex, the trough is due to the flow aligning parallel with the hot-wire. Ideally, the hot-wire signal would approach zero magnitude when the flow aligns with the wire. However, in reality the flow still cools the hot-wire, thus increasing the magnitude of the signal at the trough. It is also likely that a radial component of velocity increases the hot-wire signal in this case.

This is strong experimental evidence, both from static pressure and hot-wire measurements, of the presence of a radial vortex forming part of the stall cell, or spike. The presence of the tight vortex near the leading edge explains why the most clear sign of the spike is detected near the leading edge by a sharp "spike" in pressure (e.g., as in Figure 5.1). It is therefore likely that the vortex observed here is of the same structure as the radial vortex reported by Inoue et al. (2000) in a study of the propagation of an early stall cell.

5.3.4 Summary of Established Spike Study

The results of this section show that the spike, as detected with the traditional approach, is already established as a propagating stall cell. This demonstrates the limitation of the traditional method of detecting stall inception. The approach

of using 6 to 8 probes equally spaced around the circumference at or upstream of the rotor leading edges does not provide adequate spatial resolution to study stall cell formation. The sparse probe distribution, and filtering out the blade passing signal, makes it impossible to resolve the origins of the spike disturbance.

It is thus clear that better temporal and spatial resolution is needed to investigate stall inception. In the following section, additional instrumentation is used to track the spike disturbance backwards in time to find its true origins.

5.4 Study of Nascent Spike Propagation

In the previous section, concentrated instrumentation was placed where conventional traces indicate the first sign of the spike disturbance. It was then determined that the spike at this location was already established as a stall cell. In this section, the true origin of the spike is sought. The established spike is tracked back in reverse chronological order to find its first detectable origins. Going backwards in time is done by tracking a spike back anti-clockwise around the compressor. For this purpose, a higher temporal and spatial resolution of circumferentially spaced probes will be required.

First, the traditional circumferentially spaced traces are revisited in high frequency resolution (not applying the additional low-pass filter used in Section 5.2 which filtered out the blade passing frequency). After this, the spike is tracked back toward its origins with more closely spaced transducers set a rotor pitch apart. The general idea is to first use the conventional seven circumferential transducers to identify a spike where it is obvious, and then to use extra probes to track it back in time until the disturbance is no longer identifiable. This circumferential position will then be used in a later section (5.5) to study the origins of the embryonic spike.

5.4.1 High Frequency Resolution of the Traditional Stall Inception Traces

When searching for the first detectable origins of the spike, it is necessary to improve both the spatial resolution of the measurements (i.e., more instrumentation circumferentially) and the temporal resolution (i.e., higher frequency resolution). In Section 5.2, the pressure traces were low-pass filtered to provide clarity in Figure 5.1, but this entailed the loss of higher frequency information.

Figure 5.5 shows the same stall inception event but without the additional low-pass filter applied to remove the blade passing frequency. As before, the first clear sign of the spike is observed at circumferential position C. However, by zooming in on this location, Figure 5.6 reveals there is some sign of instability at a still earlier position, i.e., at position B.

On its own, the instability at circumferential position B is barely significant, but as it occurs in line with the expected propagation rate of the spike, it is possibly a nascent form of the spike. More spatial resolution is needed to examine this and to track the spike back still further to its origin. This will be done in the following section.

5.4.2 Tracking the Spike Back in Time

To increase the spatial resolution of the stall inception traces, pressure transducers are now placed a pitch apart in the region spanning circumferential positions G, A, B, and C. This is shown in Figure 5.7. At each of the red dashes, a transducer is placed at axial position +1, i.e., near the blade leading edges. This makes a total of 19 transducers, each spaced a pitch apart. These transducers are identified by their circumferential position. The first transducer following circumferential location G is G.1, the second G.2, and so on, moving in the direction of blade rotation.

As before, the original seven evenly spaced circumferential probes (marked by crosses in Figure 5.7) are used to detect the first sign of the spike in the traditional

manner; only cases where the spike is first clearly observed at circumferential location C are used for further analysis in the present study.

The pressure traces from the pitch apart transducers (from G.1 to B.5 in Figure 5.7) are examined by plotting each trace one above the other and tracking the spike from where it is clearly observed back to its origins. The position of the pitch apart traces relative to the traditionally spaced traces is shown in Figure 5.8. The red box indicates the region which will now be used to present the results from the pitch apart traces.

A typical stall event is shown in Figure 5.9. Each horizontal line of data is the signal from one transducer, labelled on the left-hand side to correspond with its circumferential location (Figure 5.7). Vertical dotted lines indicate rotor revolutions. First, a description is given of how to track the same physical blade through these traces. This makes it easier to then discuss how the spike disturbance is tracked backwards in time.

Two solid parallel lines have been drawn in Figure 5.9 to represent the location of the same physical blade (blade 15) as it passes each transducer in turn. To follow one blade passage (timewise), start at the red circle in the lower left hand corner of Figure 5.9. This represents blade 15 at circumferential location G. Follow the solid line up and to the right to track blade 15 to the top trace (station B.5). The blade then travels around the circumference of the compressor and reappears at location G.1 as indicated by the black dot. Alternatively, blade 15 can be tracked backwards in time by starting at the square (at the top of the solid line) and tracking in the other direction, down and to the left.

The path of a spike can easily be seen near rotor revolution 6. With the help of the seven circumferential probes in Figure 5.8, however, it is clear that the same disturbance was in existence one revolution earlier. Its signature is well defined at the top of Figure 5.9 near revolution 5. Two dashed lines have been drawn in Figure 5.9 to help identify the spike disturbance. The arrows point in the timewise direction. The distance between the lines tracking the spike is greater than the distance between the solid lines tracking a particular blade. Therefore, in the absolute reference frame, the spike travels slower, propagating at 77% of rotor speed.

The main interest is the origin of the spike disturbance, i.e., the first appearance of a disruption to the normal blade passing pattern. More detail of the spike is needed, so Figure 5.10 zooms in on the blade passages surrounding revolution 5 where the spike first appears. Starting from the top (B.5) of the dashed line in Figure 5.10, the spike can be tracked backwards by following the dashed line down and to the left. The dashed line is slightly to the right of the disturbance (at the propagating edge) so as not to obstruct the view of the disturbed passages. Physical blade numbers are labelled at convenient intervals under the blade suction side trough to assist the discussion. Tracking back from station B.5, where the disturbance is observed most clearly in passage 11-12, the disturbance is easily recognizable until station A.7 (where passage 12-13 is most affected). The disruption to the normal blade passing pattern continues to track to station A.5 in passage 13-14. Finally, the disturbance can be tracked back only very faintly to its earliest sign at station A.2 in passage 14-15.

In Figure 5.10, evidence for the earliest, or "embryonic", spike formation was observed in the region from stations A.2 to A.5. This same pattern was observed in dozens of cases. The development of the spike is very repeatable in this region. Not only is the spike very likely to form at this location of the compressor (in about three quarters of cases, as discussed earlier), but the spike also almost always forms from the same blade (in 91% of cases, the spike forms in the region of blade 15). Hence, these results show the formation of the spike can be reliably investigated in the region of stations A.2 to A.5. These stations will be at the centre of a region of highly concentrated instrumentation between stations G.7 and A.6 (marked by a red line on the axis in Figure 5.10) to be used in the following section to investigate the formation of the embryonic spike in great detail.

Before moving on to the next section, it is worth discussing the propagation of the spike disturbance observed in Figure 5.10. It is interesting that the spike disturbance appears to propagate from the moment it forms, as opposed to reaching a critical size before propagating. At the earliest stages where only one to two passages are affected, Figure 5.10 shows a trajectory drawn from the disturbance at station A.2 to station B.5. From this trajectory, the speed of propagation is found to be 77% of rotor speed. This speed is consistent with the propagation of

the spike at a later stage in its development as noted earlier (the two revolutions of the spike shown in Figure 5.6 show propagation at 77% of rotor speed) where the size of the spike disturbance has grown to six passages. The growth of the stall cell from one passage to six passages has not affected its propagation speed. One might have expected the speed of propagation to slow down as the size of the stall cell increases, as it is known to do as the state of fully developed rotating stall is reached.

More detail is needed in order to better understand the nature of the embryonic spike formation, which will be presented in the following section.

5.5 Study of Embryonic Spike Formation

In the previous section, a region of the compressor was identified where there is a good possibility of capturing the formation of an embryonic spike. In this section, a high concentration of unsteady pressure transducers and hot-wire probes are used to investigate the formation of the spike. The objective is to record a sufficient number of similar stall events so as to produce instantaneous (pressure) and ensemble averaged (velocity) pictures of the stall inception event. First, the set-up of the instrumentation and new hot-wire methods will be discussed; then, detailed flow maps of the stall event will be discussed.

5.5.1 Methodology to Investigate Spike Formation

A total of 40 fast response pressure transducers and 3 miniature hot-wires were used to investigate the spike formation. The methodology is described according to the instrumentation and its purpose in three parts: (1) the configuration of the pressure transducers; (2) the configuration of the hot-wire probes; (3) the methods used to obtain flow direction during the stall event from the hot-wire measurements.

5.5.1.1 Pressure Transducer Configuration

The majority of pressure transducers are concentrated in the area identified in the previous section as being the most likely region for the formation of the embryonic spike. In addition, some probes must be reserved for placement around the annulus in order to select suitable stall events.

The placement of the pressure transducers is described in three groups: probes spaced around the annulus used to detect suitable stall inception cases, concentrated probes used to track selected spikes back to their earliest detectable origins, and highly concentrated arrays of probes used to study the embryonic spike formation in this region.

Detection of suitable stall inception events. It was found that three probes spaced around the annulus are sufficient to detect and select the suitable stall events. These probes are placed near the rotor leading edge at positions B.5, E and G (marked with stars in Figure 5.11). Using these probes, only those cases were selected for further study where the first clearly detectable spike is observed at circumferential location B.5. For the stall events selected, care was taken to ensure the spike continued around the annulus and led to fully developed rotating stall. This is a necessary requirement to eliminate the possibility of studying pre-stall disturbances that do not lead to stall inception.

Tracking the nascent spike to the concentrated probe region. The stall events selected with the three circumferential probes described above provide a rough basis for finding those stall events most likely to have originated where the measuring probes are concentrated. However, three probes are not sufficient to determine if the spike actually originated in this region.

Additional probes were placed near the leading edge at stations B.5, B, A.6, A.4, A.2, G.7 and G, as shown in Figure 5.11. The spike identified at position B.5 (for selected cases as described above) is then tracked backwards to its origins in a similar method as was described in Section 5.4.2. Stall events were selected where the earliest detectable sign of a disturbance occurred at station A.2. Signals from stations G.7 and G were carefully analyzed to check if a disturbance was visible

prior to station A.2, in which case that stall event was discarded (as this indicates the formation of the spike occurred before the concentrated probe region).

Arrays of concentrated probes in the region of spike formation. The concentrated probe region is located from stations G.7 to A.6 shown in Figure 5.11. Pressure transducers are mounted flush with the casing wall in arrays at stations G.7, A.2, A.4, and A.6. All probe arrays are shown in Figure 5.11, bottom. As can be seen, each pressure transducer array is separated by an array with hot-wire access holes. Note: it is not feasible to place instrumentation further upstream than position +2 due to the presence of a structural flange upstream of the rotor blade row.

5.5.1.2 Hot-wire Configuration

Miniature hot-wires were used to obtain velocity information in the concentrated probe region. This section discusses how the hot-wires are set-up. The miniature hot-wire design was described in Section 3.6. For this investigation, the height of the hot-wire from the casing was set at 50% of the tip clearance gap unless specified otherwise.

The hot-wire configuration is illustrated in Figure 5.11. Three hot-wires are installed, one each at stations A.1, A.3, and A.5, in the same relative axial position. One such configuration is shown in Figure 5.11, bottom. The hot-wire positions are indicated by the filled green circles to show they are located at axial position +1 at each respective station. The other (unfilled) access holes are plugged flush with the casing. For each configuration, the hot-wires are turned to four different orientations, each 45° apart. When all four orientations have been tested for one configuration, the hot-wires are then moved to the next axial position to make a new configuration. This process is repeated for the axial positions shown in Figure 5.11.

The hot-wires are recorded simultaneously with the fast response pressure transducers. For each of the four hot-wire orientations at each configuration, the compressor was stalled at least 10 times according to the methods described in Section 3.8.

5.5.1.3 Hot-Wire Analysis: Obtaining Flow Vectors at Stall Inception

This section describes the methodology used to produce maps of instantaneous velocity vectors covering the process of stall cell formation.

The formation of the stall cell is a transitory event, so hot-wire data must be analyzed differently from the way it was to produce the ensemble averaged flow vectors presented in Chapter 4. The hot-wire vector algorithm is described in Section 3.6.3. For flow measurements of a transitory event such as stall inception, the ensemble average input to the algorithm must be composed of data from repeated instances of the stall event (rather than successive revolutions of the rotor at a constant flow coefficient). Data from multiple stall events build an ensemble for each hot-wire orientation, and multiple orientations are then used in the algorithm to determine flow vectors. It is thus necessary to carefully select repeatable stall events to obtain the best accuracy of the flow vectors. The selected stall events must start at the same circumferential location in the compressor (where the instrumentation is situated), from the same blade (to avoid error from small differences among passages), and at the same phase of development.

Suitably repeatable stall events are selected in the following manner. The pressure transducer configuration described in the previous section is used to select the stall events where the first sign of a disturbance is observed in the concentrated probe region; this occurs in at least 70 out of 100 events as discussed earlier. The raw pressure and hot-wire traces of these selected events were then examined and compared. It was found that of the stall events selected, not all were at precisely the same stage of development. In roughly half of the selected cases, the earliest sign of the spike disturbance was observed to affect the same blade passages with the same magnitude disturbance as it passed over the concentrated probe region. The disturbance at this stage is referred to as a "repeatable stall event" in the remainder of this chapter. A collection of repeatable, similarly sized stall events is thus built up and used to produce the velocity maps of the stall inception process which are presented in the next section.

Before moving on to the results, it is important to note that the level of uncertainty in the stall inception velocity vectors is inherently larger than for those

produced at a constant flow coefficient because the selection criteria limit the number of stall events available for ensemble averaging. Section 3.6.3 discusses how the uncertainty was examined, and steps taken to establish confidence in the results. The accuracy of the vectors is $\pm 9^\circ$ at the leading edge and $\pm 4.5^\circ$ at the trailing edge. Considering that the flow vectors change by more than 180° within a blade pitch at the leading edge, this level of uncertainty is reasonable.

The flow maps presented in the following section are the product of recording more than a thousand stall inception events. Of those, a few hundred events were directly used in the production of the flow maps. Although each stall inception event is slightly different, consistent patterns do emerge.

5.5.2 Spike Formation Results

The early development of a spike over the course of seven pitches is described in this section. Static pressure contours and velocity vectors are used to show the emergence of a disturbance and its development into a stall cell. The static pressure measurements are examined first.

Static Pressure Contours in the Concentrated Probe Region

The pressure transducer arrays, at stations G.7, A.2, A.4, and A.6 from Figure 5.11, are used to make static pressure contour plots of the flow as the blades pass by. A typical result is shown in Figure 5.12. The top contour plot represents the information from array G.7. The next contour frame is located at A.2 where the rotor has travelled two blade pitches. Similarly, the next two contour maps are each two blade pitches apart. In each contour plot, the blades travel from right to left, and the axial direction is downwards (one blade is shown at the top left). The contours of static pressure are on the same absolute scale for each array, with red being the highest pressure and blue the lowest pressure. Three blades are labelled. Looking at the same blade passage from the top frame to the bottom represents the change in flow conditions in that blade passage over the course of seven pitches. What is shown is a progression from a stable state to the earliest form of a stall cell (which is referred to as the formation of an embryonic

spike). This progression will be discussed here in chronological order, starting from station G.7.

At station G.7, the behaviour in the passages surrounding blade 15 is visually different. The tip leakage vortex of passage 15-16 is recognized by a thin trace of lower pressure aligned with the blade (marked with an arrow). The tip leakage vortex in passage 14-15 is broader and has a different trajectory (NB: both vortices are very firmly within the blade passage). How significant to stall inception is the unique behaviour in these passages? By observing these passages at *stable* conditions near stall, the different character in the two passages was found to be a manifestation of what makes these passages different from the norm. Higher flow unsteadiness and passage to passage flow variations were found in these passages as was discussed in the previous chapter, Section 4.4. It was shown in the previous chapter that the higher steady and unsteady flow variations in these passages are linked to a local irregularity in blade spacing. It is possible that the unique character of these passages increases the likelihood that a new disturbance will form here; this will be explored in a later section. At present, it is simply important to note that the unique behaviour observed in passages 15-16 and 14-15 is also observed intermittently at stable conditions. Hence, at this location (G.7 in Figure 5.12) there is no sign yet of the emerging spike disturbance.

Two passages later, at station A.2, the tip leakage vortex in passage 15-16 has changed and appears to have broken up or been influenced by a new disturbance. Trails of lower pressure (yellow regions, circled) extend from where the leakage vortex was previously found. The aft pressure in passage 15-16 is also depressed.

Two passages later, at A.4, the tip leakage vortex to the right of blade 16 is unrecognizable. The pressure on the suction side of blade 16 is even lower near the trailing edge, an indication that the flow on the blade is possibly separated. The aft pressure in passage 14-15 is now also slightly lower. The tip leakage vortex leaving blade 15 is unsteady; two tails are seen instead of one.

Finally, two passages later at A.6, there is still evidence of a suction side separation on blade 16 (a spot of yellow at 70% chord) and blade passage 14-15 is fully disturbed. A low pressure spot (labelled "A") is observed in passage 14-15 near the pressure side of blade 14 and wisps of low pressure (yellow) are shedding

from the blade. This low pressure spot is reminiscent of the low pressure spot seen in Figure 5.3 which was observed when the spike was at a later phase of its development (Section 5.3). Again, the possibility of a radial vortex exists (Inoue et al. (2000)).

What has been observed in Figure 5.12 is a very subtle disturbance which has formed in passage 15-16 near station A.2. The disturbance propagates by one blade passage over the course of four rotor pitches, leading to a more distinct disturbance in passage 14-15 at station A.6. It is also interesting to observe that the disturbance begins to propagate right from the outset and that an Inoue-type vortex is involved in the process.

The following section presents three vector flow maps corresponding to the tip clearance flow field at the stations in between the static pressure contours shown in Figure 5.12.

Tip Clearance Velocity Vectors of Embryonic Spike Formation

This section looks at the formation of the embryonic spike by examining velocity vectors in the absolute reference frame at three stations. The stations, A.1, A.3, and A.5 (Figure 5.11), alternate between the stations of static pressure arrays that were discussed in the previous section (Figure 5.12). The vector flow maps are shown in Figures 5.13, 5.14 and 5.15. The vector plots are sandwiched between the static pressure contours from Figure 5.12 that occur one pitch before and one pitch after each vector plot so the contour plots can be referenced easily. The vector plots are also presented in greater detail in Figures 5.16 to 5.18.

Figure 5.13 shows the earliest vector flow map, at station A.1. The first signs of a disturbance to the vectors in Figure 5.13 are circled in passage 15-16 at about 10-25% axial chord. These disturbances are in the region of the interface between the through and reversed flow, at the axial location where it is most vigorous. For reference, the steady-state interface is illustrated as a dashed line in passage 14-15 which is still stable. In passage 15-16, however, a similar interface line cannot be drawn because there are new regions of reversed flow (circled). The balance between the reversed and incoming flow, in the form of the tip leakage

vortex, is no longer present. This agrees with the observations made previously in connection with the static pressure contours. The circled disturbances seen in the vector field are in the same region in passage 15-16 as the first sign of a disturbance seen in the static pressure contours at station A.2. From the pressure contours it was observed that the tip leakage vortex broke down or was affected by a new disturbance in such a way as to make it unrecognizable. Taken together, the velocity and static pressure results show the onset of the embryonic spike occurs when the boundary between the reversed and incoming flow has been destabilized.

Figure 5.14 shows the vector field two pitches later, at station A.3. Again, the vector field is sandwiched between the contour plots one pitch earlier (A.2) and later (A.4). At station A.3, the vectors in passage 15-16 show almost no incoming flow beyond 10% axial chord and an expansion in the extent of the reversed flow at 25% axial chord. The tip clearance flow in passage 15-16 is thus significantly altered and a three-dimensional disturbance with some radial inflow is the only way to balance the flow vectors. The vectors in passage 15-16 clearly show the tip leakage vortex cannot exist in its traditional form; some other flow structure must be present to cause the unusual flow pattern in this passage. This observation is in agreement with the surrounding contour plots. At station A.2, the tip leakage vortex appeared to break down in passage 15-16, and later at A.4 the pressure contours show no recognizable sign of the vortex. In addition, low pressure wisps (yellow) in passage 15-16 at stations A.2 and A.4 are indicative of a more complicated flow structure. As a final observation at this stage, the vectors in passage 14-15 show an increase in reversed flow between 25 and 50% axial chord, but this passage still appears to be stable.

Figure 5.15 shows the vector field two pitches later, at station A.5. There is now almost no through flow entering passage 15-16. Reversed flow from the rear of the passage continues up to and beyond the leading edge. There is a fan of reversed flow just upstream of blade 15, indicating the movement of flow from passage 15-16 to passage 14-15 within the tip clearance gap. Passage 14-15 now has a similar disturbance at 10-25% axial chord (circled) as passage 15-16 had at station A.1. The disturbance has propagated by one pitch, from passage 15-16 at station A.1, to passage 14-15 at station A.5. The disturbance circled at 10% axial chord in

passage 14-15 at station A.5 lines up with the low pressure spot "A" seen in the same passage in the static pressure contour plot at station A.6. The low pressure spot, attributed to an Inoue-type radial vortex, is at the propagating edge of the newly formed stall cell. These results indicate that the radial vortex forms when the embryonic spike disturbance propagates for the first time.

5.5.3 Summary of Embryonic Spike Formation

The static pressure contours and vector maps presented in this section (5.5) show the formation of the embryonic spike in previously unseen detail. The stall cell has been shown to form as the result of a transition in the balance between incoming and reversed flow. Before stall inception, the tip leakage vortex provides a relatively stable boundary between the reverse tip leakage flow and the incoming flow. In each passage, the reversed flow is swept radially inwards into the tip leakage vortex such that incoming flow can pass through inboard of the vortex and the reversed flow. The onset of the embryonic spike disturbance occurs when this boundary between the incoming and reversed flow is destabilized. The spike disturbance appears at about 25% axial chord when the tip leakage vortex no longer forms a clear boundary between the reversed flow and the incoming flow.

What causes the boundary between the reversed flow and incoming flow to destabilize? One possible explanation is that the disturbance to the boundary is the breakdown of the vortex itself due to the amplification of some minor incoming disturbance. The disappearance of the vortex coincides with the formation of the embryonic spike in that passage.

After the onset of the embryonic disturbance, reversed flow increasingly penetrates forward into the passage. Reversed flow from the disturbed passage was then observed to leak into the neighbouring passage near the leading edge. This step is accompanied by the appearance of a radial vortex and marks the initial propagation of the spike. The disturbance at this stage is no longer embryonic. The growth of the disturbance to this extent would alter the inflow, outflow and tip clearance flow of the neighbouring passages. A stall cell has been formed.

The time from the onset of the disturbance to its propagation into the neighbouring passage is about four or five pitches. This is a propagation speed of 75-80%, and is consistent with the observations in Section 5.4.

5.6 Discussion

This chapter has presented an experimental investigation of stall inception starting from a clearly detectable spike disturbance and tracking it back to its earliest origins. This section discusses these observations and their wider implications; suggestions for future research are also made. The discussion is in three parts: (1) the role of steady and unsteady flow variations in stall inception; (2) the propagation or decay of the embryonic spike; and (3) discussion of existing stall inception models in light of the current findings.

5.6.1 Role of Steady and Unsteady Flow Variations in Stall Inception

This section discusses a possible link between the steady and unsteady flow variations observed near stall and the formation of the embryonic spike.

It was shown in Section 4.4 that values for two parameters quantifying unsteadiness and passage to passage flow variations increase as stall is approached. The passage unsteadiness parameter quantified the unsteadiness of the flow in a passage relative to its own average behaviour, each time the rotor passed the same circumferential position. The passage to passage variation parameter quantified the flow variation for each of the 51 blade passages relative to the average flow behaviour in all of the passages. A high value indicates a particular passage is more unique than the other passages.

Although these parameters increase generally as stall is approached, the behaviour of all passages does not change uniformly. The tip clearance flow in a minority of passages is more unsteady and unique than in most other passages. The increase in unique and unsteady behaviour in these passages as stall is approached

was associated with the amplification of disturbances in the shear layers due to small physical irregularities. Flow disturbances in the region of these physical irregularities are amplified more near stall than at design conditions because the adverse pressure gradient is higher, which causes shear layers to be more sensitive to small flow variations; this was discussed in Section 4.4.

In the present chapter, it was found that the embryonic spike originates most often (more than 70% of the time) in the region of the circumference where unsteadiness was found to be highest. In addition, the embryonic spike was found to originate about 90% of the time from the blade associated with high values of the unsteadiness and passage to passage variation parameters (i.e., the blade passage with more unique and unsteady tip clearance flow behaviour compared to all other passages). The unique and unsteady behaviour in this passage prior to stall may explain why the embryonic spike is most likely to form in this region. The first sign of the embryonic spike was observed at the interface between the incoming and axially reversed flow in the tip clearance gap, one of the most vigorous shear layers in the rotor flow field.

This suggests a possible link between stall inception, physical irregularities, and steady and unsteady flow variations. Such a link is difficult to prove, though. Stall inception is most likely to, but does not *always*, occur in the regions identified to have the highest unsteadiness and unique flow behaviour. All shear layers around the annulus amplify disturbances to some extent, depending on the local and instantaneous flow field. There is also an inherent degree of uncertainty introduced by other factors, such as inlet turbulence and machine vibrations, which were not controlled in this study.

Despite the uncertainty, it has been established that machine imperfections and the unsteady and non-uniform behaviour of the tip clearance flow (discussed above and in Section 4.4) are important factors in spike type stall inception. Further investigations into unsteady boundary conditions (such as inlet turbulence and various machine imperfections) would be valuable in determining which unsteady conditions have the greatest impact on the near stall flow field and stall inception. It is now clear, however, the physical location of most interest in terms of stall inception studies is located in the blade passage at about 20 to 30% axial chord downstream of the rotor leading edge plane. This observation explains

why the traditional approach to stall inception detection (with probes ahead of the rotor face) only detects established stall cells instead of the embryonic spike disturbance.

5.6.2 Stall Cell Propagation and Decay

In this chapter three terms were used to broadly describe three phases of the spike development. "Embryonic spike" refers to the earliest development of the spike, its first appearance and growth within a single passage. The term "nascent spike" refers to the early growth or decay in magnitude of the propagating spike, or stall cell, at a phase in its development before it was normally detected with the traditional approach of placing instrumentation upstream of the blade row. If the spike continues to grow in magnitude, it becomes an "established spike", by which is meant the spike leads irreversibly to fully developed rotating stall.

Not all spikes that form become established. In the nascent form, the spike disturbance can grow or decay. In Section 5.4 the speed of the propagating edge of the stall cell was shown to be constant. The growth or decay in the magnitude of the spike (in terms of the number of passages encompassed by the disturbance) is therefore determined by the rate of recovery of the receding passages. A nascent spike will lead to an established form that goes on to fully developed rotating stall if the spike propagates faster than the recovery of the receding edge of the spike disturbance. On the other hand, if the passages at the receding edge of the spike recover faster than the speed of propagation, then the stall cell shrinks and disappears as it moves around the annulus.

These observations of the embryonic spike formation and growth suggest two strategies which might be employed to delay stall inception:

(1) by preventing the formation of an embryonic spike in the first place. Casing treatment could accomplish this by entraining reversed tip leakage flow and/or injecting flow near the casing wall in the downstream direction. This might prevent the destabilization of the boundary between the incoming and reversed flow in the tip clearance gap.

(2) by speeding the recover of the receding passages of a spike disturbance to stop its progression to an established spike. This might be accomplished by injecting flow near the casing wall in the downstream direction in order to convect the disturbance out of the passage as quickly as possible.

It would be interesting to investigate if these suggested stall delay mechanisms are actually responsible for the successful functioning of existing casing treatments such as slots, grooves and re-injection systems.

5.6.3 Implications of Embryonic Spike Observations

In the present work, the formation of the spike disturbance has been shown to be a very subtle process. The initial spike disturbance occurred within the passage and grew in magnitude. At a later phase in the development of the spike, tip leakage flow (not formed as a vortex) was observed to extend forward and enter the neighbouring passage. In other words, the forward movement of the tip leakage flow is an effect of a maturing spike rather than the origin of it. In addition to the studies described in this chapter, further instrumentation was placed ahead of and behind the blade row in a range of radial positions in the outer 5% of span. No evidence could be found for forward or rearward spillage of the tip leakage flow or vortex into the neighbouring passage during the formation of the embryonic spike.

These observations are relevant to the current discussion in the published literature about the role of forward spillage in spike stall inception. The forward spillage hypothesis suggests that the alignment of the interface between the incoming flow and the reversed tip leakage flow with the rotor leading edge plane is the unstable flow condition which leads to spike stall inception (when the tip leakage flow spills forward of the leading edge of the neighbouring blade). Vo et al. (2008) set out a criteria for spike stall inception stating that forward spillage of tip leakage flow is one of two events necessary to initiate stall.

The present study does not agree with forward spillage as a criteria for spike stall inception for two reasons. First, the interface between the incoming flow and the reversed tip leakage flow does not align with the rotor leading edge plane

just before or at stall inception. Second, forward spillage of tip leakage flow was not observed to occur during the formation of the initial spike disturbance. Therefore, it is concluded that if forward spillage occurs in this compressor, it is a consequence of the formation of the spike, not the cause of it.

The following discussion will briefly review past stall inception investigation methodology in light of the new observations made in the present study. As was discussed in Section 2.3.2 of the Literature Review, most previous experimental work has relied on measurements taken upstream (or downstream) of the blade row to locate the point of stall inception. Apart from a few overtip pressure measurements, there are almost no measurements in the path of the rotor blades. The current work shows that the inception process grows from a small disturbance inside the blade passage and that sparse instrumentation upstream of the blade row is unlikely to detect the very first signs of flow breakdown. In most cases, upstream instrumentation would only detect the stall cell after it has propagated some distance and grown in size. CFD studies also seem to suffer from the same problem in that the stall event is often analyzed where the spike is first clearly observed rather than where it is embryonic and difficult to detect.

Experimental and computational investigations supporting the forward spillage hypothesis (e.g., Deppe et al. (2005) and Chen et al. (2008)) provide the spatial or temporal resolution equivalent to observing the spike formation at one circumferential location or on a once per rotor revolution basis. This resolution is too low to observe the progression of spike formation described in the current work. Instead, the spike examined in these and other past studies was likely already an established stall cell.

It can thus be concluded that the observations leading to the forward spillage hypothesis were actually observations of the effect, rather than the cause, of the embryonic spike. The observations were attributed to the mechanism of spike stall inception because the subtleties of spike formation have not previously been appreciated. Similarly, studies supporting the critical incidence and blockage growth hypotheses as stall inception mechanisms have not been investigated by direct observation. Rather, they are based on trends in the flow field as stall is approached.

Studying the spike after (rather than during) its initial formation may be the underlying cause for the wider uncertainty about the stall inception mechanism. The present work shows the importance of sufficient instrumentation to observe the spike formation process. In order to further test existing hypotheses, it would be valuable to investigate the flow within the blade passage (radial measurements) at the formation of the spike, in particular the role of suction side separations and other three-dimensional structures that could not be observed with the tip clearance gap measurements presented here. Such studies might also provide insight into the preference of a compressor to stall by means of a modal or spike type disturbance.

5.7 Conclusions

1) A high concentration of instrumentation was used to investigate spike stall inception. This investigation has shown the importance of concentrated instrumentation and of the necessity of observing the flow within the blade row and in blade to blade detail during the stall inception process.

2) Detailed measurements of the tip clearance flow field show the physical location of most interest in terms of stall inception studies is situated in the blade passage at about 20 to 30% axial chord downstream of the rotor leading edge plane. For early detection, instrumentation thus needs to be in or over the tip region, not upstream or downstream of the blade row.

3) It was found that the formation of the embryonic spike occurs when the interface between the incoming flow and the reversed tip leakage flow is destabilized. A breakdown of the tip leakage vortex itself due to the amplification of a minor incoming disturbance is the final result of this process.

4) After the onset of the embryonic disturbance, reversed flow increasingly dominates the passage. The disturbance grows with the increase in reversed flow, and is accompanied by flow separation from the suction side surface within the affected passage. This initial development of the disturbance occurs in the time it takes the rotor to turn three blade pitches.

5) Following the initial growth, the embryonic disturbance propagates to the neighbouring passage when tip leakage flow spills forward of the blade leading edge. At the same time, a well defined low pressure spot is observed near the rotor inlet face at this first propagation of the spike disturbance. The low pressure spot is thought to be similar to an Inoue-type radial vortex. Inoue et al. (2000) suggested that a radial vortex is attached to the blade suction side and casing within the stalled passages. The vortex is hypothesized to form when circulation is lost as a result of flow separation. The present study provides the first experimental evidence that the formation of a radial vortex does indeed occur when the embryonic disturbance propagates for the first time.

6) It has been shown that the initial embryonic disturbance itself is not associated with the forward movement of the tip leakage vortex nor triggered by the forward spillage of tip leakage flow. The forward spillage of tip leakage flow occurs after the development of the embryonic disturbance. Therefore, the forward spillage hypothesis discussed in recent literature is not a universal mechanism for spike stall inception, but rather a feature of the spike after its initial formation.

7) The measurements have shown that many observations of stall inception reported in the literature could not possibly have resolved the embryonic spike formation because this occurs inside the blade passage. It was found that the traditional method of detecting stall inception (using filtered traces from sparsely spaced probes upstream of the rotor face) does not detect the spike disturbance until about 1/4 of a rotor turn after its true origin. Most observations of stall inception reported in the literature are thus of an established disturbance which has already propagated by 2 or 3 passages from its origin. Investigations based on the study of an established spike, instead of the embryonic disturbance, have contributed to the confusion surrounding the mechanism of spike stall inception.

8) Statistical measurements have shown the embryonic spike originates 70% of the time from the same circumferential region of the annulus and 90% of the time from the same blade passage. The most critical circumferential region, and the most critical blade, are the same as those that were found to have high unsteadiness and the most unique tip clearance flow behaviour in the previous chapter. It has been suggested that this unique and unsteady behaviour is linked to machine imperfections.

9) It has been shown for the first time that the embryonic spike propagates from inception and continues to propagate at 77% of rotor speed even as the spike grows in size (the number of disturbed passages increases from 1 to 6 passages over the course of less than a 1/3 turn of the rotor).

10) Not every embryonic spike that forms will become established and complete the stall inception process. If the passages at the receding edge of the disturbance recover faster than the speed of propagation, the stall cell shrinks and disappears as it moves around the annulus. The repeated formation, healing and disappearance of embryonic disturbances is a commonly observed feature of stall onset.

Chapter 6

Extraction/Re-Injection Casing Treatment

6.1 Introduction

Stall is avoided by restricting the compressor operating point to a safe distance from the stability limit. In some cases the application of casing treatment to the outer wall of the compressor annulus over the rotor tips may be used to regain a part of the restricted operating range. This gain in surge margin may be used to allow engine operation at higher efficiencies or to reduce engine weight by removing a bulkier technology that provided the same stall margin improvement, such as variable stator blades. The benefits of the increased stall margin provided by the casing treatment must, of course, outweigh any efficiency penalty which the casing treatment might introduce.

One possible way of regaining operating range is with the application of a casing treatment which extracts air from a high pressure location in the compressor and re-injects it through discrete loops into the rotor tip region. The air may be injected passively (steady injection driven by the prevailing pressure difference) or actively (pulsed injection controlled by measurements taken in the flow field).

Steady injection has been shown to provide adequate stall margin. Strazisar et al. (2004) and Suder et al. (2001), for example, report 6% stall margin improvement

for 1.3% and 2% of annulus flow re-circulated. Both studies indicate that an increase in mass averaged axial velocity in the tip region is correlated to stall margin improvement.

Active control is usually tailored to a specific stalling mechanism (see, for example, Gysling and Greitzer (1995) and Weigl et al. (1998)) or applied to remedy a restricted operating range due to inlet distortion (see Spakovsky et al. (1999a,b)). These studies show that active control can achieve at least the same stall margin improvement as steady injection, but with a lower volume of injected air. This is advantageous: less worked flow is extracted for re-circulation, and so the impact on efficiency is lower. However, as axial compressors often exhibit a wide range of stalling mechanisms other than spikes and modes (Day et al. (1999)), a general purpose passive treatment is a better option - provided, of course, the problem of efficiency loss can be overcome.

These and other published re-circulating designs rely on air extracted from ports downstream of the rotor row in question, or from even further back in the compressor. In such cases the downstream pressure driving the re-circulated flow is relatively constant, and hence flow is re-circulated at all operating flow rates - including at design where loss of efficiency can least be tolerated. Re-circulation is really only needed near stall where it fulfils its objective of delaying stall onset. Air re-circulation near design operating conditions can be controlled with valves; however, this increases the weight and risk of the system.

The present study aims to passively self-regulate the extracted flow by seeking a better air extraction location, one that will selectively re-circulate a small amount of air at design conditions and a larger amount near stall. Minimizing the re-circulated flow at design will reduce the efficiency penalty of the system.

A similar, strategically placed re-circulation system is often used in centrifugal compressors; see, for example, Hunziker et al. (2001). In a centrifugal machine, the result of flow re-circulation is to improve the operating range by re-matching flow volumes, much as is done by handling bleed in axial compressors. The similarity in the re-circulation system between centrifugal and axial compressors is limited, however, because the amount of air re-circulated is different (5% in the

centrifugal case as opposed to 0.25% in the current axial case) and stall margin gain is achieved by flow re-matching rather than delaying stall inception.

A sketch of the system is shown in Figure 6.1. The casing treatment proposed here has three principal components: an extraction hole, an injection nozzle and a connecting loop. The extraction hole (1) bleeds flow from over the rotor tips. The flow passes through the connecting loop (2) and is then directed by the injection nozzle (3) toward the leading edge tips of the same blade row. The pressure difference between the extraction hole and the injection nozzle drives the flow through the loop. The approach adopted here is to self-regulate the re-circulated air by making use of the changes in the overtip pressure field that occur as the compressor is throttled toward stall.

The objective of the new overtip re-circulation system is to provide a low weight and low complexity system for the first stage of a high pressure compressor. The proposed design is evaluated based on its ability to provide useful stall margin improvements (2 to 4%) coupled with little ($< 0.5\%$) or no loss of efficiency at design conditions. The present study includes efficiency measurements (not often reported in the literature), and a direct comparison with another form of casing treatment evaluated in the same machine.

This work will be presented in six steps.

1) The pressure and velocity maps presented in Chapter 4 form the basis of the present work. These results are used in a simple model to explain the self-regulating capability of the new casing treatment and to predict the best extraction hole location.

2) The optimization of the extraction hole is presented. The overtip location and shape are tuned to changes in the tip clearance flow field as the compressor is throttled from design to near stall conditions. The location and shape of the hole are chosen such that re-circulation through the loop is minimized near design conditions, and maximized as stall is approached. This should give rise to a casing treatment which will maintain compressor efficiency and will extend the operating range of the machine.

3) The injection nozzle is optimized and the complete casing treatment is tested

in full annular form using 12 or 24 discrete re-circulation loops. Three injection nozzle geometries are considered, and the optimal angle and position of injection are investigated.

4) The effectiveness of the casing treatment is examined when the mechanism of stall inception in the compressor is changed.

5) The optimized extraction/re-injection design is compared to a single circumferential casing groove. This allows a rare comparison of two casing treatment designs in the same machine. A variation of the casing treatment design is investigated where the extraction/re-injection system is integrated with the circumferential groove.

6) The viability of the design is considered in a high-speed compressor and design recommendations are made.

6.2 Simple Model based on Rotor Overtip Flow Field Results

The investigation presented in Chapter 4 yielded pressure and velocity maps of the flow in the tip gap region that formed the basis of the present work. From the changes observed in the flow field as the compressor is throttled toward stall, the possibility arises of a new casing treatment design that will tune itself to the prevailing compressor operating conditions. This concept is first described with the assistance of the overtip results. Then, a simple model based on these experimental results is used to test the self-regulating hypothesis which forms the basis of the new casing treatment design.

Figure 4.2 shows the casing static pressure map at compressor design conditions. It can be seen that the maximum pressure difference across the blade (pressure side to suction side) occurs at about 25% axial chord.

In contrast, the static pressure field at the near stall condition is shown in Figure 4.3. The maximum pressure difference across the blade has increased in magnitude and has moved toward the leading edge, to about 10% axial chord.

As a result, the velocity vectors near design in Figure 4.8 have changed size and direction compared those near stall shown in Figure 4.9.

An appropriately placed air extraction hole would take advantage of the above changes in pressure and flow direction to produce a self-regulating extraction system. The static pressure fields in Figures 4.2 and 4.3 will be used to estimate the best position for the extraction hole using the simple model described below.

Flow through the re-circulation loop will primarily be driven by the pitchwise averaged static pressure difference between the extraction hole and the injection port, $\Delta P = \overline{P}_{EX} - \overline{P}_{INJ}$, i.e., the pressure difference between positions 1 and 3 in Figure 6.1. The best extraction hole location will be one that maximizes flow re-circulation at near stall conditions (maximize ΔP_{NS}) and to minimize flow re-circulation at design conditions (minimize ΔP_D). **If there is an optimum location for an extraction hole, based on more re-circulation near stall and less re-circulation at design, it will show up as a maximum of the function** $\Delta P_{NS} - \Delta P_D$.

To evaluate ΔP, the pitchwise averaged static pressure at each of ten chordwise positions (from the leading edge to the trailing edge in Figures 4.2 and 4.3) is used for $\overline{P}_{EX}$. The pressure for the injection location, $\overline{P}_{INJ}$, is taken from the static pressure at 10% axial chord upstream of the rotor leading edges. The pressure difference ΔP is evaluated at near stall and design conditions and used to produce the function $\Delta P_{NS} - \Delta P_D$. This is shown in non-dimensional form in Figure 6.2. The maximum of the function suggests the best axial location for the extraction hole will occur at 35% axial chord.

It is clear that having the extraction hole at a part-chord position will produce less driving pressure for the re-circulating flow than if the hole were further downstream, at the exit of the blade row for example. This disadvantage is, however, outweighed by having a self-regulating system that minimizes re-circulated flow at design conditions. Figure 6.3 shows the difference between a re-circulation loop using an extraction hole at 100% chord and one using a hole at 35% chord. At 100% chord, the pressure difference driving the re-circulation is more or less constant from design to stall. At 35% chord there is a clear rise in the driving pressure as the flow coefficient is reduced toward stall. This rise is a natural

consequence of the forward shift in blade loading which occurs as the flow rate is reduced.

Having used a simple model to find the best position for the extraction hole, it now remains to check that this position is in fact the best and to find the optimal shape and orientation of the hole.

6.3 Extraction Hole Optimization

It is not sufficient to rely on a model based on the pitchwise averaged static pressure measurements to choose the location of the extraction hole. The changing *velocity* field also plays a part and so the only real measure of merit is the flow rate through the re-circulation loop.

The extraction hole optimization was carried out on the large Deverson compressor. Past experience (Hathaway (2006)) indicates that casing treatment function is not sensitive to compressibility effects; i.e., the function in a low-speed compressor is indicative of high-speed performance.

A single extraction/re-injection loop was used to optimize the extraction hole, as shown schematically in Figure 6.4. A composite block was fitted to the compressor casing over the rotor tips and extraction holes were cut through the block at various axial locations and angles as shown in Figure 6.5. There are many holes in this block but only one is open for testing at a time; the others are blocked with the green modelling clay seen in the photo.

The flow is extracted through the block at the compressor casing surface, directed around the outside of the compressor via a piece of plastic tubing, and re-injected upstream of the rotor row through a round hole 70% axial chord upstream of the blade leading edge. The location of the injection hole was influenced by constraints of the rig; however, its position is not important at this stage provided it gives a representative static pressure level against which to optimize the extraction hole.

The extraction holes were produced by drilling through the composite block with

no rounding of the break-through edges. The resulting surface profile of the hole is an ellipse. The angular orientation of the extraction hole is defined in two planes: the surface offtake angle and the tangential offtake angle. The surface offtake angle is the angle of the extraction hole relative to a plane tangent to the surface of the casing wall; a surface offtake angle of 30° is shown in Figure 6.4. (This angle is used in all test cases presented here as smaller angles were found to create a hole with an edge of material too thin for reliable production.) The tangential offtake angle, on the other hand, is defined relative to a line tangential to the casing surface in the direction of blade rotation as shown in Figure 6.6.

The flow rate passing through the loop is measured using a miniature Venturi meter as shown in Figure 6.4. A hot-wire probe is also shown in Figure 6.4. This probe was used to measure the pulsation amplitude in the re-circulation loop caused by the blade passing over the extraction hole. The mass flow through the loop oscillates about ± 20% of the averaged value. Although this oscillation is significant, it does not in itself turn the injection on and off, and is a lower magnitude than that needed to be considered a pulsed jet. The results presented in the following sections quote the average mass flow through the re-circulation loop. For each parameter variation discussed below, the mass flow rate through the re-circulation loop was measured at three flow coefficients: one near stall, $\phi = 0.43$, one mid-range, $\phi = 0.465$, and the other near design, $\phi = 0.50$.

6.3.1 Axial Location of Extraction Hole

The axial location of the extraction hole was optimized using a 0° tangential angle as defined in Figure 6.6. The location of the hole was varied from 10% to 90% axial chord. The results are shown in Figure 6.7, reporting the percentage of the total incoming flow which is extracted and re-circulated through the loop. At all operating conditions, the figure shows a general increase in re-circulated mass flow as the hole location is moved rearward. This is expected, as the circulation is driven by the average pressure difference between the extraction and injection holes. This pressure difference increases with axial location because of the general pressure rise through the blade row.

The trend of the re-circulated mass flow versus the axial position of the extraction hole is different at compressor design and near stall conditions (Figure 6.7). At design conditions, the blue line shows the re-circulated mass flow increases continuously in a parabolic manner as the extraction hole moves downstream. At near stall operating conditions, the green line shows the re-circulated mass flow increases rapidly at first and then levels off.

The most important aspect of Figure 6.7 is the vertical distance between the blue and green lines, as this represents the change in the re-circulated mass flow as the compressor is throttled from design to near stall conditions. To achieve an effective self-regulating system, the objective is to find the maximum vertical distance between the two lines. Figure 6.7 shows the greatest vertical distance is in the region between 30% and 40% axial chord. For an extraction hole located in this region, the re-circulated mass flow near design conditions is about half of that re-circulated near stall. This location thus achieves the desired self-regulating aspect of the new casing treatment design, and agrees with the optimum location found by the simple model in Figure 6.2.

All further angle and shape optimization is completed with the extraction hole set in the "sweet spot" region centred at 35% axial chord.

6.3.2 Tangential Offtake Angle

The tangential offtake angle, as defined in Figure 6.6, was varied from $-30°$ to $+20°$; the results are shown in Figure 6.8. The lines are nearly parallel, indicating low sensitivity of the re-circulated mass flow to tangential angle. The re-circulated mass flow near stall (green line) is maximized when the tangential offtake angle is in the range $-20°$ to $0°$. For this range, the re-circulated mass flow near design conditions (blue line) is lowest at a tangential offtake angle of $-20°$. An offtake angle of $-20°$ is thus chosen as the optimal angle for the self-regulating extraction hole. At an axial location of 35% chord, and an offtake angle of $-20°$, the extraction/re-injection loop re-circulates about twice the mass flow near stall as it does near design.

The optimum axial location (35% chord) and tangential offtake angle ($-20°$) determined here are represented by the oval and trajectory vector sketched in Figures 6.9 and 6.10. They show the casing static pressure contours with absolute velocity vectors at 50% tip clearance height, for design and near stall conditions. Figure 6.9 shows at design conditions, half of the flow vectors at the pitchwise position of the extraction hole are misaligned with the trajectory. In contrast, at the near stall condition shown in Figure 6.10, most of the flow vectors are aligned with the trajectory of the extraction hole.

As can be seen, the optimization experiments have produced an extraction hole which is misaligned with the flow vectors at design conditions (where minimum flow extraction is required), and aligned with the prevailing flow direction near stall (where maximum extraction is required). This orientation of the hole thus aids flow extraction near stall because the favourable flow direction reduces entry losses.

6.3.3 Extraction Hole Shape

With the optimal axial chord location and tangential offtake angle defined, the geometrical shape of the extraction hole can be investigated. The extraction hole shapes chosen for investigation are shown in Figure 6.11, their cut profiles being viewed as on the casing surface. The casing surface area of each hole is the same. The first shape is a simple hole drilled through the surface at an angle, hence the elliptical profile on the surface. The second shape, the stretched ellipse, shows a wider opening in the direction of the offtake trajectory; this shape was meant to further minimize the entrainment of flow near design conditions. The third shape, a slot, widens the opening of the extraction hole along a tangential line; this was done in the hope of extracting as much axially reversed flow as possible at conditions near stall. The latter two were produced using a 3D rapid prototyping printer.

The results for the extraction hole shape optimization are shown in Figure 6.12. It can be seen that changes to the extraction hole shape have little effect on the re-circulated mass flow. Further, the effect of the individual shapes was to either increase or decrease the re-circulated mass flow at all flow coefficients, not just

near stall as is desired. In addition to the geometries shown in Figure 6.11, the sensitivity of the extraction hole to profiling of the lip edges was also investigated. None of the tested profiles produced any measurable advantage.

As none of the additional hole shapes enhanced the self-regulating feature of the extraction system, the drilled hole (elliptical surface profile) was maintained for ease of manufacture.

6.3.4 Extraction Hole Optimization Summary

It has been shown that it is possible to find an optimum flow extraction configuration which is self-regulating in its ability to re-circulate a minimum amount of flow at compressor design conditions and a maximum amount of flow near stall. An optimized loop will re-circulate about 0.01% of the annulus flow near stall, and half that near compressor design conditions. This self-regulating feature is essential for an effective form of casing treatment which aims to maintain compressor efficiency at design conditions and extend operating range near stall.

6.4 Injection Nozzle Design Optimization

The injection nozzle is the second component of the new extraction/re-injection design that needs to be optimized. The objective of this section is to develop an injection nozzle that will provide the greatest possible stall margin improvement from the air provided by the extraction hole discussed in the previous section. In addition, the nozzle design should minimize impact on the efficiency of the compressor. The optimization of the nozzle will include the manner of air injection (into the main stream or along the casing), the direction of injection (axial or swirling) and the position of the nozzle relative to the rotor leading edge.

A single injection nozzle will not have a measurable effect on compressor performance and therefore multiple injection nozzles (12 or 24) will be tested in full annular form. For practical reasons, the full annular testing will be performed in the smaller Mini-Deverson compressor. This single stage machine is a scaled

down model of the larger Deverson compressor. Both compressors are nearly identical in specifications and performance; details are shown in Table 3.1, Chapter 3. The Reynolds number of the smaller rig is slightly lower; however, this does not affect the similarities in performance of the two compressors. The pressure and efficiency characteristics of the two machines are nearly identical, as is the stalling behaviour (spikes).

The Mini-Deverson compressor is a vertical axis machine built up of multiple aluminium rings. These rings are stacked one on top of the other and can be recognized by the horizontal lines in Figure 6.13. In order to test the new casing treatment, the aluminium casing ring that sits over the rotor tips has been replaced by a ring of rapid prototyped plastic segments. These segments can easily be replaced and rearranged to create numerous experimental variations.

Pressure and efficiency characteristics were measured by continuously recording the inlet and casing pressures as the compressor was slowly throttled into stall. The efficiency and pressure rise characteristics for each test case were repeated several times to ensure representative results. For each parameter studied, back-to-back tests were performed and the smooth wall case was measured at the beginning and end of each set of measurements. In this way, it was possible to ensure results are reliably comparative. (The variables used in the performance characteristics are defined in Section 3.7.)

6.4.1 Injection Nozzle Geometries

Three injection nozzle shapes were considered, as shown in Figure 6.14. All three injection nozzles have the same exit area.

The round injector design is simply a hole drilled at an angle of 30° to the casing surface; this would be the simplest design to manufacture. The injected flow is meant to interact with the main flow like a vortex generator jet producing a general increase in axial momentum in the tip region; see Hansen and Bons (2006).

The slot and converging injector designs, on the other hand, inject the flow as close to the casing surface as possible to minimize mixing between the injected jet

and the main through flow. The intent of the two "shaped" designs is to energize the casing boundary layer in the vicinity of the rotor tips. The slot injector design has a straight section just before the exit which is intended to straighten the flow before injection. The converging injector design is intended to accelerate the flow continuously so as to reduce the build-up of boundary layer in the nozzle.

The difference in the design intent between the round and shaped injectors is investigated first by comparing the round and slot injection nozzles using an external air supply. The two shaped designs injecting the flow close to the casing wall (the slot and converging injectors) are compared with each other as a final step.

6.4.2 Injector Optimization with External Air Supply

The optimization of the injection nozzle is carried out in isolation from the extraction/re-injection loop by supplying the injector with flow from an external air supply. This approach makes it possible to regulate the amount of injected air and simplifies the testing arrangement.

Special injection nozzle segments were produced for the compressor; see Figure 6.15. The leftmost piece shows a segment as viewed from outside the compressor. This segment is made up of two pieces: a removable plug containing the injection nozzle and a larger piece making up the body of the segment. The second segment from the left shows the same piece but viewed from inside the compressor. A slot design injection nozzle can be seen. To the right are two views of the removable plug. The direction of injection can be changed by rotating the plug using the protruding wings. A protractor printed into the outside of the piece (seen far left) is used to set the angle of injection. The far left piece in Figure 6.15 shows a round hole in the back of the plug. Tubing is inserted into this hole and connected to a central manifold to which external air is supplied. Twelve such injector segments are evenly distributed around the annulus. The injection nozzle exit is located 50% axial chord upstream of the rotor leading edge. When using the external air supply, the most convenient way of expressing flow rate is to use a velocity ratio such as V_i/V_x, where V_i is the injected flow velocity, and V_x is the average axial velocity through the stage.

Injection Nozzle Design (Penetrating vs. Wall Jet)

The round and slot injector designs shown in Figure 6.14 were compared in order to determine whether it is more beneficial for the injected flow to mix with the main stream or to follow the casing wall with a minimum of mixing.

The injected flow is directed axially downstream in these tests. The injection velocity is determined by the mass flow rate and the exit area of the injection nozzle. The external air supply is controlled to provide three levels of injected velocity ratio: $V_i/V_x = 1$, $V_i/V_x = 1.5$, and $V_i/V_x = 2$. Figure 6.16 shows the total-to-static pressure rise characteristics for the slot and round injector designs at these velocity ratios. The black line in all plots is the original smooth wall configuration of the compressor. The sharp peak of the characteristic is the lowest stable flow coefficient before the compressor stalls. The results in Figure 6.16 show the slot design injectors provide a stall margin improvement more than double that of the round hole design. This is observed at each level of injected velocity. This indicates the injected air is most effective when injected close to the casing wall with minimal mixing. This conclusion is in line with others reported in the literature, e.g., Strazisar et al. (2004) and Weigl et al. (1998).

Angle of Injection

Injection angle studies are reported in the literature but consensus is not achieved. Suder et al. (2001) and Strazisar et al. (2004) showed axial injection is best (with axial inflow). However, other studies with axial inflow show different results. D'Andrea et al. (1997) indicated an injection angle of 30° in the direction of rotation was optimal in a low speed compressor. Another injection study in a low speed compressor by Deppe et al. (2005) indicated optimum injection was achieved at 75° against the direction of rotation. Finally, Weigl et al. (1998) reported that 15° against the direction of rotation was best (also with axial inflow) in a transonic rig. Because of the apparent "compressor specific" nature of the best injection angle, optimization is a necessary step in the current work.

The angle of injection was varied from $-90°$ to $+90°$ using the rotating plugs shown in Figure 6.15. Axial injection is defined as 0°, and injection in the direction

of blade rotation is defined as positive. The slot type injectors are used for this work.

Figure 6.17 shows the results for $V_i/V_x = 2$. Again, the black characteristic line indicates the smooth wall configuration. Each coloured characteristic line indicates that all 12 injectors have been rotated to direct the flow to the angle specified in the legend. The results in Figure 6.17 show axially injected flow improves the stall margin the most. Results for other injected velocity ratios lead to the same conclusion.

6.4.3 Injection Nozzle Integrated with Re-circulation Loop

The optimization process continues with the slot design injection nozzle as an integrated part of the complete extraction/re-injection system. The axial position of the nozzle is tested at two locations: 10% and 50% axial chord upstream of the rotor leading edge. The best axial location is then used to compare the two injection nozzle shapes which inject flow close to the casing wall: the slot and converging design injectors (Figure 6.14).

A complete extraction/re-injection loop segment is shown in Figure 6.18, left. The extraction hole is at the lower right hand corner of the segment. The hole extends into a loop which leads to the slot injection nozzle, seen on the left side of the segment. The injection nozzle is deliberately offset circumferentially from the extraction hole; this is done to minimize the possibility of overheating due to repeated re-circulation of the same flow.

All tests were conducted in full annular form with 12 or 24 loop segments evenly distributed around the annulus, Figure 6.18, right. The optimized extraction hole design from the previous section is used and the air is injected axially downstream. The injected velocity ratio of the complete extraction/re-injection loops is just above $V_i/V_x = 1$.

Axial Location of Injection Nozzle

Figure 6.19 shows that with the injection nozzles at 10% and 50% axial chord upstream of the rotor face, the same improvement in stall margin (2.2%) is achieved. The efficiency characteristics, on the other hand, are very different. The loops injecting at 50% axial chord upstream of the rotor leading edges incur an efficiency penalty of 1.5%. The loops injecting at 10% axial chord upstream of the rotor leading edge fair better with a drop in maximum efficiency of only 0.4%.

The axial location influences the amount of spreading that occurs in the injected jet before it reaches the rotor face. Although the results here show the spreading has not affected the stall margin improvement, it has affected the efficiency of the compressor. The lower efficiency in the case of the injectors located further upstream may be due to the injected flow having more time to mix out.

Injection Nozzle Geometry (Slot vs. Converging Design)

The two injection nozzle designs which inject flow close to the casing wall are now compared: the slot and converging design injectors (Figure 6.14). This final optimization takes advantage of the previous results by injecting axially and placing the injection nozzles 10% axial chord upstream of the rotor leading edge.

Figure 6.20 shows the performance results for the slot and converging designs. The blue line shows a stall margin improvement of 2.2% relative to the smooth wall case. The slot design injectors incur an efficiency penalty with a drop in maximum efficiency of 0.2%. With 12 converging type injectors installed, the red line shows an identical 2.2% improvement in the stall margin. The converging injector outperforms the slot injector design, though, by having less impact on the compressor efficiency. The maximum efficiency with the converging injection nozzles is 0.4% higher than that of the smooth wall configuration. While this is not a large gain in efficiency, it does demonstrate this casing treatment design extends the stall margin without a negative impact on the work done by the stage.

The converging injector design is different from the slot injector design in that it

accelerates the flow continuously to the injection exit, and injects it smoothly on the casing surface. It is possible the converging injector design is more efficient for the same reason the axial injection closer to the rotor face (in the previous section) was more efficient. Both affect the radial extent of the injected jet when it reaches the rotor face. These results indicate the injector design is a critical parameter influencing the efficiency of the extraction/re-injection system.

Finally, a total of 24 loops were installed and tested by combining 12 converging design injector loops and 12 slot design injector loops. This combination of loop designs is acceptable: both the slot and converging designs inject flow close to the casing wall and both designs provided the same stall margin improvement when tested separately. The stall margin improvement with 24 loops increases to 3%, compared to 2.2% with 12 loops. This is a disappointingly low increase for double the number of extraction/re-injection loops. The reasons for this are investigated in the next section.

6.5 The Influence of Stalling Mechanism

The aim of this section is to investigate the influence of the compressor stall inception mechanism on the effectiveness of the extraction/re-injection casing treatment. A study published by Houghton and Day (2010) found the maximum benefit of casing treatment is only achieved if the compressor stalls by means of a spike stalling mechanism (where inception occurs near the casing). They concluded that casing treatment becomes less effective the more modal the stall inception mechanism becomes (where the spanwise extent of the inception process is greater).

The Mini-Deverson compressor with a smooth wall stalls by means of a spike mechanism. However, fast response pressure measurements indicate that the stalling mechanism is modal with casing treatment installed. The study by Houghton and Day (2010), using a different compressor, suggests that if the rotor stagger is changed, the stall inception mechanism might also change. If the stall inception mechanism changes, an improvement in the stall margin brought about by the casing treatment might be expected.

With the rotor stagger in the Mini-Deverson compressor increased by 2°, the stalling mechanism of the compressor, with the casing treatment installed, did in fact change from modes to spikes. The blue line in Figure 6.21 shows the 12 loops (with converging design injection nozzles) now provide 2.6% stall margin improvement and no change in stage efficiency. The red line shows the stall margin improvement has more than doubled to 6.1% with 24 loops. The drop in maximum efficiency in this case is 0.8%. (Again, 12 of the loops are slot design injection nozzles and 12 are the converging design.) Figure 6.20 shows that the converging injector design is more efficient than the slot injector design. For this reason, it is expected that the efficiency might improve if all 24 injection nozzles were of the converging design.

These results are summarized in the first two rows of Table 6.1 to compare the performance of the casing treatment before the re-stagger (modal stalling mechanism) to the performance after the re-stagger (spike stalling mechanism). The groove casing treatment results listed in the table will be discussed in the next section.

The table shows that for each casing treatment, a greater stall margin improvement is possible when the stalling mechanism is with spikes. Modal stall inception curtails the effectiveness of casing treatment, as was suggested by Houghton and Day (2010).

6.6 Single Circumferential Groove

The new extraction/re-injection design was compared to a circumferential groove tested in the same compressor. The design of the single groove was based on a parametric study reported by Houghton and Day (2011). The leading edge of the groove was at 50% chord, with a width of 14% axial chord and a depth of 28% axial chord. Figure 6.22 shows a photograph of the installed groove design.

The groove design was tested in the Mini-Deverson compressor both before the re-stagger (modal stall inception) and after the re-stagger (spike stall inception). The groove provided no stall margin improvement or efficiency penalty before the

Stalling Mechanism (w/treatment installed)	Modal		Spike	
	SMI	$\Delta\eta$	SMI	$\Delta\eta$
Extraction/Re-injection				
12 loops	2.2%	+0.4%	2.6%	0%
24 loops	3.0%	-0.6%	6.1%	-0.8%
Circumferential Groove	0%	0%	2.3%	+0.2%
Groove + 24 loops	2.0%	-0.2%	5.0%	-0.4%

Table 6.1: Casing treatment performance summary: stall margin improvement and change in maximum efficiency.

re-stagger and 2.3% stall margin improvement and a slightly favourable change to efficiency when spikes were present after the re-staggering.

These results are included in Table 6.1. When comparing the performance of the groove with the 12 loop extraction/re-injection casing treatment, for spike type stall inception the performance is nearly identical. Considering the complexity of the extraction/re-injection system, the circumferential groove may be more advantageous when only the spike stalling mechanism is expected. However, when stall occurs via modes, the extraction/re-injection system provides some stall margin improvement (2.2%) whereas the groove provides none. In this case, the added complexity of the extraction/re-injection system may be acceptable. Changing the number of loops in the extraction/re-injection system may also be used to adjust the SMI if more is needed.

6.7 Re-Circulating Groove

As an extension to the single groove casing treatment, the extraction/re-injection casing treatment was incorporated into the circumferential groove design described above. Discrete extraction holes integrated within the groove direct flow through a loop to the injection nozzles. The nozzles inject axially from 10% axial chord upstream of the rotor leading edges and are of the converging design. Figure 6.23 shows a photograph of the re-circulating groove design. As can be

seen, the discrete loop segments are separated by groove only segments; 24 evenly distributed loops were installed.

The re-circulating groove design was tested both before the re-stagger (modal stall inception, Figure 6.24) and after the re-stagger (spike stall inception, Figure 6.25). The results are summarized in Table 6.1. The re-circulating groove did not exhibit a combined benefit from having both the groove and tip injection. Instead, the re-circulating groove (with 24 loops) provided a slightly lower stall margin improvement (5%) than when 24 discrete extraction/re-injection loops were installed (6.1%). This is surprising, as the re-circulating groove has a higher driving pressure through each loop than its discrete counterpart because its extraction point is further downstream (57% axial chord as opposed to 35% axial chord). It is possible that the re-injected flow is entrained into the groove and this limits its effectiveness downstream of the groove.

In the previous chapter, the first signs of the embryonic spike were observed in the blade passage between 10 and 25% axial chord, and associated with axially reversed flow in the tip gap. If the extraction/re-injection casing treatment functions by preventing the embryonic spike from forming or developing, it is likely the injected jet does so by reducing the amount of axially reversed flow coming from the rear of the passage. Further tests are needed to judge the importance of the axial extent of the injected jet.

6.8 Performance and Recommendations

The self-regulating extraction/re-injection design fulfilled the initial design objectives of providing a modest stall margin improvement (2 to 4%) with little ($< 0.5\%$) or no loss of efficiency at design conditions. As seen in Table 6.1, with 12 loops, the initial aim has been met. When 24 loops are installed, a higher stall margin improvement is achieved but with an unacceptable efficiency penalty. Part of this may be due to using the less efficient slot design injectors for 12 of the 24 loops. The efficiency is expected to improve if all 24 injectors were of the converging design.

The extraction/re-injection casing treatment design presented here was shown to provide at least a 2% stall margin improvement with 12 loops (re-circulating less than 0.13% of the inlet mass flow near stall and half that at design) and up to 6% stall margin improvement with 24 loops (re-circulating 0.25% of the inlet mass flow near stall and half that at design). This amount of re-circulated mass flow compares favourably to previous work. Strazisar et al. (2004) report 4-6% stall margin improvement with 0.7 to 1.3% of annulus flow re-circulated, and Suder et al. (2001) report 6% stall margin improvement with 2% of annulus flow injected.

The results in Table 6.1 indicate the extraction/re-injection system proposed in this paper may be an improvement on existing re-circulating casing treatments. However, a true comparison cannot be made with other re-circulating systems reported in the literature because efficiency measurements are rarely reported. None are included in the following comparable studies: D'Andrea et al. (1997); Deppe et al. (2005); Gysling and Greitzer (1995); Spakovsky et al. (1999b); Strazisar et al. (2004); Suder et al. (2001); Weigl et al. (1998).

As a final step, CFD simulations were examined of the flow field in the tip gap region of a six stage fixed geometry Trent-style high-pressure compressor*. The first two rotor rows are transonic. The tip region calculations for the high speed compressor showed similar changes in the pressure and velocity fields accompanying changes in compressor flow rate as were discussed in the introduction. Using these calculations, an analysis of the casing pressure field was conducted to find the optimum extraction hole location for the first rotor row, as was done in Figure 6.2 for the Deverson compressor. The model applied to the high speed machine (Figure 6.26) produced a well defined peak in the pressure difference function at 30% chord. As the presence of a "sweet spot" is the main driver of the self-regulating action, it is concluded that the new casing treatment design might also be effective in a high speed machine.

In general, all axial flow compressors demonstrate a forward shift of blade loading as the flow rate is reduced toward stall. This forward shift is sufficient to suggest that all axial compressors will exhibit some self adaptability in terms of pressure

*Unpublished data made available through the European project NEWAC; see Rolt and Kyprianidis (2010).

driven re-circulation. It is thus possible that the new casing treatment may be usefully applied in other compressors.

6.9 Conclusions

1) A new form of overtip re-circulating casing treatment for axial compressors has been designed and tested. The system met design objectives and has the ability to self-regulate the amount of air being re-circulated. A minimum amount of air is re-circulated at compressor design conditions (thus minimizing any loss of efficiency) and a maximum amount of air is re-circulated near the stability limit (thus maximizing stall margin).

2) In a departure from previous re-circulating systems in axial compressors, the new casing treatment makes use of air extraction from over the rotor tips, rather than from downstream of the row or stage. The self-regulating capability of the system functions by making use of changes in the overtip pressure and velocity fields which accompany changes in compressor flow rate. New high resolution pressure and velocity measurements in the tip clearance gap are used to explain why the new treatment possesses self-regulating capabilities.

3) The measurements show that a reasonable level of stall margin improvement, and a reasonable level of self-regulation, in terms of the amount of air re-circulated, can be achieved by locating the extraction hole at about 35% chord downstream of the rotor leading edges. The best chordwise location for the air extraction hole will differ from compressor to compressor depending on the blade loading profile.

4) It has been shown that the angular orientation of the extraction hole (relative to the tangential direction of blade travel) is important in achieving the self-regulating feature of the new design. This is explained in terms of entry losses which depend on the prevailing tip clearance velocity field.

5) The injection nozzle design was shown to influence the effectiveness of the extraction/re-injection system. The optimum injection nozzle confines the injected flow as close to the casing wall as possible. Parameters which affect the

spreading of the injected jet, such as axial location and injection geometry, were important in this regard.

6) It was shown that the new extraction/re-injection design is preferable to a single circumferential groove when both spike and modal stall inception can be expected - or when more stall margin improvement is needed than a groove can provide.

7) The type of stall inception mechanism (spikes or modes) in a given compressor has recently been shown (Houghton and Day (2010)) to be important in determining the effectiveness of casing treatment. The current work, using a different compressor, confirms this observation. The current work shows overtip casing treatment is less effective if the compressor has a disposition to stall in modal form.

8) Stall margin improvements between 2.2 and 6.0% were achieved depending on the number of re-circulating loops and on the compressor stalling mechanism. Efficiency penalties at the compressor design condition varied between 0 and 0.8% for less than 0.25% of the inlet mass flow re-circulated near stall and half that at design. In general, modest stall margin improvements (2%) were possible without any loss of compressor efficiency at design conditions.

9) A simple model using casing static pressure measurements has been formulated to predict the best location for the air extraction hole. The model maximizes the difference in re-circulation driving pressure between design and near stall operating conditions. Application of the simple model using CFD derived pressure maps for an aero-engine compressor suggests a similar self-regulating casing treatment design will be effective in high speed machines.

Chapter 7

Conclusions

Advances in aero-engine stability require a better understanding of compressor rotor tip clearance flows. Tip clearance flows are central to discussions on compressor efficiency, stall inception, and casing treatments. Stall inception, in particular, is a topic of continued research. After more than half a century of aero-engine stall and surge investigations, the mechanism for the onset of stall is still debated. The consequences of this lack of fundamental understanding are significant to both design and operating costs. The stability limit of a new compressor cannot be accurately predicted by computational means, so the influence of design changes must be assessed with costly surge testing. The design of casing treatments, which are used to delay stall, must therefore also be developed experimentally. Finally, the need for a safety imposed stall margin often restricts operation to regions of less than optimal efficiency. It is thus clear that successful research on stall inception and tip leakage flows will have far reaching benefits when new compressors are designed.

7.1 Tip Clearance Flow at Stable Conditions

Experiments to measure static pressure, total pressure, and velocity fields in the rotor tip clearance gap were carried out at design and near stall flow conditions. Overtip flow maps were presented to show the flow field at three radial depths.

7. CONCLUSIONS

The measurements from these overtip flow studies are thought to be the most detailed experimental measurements available of their kind. Applications for these results include a range of interests. In the present study, the overtip flow maps form the foundation of the stall inception investigation and are used in the development of a new casing treatment design. Experimental observation of the tip clearance flow field may also be of interest for future research on loss mechanisms and as validation for CFD simulations.

1) It was shown that the tip clearance flow field is very dynamic. The flow direction at some axial locations was shown to change direction by a full 360° from blade to blade. Two distinct regions of axially reversed flow were shown - one near the maximum pressure difference across the blade tip, and the other in the aft portion of the passage. The reversed flow in these regions increases dramatically in magnitude and extent when the compressor is throttled from design to stall.

2) The tip leakage vortex is generated by the interaction of the incoming flow with the tip leakage flow. As stall is approached, the trajectory of the tip leakage vortex was shown to change direction, but not by nearly as much as is required to bring the trajectory of the vortex to the rotor leading edge plane. Forward spillage of tip clearance flow into the neighbouring passage has been shown by some researchers to coincide with the onset of stall and has been hypothesized to be a criteria for the onset of spike stall inception. In the compressor used for the present work, measurements just before stall indicate that forward spillage is unlikely to occur. In the following section, measurements during the stall inception process will be discussed which further conclude that forward spillage as a mechanism of spike stall inception does not occur in this compressor.

3) The measurements show that unsteadiness and passage to passage flow variations increase in general as stall is approached, but that this change is not uniform around the annulus or from one passage to the next. The greatest level of unsteadiness is observed where the tip clearance flow is most vigorous, at about 35% axial chord.

4) At conditions near stall, it was found that the tip clearance flow behaviour in a few blade passages was more unique, and was also the most unsteady, compared

to the behaviour of all other passages. It was found that small variations in blade to blade spacing near the tips was correlated to the variation observed in the tip clearance flow field of the most disturbed passages. The amplification of flow disturbances near physical irregularities in the blading may be explained by the increased sensitivity of shear layers as the adverse pressure gradient encountered by the flow increases (which occurs as stall is approached).

5) The sensitivity of the near stall flow field to physical irregularities and the small disturbances they amplify may be of interest to CFD research. These measurements highlight the level of flow irregularity in a real compressor and suggest that CFD predictions of stall onset will improve in accuracy if small physical details and imperfections are reflected in the meshing.

7.2 Spike Stall Inception

A high concentration of instrumentation was used to investigate spike stall inception. This made detailed observations of the origins of the spike disturbance possible. The traditional approach to studying stall inception has always made use of sparse instrumentation placed upstream or downstream of the affected blade row. The current study shows the importance of concentrated instrumentation and of the necessity of observing the flow within the blade row and in blade to blade detail during the stall inception process.

1) Detailed measurements of the tip clearance flow field show that the physical location of most interest in terms of stall inception studies is situated in the blade passage at about 20 to 30% axial chord downstream of the rotor leading edge plane. The measurements show that the formation of the embryonic spike occurs when the interface between the incoming flow and the reversed tip leakage flow is destabilized. A breakdown of the tip leakage vortex itself due to the amplification of a minor incoming disturbance is the final result of this process.

After the onset of the embryonic disturbance, reversed flow increasingly dominates the passage. The disturbance grows with the increase in reversed flow, and is accompanied by flow separation from the suction side surface within the affected

passage. This initial development of the disturbance occurs in the time it takes the rotor to turn three blade pitches.

2) Following the initial growth, the embryonic disturbance propagates to the neighbouring passage when tip leakage flow spills forward of the blade leading edge. At the same time, a well defined low pressure spot is observed near the rotor inlet face at this first propagation of the spike disturbance. The low pressure spot is thought to be similar to an Inoue-type radial vortex.

Inoue suggested that a radial vortex is attached to the blade suction side and casing within the stalled passages. The vortex is hypothesized to form when circulation is lost as a result of flow separation. The present study provides the first experimental evidence that the formation of a radial vortex does indeed occur when the embryonic disturbance propagates for the first time.

3) It has been shown that the initial embryonic disturbance itself is not associated with the forward movement of the tip leakage vortex nor triggered by the forward spillage of tip leakage flow. The forward spillage of tip leakage flow occurs after the development of the embryonic disturbance. Therefore, the forward spillage hypothesis discussed in recent literature may not be a universal mechanism for spike stall inception, but rather a feature of the spike after its initial formation.

It was found that the traditional method of detecting stall inception (using filtered traces from sparsely spaced probes upstream of the rotor face) does not detect the spike disturbance until about 1/4 of a rotor turn after its true origin. It is now clear that many observations of stall inception reported in the literature could not possibly have resolved the embryonic spike formation because this occurs inside the blade passage. In most cases, the spike has thus been detected when it is already an established disturbance. Investigations based on the study of an established spike, instead of the embryonic disturbance, have contributed to the confusion surrounding the mechanism of spike stall inception. For early detection, instrumentation needs to be in or over the tip region, not upstream or downstream of the blade row.

4) Statistical measurements have shown that in the compressor used for the present work, the embryonic spike originates 70% of the time from the same circumferential region of the annulus and 90% of the time from the same blade

passage. The most critical circumferential region, and the most critical blade, are the same as those that were found to have high unsteadiness and the most unique tip clearance flow behaviour. It is thought that local physical irregularities give rise to increased shear layer sensitivity, i.e., small disturbances are more readily amplified. Due to the unpredictable nature of flow unsteadiness and its effect on shear layers, a degree of uncertainty will always exist as to the precise location of spike formation, i.e., the spike disturbance may not always originate from the same physical location and the same blade.

5) It has been shown for the first time that the embryonic spike propagates from inception and continues to propagate at 77% of rotor speed even as the spike grows in size (the number of disturbed passages increases from 1 to 6 passages over the course of less than a 1/3 turn of the rotor). One might have expected the initial speed of propagation to slow down as the size of the stall cell increases, but in the compressor used for the present work, the speed of propagation only begins to slow down once multiple spikes have formed and they begin to coalesce into fully developed rotating stall.

6) Not every embryonic spike that forms will become established and complete the stall inception process. If the passages at the receding edge of the disturbance recover faster than the speed of propagation, the stall cell shrinks and disappears as it moves around the annulus. The repeated formation, healing and disappearance of embryonic disturbances is a commonly observed feature of stall onset.

7.3 Casing Treatment

A new form of overtip injection casing treatment for axial compressors has been proposed and tested. The casing treatment is local to the rotor blade row, and, using discrete loops, air is extracted from over the rotor blade tips and re-injected upstream of the same blade row near the leading edges at the casing. The novel feature of the system is its ability to self-regulate the amount of air being re-circulated. A minimum amount of air is re-circulated at compressor design conditions (thus minimizing any loss of efficiency) and a maximum amount of air is

re-circulated near the stability limit (thus maximizing stall margin). A parametric study was conducted to produce an effective working design.

1) It has been shown that the new self-regulating system ensures maximum stall margin benefit with minimum loss of efficiency at design conditions. The system achieved stall margin improvements between 2.2 and 6.0%. Efficiency penalties at the compressor design condition varied between 0 and 0.8% for less than 0.25% of the inlet mass flow re-circulated near stall and half that at design. In general, modest stall margin improvements (2%) were possible without any loss of compressor efficiency at design conditions.

2) The self-regulating capability of the new system is made possible by the unique overtip location of air extraction. By placing the extraction hole over the rotor tips, the system makes use of changes in the over-tip pressure and velocity fields, which accompany changes in compressor flow rate, to regulate the amount of re-circulated flow. The air extraction location over the rotor tips is a departure from previous re-circulating systems in axial compressors, where air is usually extracted from downstream of the row or even from a rearward stage.

3) The measurements show that a reasonable level of stall margin improvement, and a reasonable level of self-regulation, in terms of the amount of re-circulated air, can be achieved by locating the extraction hole at about 35% chord downstream of the rotor leading edges. The best chordwise location for the air extraction hole will differ from compressor to compressor depending on the blade loading profile.

4) A simple model using casing static pressure measurements has been formulated to predict the best location for the air extraction hole. The model maximizes the difference in re-circulation driving pressure between design and near stall operating conditions. The model has been shown to work well using pressure field measurements from the compressors used in the present work. Furthermore, application of the simple model using CFD derived pressure maps for an aero-engine compressor suggests that a similar self-regulating casing treatment will also be effective in high speed machines.

5) It was shown that the angular orientation of the extraction hole (relative to the tangential direction of blade travel) is also important in maximizing the

self-regulating feature of the new design. The optimum angle of extraction corresponds to the prevailing flow direction at near stall conditions. This minimizes entry losses at those conditions when maximum re-circulation is desired.

6) The injection nozzle design was shown to influence the effectiveness of the extraction/re-injection system. The optimum injection nozzle induces the injected flow to remain as close to the casing wall as possible. Parameters which affect the spreading of the injected jet, such as axial location and injection geometry, were important in this regard.

7) It was shown that the new extraction/re-injection design is preferable to a single circumferential groove when both spike and modal stall inception can be expected - or when more stall margin improvement is needed than a groove can provide. In agreement with previously published studies, the current work showed that overtip casing treatment is most effective when the compressor exhibits spike-type, rather than modal, stall inception.

7.4 Recommendations for Future Work

The present work has highlighted the significance of machine imperfections in exciting steady and unsteady flow variations. It would be interesting to examine this in more detail. Experimental investigations on this topic might consider a range of physical irregularities that realistically occur in aero-engine compressors. What types of machine imperfections have the greatest effect on the near stall flow field? Another question relating to machine imperfections concerns CFD calculations where each blade is an exact copy of its neighbour. Can CFD calculations be improved by introducing unsteady boundary conditions and machine imperfections that are known to exist in a real compressor?

The investigation of spike stall inception in this work is based on the results from one machine. It would be interesting to perform a similar study of the embryonic spike formation on other machines. In addition to the high concentration of instrumentation in the tip clearance gap used in this work, rotating probes within the blade passage where the spike is most likely to form would be useful.

For computational studies which aim to simulate the formation of a stall cell, it would be valuable if a higher temporal and spatial resolution of the actual spike formation were reported in similar detail to that presented in the current experimental work. It often appears that the finer details of stall inception are overlooked in many CFD studies.

The extraction/re-injection casing treatment proposed in this work is a proof of concept design and could not explore all possible avenues of optimization. It would be interesting to investigate the pulse timing of the injected air. Although air is continuously re-circulated through the loop, it pulses with each blade passing. The phase of the injected air relative to the pitchwise location of the passing blade could be altered by varying the circumferential distance between the extraction and injection ports.

It would also be interesting to further explore the optimization of the injection nozzle, as this was shown in the present work to significantly influence the effectiveness of the casing treatment. The mechanisms behind the optimal angle of injection and the jet height may be important. In this regard, it would be useful to make detailed tip clearance flow measurements in the presence of this casing treatment to investigate how injected flow into the tip clearance gap changes the flow structure.

Finally, it would be useful to measure the performance of the casing treatment proposed in this work on a high speed machine to determine if stall suppression can be achieved and if the self regulating capability also works in a transonic environment.

Figures

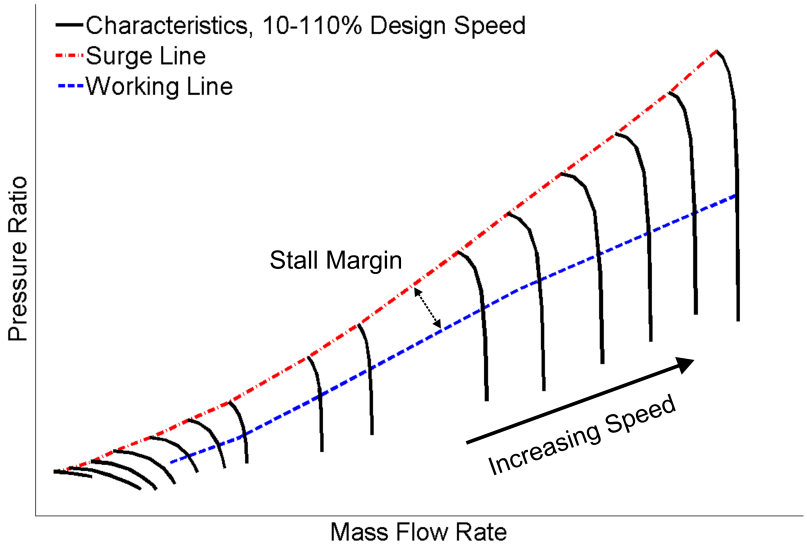

Figure 2.1: Generic high-speed compressor performance map.

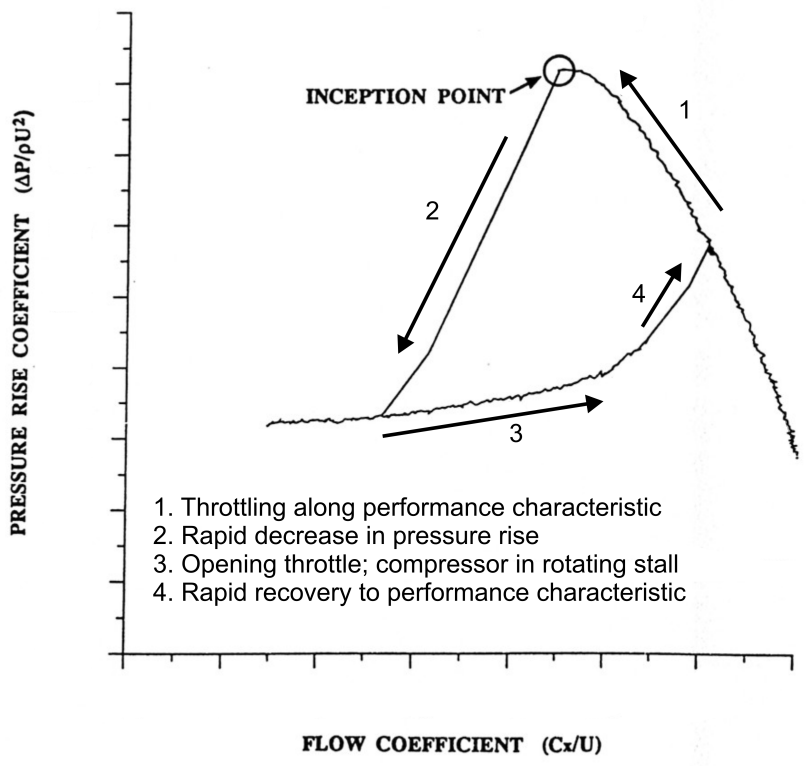

Figure 2.2: Generic performance characteristic.

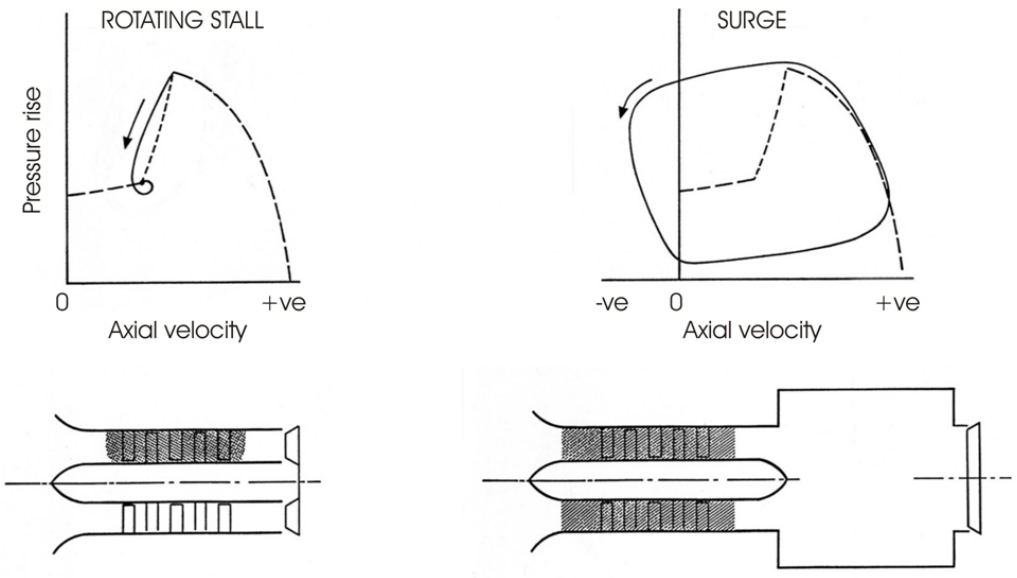

Figure 2.3: Rotating stall and surge schematics, from Day (2006b).

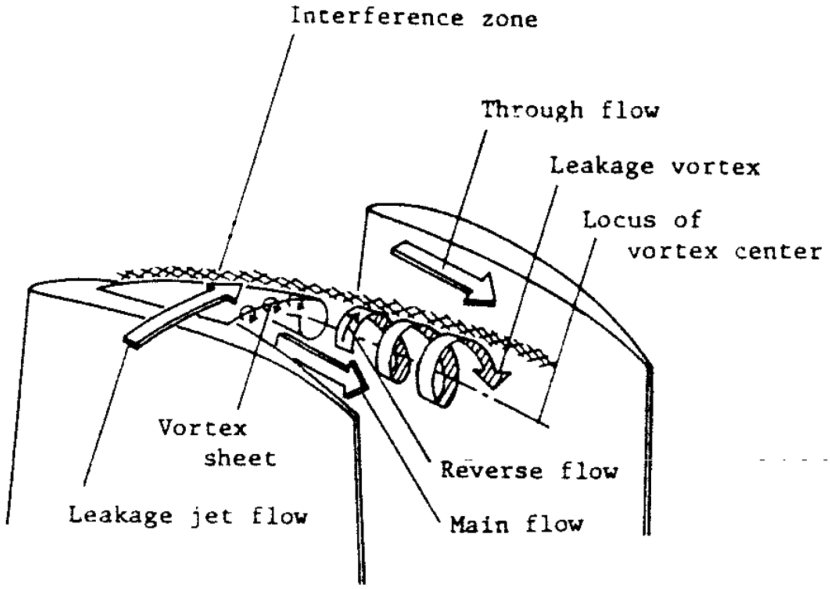

Figure 2.4: Tip leakage vortex, adapted from Inoue and Kuroumaru (1989).

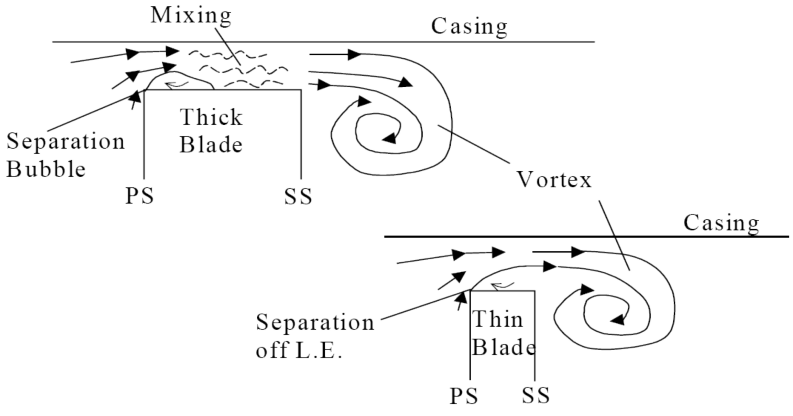

Figure 2.5: Tip leakage flow over blade tip from Glanville (2001).

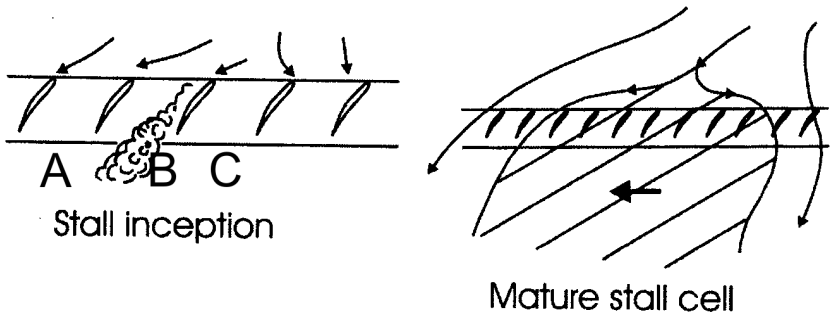

Figure 2.6: Stall inception, left; mature stall cell, right; from Stenning (1980).

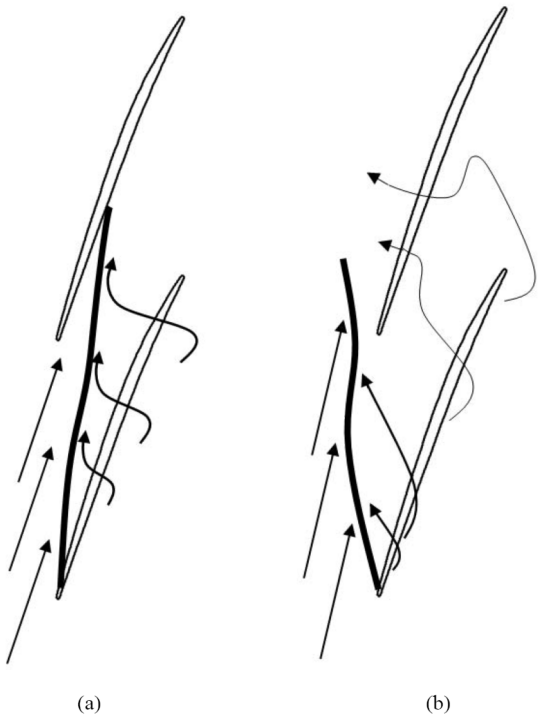

Figure 2.7: Velocity vectors at rotor tip plane; at design conditions, left; and stall, right; from Bennington et al. (2008).

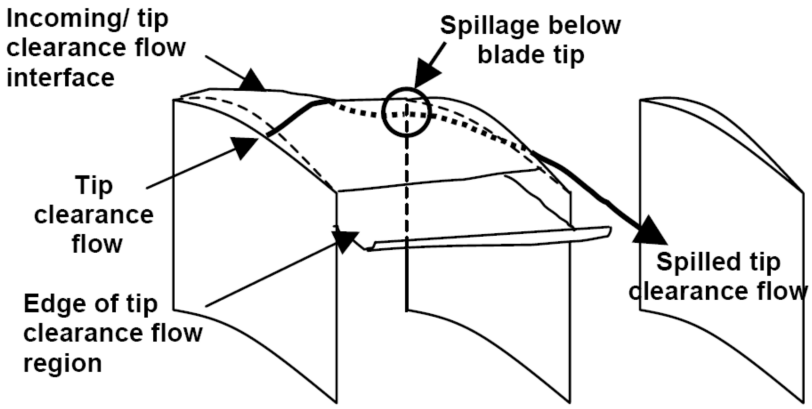

Figure 2.8: Leading edge tip clearance flow spillage, Vo et al. (2008).

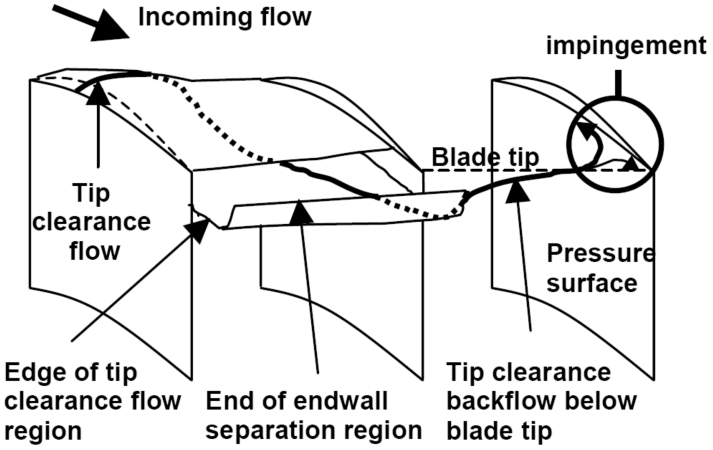

Figure 2.9: Tip clearance backflow, Vo et al. (2008).

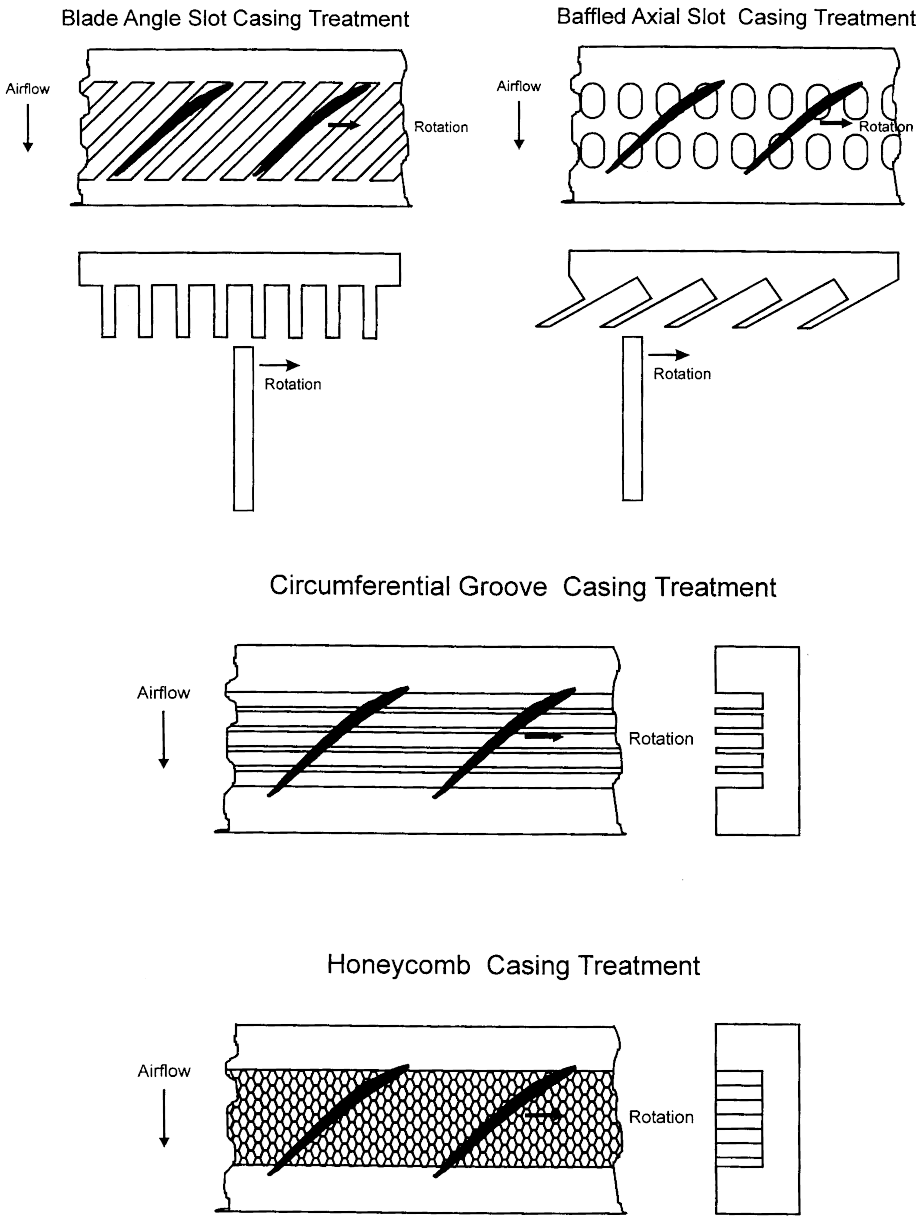

Figure 2.10: General forms of casing treatment, from Seitz (1999).

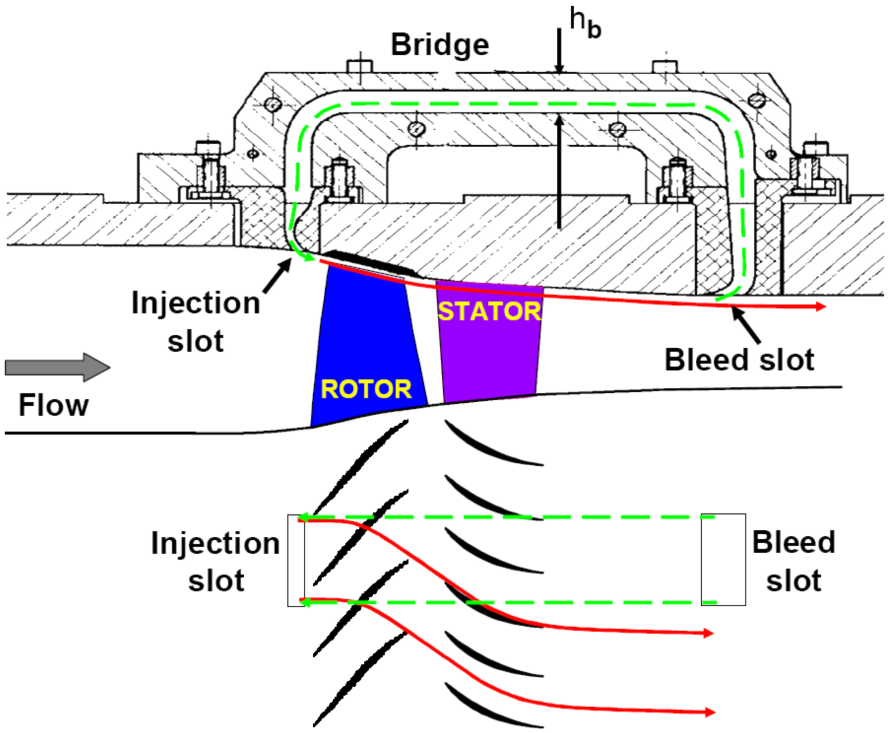

Figure 2.11: Re-circulation casing treatment and flow path through compressor, Strazisar et al. (2004).

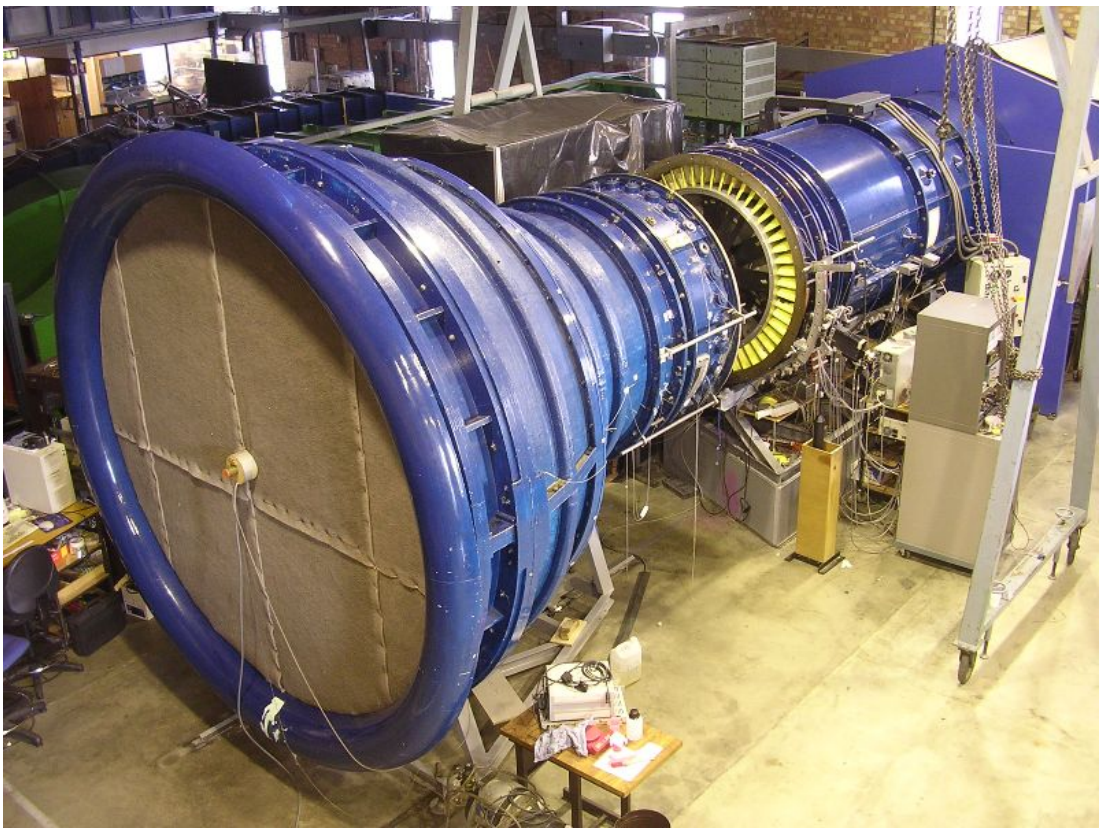

Figure 3.1: Deverson low-speed compressor rig.

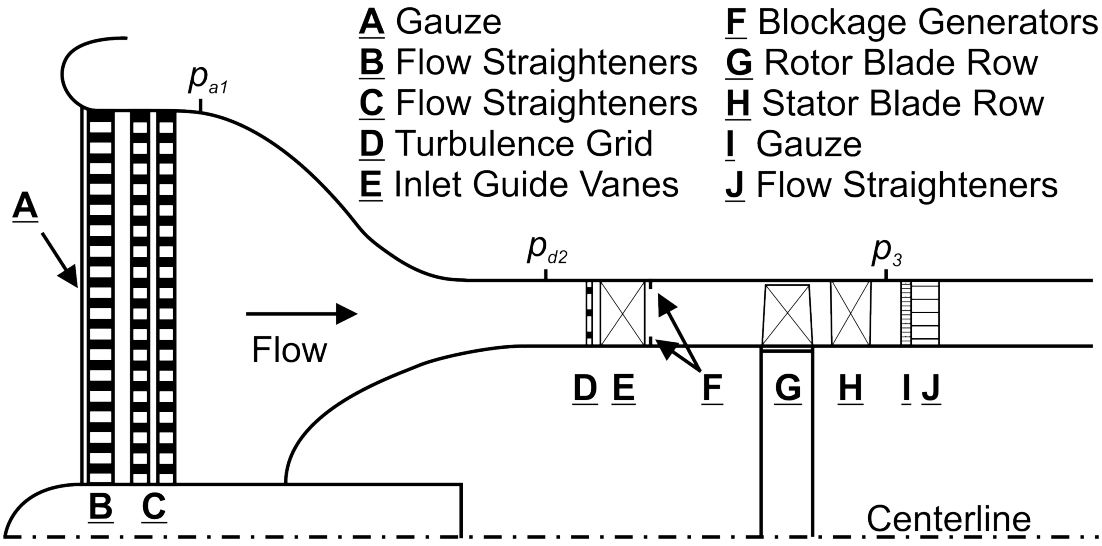

Figure 3.2: Deverson compressor rig schematic, adopted from Bolger (1999).

Figure 3.3: Mini-Deverson compressor.

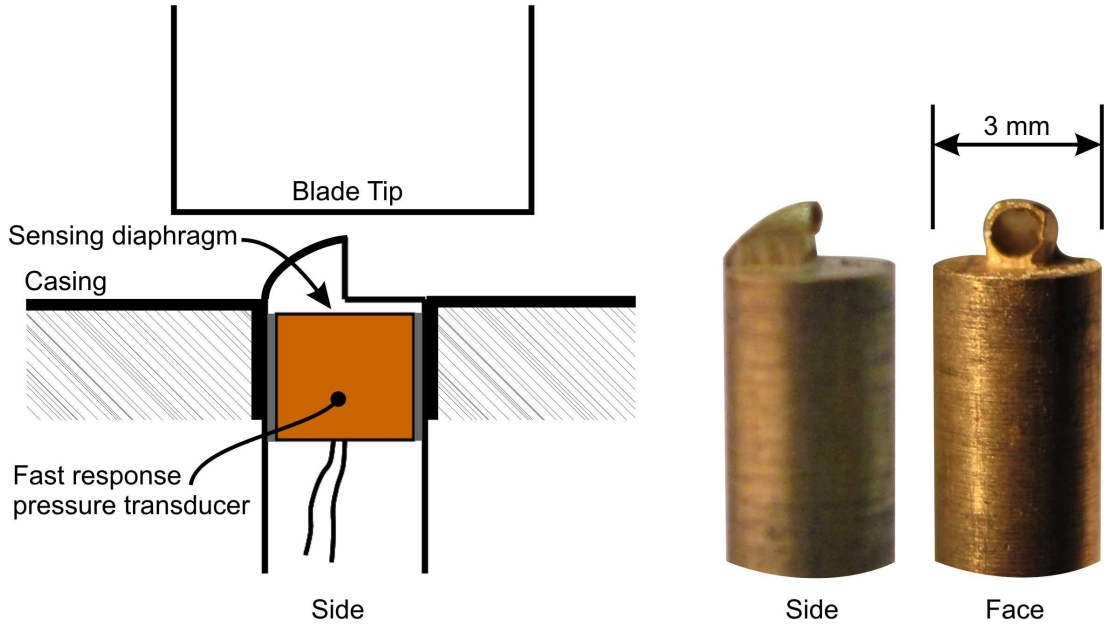

Figure 3.4: Schematic of total pressure probe relative to tip clearance gap, left; side and front view of actual probe, right.

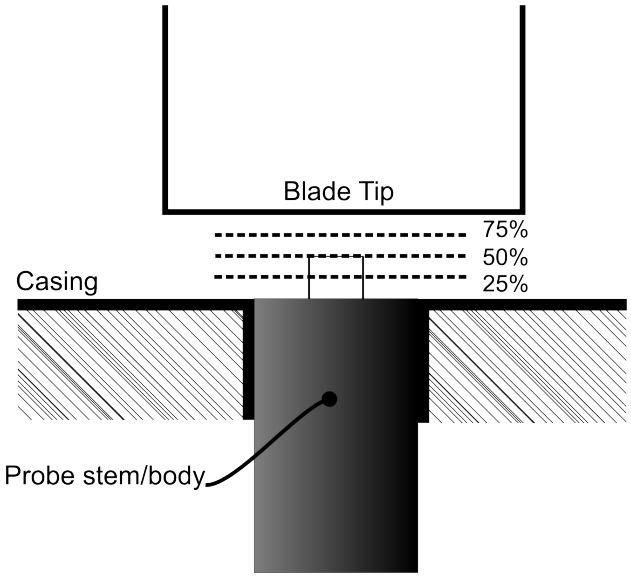

Figure 3.5: Hot-wire probe radial positions sampled in the Deverson tip clearance gap.

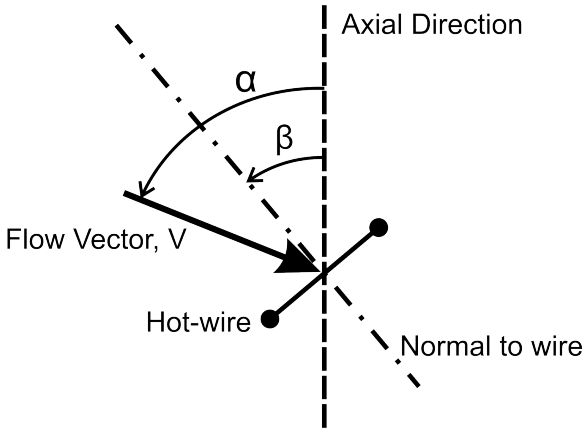

Figure 3.6: Hot-wire reference angles viewed from the probe axis.

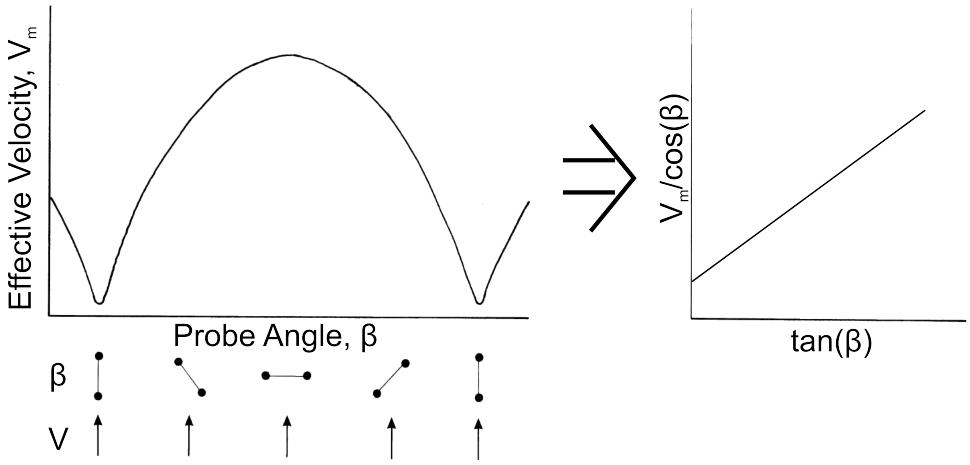

Figure 3.7: Hot-wire response at various angular settings, left; linearization of response by transforming the x and y axes, right.

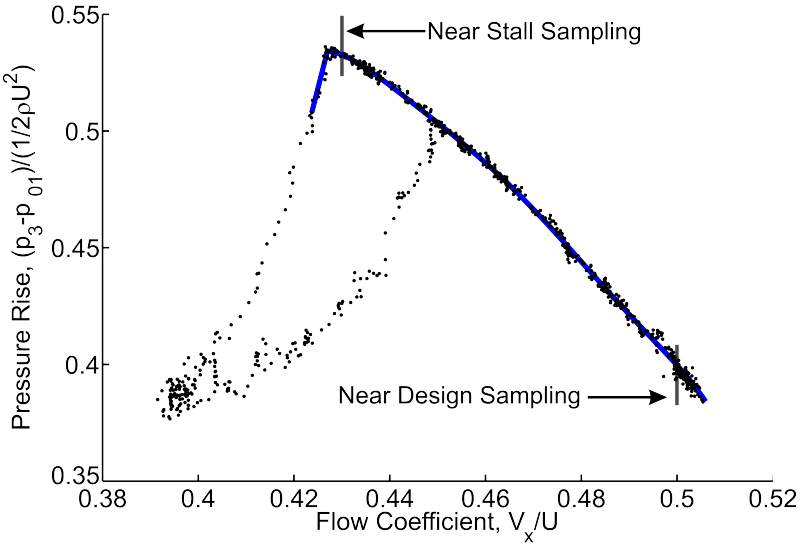

Figure 3.8: Deverson compressor total-to-static characteristic: data points from continuous measurement and curve fit. Flow coefficients for overtip measurements taken at constant flow coefficients near the design and stall conditions are marked.

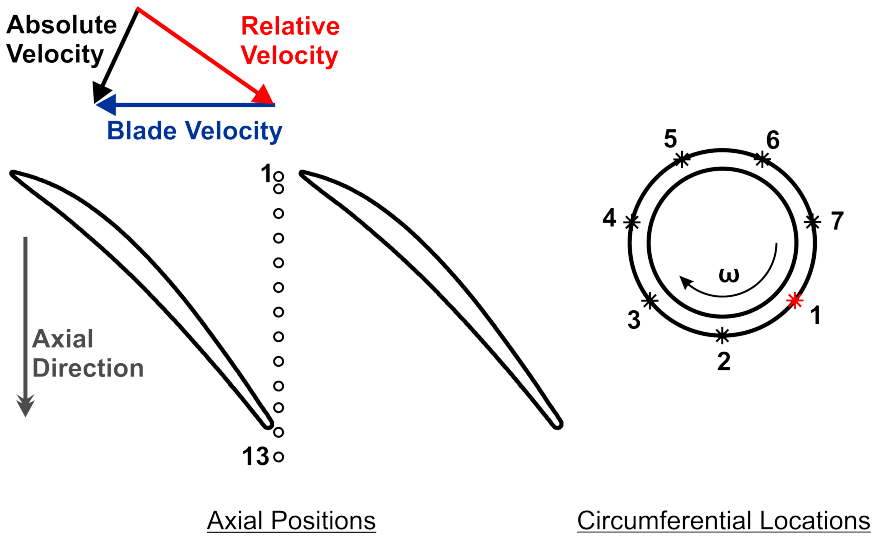

Figure 4.1: Deverson overtip schematic; axial array at circumferential position 1.

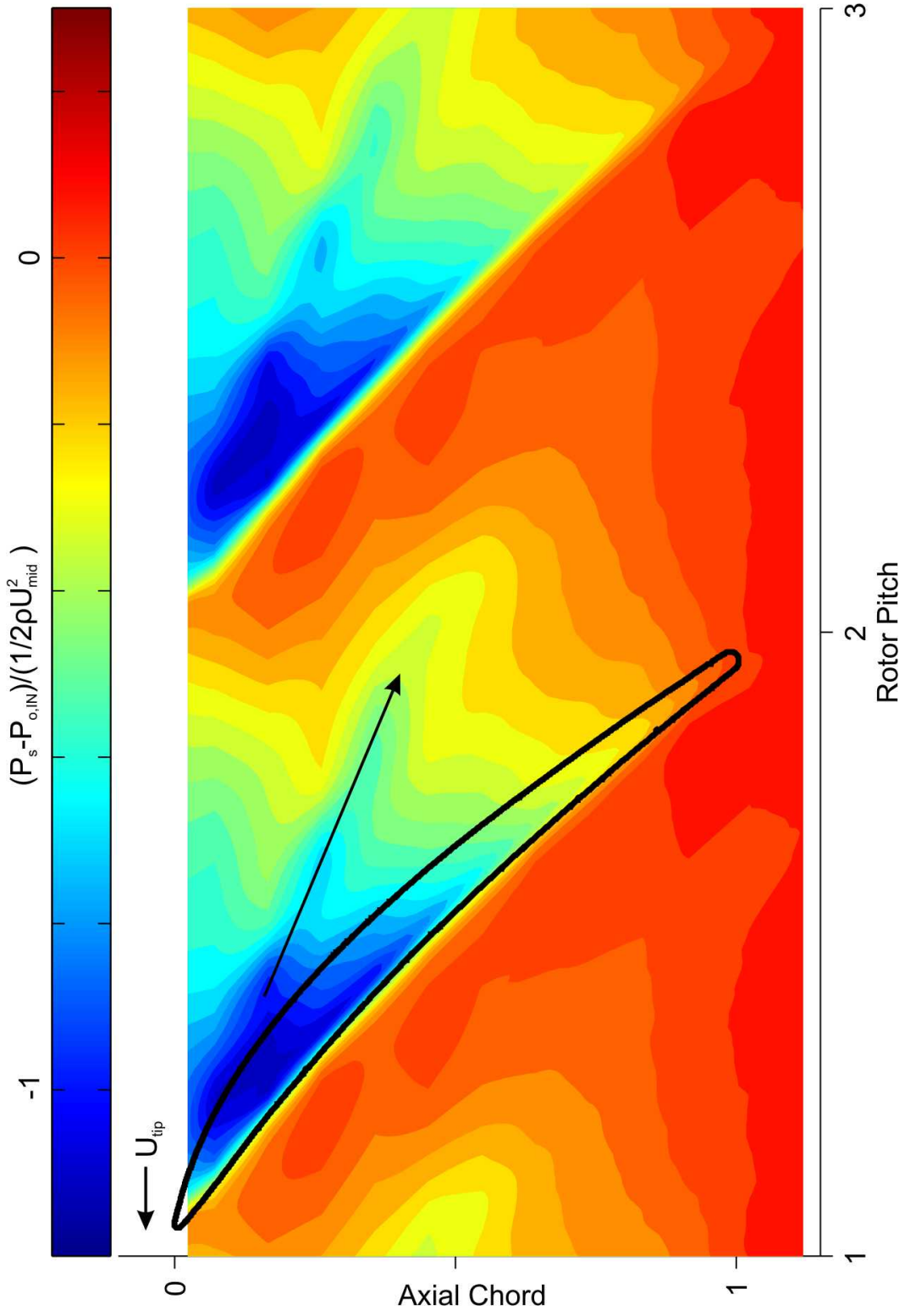

Figure 4.2: Static pressure contours at **design** flow coefficient.

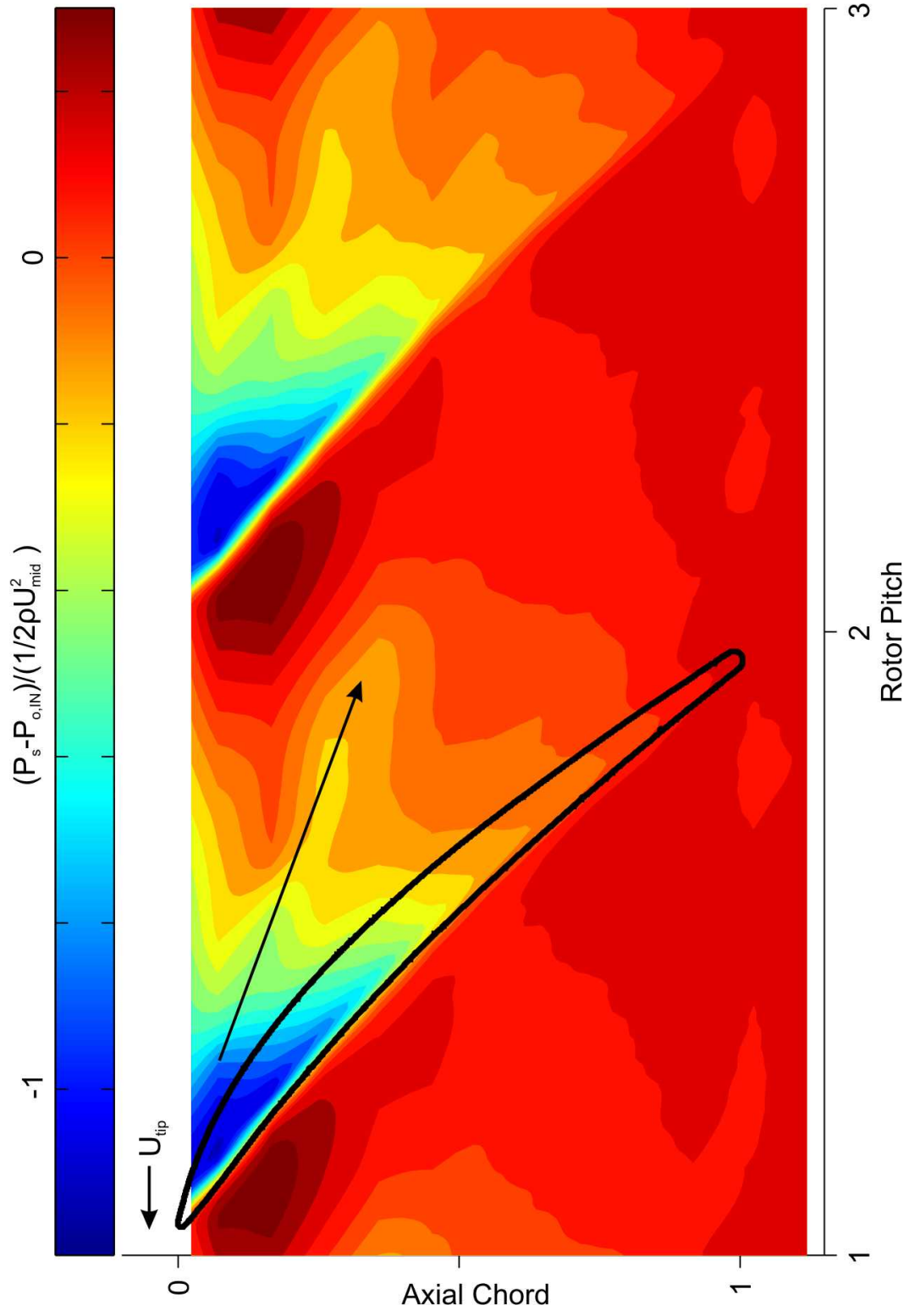

Figure 4.3: Static pressure contours at **near stall** flow coefficient.

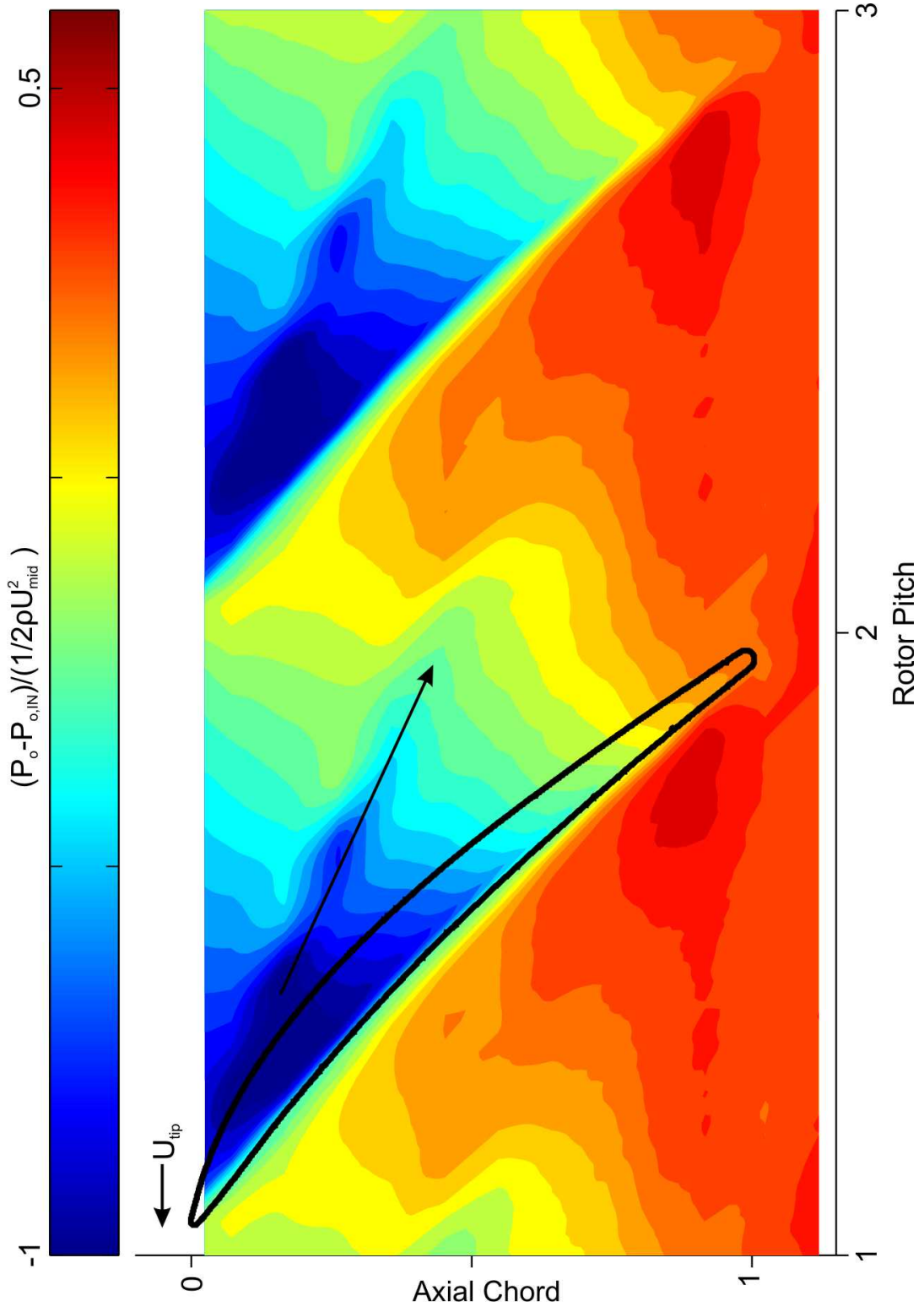

Figure 4.4: Total pressure contours at **design** flow coefficient.

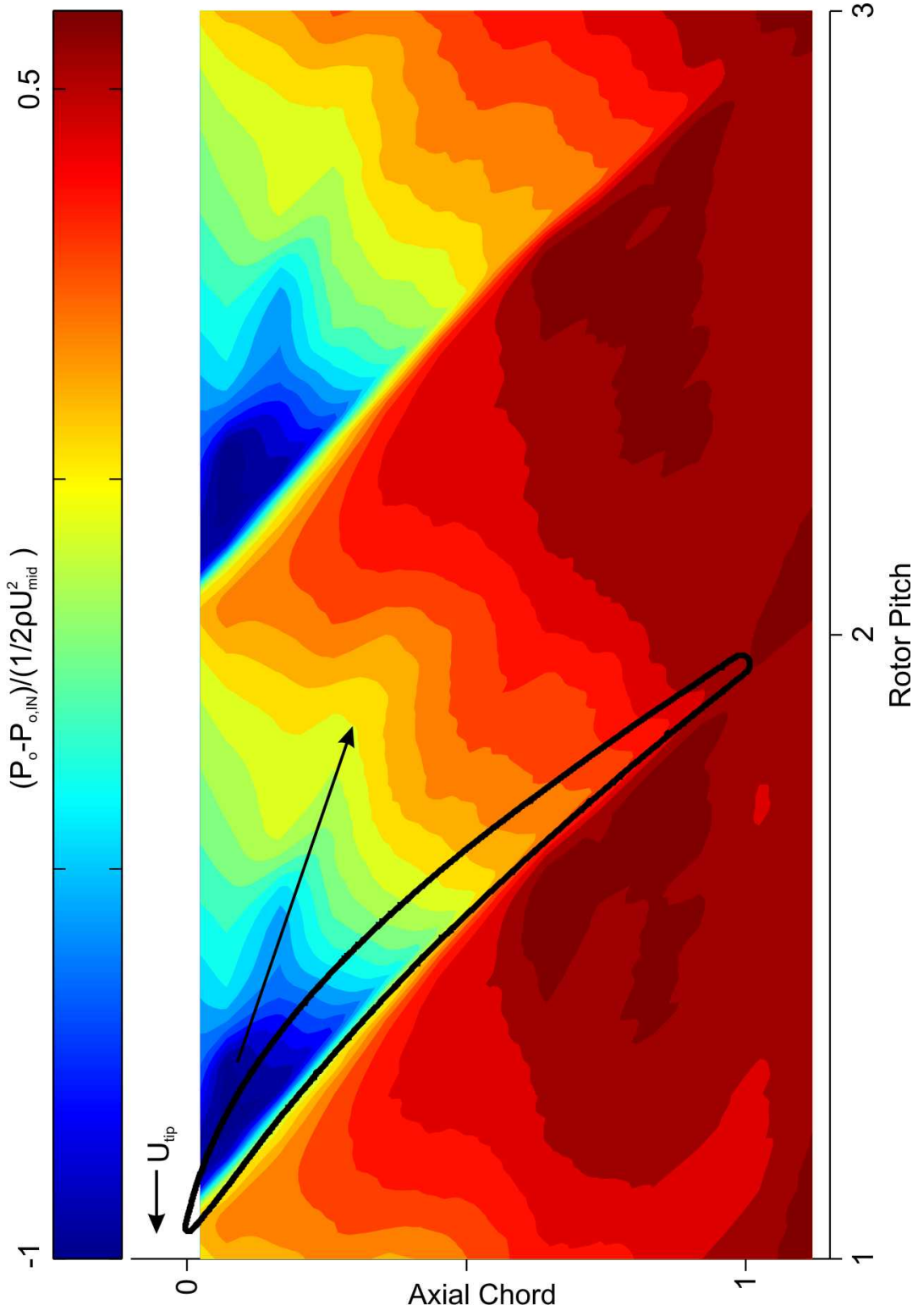

Figure 4.5: Total pressure contours at **near stall** flow coefficient.

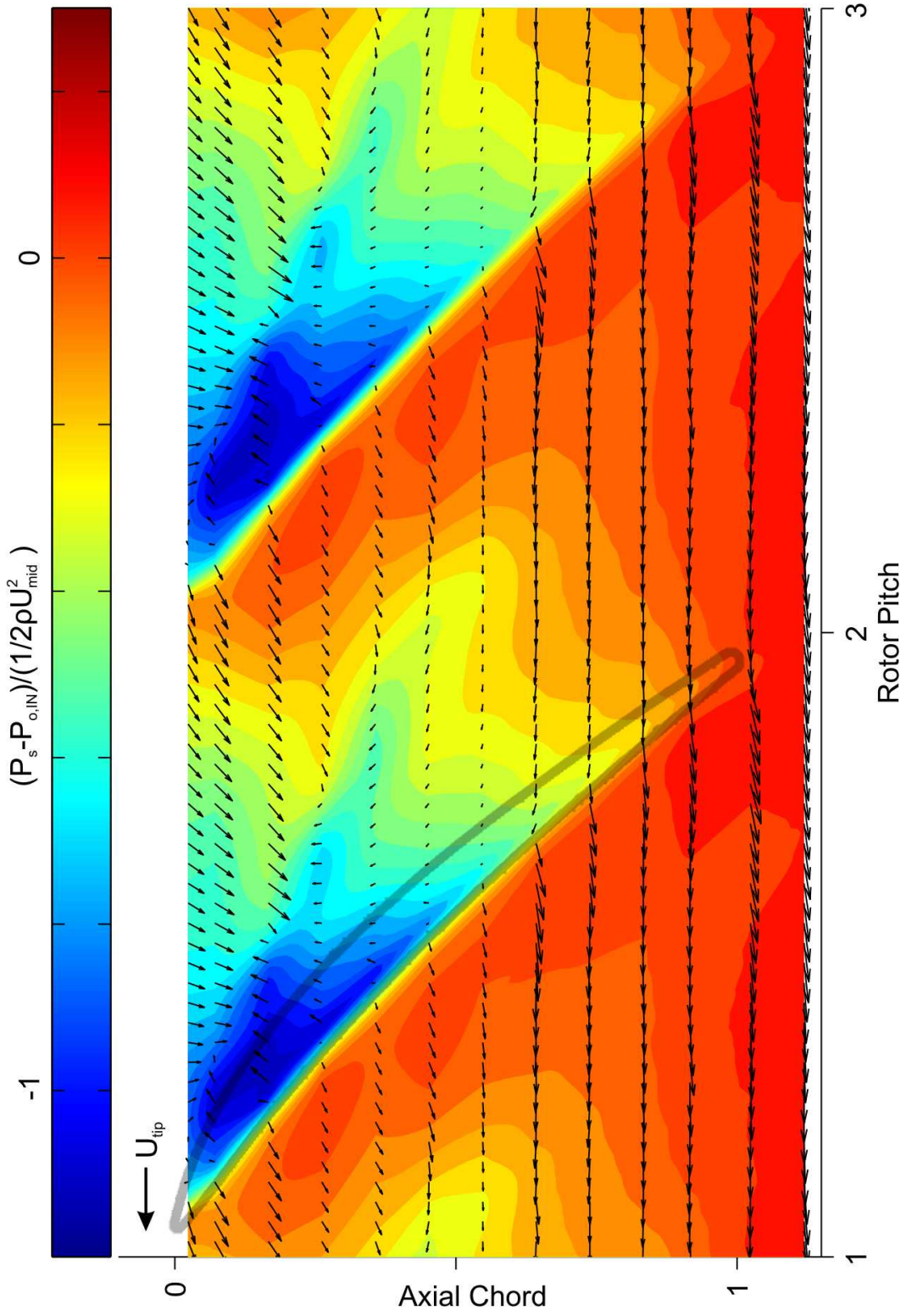

Figure 4.6: **Absolute** frame velocity vectors at 25% tip gap (**near casing**) and static pressure contours at **design** flow coefficient, every second vector shown.

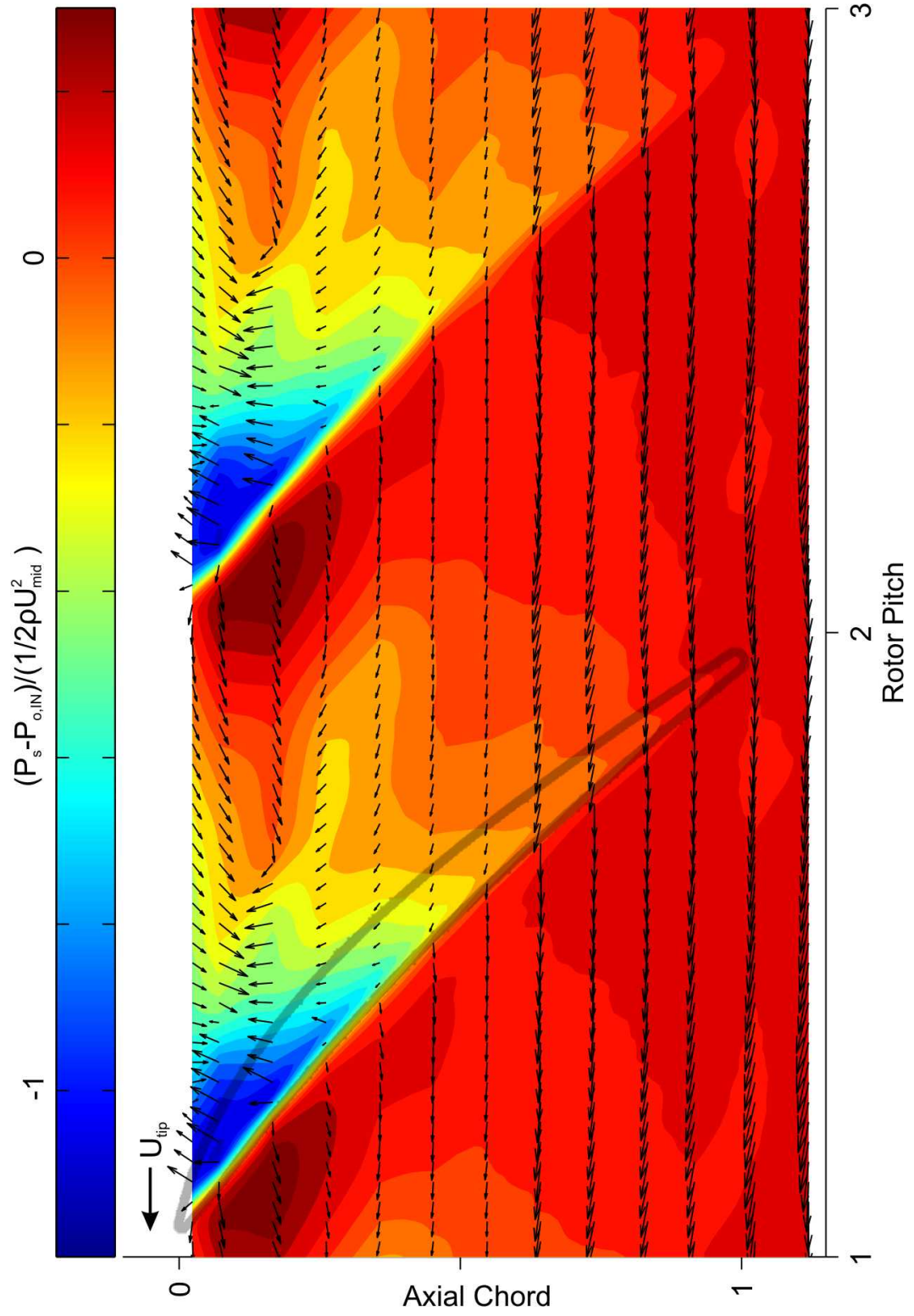

Figure 4.7: **Absolute** frame velocity vectors at 25% tip gap (**near casing**) and static pressure contours at **near stall** flow coefficient, every second vector shown.

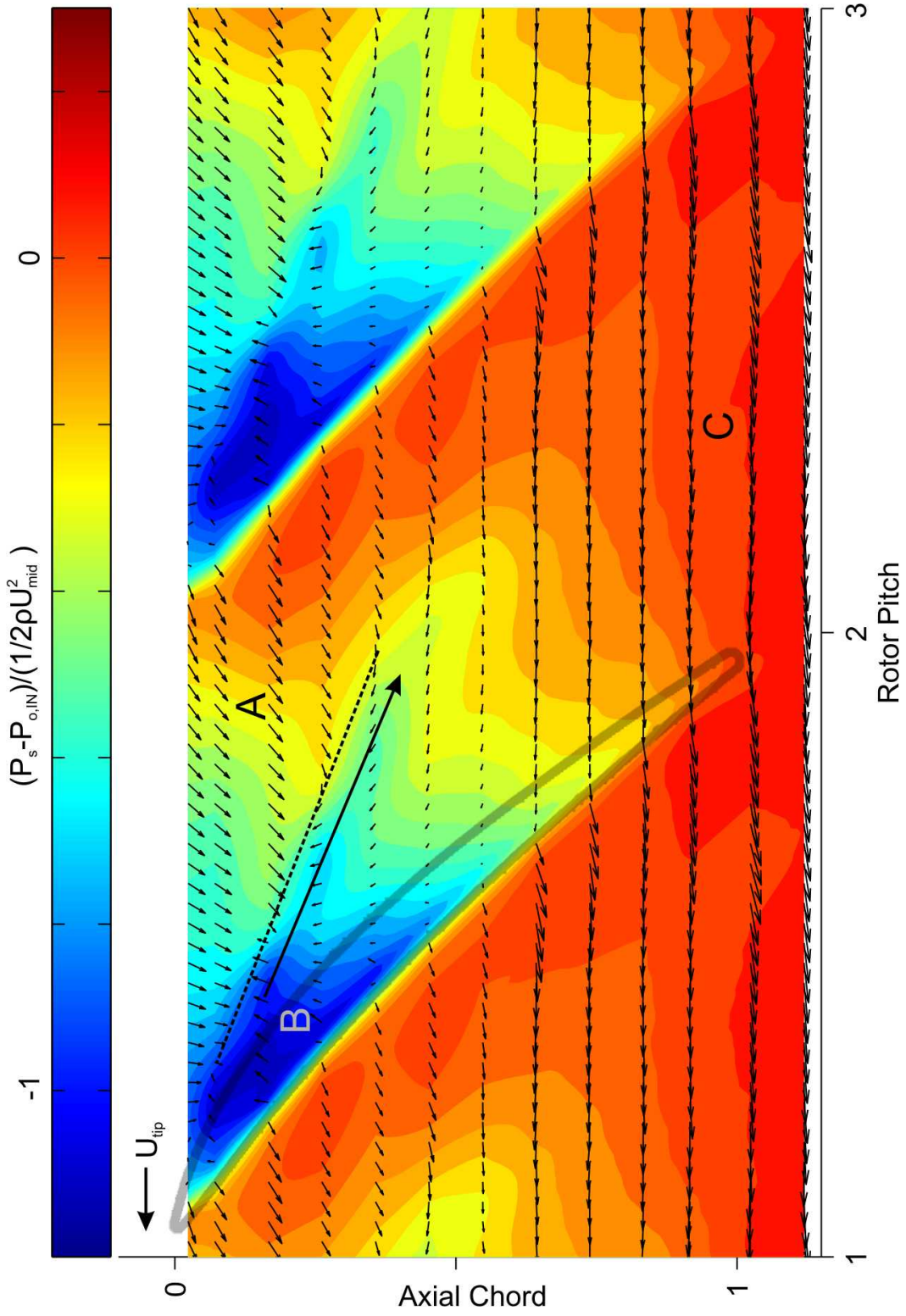

Figure 4.8: **Absolute** frame velocity vectors at 50% tip gap (**mid-height**) and static pressure contours at **design** flow coefficient, every second vector shown.

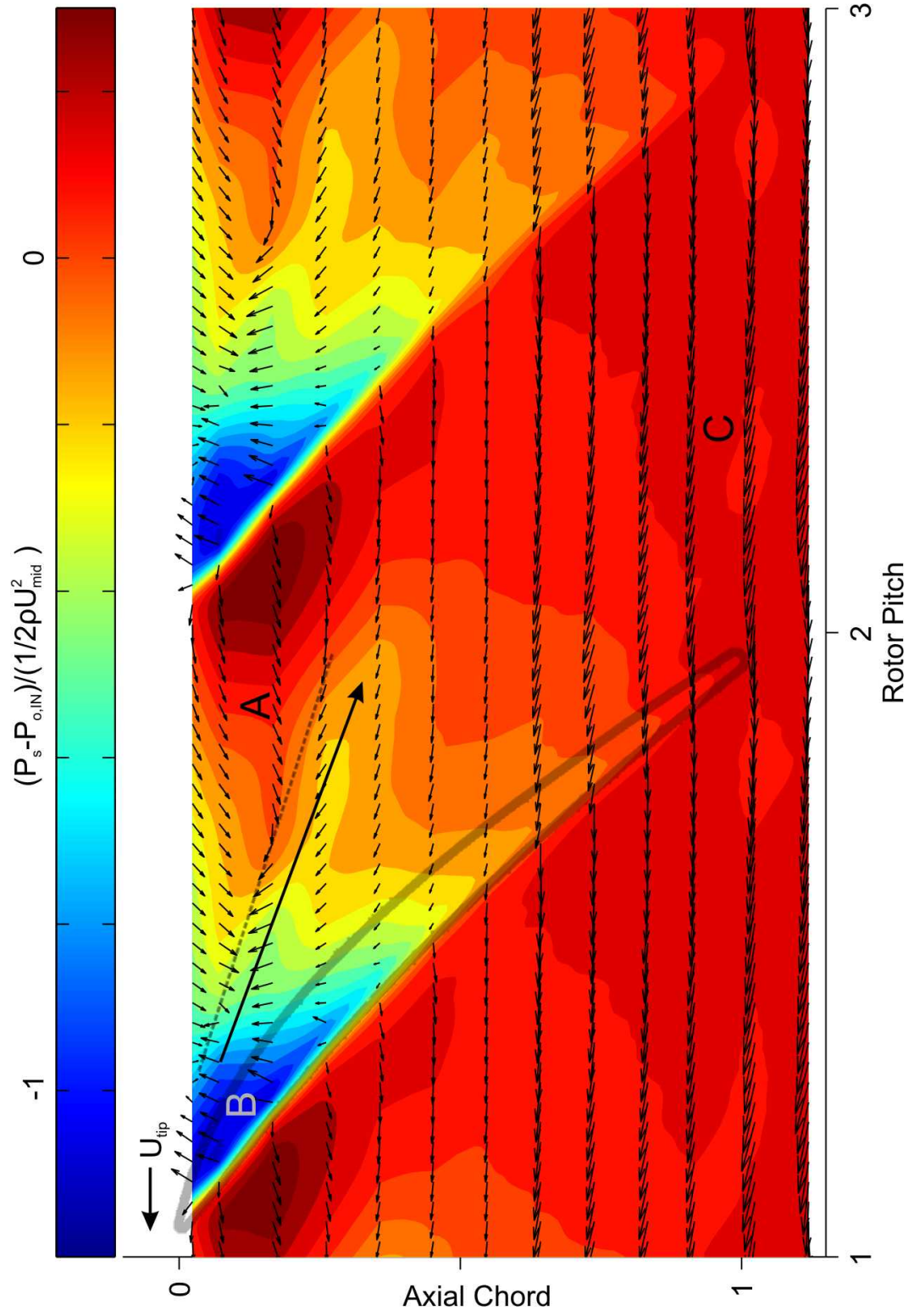

Figure 4.9: **Absolute** frame velocity vectors at 50% tip gap (**mid-height**) and static pressure contours at **near stall** flow coefficient, every second vector shown.

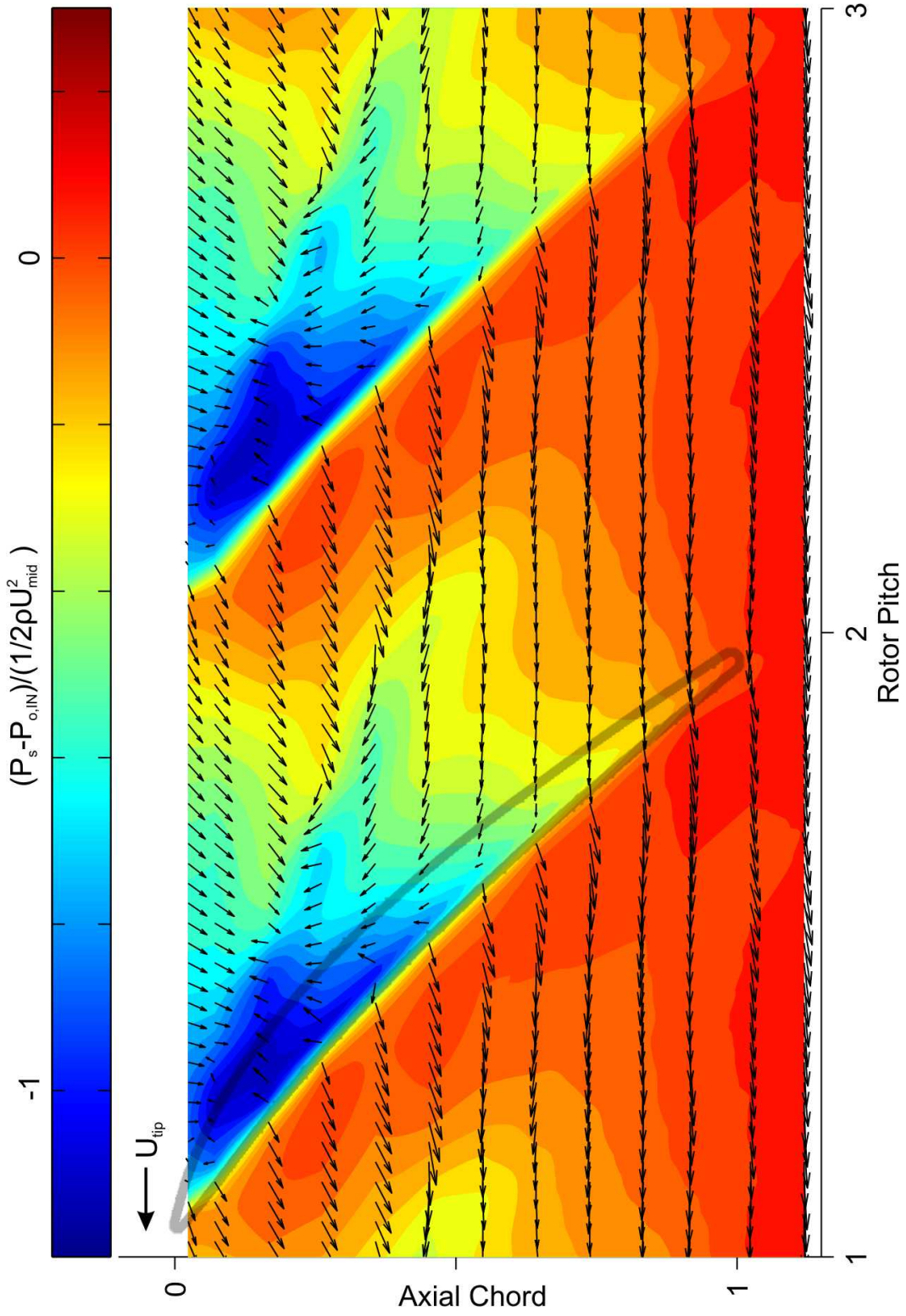

Figure 4.10: **Absolute** frame velocity vectors at 75% tip gap (**near blade tip**) and static pressure contours at **design** flow coefficient, every second vector shown.

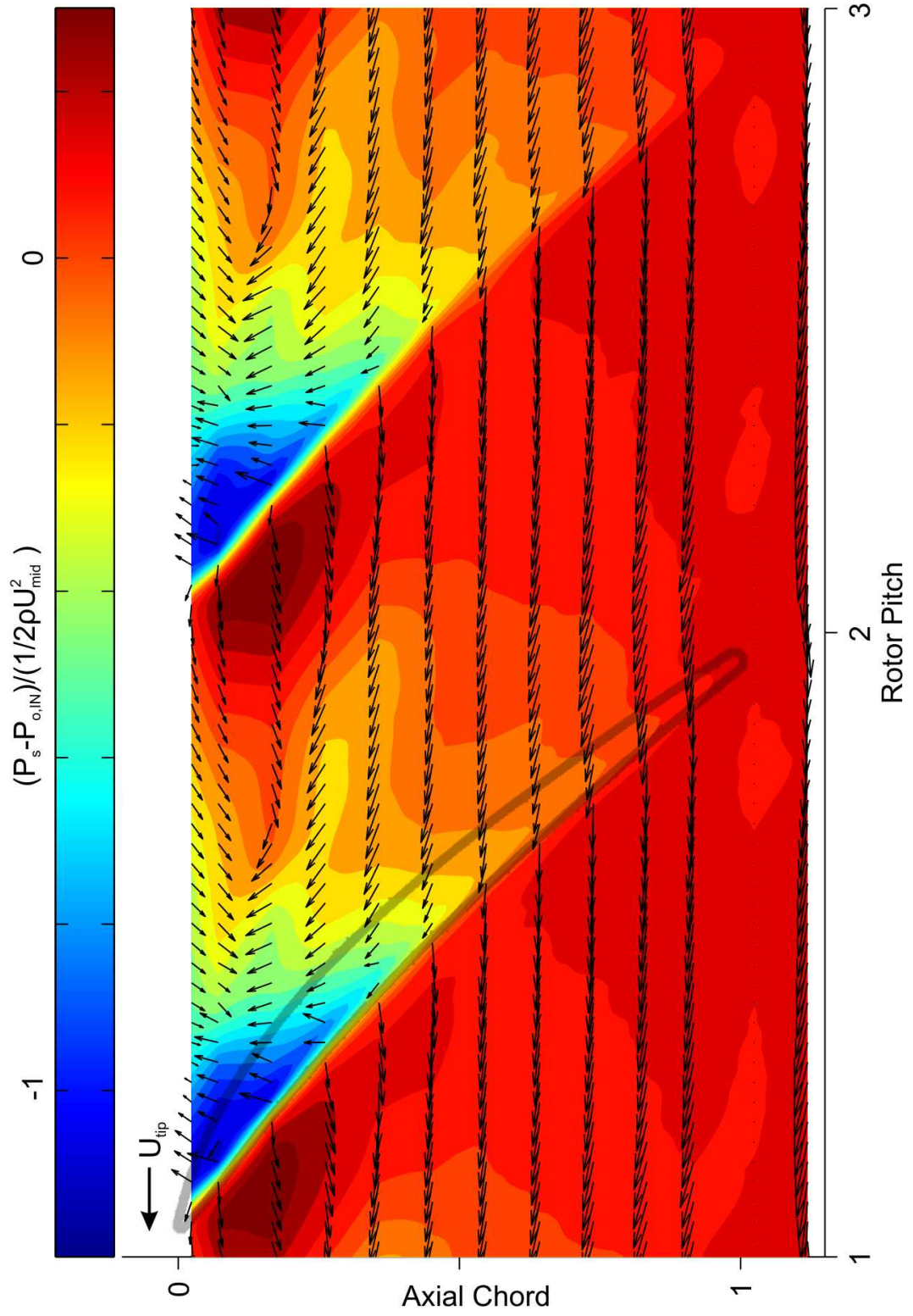

Figure 4.11: **Absolute** frame velocity vectors at 75% tip gap (**near blade tip**) and static pressure contours at **near stall** flow coefficient, every second vector shown.

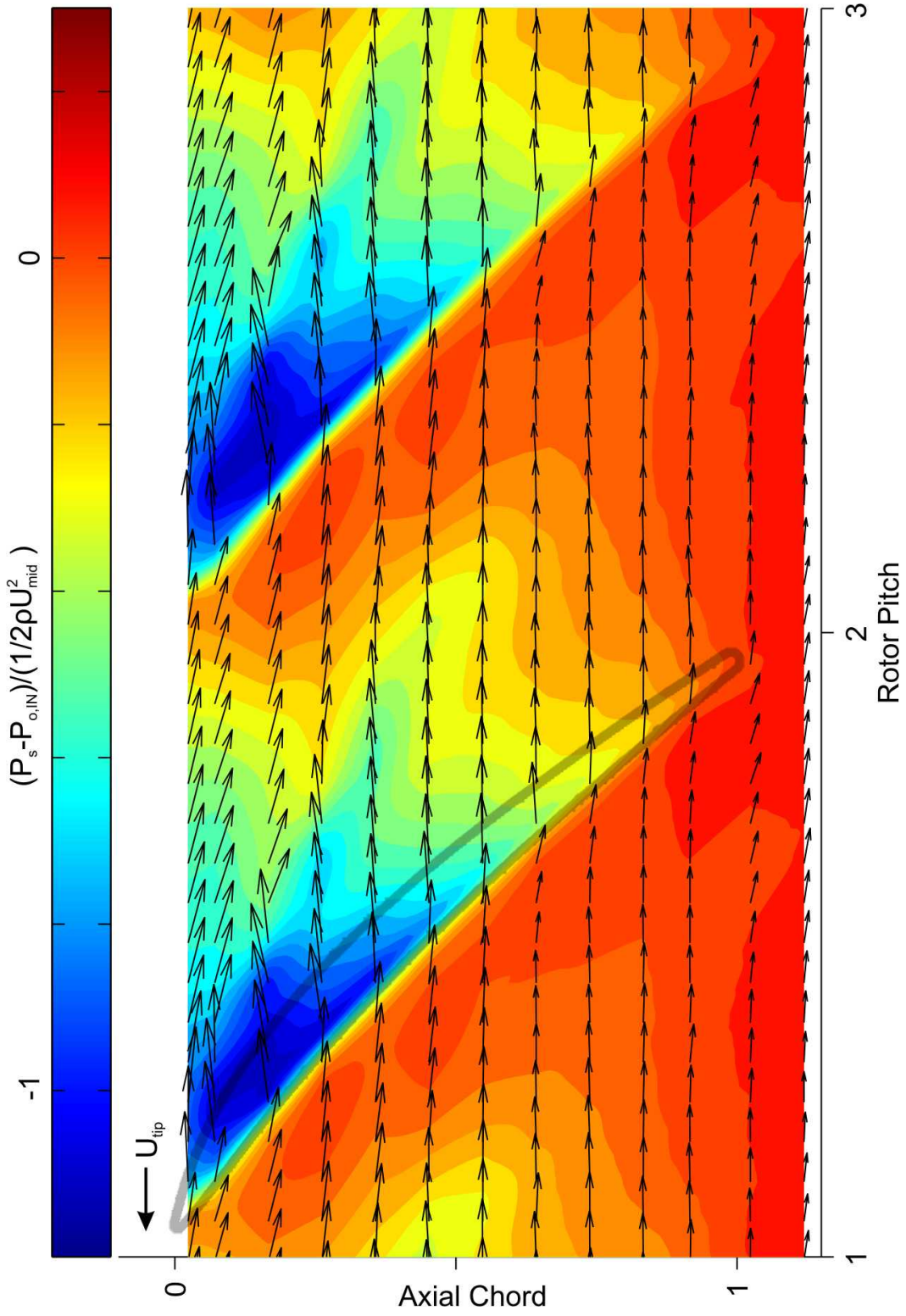

Figure 4.12: **Relative** frame velocity vectors at 25% tip gap (**near casing**) and static pressure contours at **design** flow coefficient, every fourth vector shown.

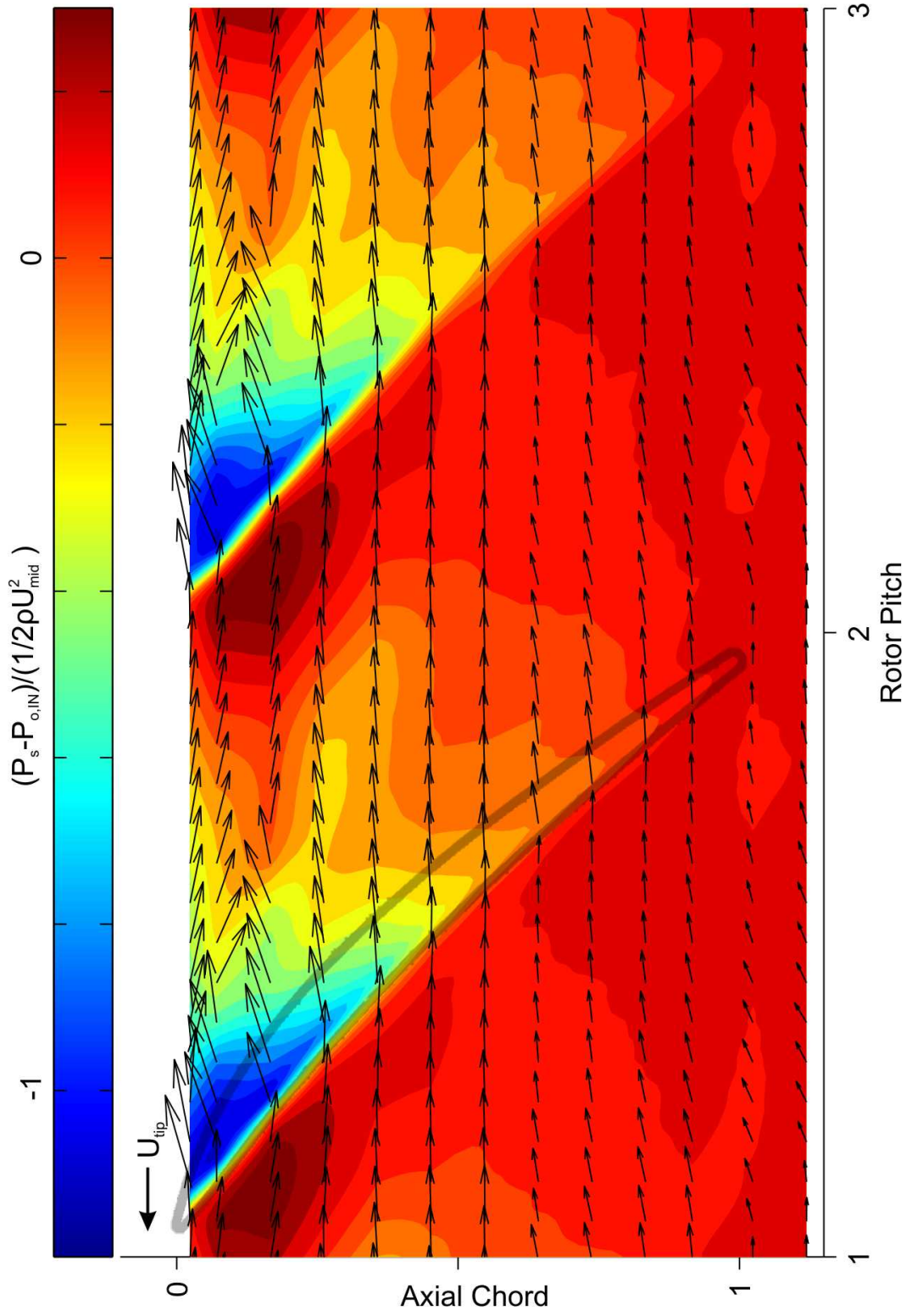

Figure 4.13: **Relative** frame velocity vectors at 25% tip gap (**near casing**) and static pressure contours at **near stall** flow coefficient, every fourth vector shown.

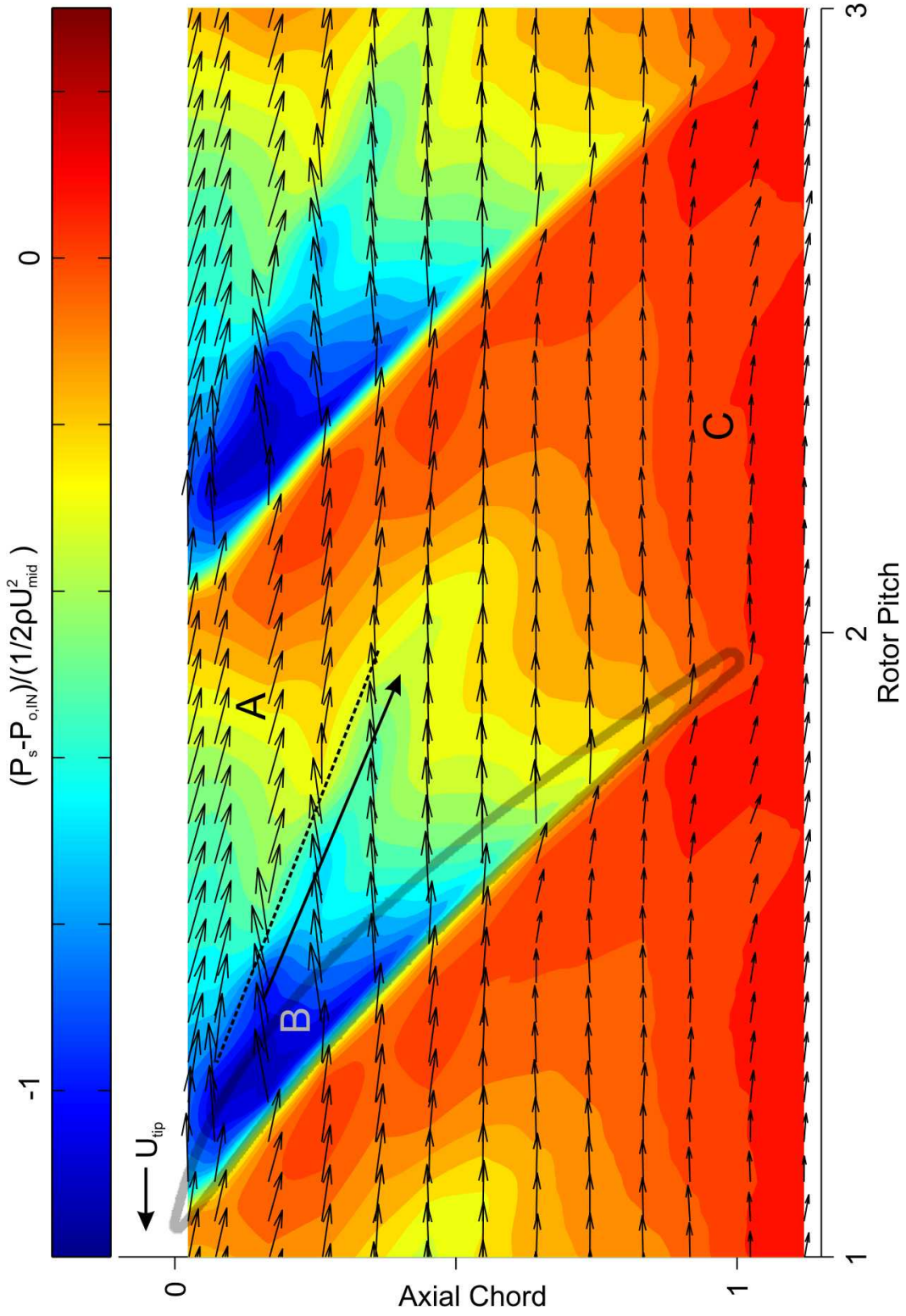

Figure 4.14: **Relative** frame velocity vectors at 50% tip gap (**mid-height**) and static pressure contours at **design** flow coefficient, every fourth vector shown.

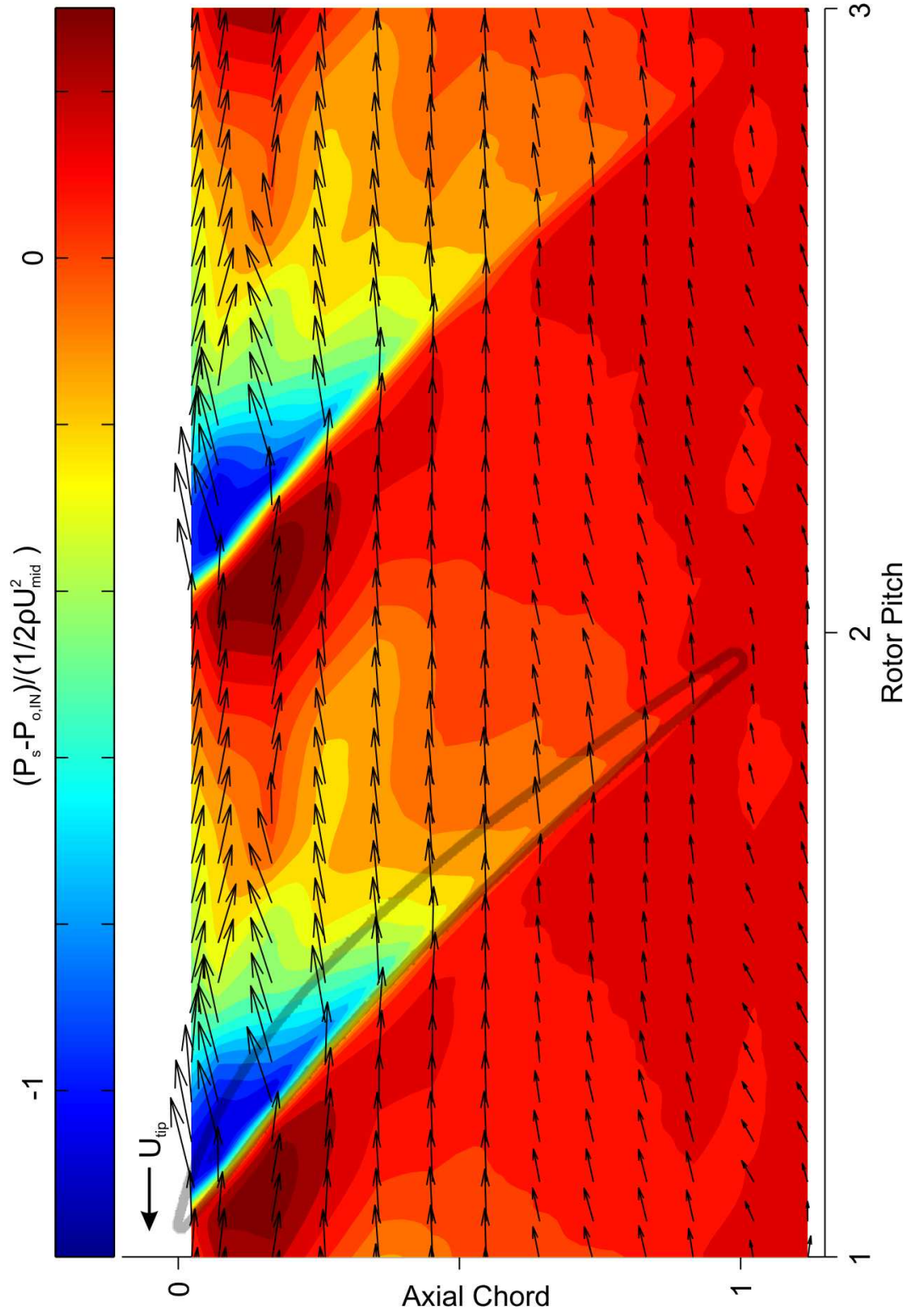

Figure 4.15: **Relative** frame velocity vectors at 50% tip gap (**mid-height**) and static pressure contours at **near stall** flow coefficient, every fourth vector shown.

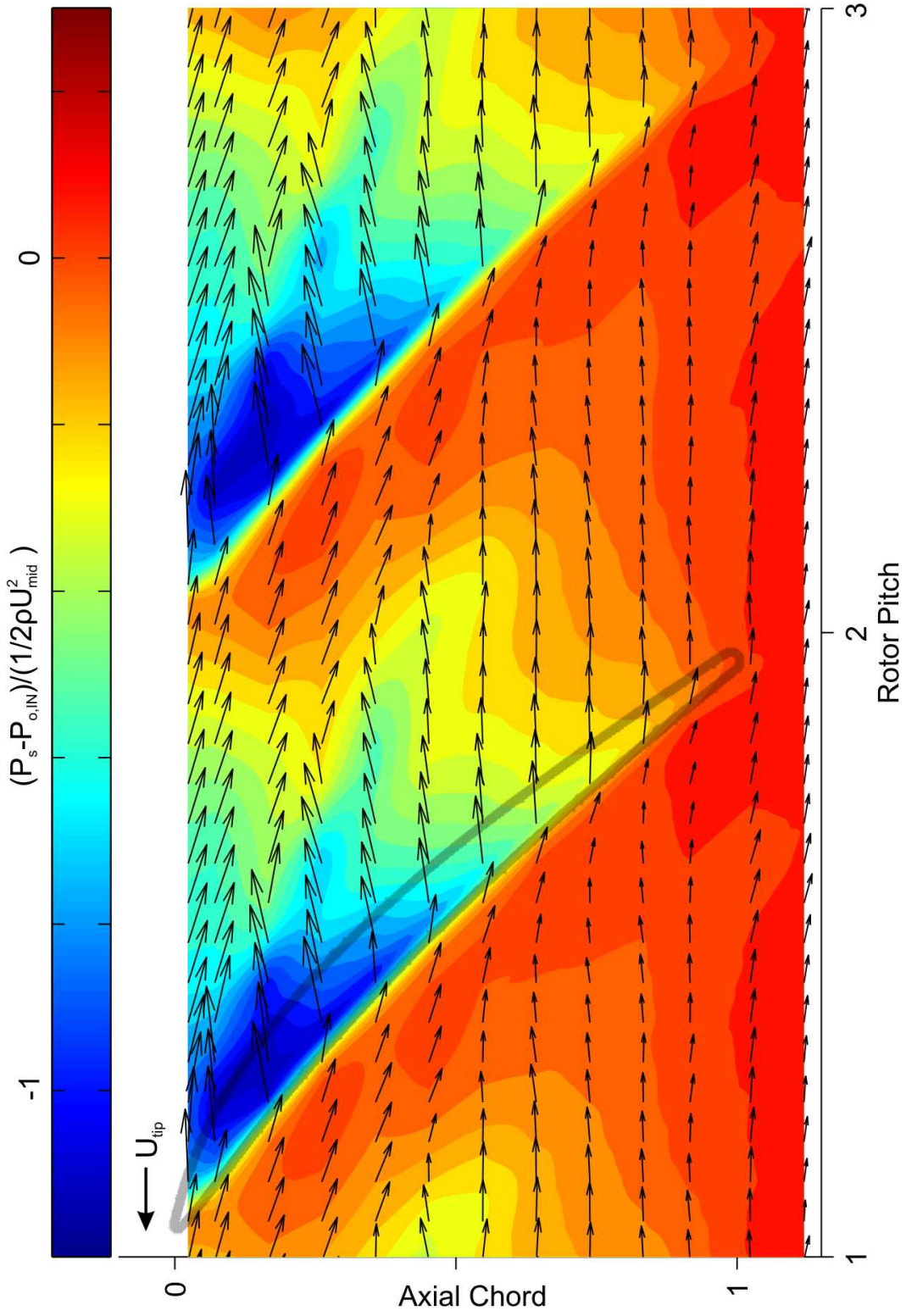

Figure 4.16: **Relative** frame velocity vectors at 75% tip gap (**near blade tip**) and static pressure contours at **design** flow coefficient, every fourth vector shown.

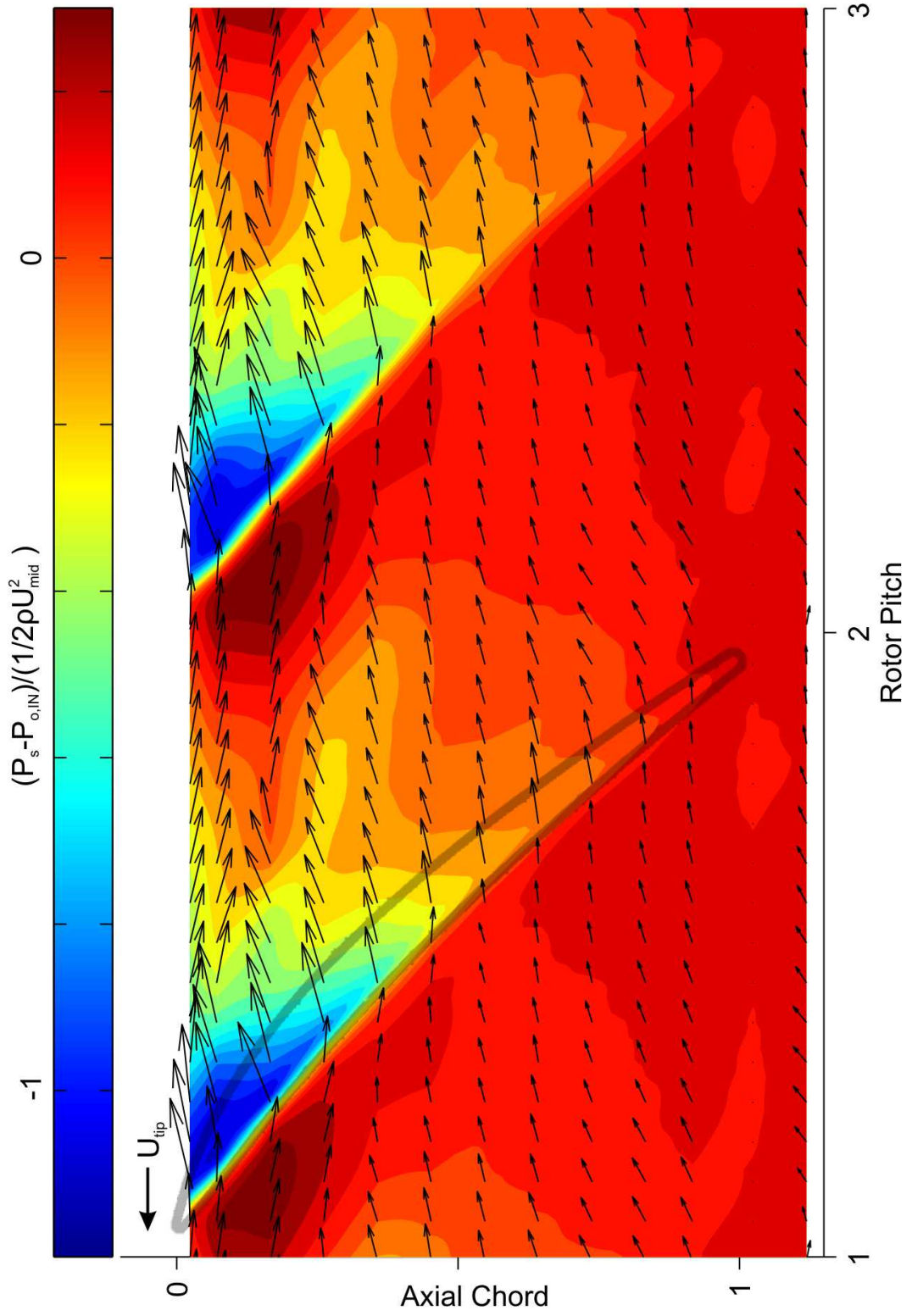

Figure 4.17: **Relative** frame velocity vectors at 75% tip gap (**near blade tip**) and static pressure contours at **near stall** flow coefficient, every fourth vector shown.

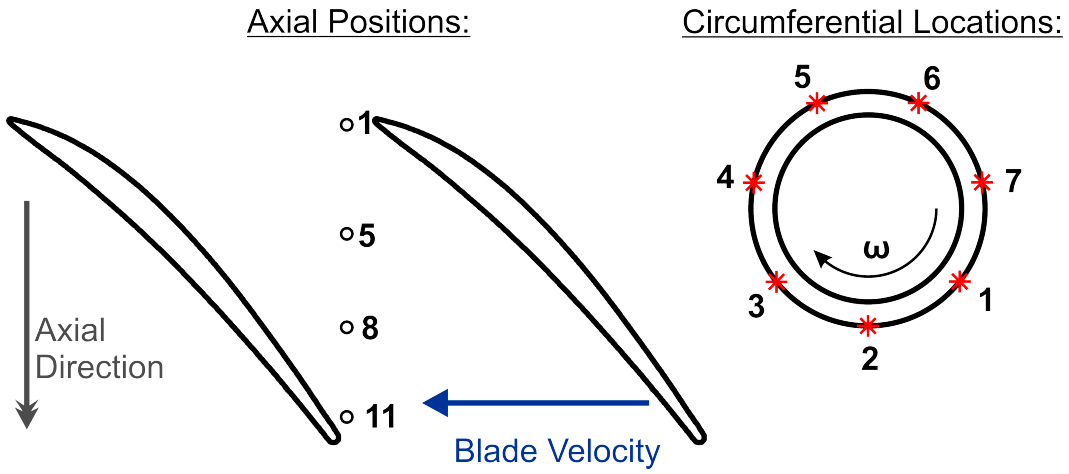

Figure 4.18: Axial array used for statistical analysis of tip clearance flow. Arrays at seven equally spaced circumferential positions.

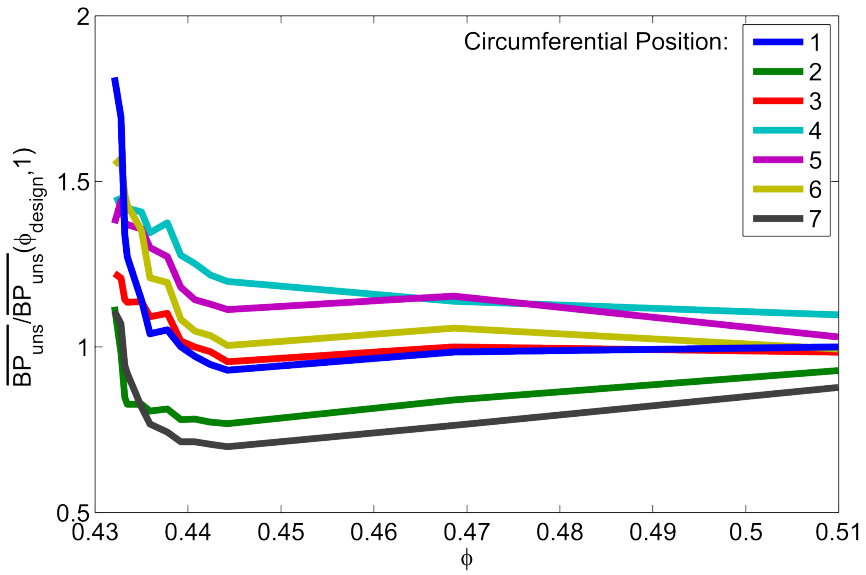

Figure 4.19: Mean passage unsteadiness, $\overline{BP_{uns}}$, at the leading edge for seven circumferential positions.

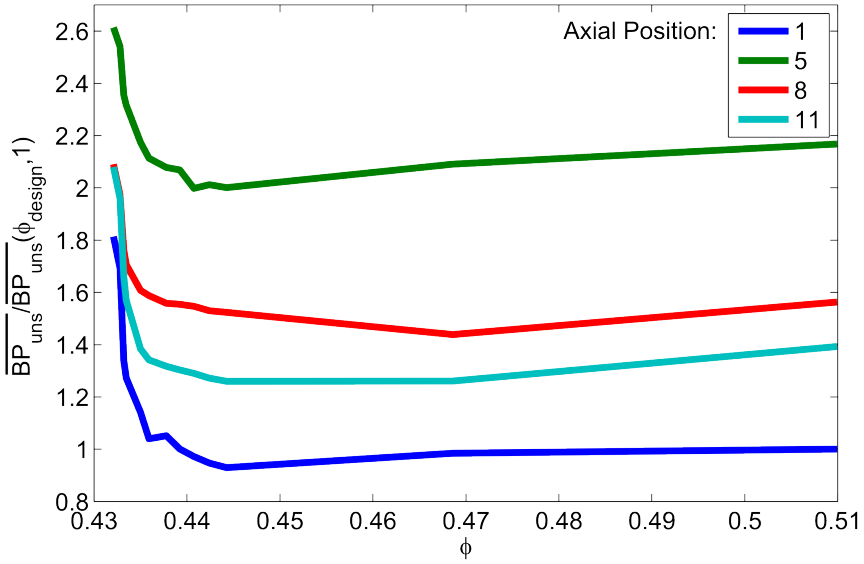

Figure 4.20: Mean passage unsteadiness, $\overline{BP_{uns}}$, at four axial positions from the leading edge (Pos. 1) to the trailing edge (Pos. 11) at circumferential position 1.

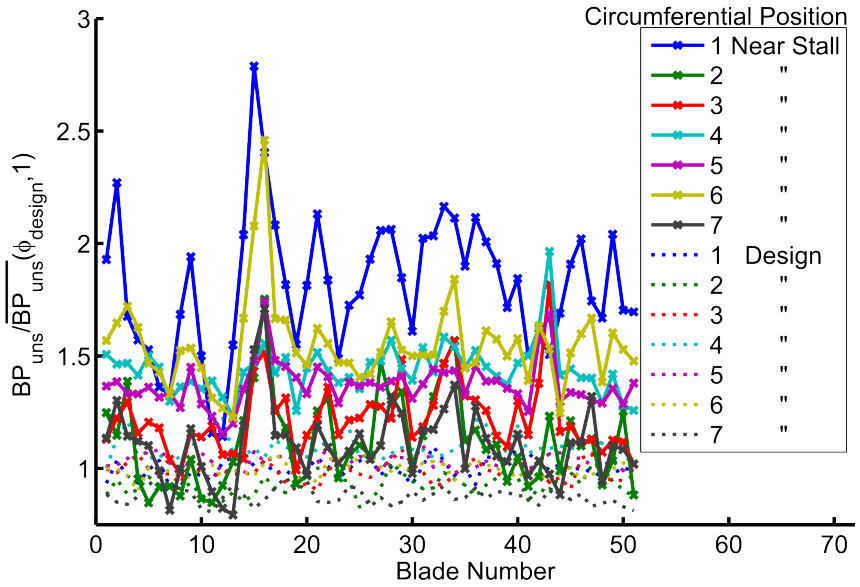

Figure 4.21: Passage unsteadiness, BP_{uns} at the leading edge for seven circumferential positions at near stall conditions, and for circumferential position 1 at design conditions (dashed line).

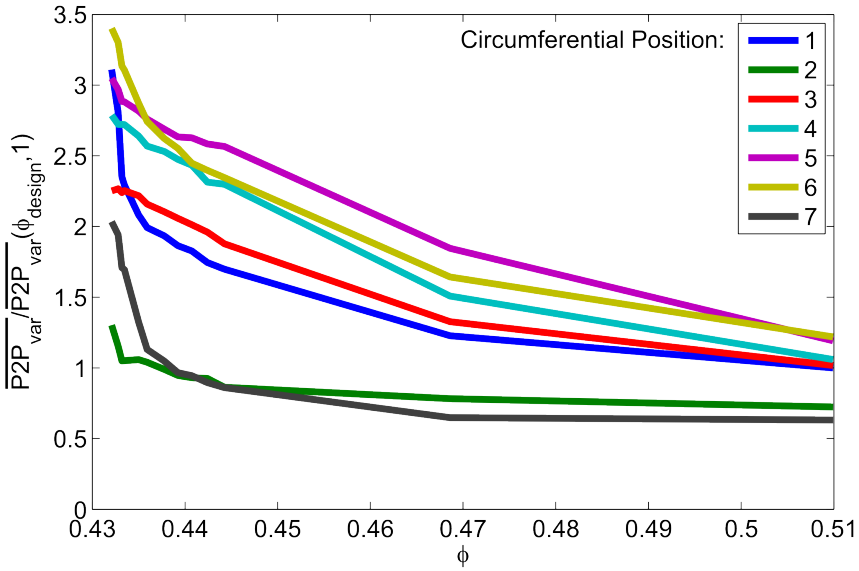

Figure 4.22: Mean passage to passage variation, $\overline{P2P_{var}}$, at the leading edge for seven circumferential positions.

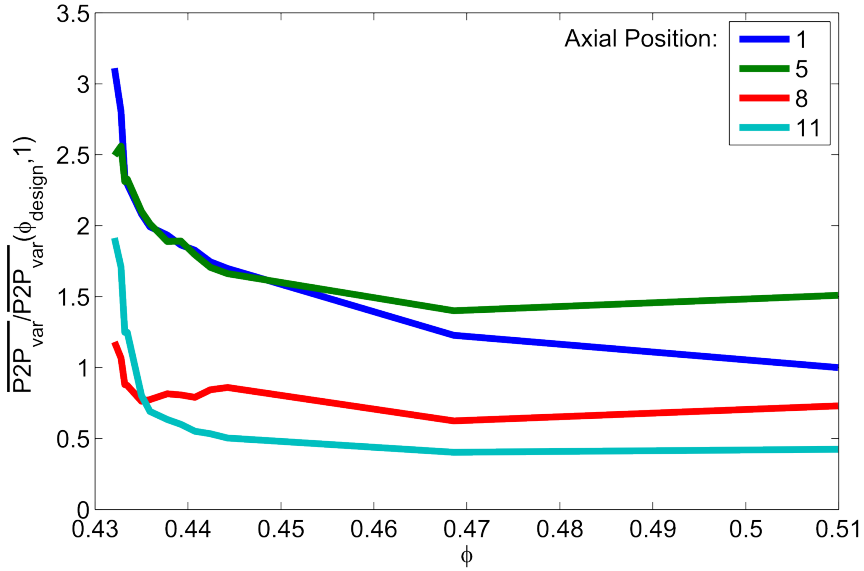

Figure 4.23: Mean passage to passage variation, $\overline{P2P_{var}}$, at four axial positions from the leading edge (Pos. 1) to the trailing edge (Pos. 11) at circumferential position 1.

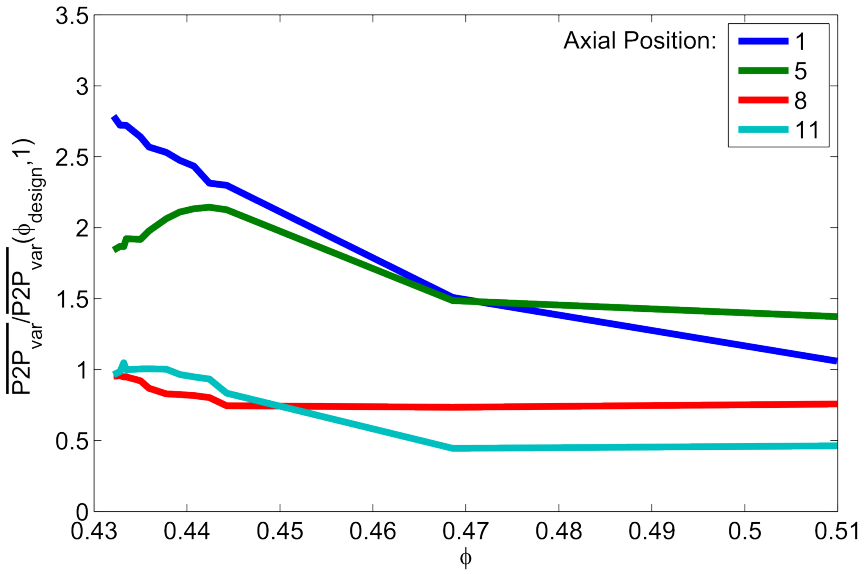

Figure 4.24: Mean passage to passage variation, $\overline{P2P_{var}}$, at four axial positions from the leading edge (Pos. 1) to the trailing edge (Pos. 11) at circumferential position 4.

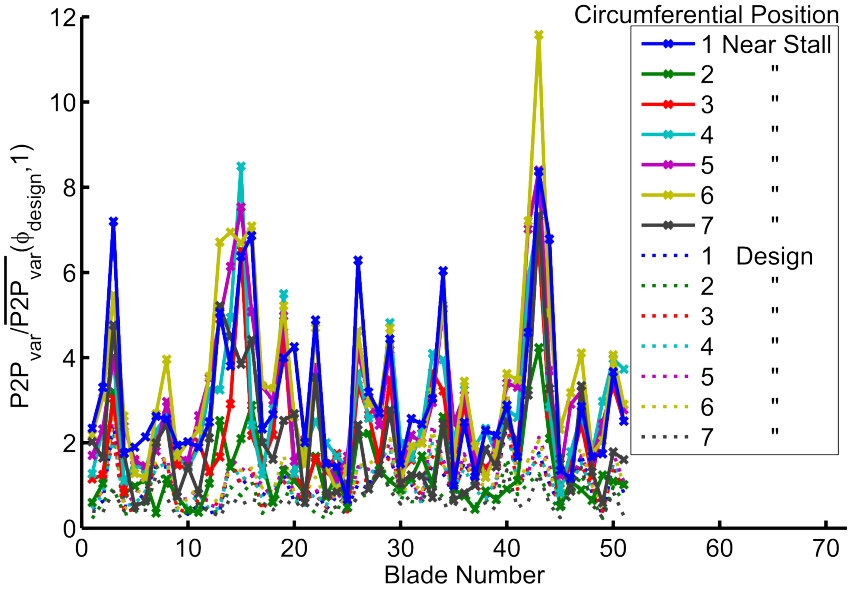

Figure 4.25: Passage to passage variation, $P2P_{var}$, at the leading edge for seven circumferential positions at near stall conditions, and for circumferential position 1 at design conditions (dashed line).

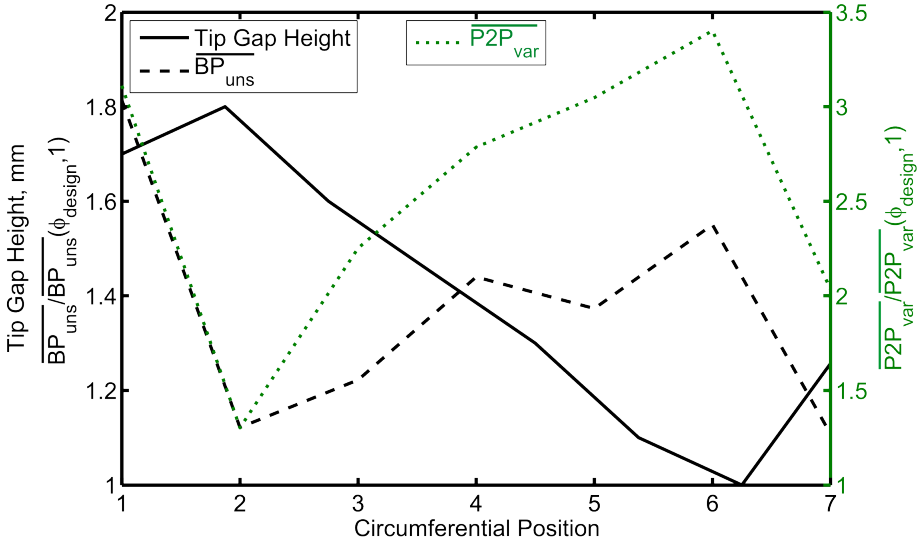

Figure 4.26: Circumferential variation in tip clearance height relative to the blade passage unsteadiness ($\overline{BP_{uns}}$) and passage to passage flow variation ($\overline{P2P_{var}}$) parameters.

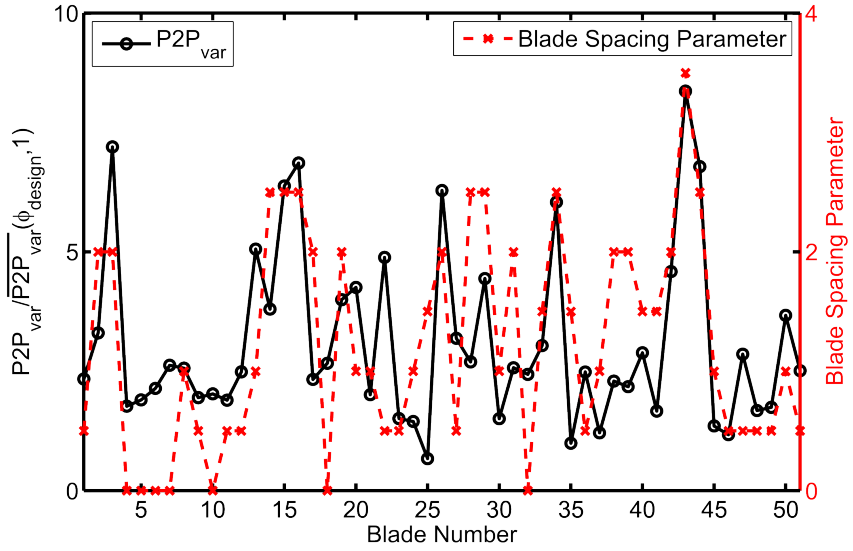

Figure 4.27: Passage to passage flow variation ($\overline{P2P_{var}}$) near stall and blade spacing parameter.

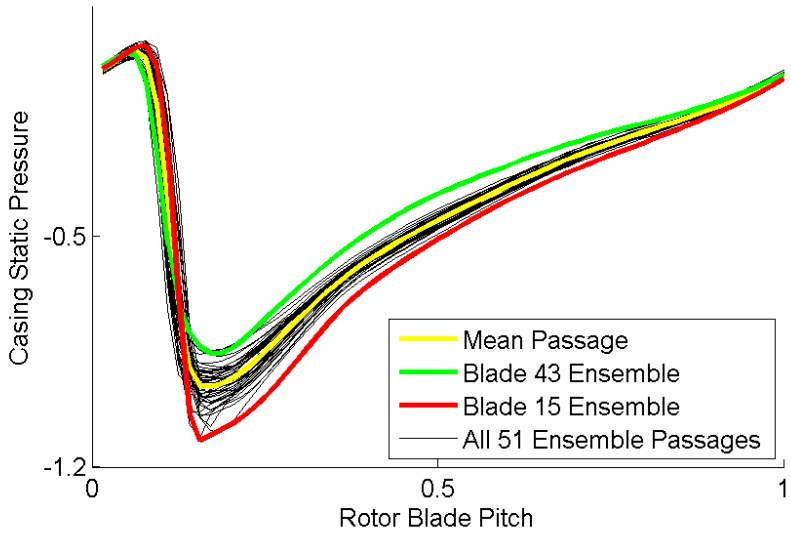

Figure 4.28: Ensemble leading edge static pressure traces for all 51 blades near stall.

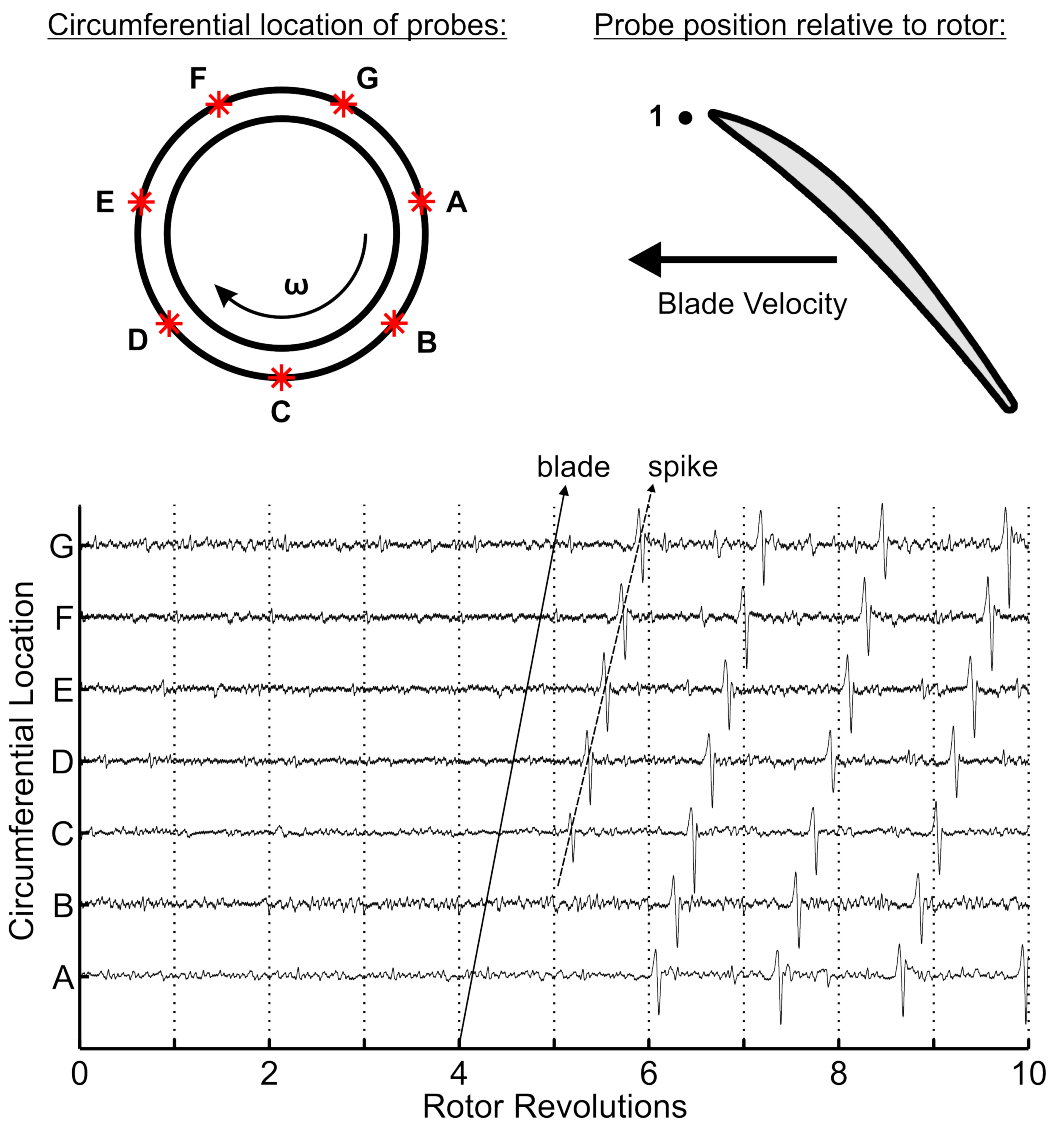

Figure 5.1: Traditional stall inception traces from leading edge pressure transducers at seven circumferential locations.

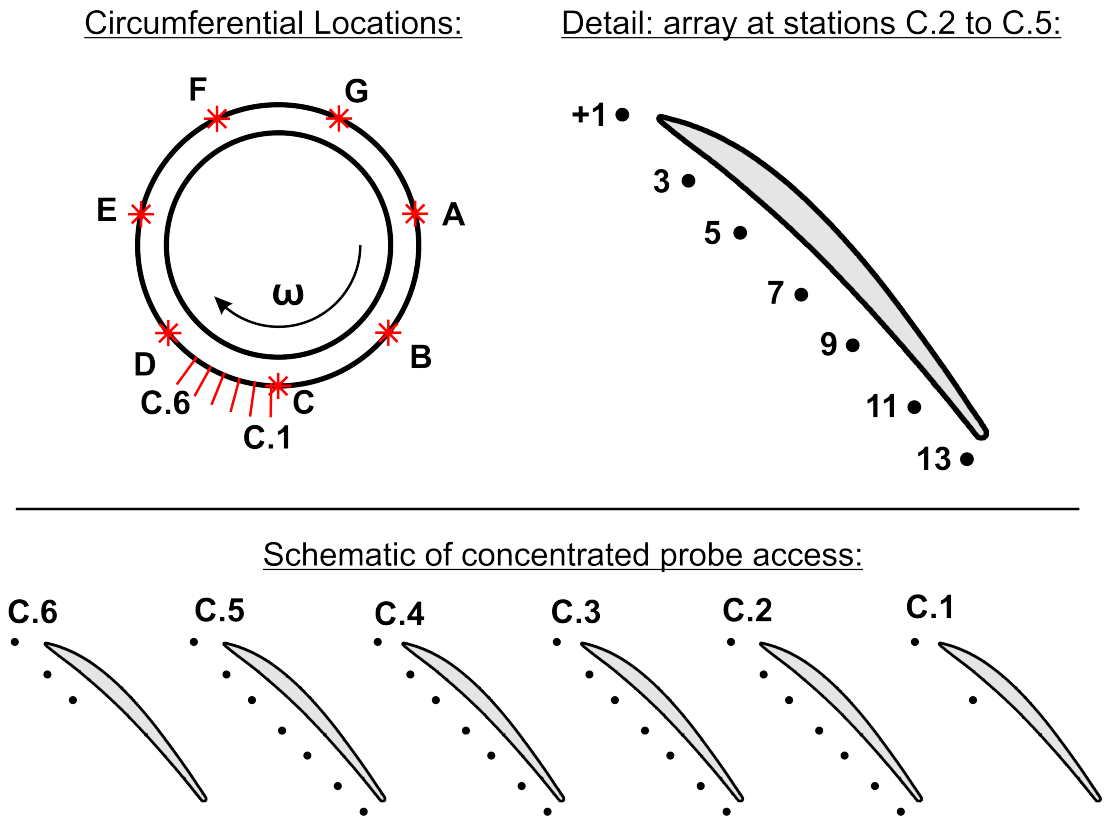

Figure 5.2: Set-up schematic and detail of rotor overtip access for study of spike at the stage of traditional detection.

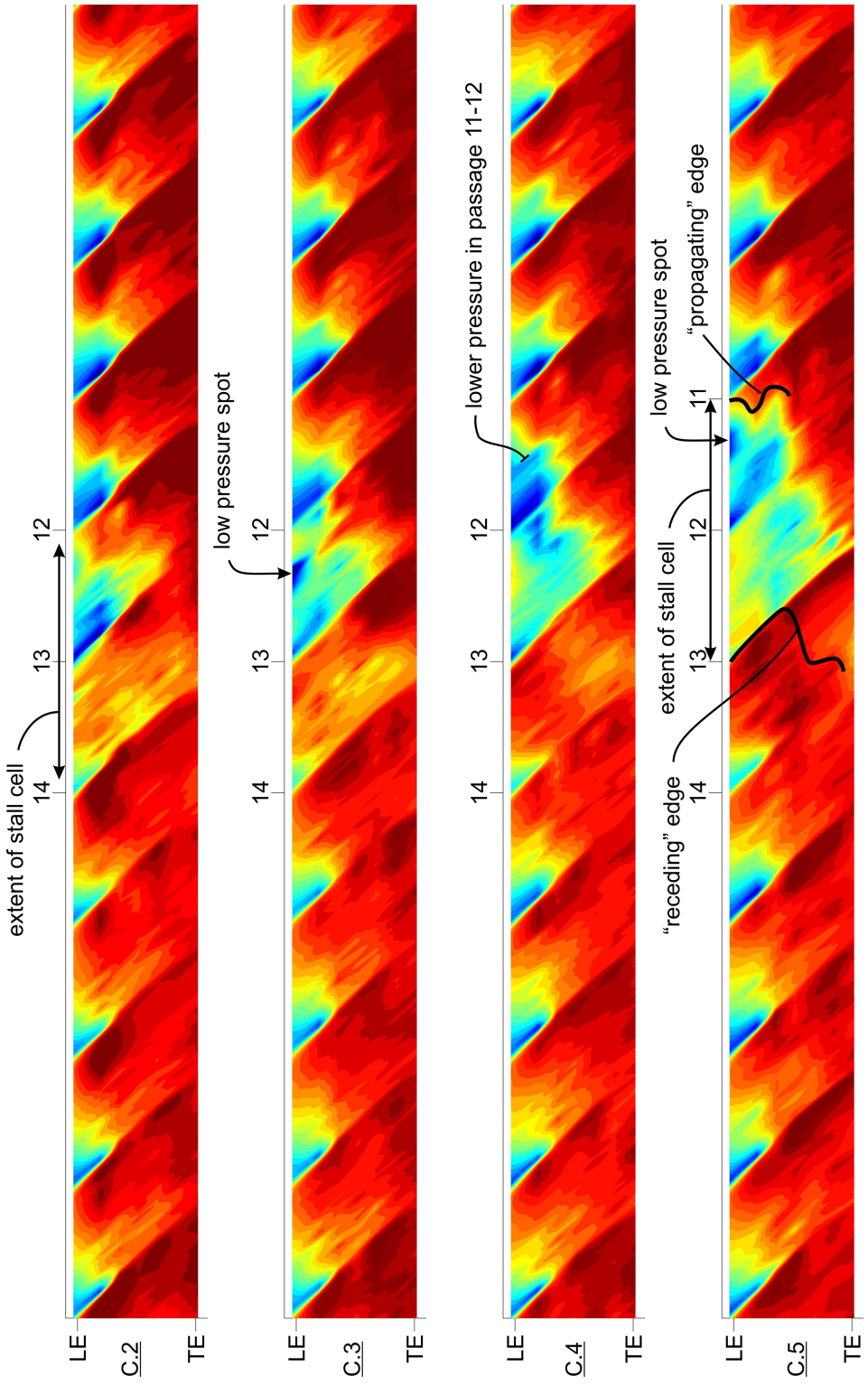

Figure 5.3: Static pressure contours of established spike over four rotor pitches.

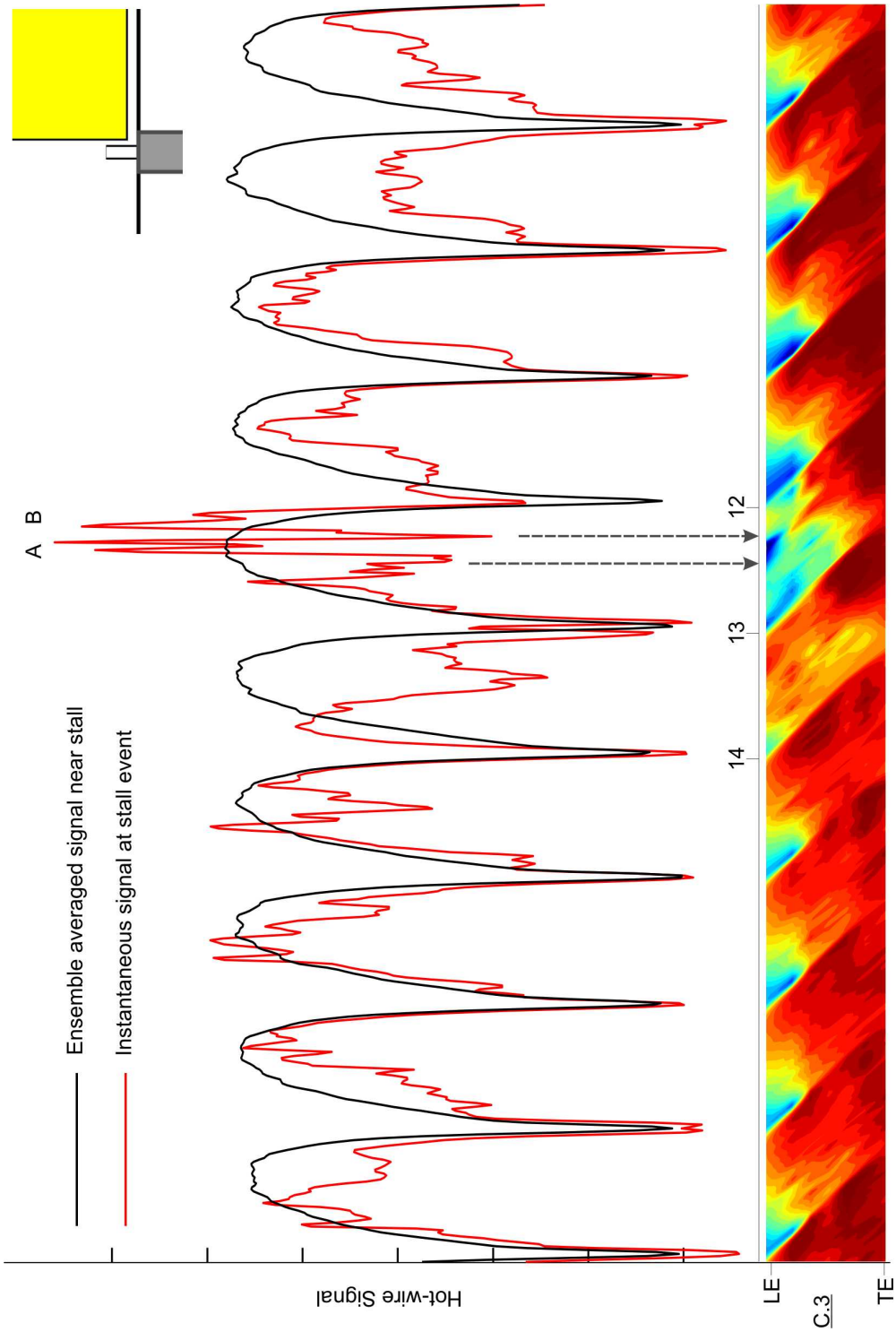

Figure 5.4: Hot-wire measurements just upstream of leading edges at station C.3. Black: ensemble averaged hot-wire signal near stall. Red: instantaneous hot-wire signal measured simultaneously with static pressure during the stall event.

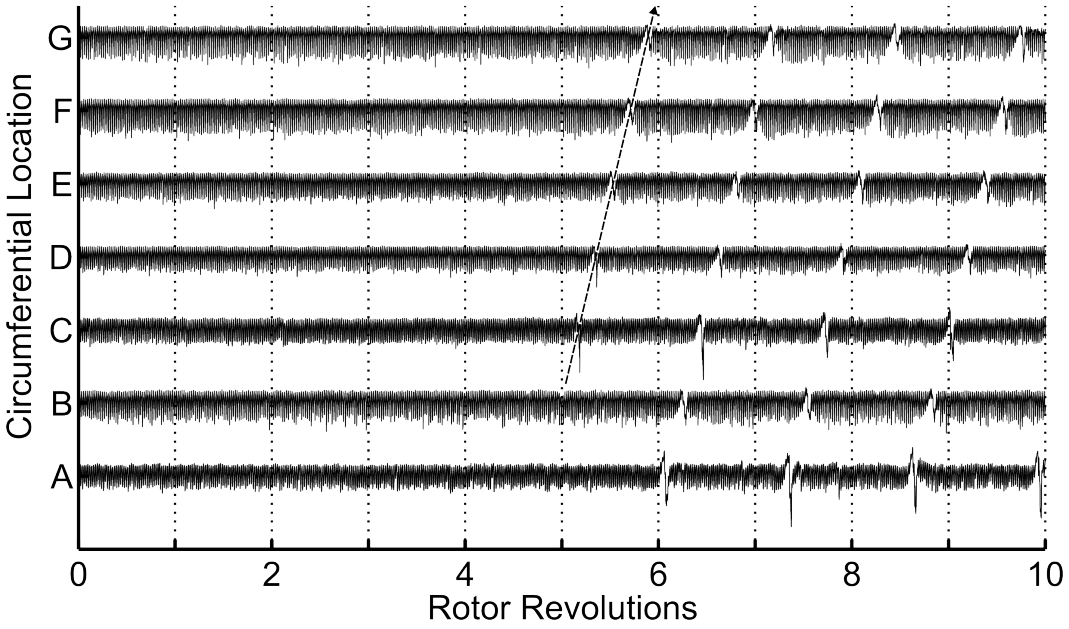

Figure 5.5: High frequency resolution stall inception traces.

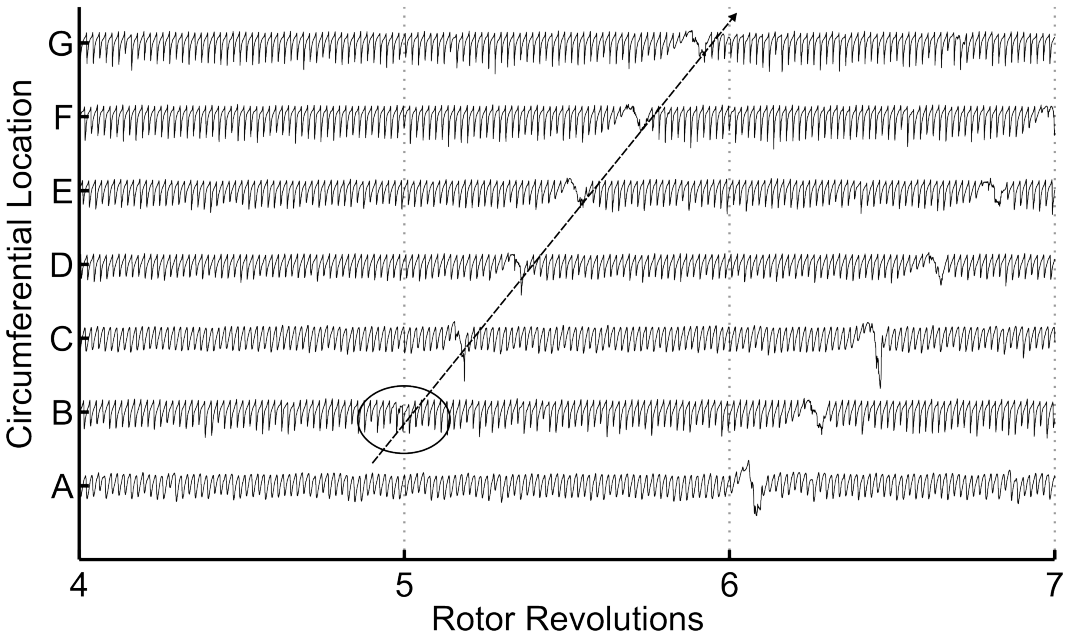

Figure 5.6: High frequency resolution stall inception traces; first sign of spike circled.

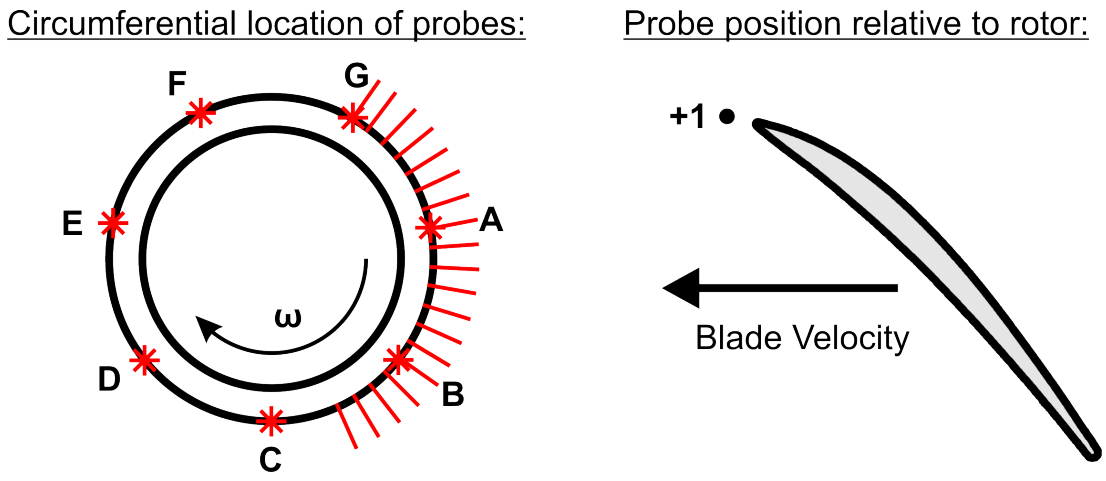

Figure 5.7: Pitch apart probe set-up for study of nascent spike propagation.

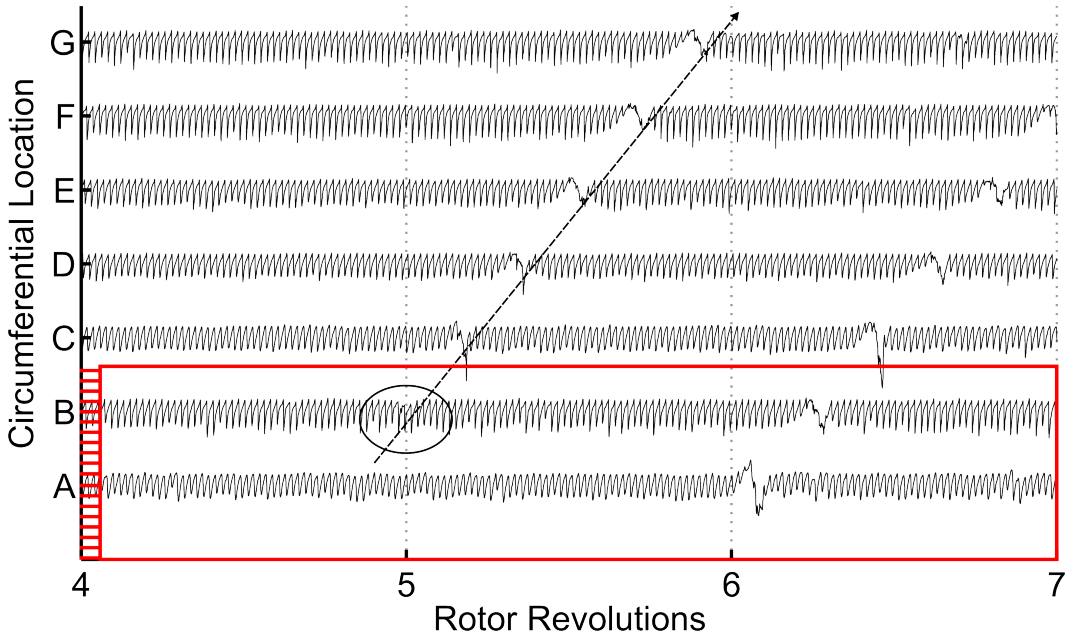

Figure 5.8: Position of pitch apart pressure transducers (red dashes) relative to traditional stall inception traces and onset of spike (circled).

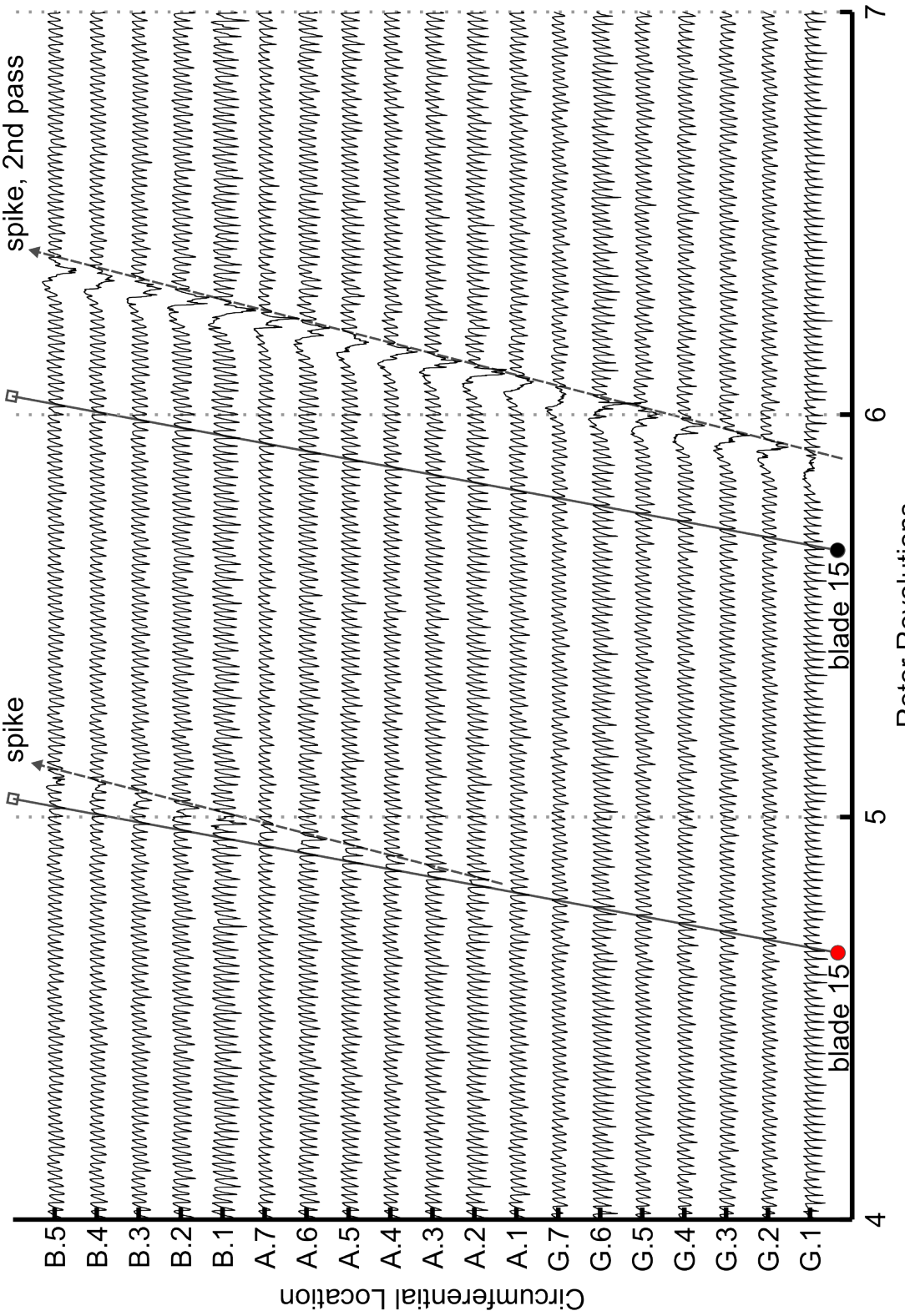

Figure 5.9: Rotor pitch apart stall inception traces.

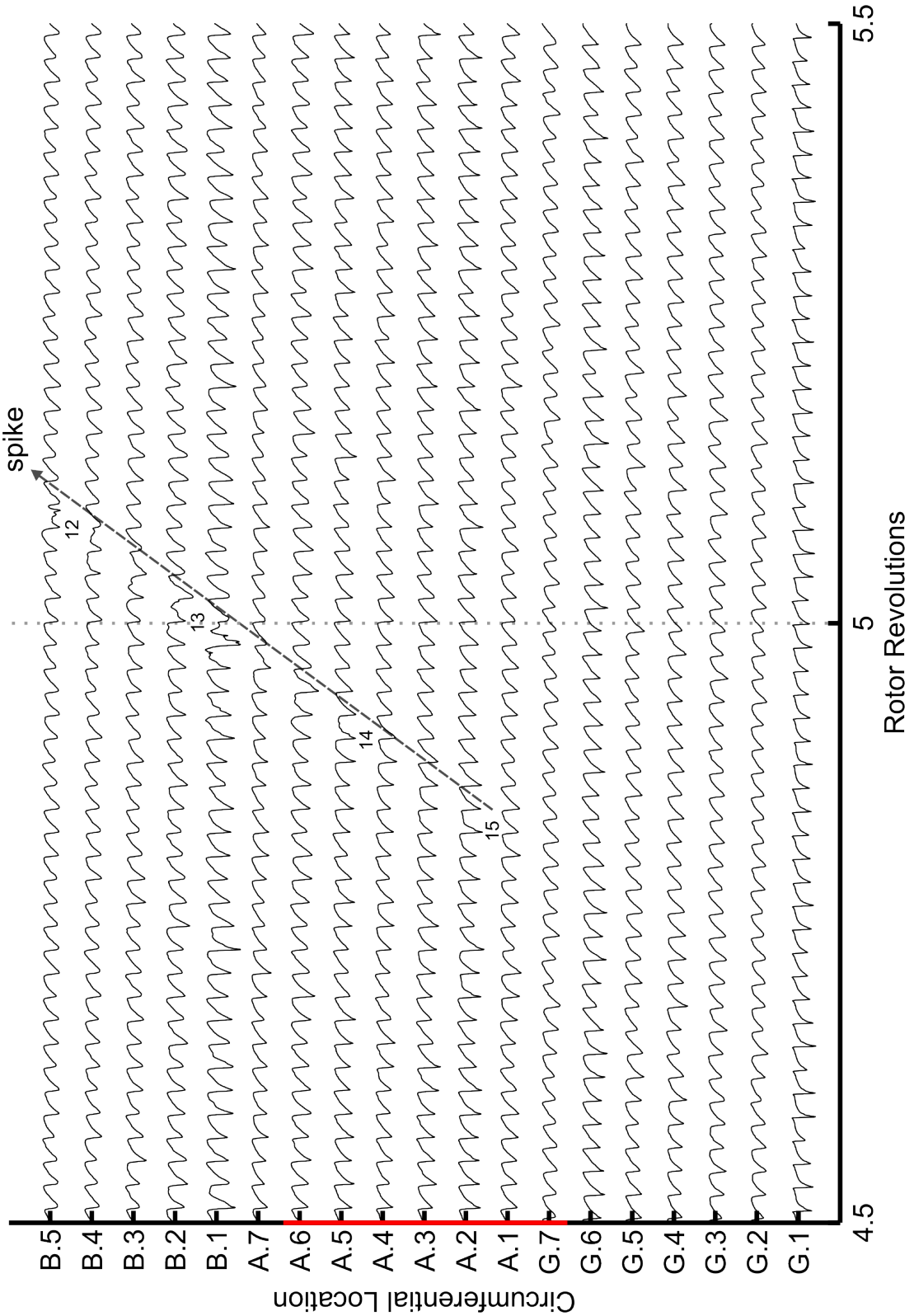

Figure 5.10: Rotor pitch apart stall inception traces.

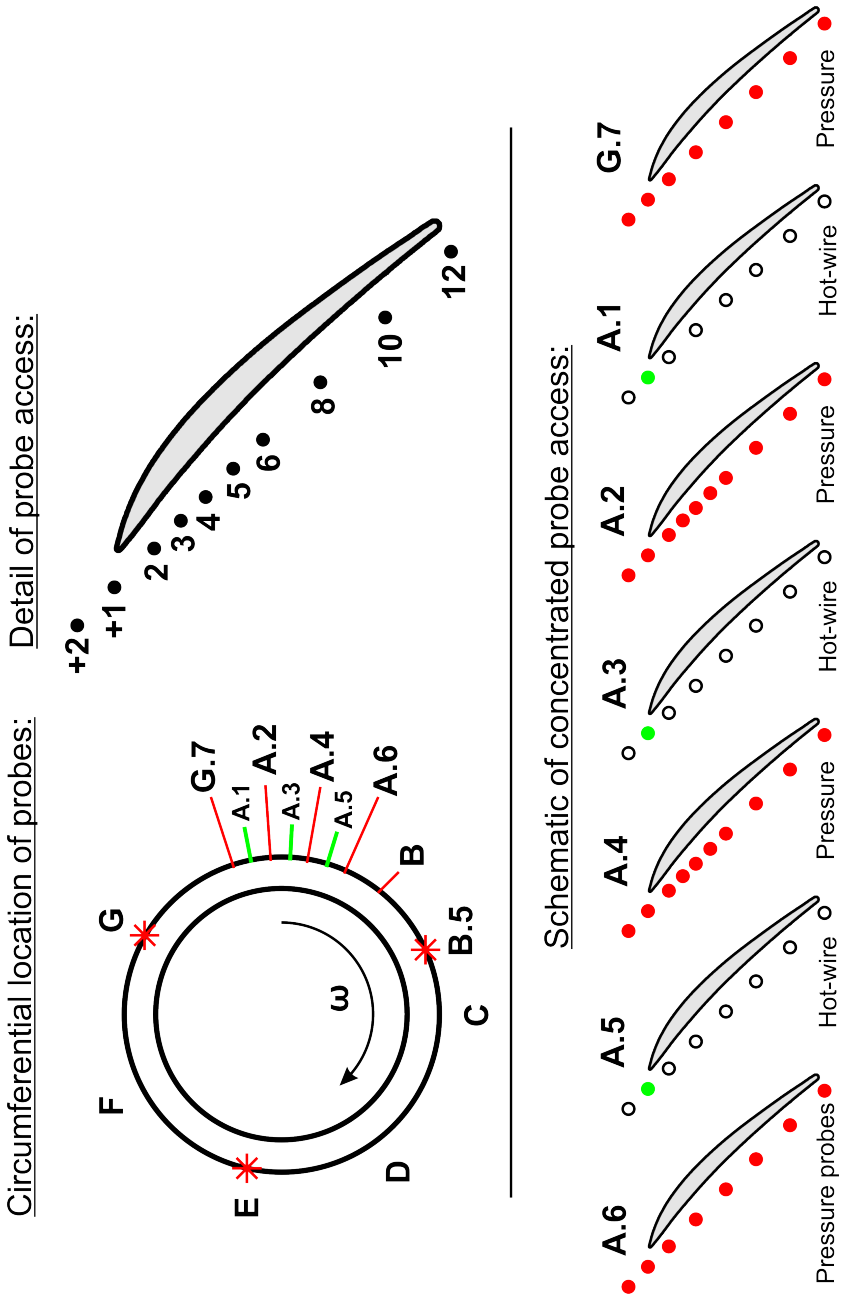

Figure 5.11: Schematic of concentrated probe access for study of spike formation. Pressure transducers, red; hot-wires, green (one configuration shown).

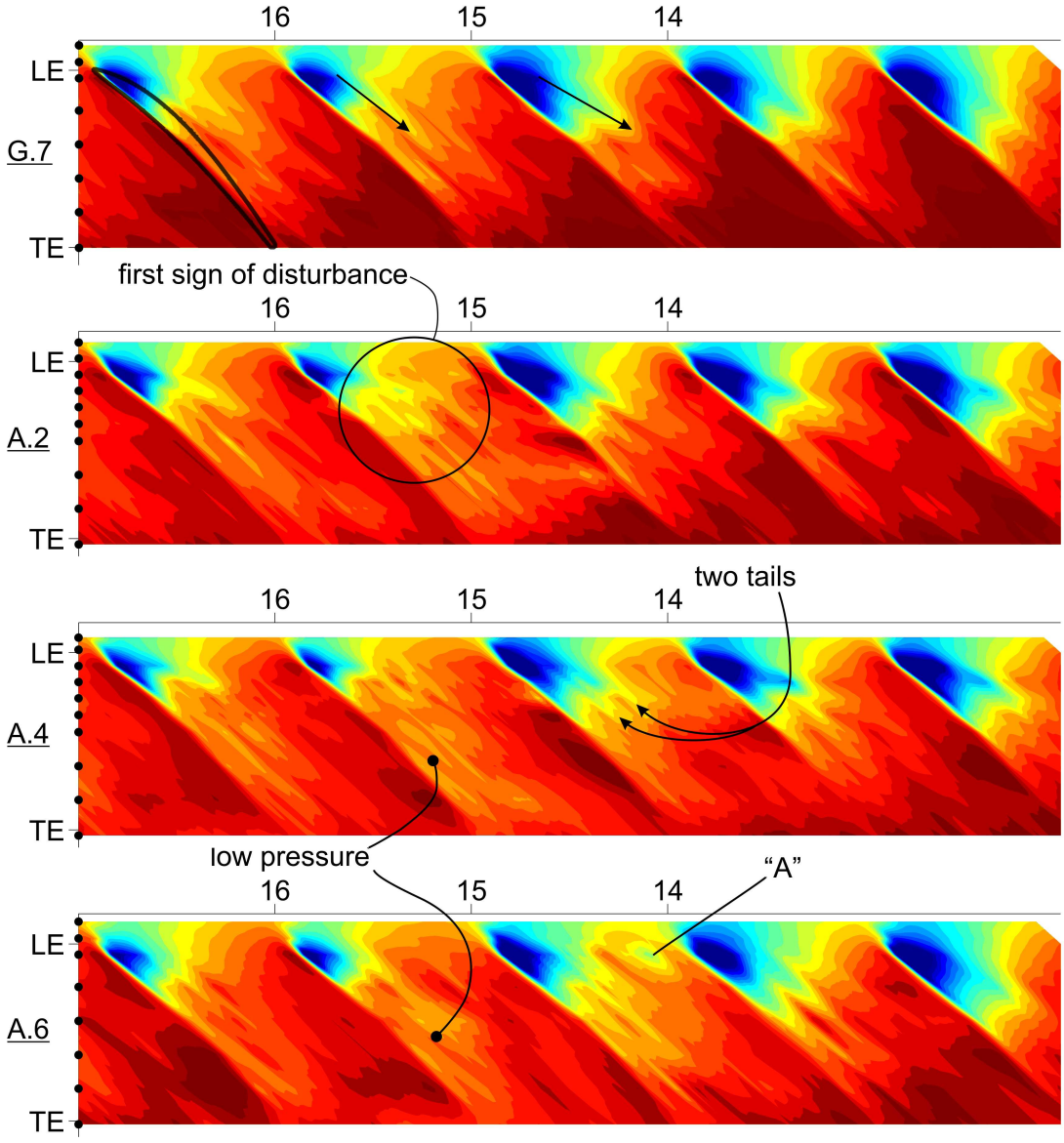

Figure 5.12: Instantaneous static pressure contours of the embryonic spike formation.

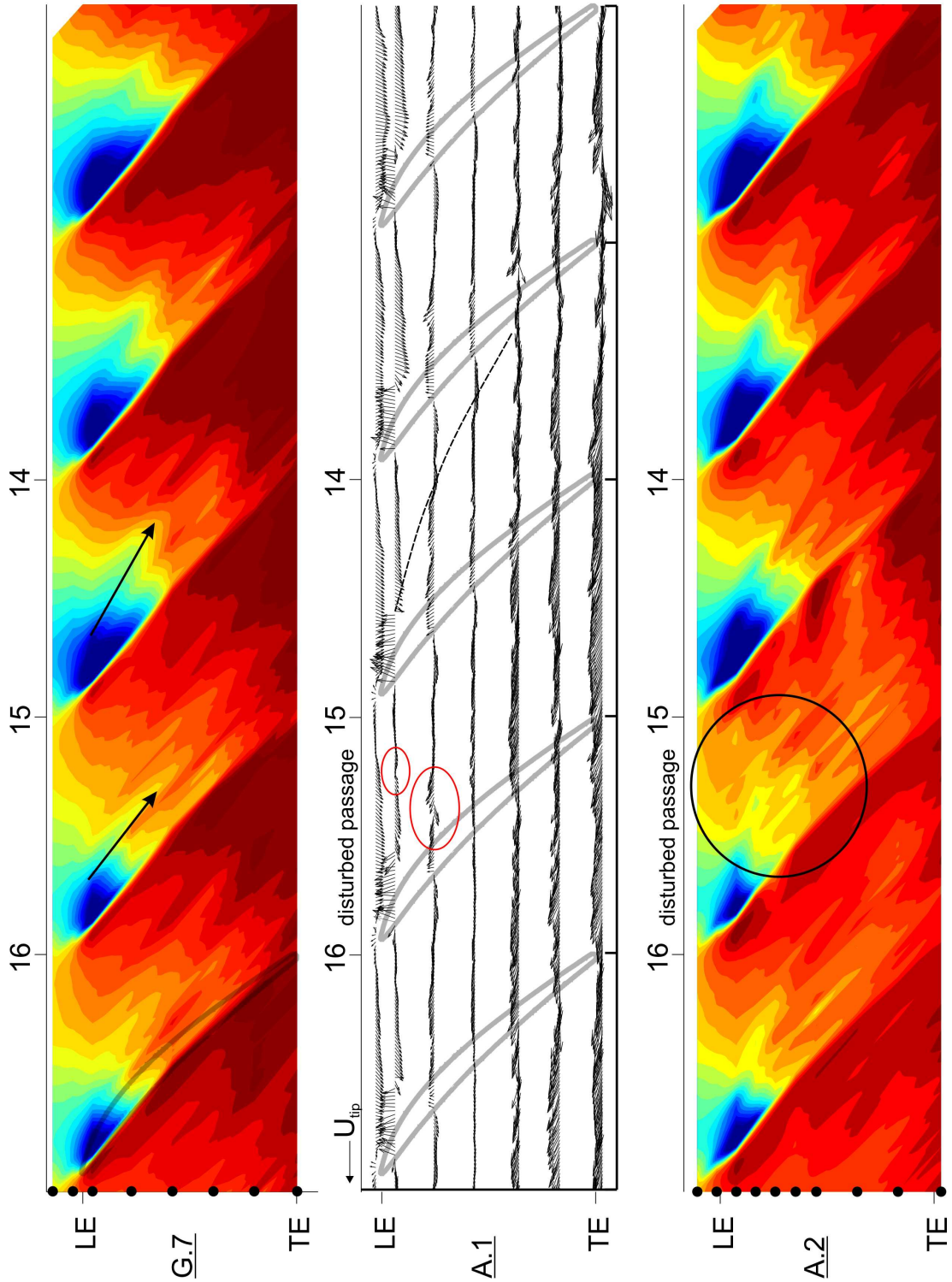

Figure 5.13: Static pressure contours and absolute frame velocity vectors of the embryonic spike formation (1 of 3).

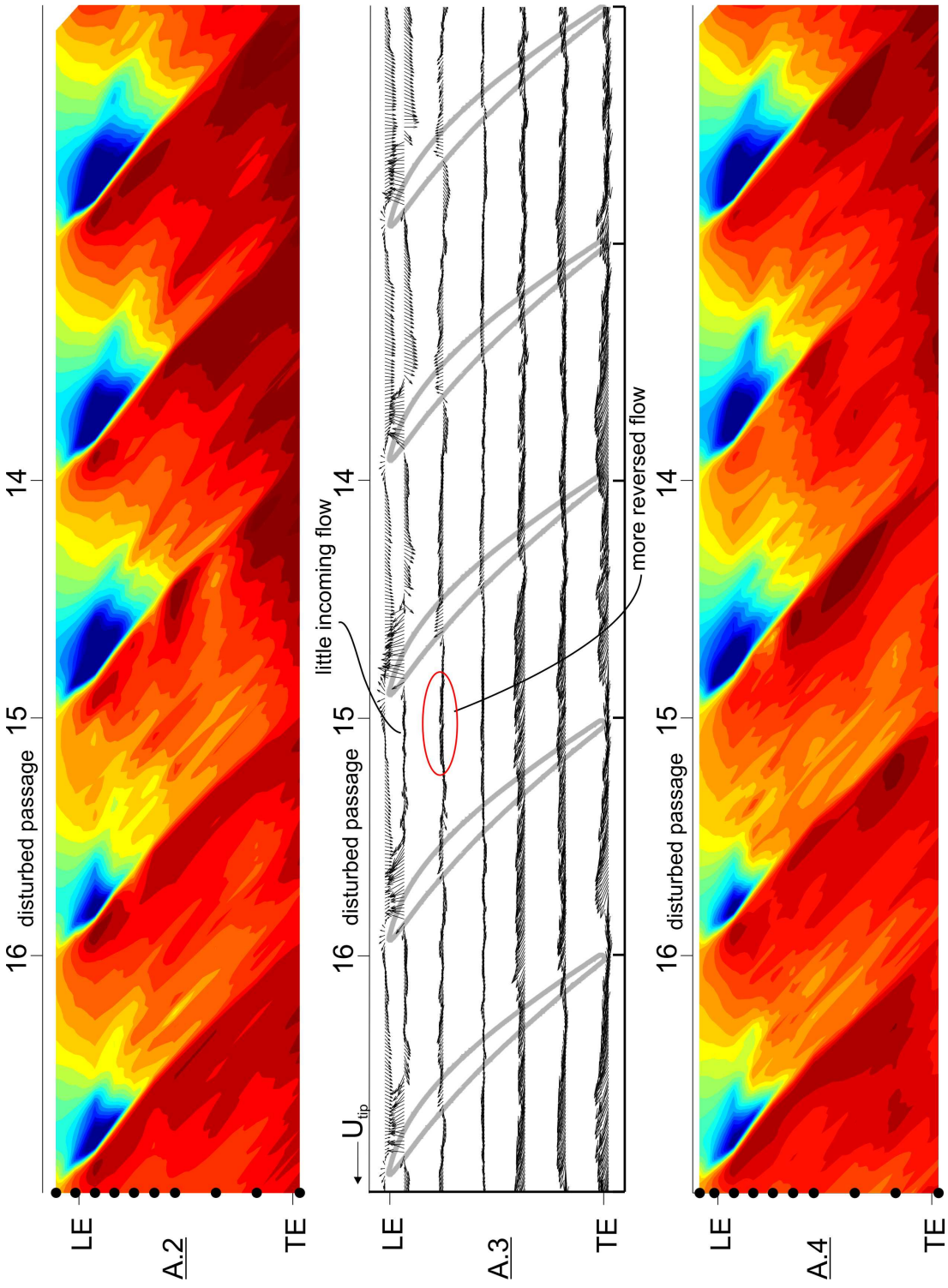

Figure 5.14: Static pressure contours and absolute frame velocity vectors of the embryonic spike formation (2 of 3).

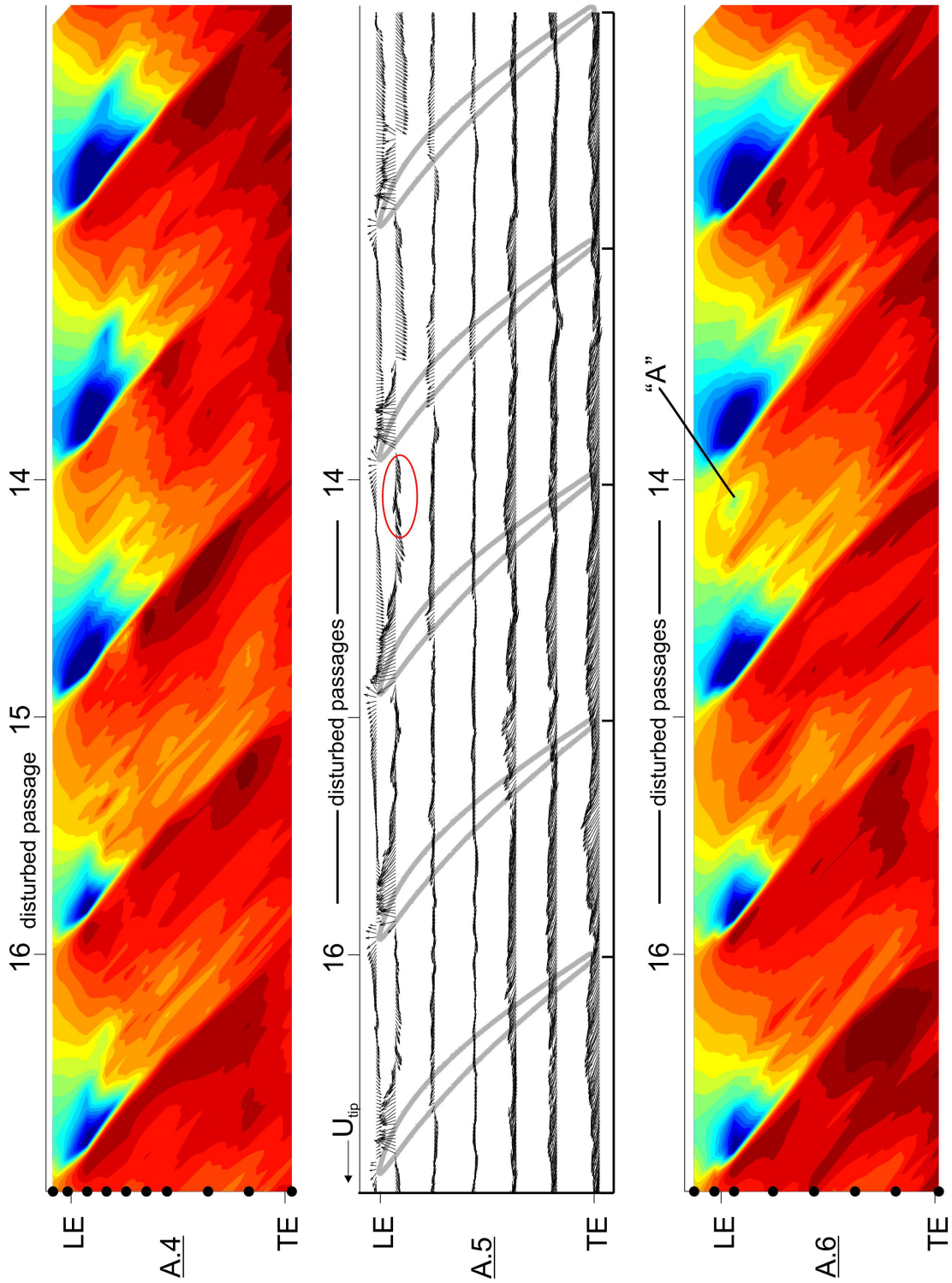

Figure 5.15: Static pressure contours and absolute frame velocity vectors of the embryonic spike formation (3 of 3).

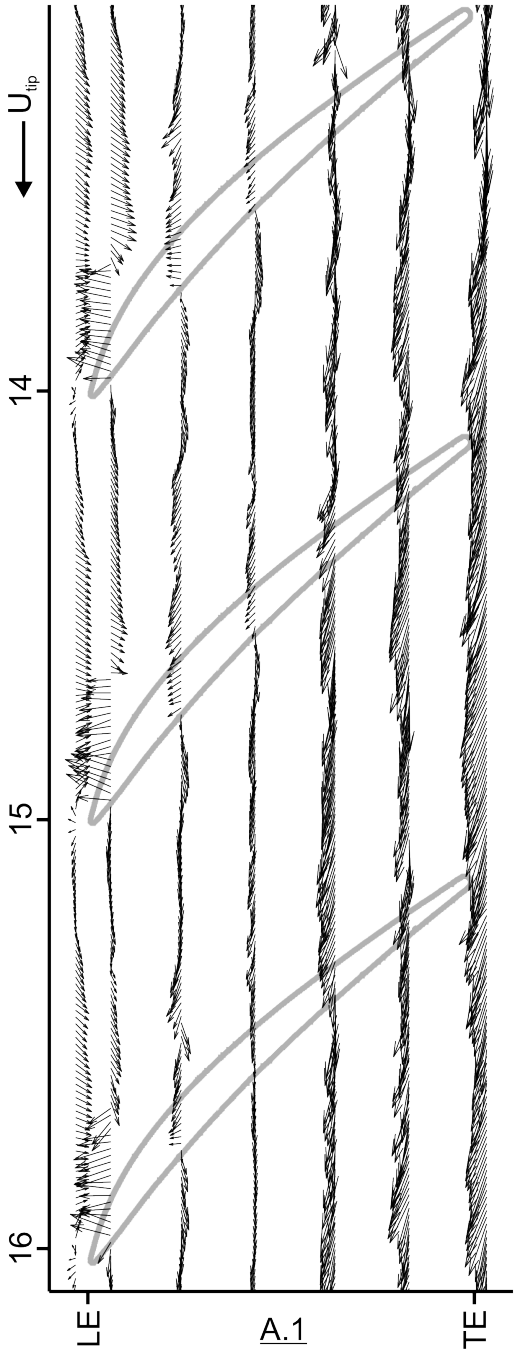

Figure 5.16: Absolute frame velocity vectors of spike formation, station A.1.

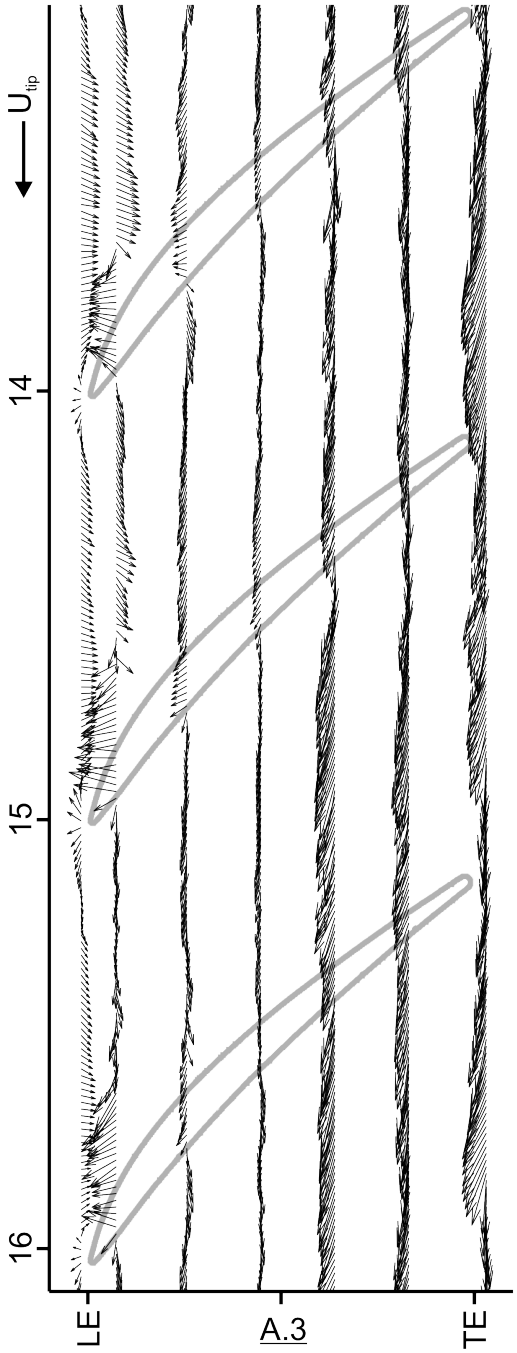

Figure 5.17: Absolute frame velocity vectors of spike formation, station A.3.

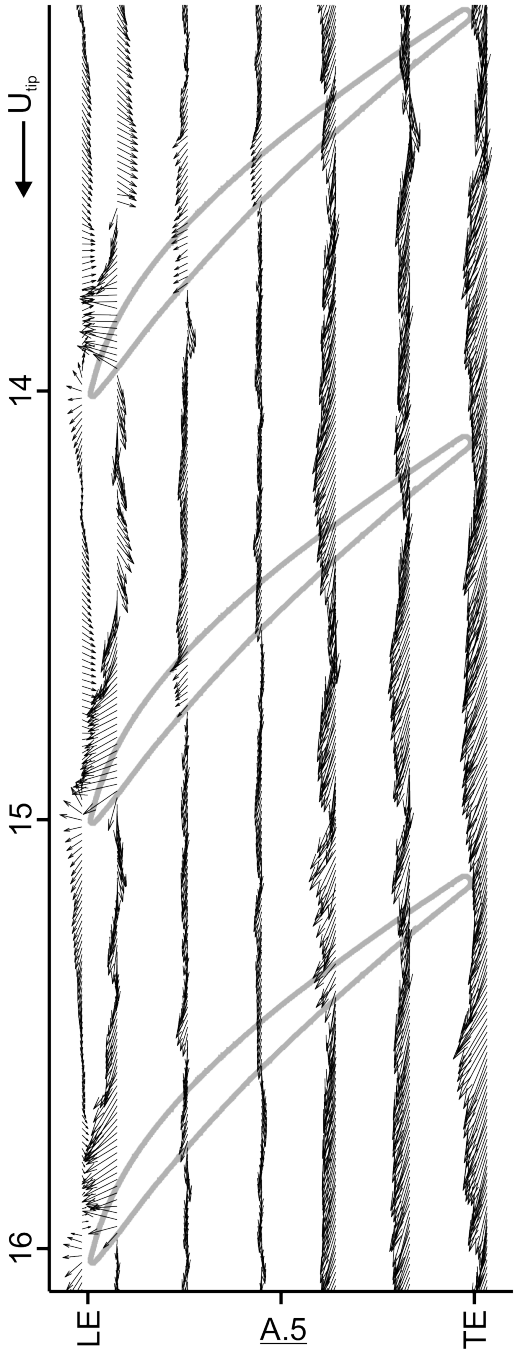

Figure 5.18: Absolute frame velocity vectors of spike formation, station A.5.

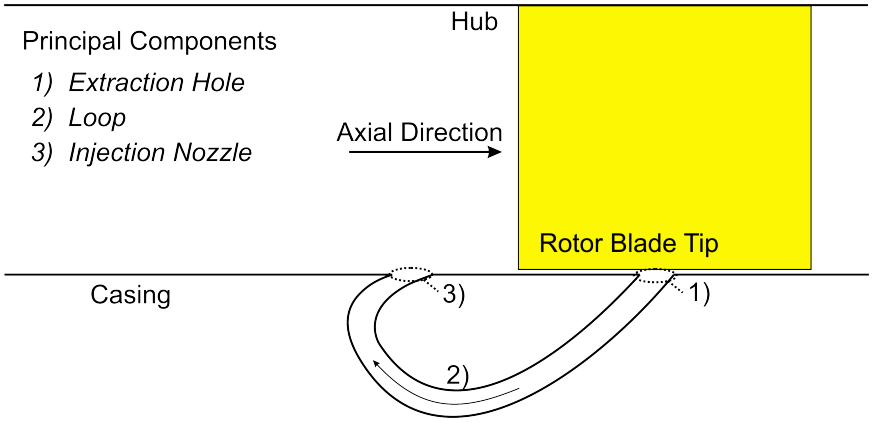

Figure 6.1: New extraction/re-injection casing treatment design.

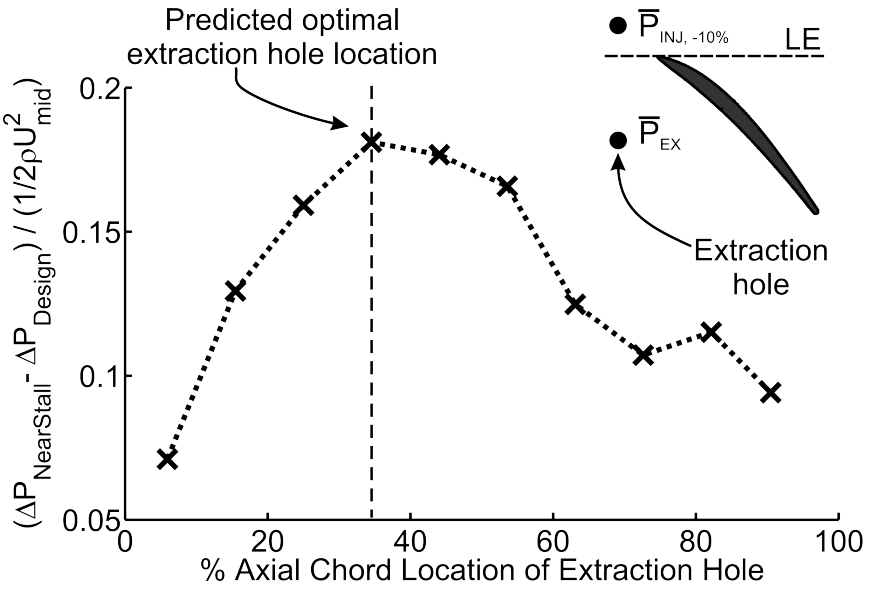

Figure 6.2: "Sweet spot" for extraction hole location predicted from re-circulation loop driving pressure ($\Delta P = \overline{P}_{EX} - \overline{P}_{INJ}$) at near stall and design conditions. Driving pressure is based on over-tip static pressure measurements (Figures 4.2 and 4.3).

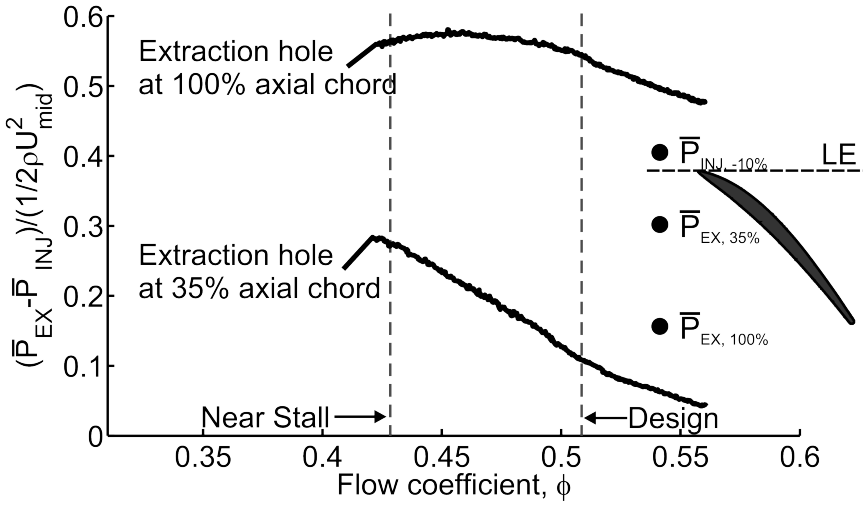

Figure 6.3: Measured characteristics of driving pressure for injection hole at 10% axial chord upstream of leading edge and for extraction holes at 100% chord and 35% chord.

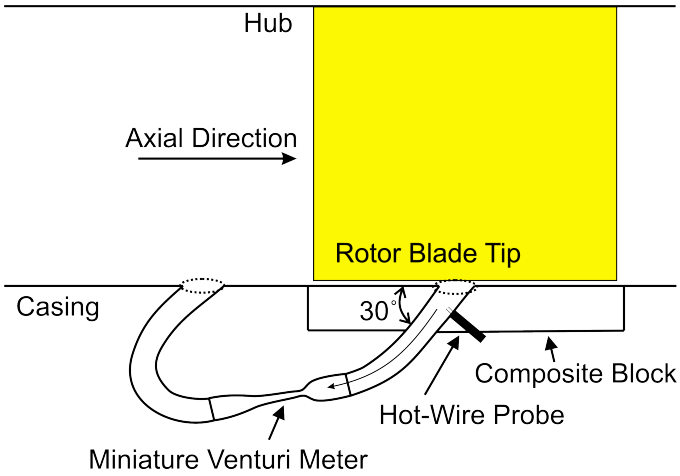

Figure 6.4: Instrumented extraction/re-injection loop.

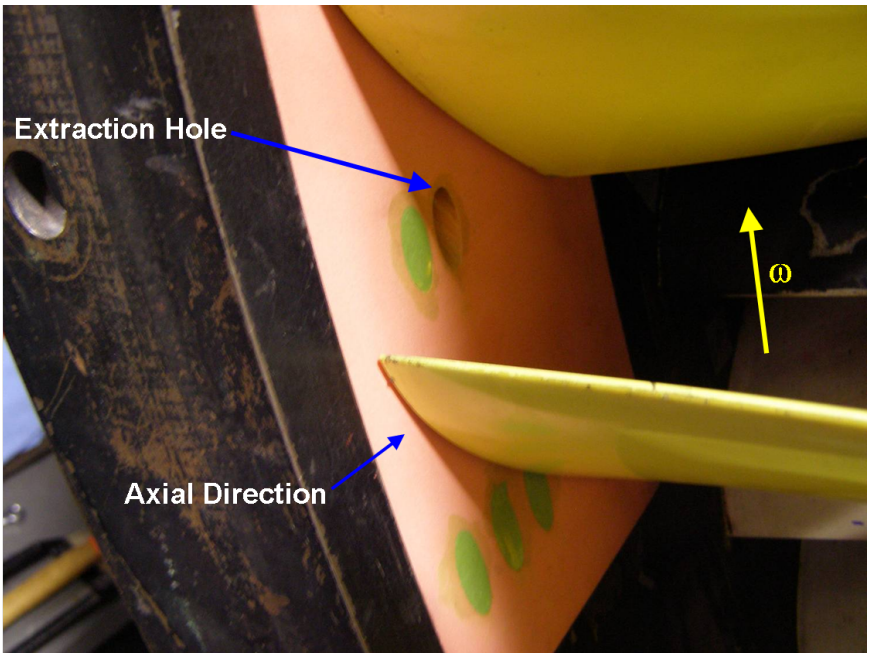

Figure 6.5: Compressor casing with composite block and extraction hole locations viewed from upstream of the rotor.

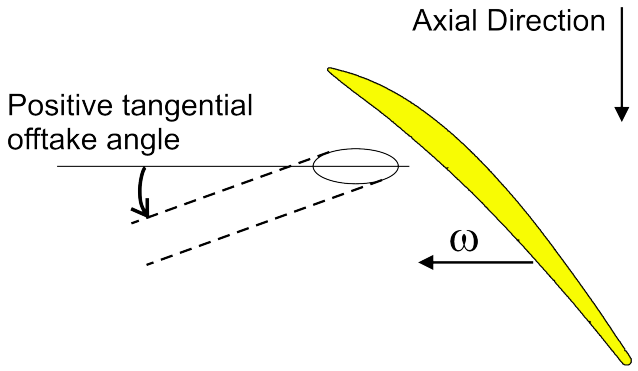

Figure 6.6: Tangential offtake angle imposed on the casing surface viewed from the hub.

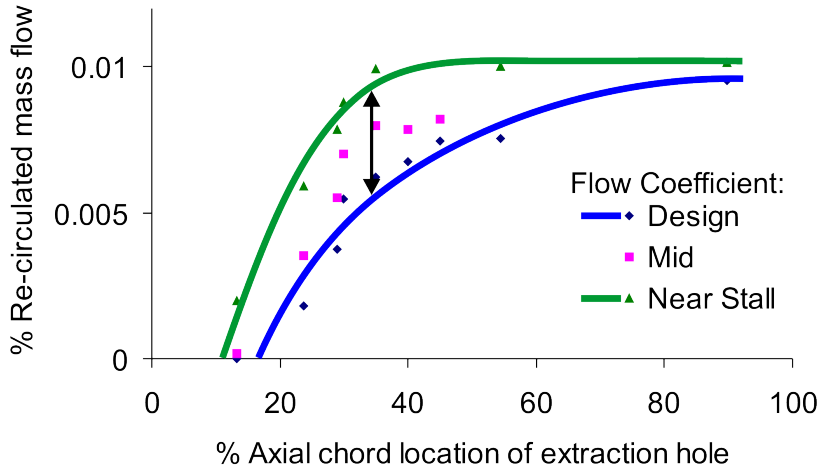

Figure 6.7: Extraction hole optimization: axial chord location.

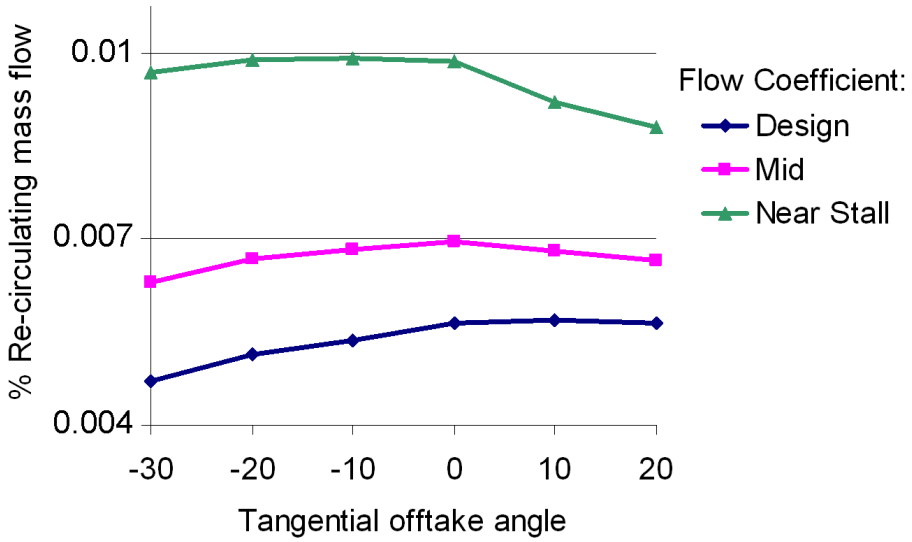

Figure 6.8: Extraction hole orientation.

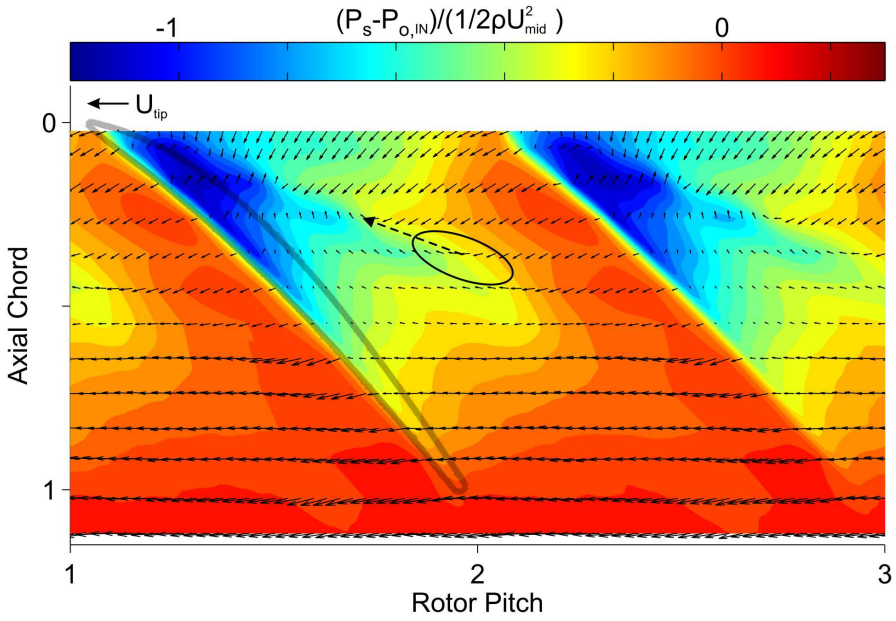

Figure 6.9: Casing static pressure contours at design with absolute velocity vectors at 50% tip clearance height. Oval and trajectory indicate optimized extraction hole location and offtake angle.

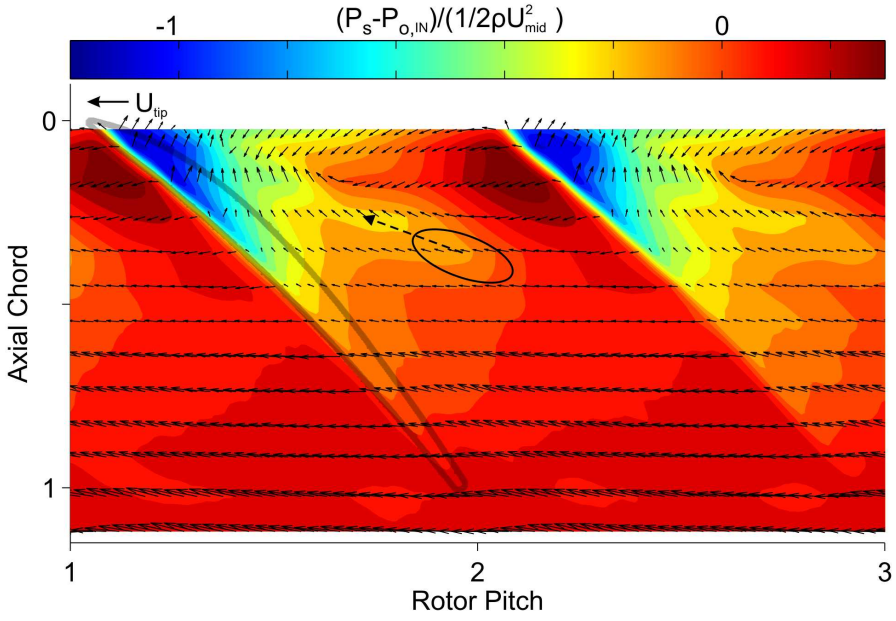

Figure 6.10: Casing static pressure contours near stall with absolute velocity vectors at 50% tip clearance height. Oval and trajectory indicate optimized extraction hole location and offtake angle.

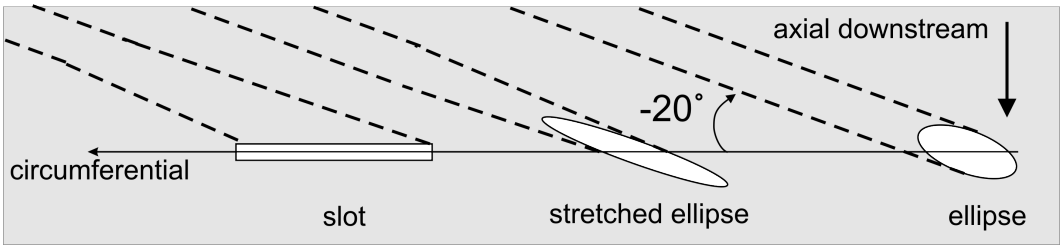

Figure 6.11: Extraction hole geometries viewed on casing surface.

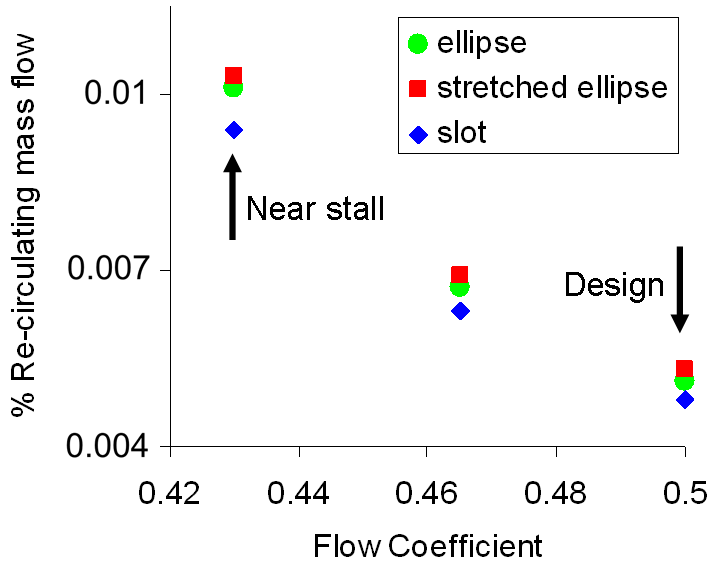

Figure 6.12: Extraction hole geometry optimization.

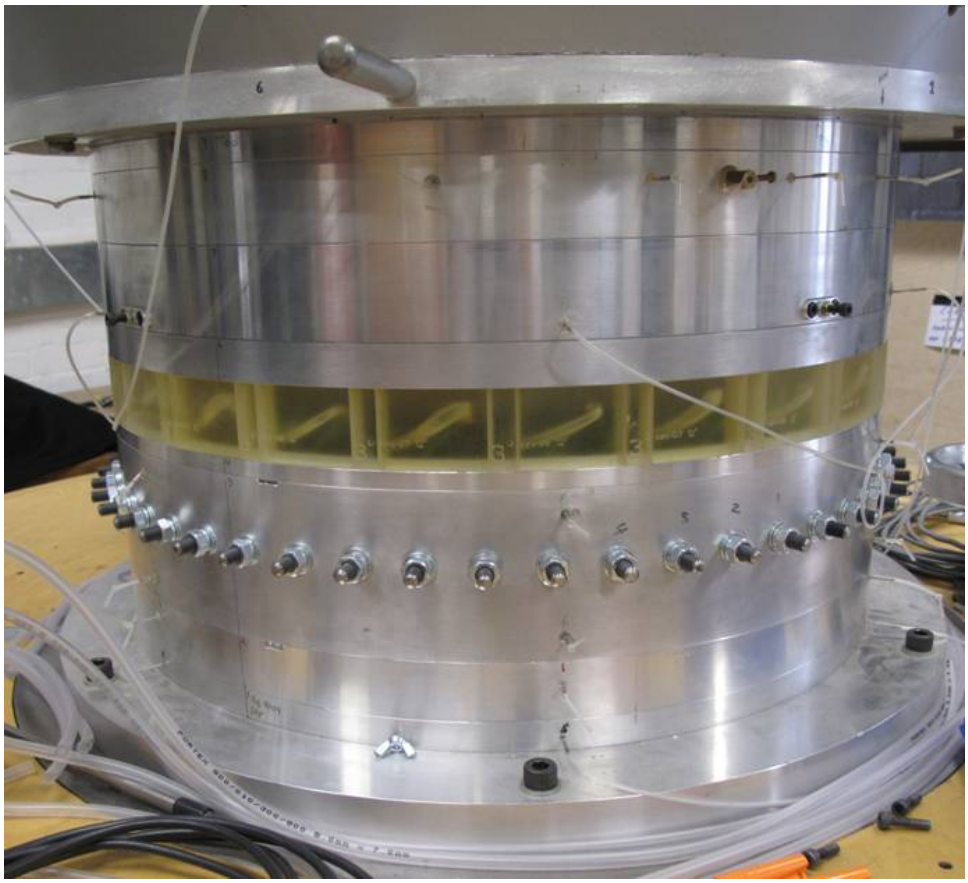

Figure 6.13: Photo of Mini-Deverson compressor with casing treatment (transparent ring) installed.

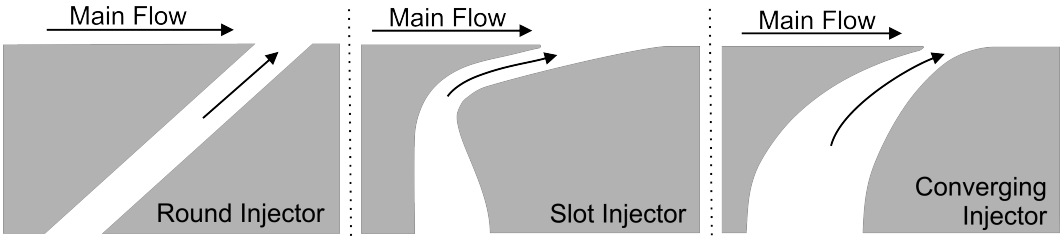

Figure 6.14: Injection Nozzle Designs.

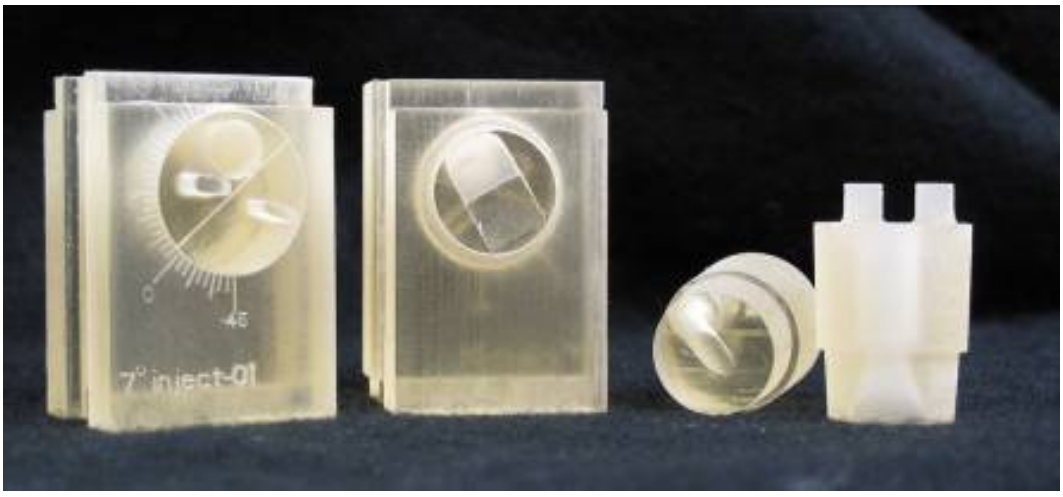

Figure 6.15: Pieces for injection nozzle testing driven by an external air supply.

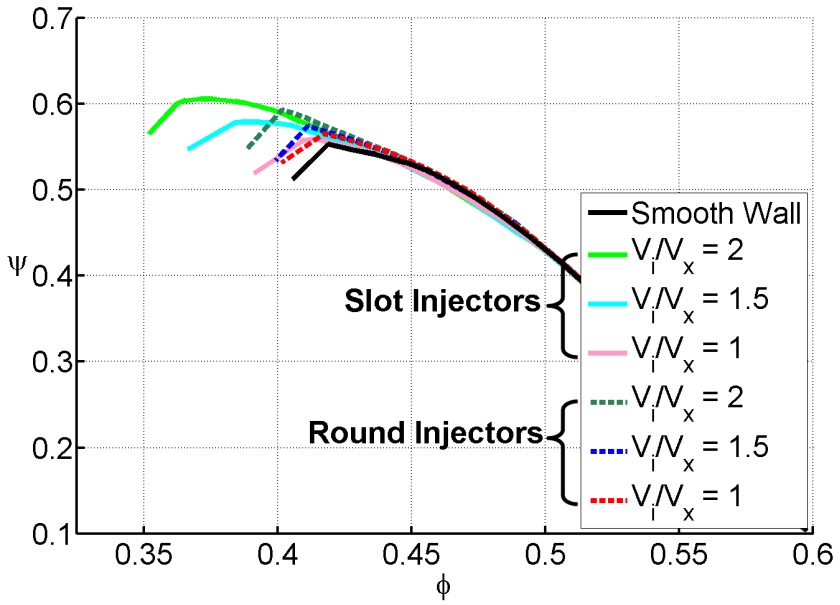

Figure 6.16: Pressure rise characteristics for 12 injectors blowing axially downstream. Comparing round and slot design injectors for three blowing strengths.

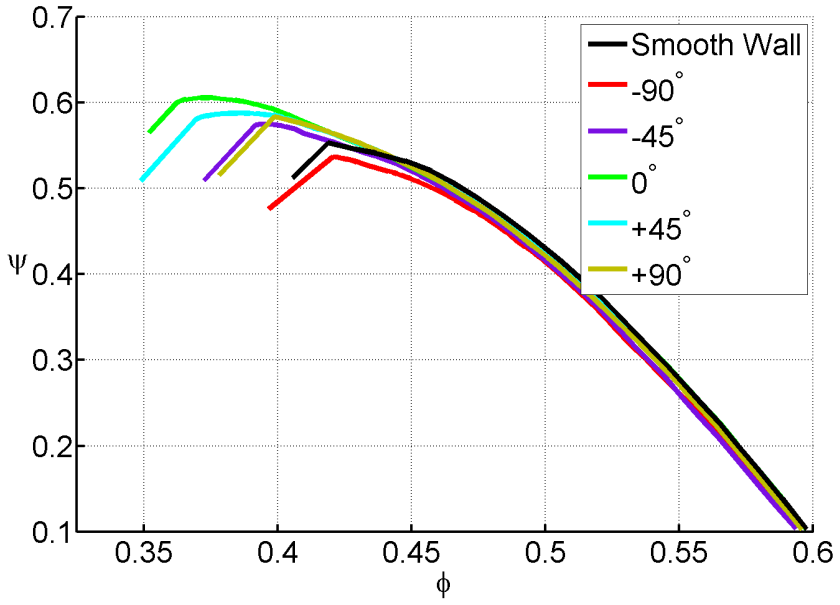

Figure 6.17: Pressure rise characteristic for various injection angles. Twelve slot injectors with $V_i/V_x = 2$.

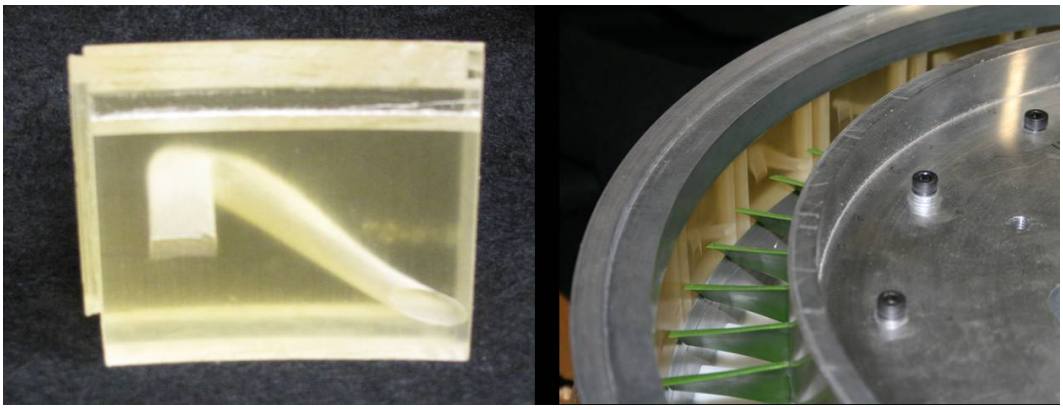

Figure 6.18: Inner detail of printed casing treatment loop, left, and casing treatment loops installed in Mini-Deverson, right.

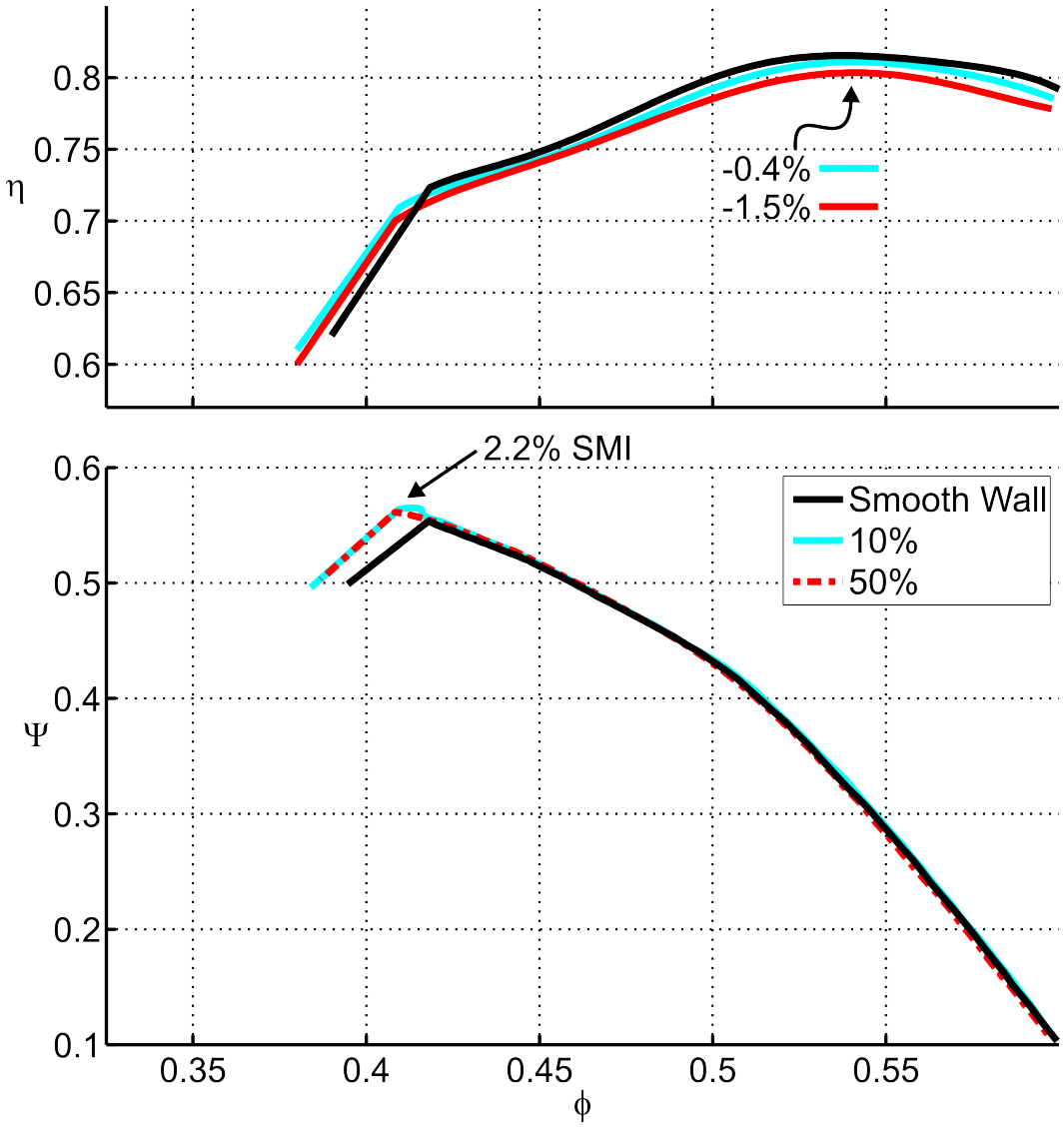

Figure 6.19: Efficiency and pressure rise characteristics for 12 extraction/re-injection casing treatment loops. The injectors are placed at 10% and 50% axial chord length upstream of the rotor leading edges. (The red line is dashed to show overlapping data.)

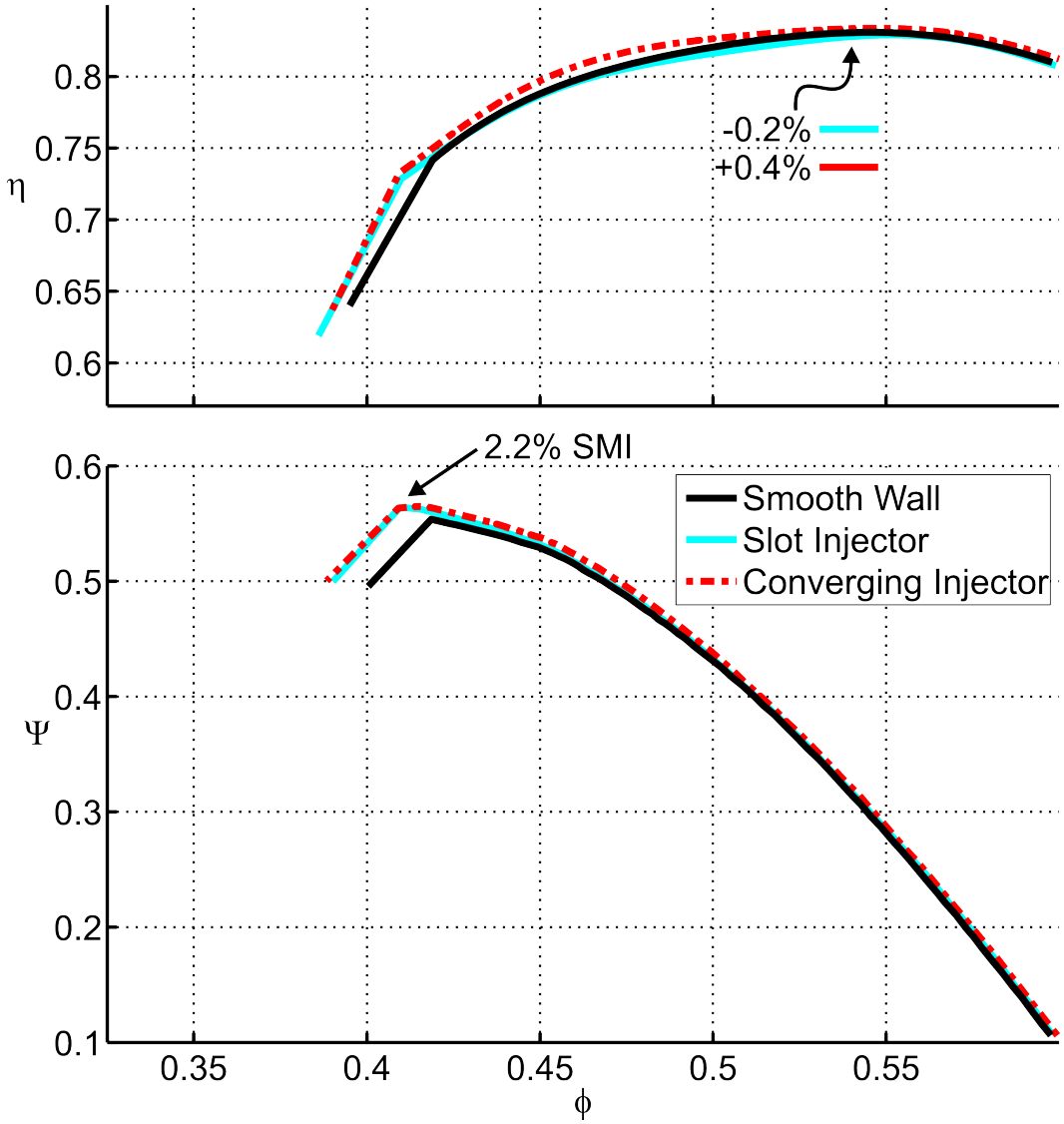

Figure 6.20: Efficiency and pressure rise characteristics for 12 extraction/re-injection casing treatment loops with two different injection nozzle designs. (The red line is dashed to show overlapping data.)

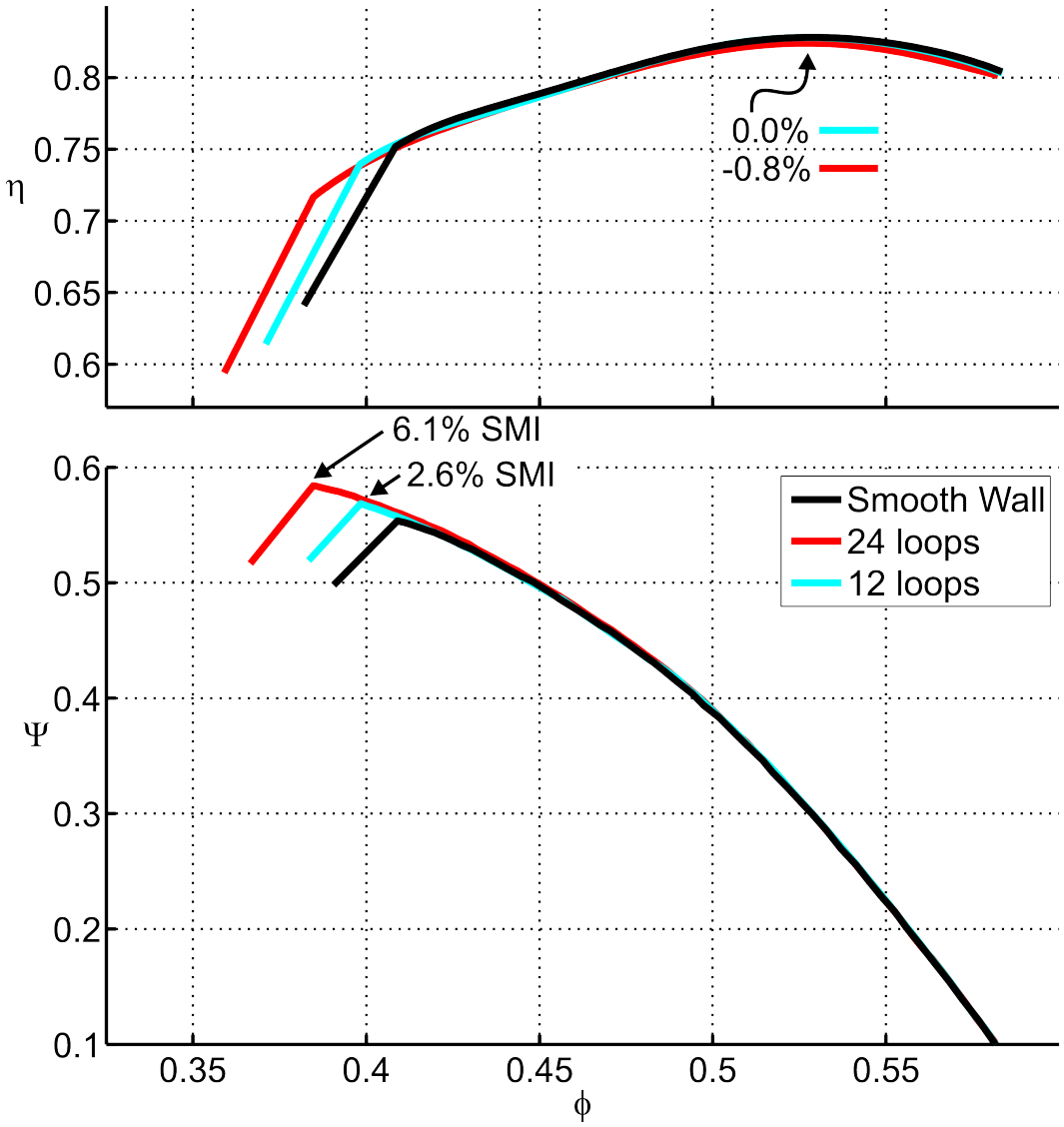

Figure 6.21: Efficiency and pressure rise characteristics for extraction/re-injection loops with rotor blades stagger increased 2°.

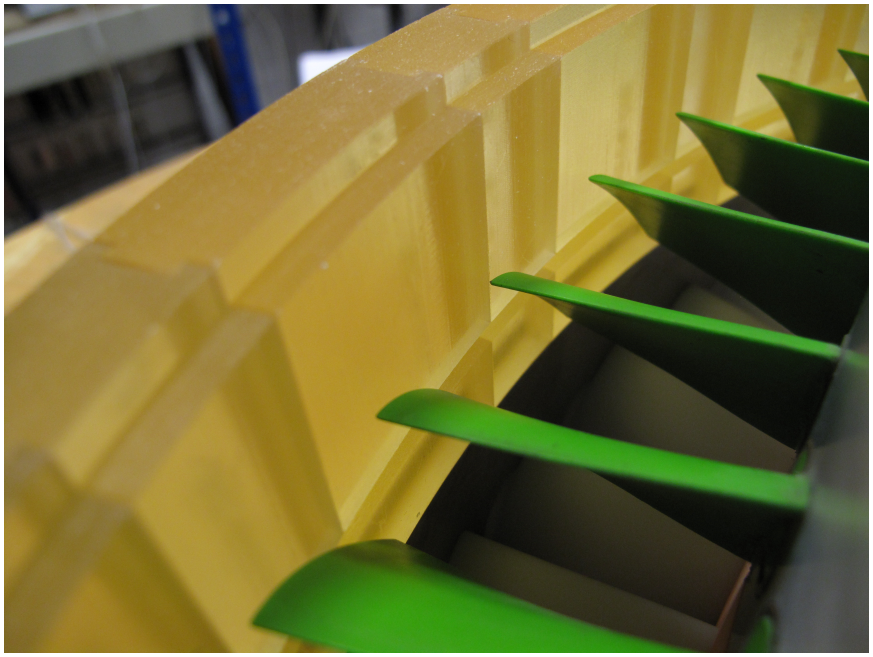

Figure 6.22: Circumferential groove.

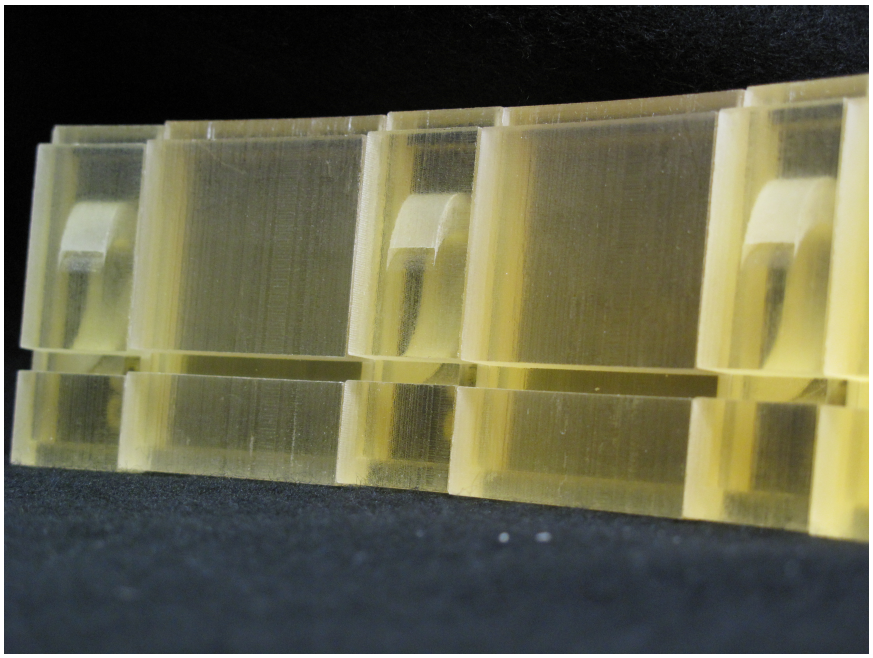

Figure 6.23: Re-circulating groove.

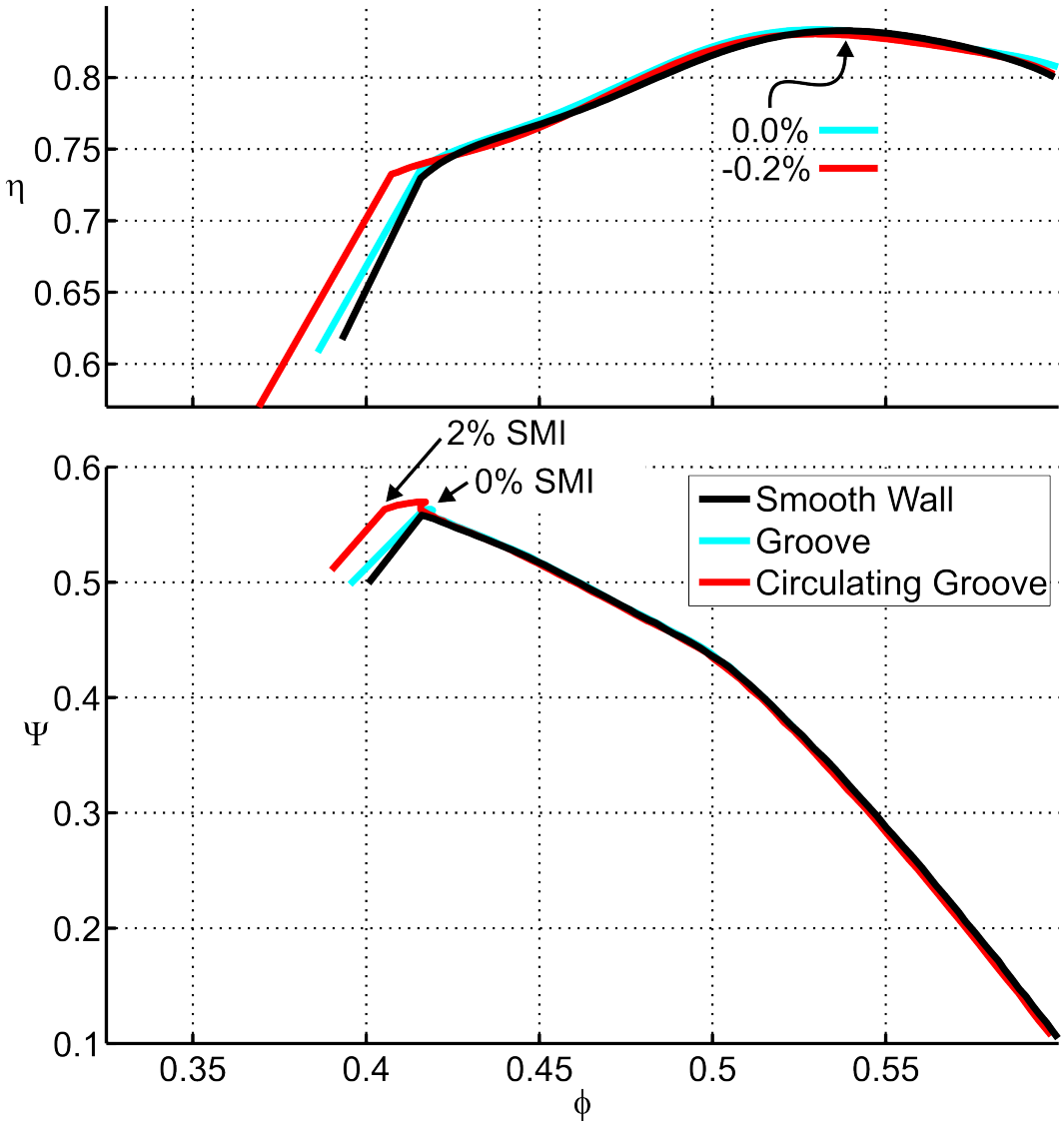

Figure 6.24: Efficiency and pressure rise characteristics for single circumferential groove and groove plus 24 extraction/re-injection loops (baseline rotor stagger).

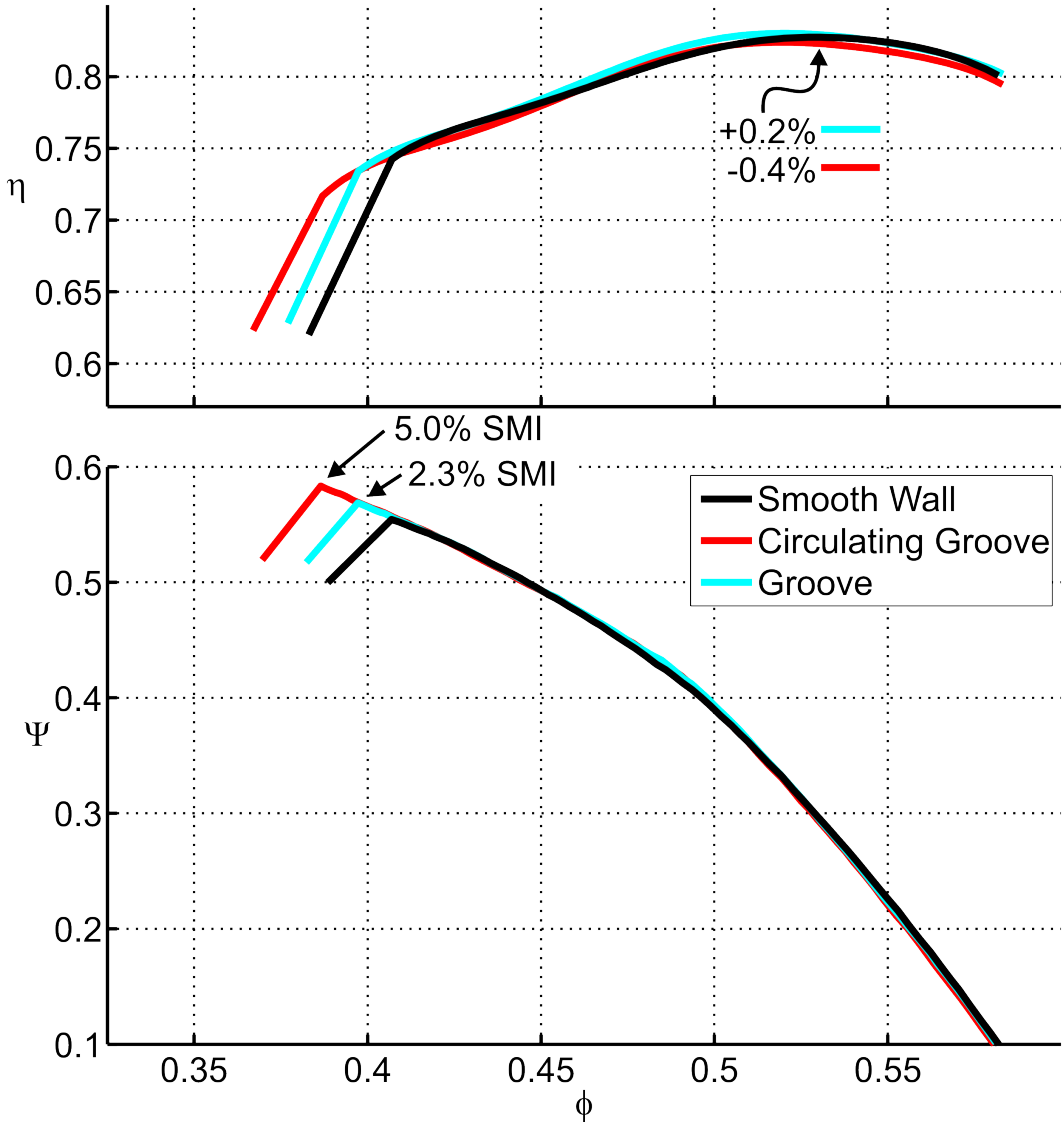

Figure 6.25: Efficiency and pressure rise characteristics for single circumferential groove and groove plus 24 extraction/re-injection loops (rotor blades stagger increased 2° from baseline).

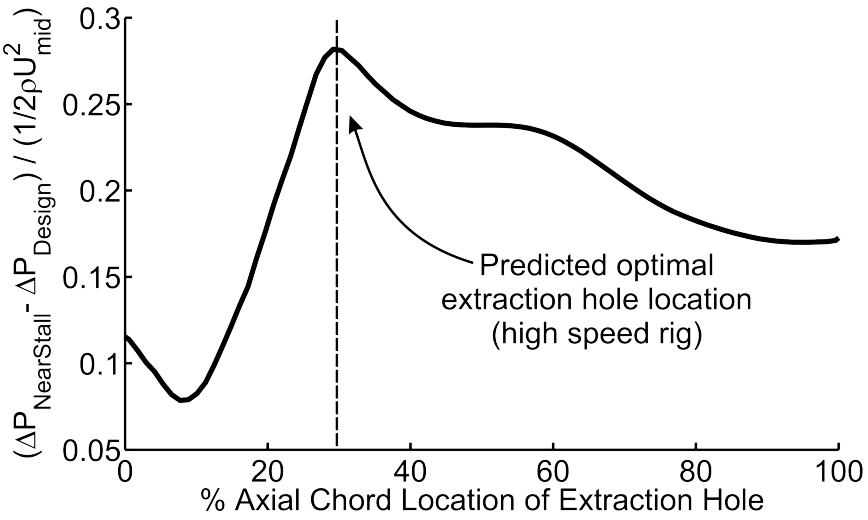

Figure 6.26: "Sweet spot" for extraction hole location in a high speed compressor predicted from re-circulation loop driving pressure ($\Delta P = \overline{P}_{EX} - \overline{P}_{INJ}$) at near stall and design conditions, as explained for Figure 6.2. Driving pressure is based on CFD casing pressure calculations.

References

J. J. Adamczyk, M. L. Celestina, and E. M. Greitzer. The Role of Tip Clearance in High-Speed Fan Stall. *ASME Journal of Turbomachinery*, 115:28–38, 1993.

S. Baghdadi. Modeling tip clearance effects in multistage axial compressors. *ASME Journal of Turbomachinery*, 118:697–705, 1996.

E. E. Bailey. Effect of grooved casing treatment on the flow range capability of a single-stage axial-flow compressor. Technical report, NASA TM X-2459, 1972.

T. G. Beckwith, R. D. Marangoni, and J. H. L. V. *Mechanical Measurements*. Addison-Wesley Publishing Company, 5 edition, 1995.

M. A. Bennington, J. D. Cameron, S. C. Morris, and C. P. Gendrich. Over rotor casing surface streak measurements in a high speed axial compressor. *ASME Conference Proceedings*, 2007. GT2007-28273.

M. A. Bennington, J. D. Cameron, S. C. Morris, C. Legault, S. T. Barrows, J. P. Chen, G. S. McNulty, and A. R. Wadia. Investigation of tip-flow based stall criteria using rotor casing flow visualization. *ASME Conference Proceedings*, 2008. GT2008-51319.

J. J. Bolger. *Three Dimensional Design of Compressor Blades*. PhD thesis, University of Cambridge, Cambridge, UK, 1999.

H. H. Bruun. *Hot-Wire Anemometry*. Oxford University Press, 1995.

J. D. Cameron, S. C. Morris, S. T. Barrows, and J.-P. Chen. On the interpretation of casing measurements in axial compressors. *ASME Conference Proceedings*, 2008. GT2008-51371.

T. R. Camp and I. J. Day. A Study of Spike and Modal Stall Phenomena in a Low-Speed Axial Compressor. *ASME Journal of Turbomachinery*, 120:393–401, 1998.

G. T. Chen, E. M. Greitzer, C. S. Tan, and F. E. Marble. Similarity Analysis of Compressor Tip Clearance Flow Structure. *ASME Journal of Turbomachinery*, 113:260–269, 1991.

J. P. Chen, M. D. Hathaway, and G. P. Herrick. Prestall Behavior of a Transonic Axial Compressor Stage via Time-Accurate Numerical Simulation. *ASME Journal of Turbomachinery*, 130:041014, 2008.

N. A. Cumpsty. *Compressor Aerodynamics*. Krieger Publishing Company, 2004.

R. Dambach and H. P. Hodson. A new method of data reduction for single-sensor pressure probes. *ASME Conference Proceedings*, 1999. 99-GT-304.

R. D'Andrea, R. L. Behnken, and R. M. Murray. Rotating stall control of an axial flow compressor using pulsed air injection. *ASME Journal of Turbomachinery*, 119:742–752, 1997.

R. L. Davis and J. Yao. Prediction of Compressor Stage Performance from Choke through Stall. *AIAA Journal of Propulsion and Power*, 22(3):550–557, 2006.

I. J. Day. The Fundamentals of Stall and Surge, Part I: Stall. *Von Karman Institute for Fluid Dynamics Lecture Series 2006-06: Advances in Axial Compressor Aerodynamics*. Belgium, 2006a.

I. J. Day. The Fundamentals of Stall and Surge, Part II: Surge. *Von Karman Institute for Fluid Dynamics Lecture Series 2006-06: Advances in Axial Compressor Aerodynamics*. Belgium, 2006b.

I. J. Day. *Axial Compressor Stall*. PhD thesis, University of Cambridge, Cambridge, UK, 1976.

I. J. Day. Stall Inception in Axial Flow Compressors. *ASME Journal of Turbomachinery*, 115:1–9, 1993a.

I. J. Day. Active Suppression of Rotating Stall and Surge in Axial Compressors. *ASME Journal of Turbomachinery*, 155:40–47, 1993b.

I. J. Day. Axial compressor performance during surge. *AIAA Journal of Propulsion and Power*, 10(3):329–336, 1994.

I. J. Day and C. Freeman. The Unstable Behaviour of Low and High Speed Compressors. *ASME Journal of Turbomachinery*, 116:194–201, 1994.

I. J. Day, T. Breuer, J. Escuret, M. Cherrett, and A. Wilson. Stall Inception and the Prospects for Active Control in Four High-Speed Compressors. *ASME Journal of Turbomachinery*, 121:18–27, 1999.

A. Deppe, H. Saathoff, and U. Stark. Spike-Type Stall Inception in Axial-Flow Compressors. *Proceedings of the 6th European Conference on Turbomachinery, Lille, France*, 2005.

A. Dickens. *Highly Loaded Compressors*. PhD thesis, University of Cambridge, 2008.

B. Dobrzynski, H. Saathoff, G. Kosyna, C. Clemen, and V. Gummer. Active flow control in a single-stage axial compressor using tip injection and boundary layer removal. *ASME Conference Proceedings*, 2008. GT2008-50214.

H. W. Emmons, C. E. Pearson, and H. P. Grant. Compressor Surge and Stall Propagation. *Transactions of the ASME*, 77:455–469, 1955.

A. H. Epstein, J. E. Ffowcs-Williams, and E. M. Greitzer. Active suppression of aerodynamic instabilities in turbomachines. *AIAA Journal of Propulsion and Power*, 5(2):204–211, 1989.

C. Freeman. The effect of tip clearance flow on compressor stability and engine performance. *Von Karman Institute for Fluid Dynamics Lecture Series 1985-05*, 1985.

C. Freeman, A. G. Wilson, I. J. Day, and M. A. Swinbanks. Experiments in active control of stall on an aeroengine gas turbine. *ASME Journal of Turbomachinery*, 120:637–647, 1998.

H. Fujita and H. Takata. A study on configurations of casing treatment for axial flow compressors. *Bulletin of JSME*, 27(230):1675–1681, 1984.

M. Furukawa, M. Inoue, K. Saiki, and K. Yamada. The role of tip leakage vortex breakdown in compressor rotor aerodynamics. *ASME Journal of Turbomachinery*, 121:469–480, 1999.

J. Glanville. Investigation into core compressor tip leakage modelling techniques using a 3d viscous solver. *ASME Conference Proceedings*, 2001. GT2001-0336.

N. Gourdain, S. Burguburu, G. J. Michon, N. Ouayahya, F. Leboeuf, and S. Plot. About the numerical simulation of rotating stall mechanisms in axial compressors. *ASME Conference Proceedings*, 2006. GT2006-90223.

E. M. Greitzer and F. K. Moore. A Theory of Post-Stall Transients in Axial Compression Systems: Part II - Application. *ASME Journal of Turbomachinery*, 108:231–239, 1986.

E. M. Greitzer, J. P. Nikkanen, D. E. Haddad, R. S. Mazzawy, and H. D. Joslyn. A Fundamental Criterion for the Application of Rotor Casing Treatment. *ASME Journal of Fluids Engineering*, 101:237–243, 1979.

D. L. Gysling and E. M. Greitzer. Dynamic control of rotating stall in axial compressors using aeromechanical feedback. *ASME Journal of Turbomachinery*, 117:307–319, 1995.

C. Hah, R. Schulze, S. Wagner, , and D. K. Hennecke. Numerical and experimental study for short wavelength stall inception in a low-speed axial compressor. *Proceedings of the 14th International Symposium for Air Breathing Engines, Florence, Italy*, 1999. ISABE 99-7033.

L. Hansen and J. Bons. Flow measurements of vortex generator jets in separating boundary layer. *AIAA Journal of Propulsion and Power*, 22:558–566, 2006.

M. D. Hathaway. Self-recirculating casing treatment concept for enhanced compressor performance. *ASME Conference Proceedings*, 2002. GT2002-30368.

M. D. Hathaway. Passive Endwall Treatments for Enhancing Stability. *Von Karman Institute for Fluid Dynamics Lecture Series 2006-06: Advances in Axial Compressor Aerodynamics*. Von Karman Institute, Rhode St-Genese, Belgium, 2006. Also published as NASA TM-2007-214409.

T. Houghton and I. J. Day. Enhancing the stability of subsonic compressors using casing grooves. *ASME Journal of Turbomachinery*, 133:021007, 2011. GT2009-59210.

T. Houghton and I. J. Day. Stability enhancement by casing grooves: The importance of stall inception mechanism and solidity. *ASME Conference Proceedings*, 2010. GT2010-22284.

T. O. Houghton. *Axial Compressor Stability Enhancement*. PhD thesis, University of Cambridge, 2010.

D. A. Hoying, C. S. Tan, H. D. Vo, and E. M. Greitzer. Role of Blade Passage Flow Structures in Axial Compressor Rotating Stall Inception. *ASME Journal of Turbomachinery*, 121:735–742, 1999.

I. H. Hunter and N. A. Cumpsty. Casing wall boundary-layer development through an isolated compressor rotor. *ASME Journal of Engineering for Power*, 104:805–818, 1982.

R. Hunziker, H.-P. Dickmann, and R. Emmrich. Numerical and experimental investigation of a centrifugal compressor with an inducer casing bleed system. *IMechE Journal of Power and Energy*, 215(6):783–791, 2001.

M. Inoue and M. Kuroumaru. Structure of tip clearance flow in an isolated axial compressor rotor. *ASME Journal of Turbomachinery*, 111:250–256, 1989.

M. Inoue, M. Kuroumaru, T. Tanino, and M. Furukawa. Propagation of Multiple Short-Length-Scale Stall Cells in an Axial Compressor Rotor. *ASME Journal of Turbomachinery*, 122:45–54, 2000.

S. Kang and C. Hirsch. Tip leakage flow in linear compressor cascade. *ASME Journal of Turbomachinery*, 116:657–664, 1994.

S. A. Khalid, A. S. Khalsa, I. A. Waitz, C. S. Tan, E. M. Greitzer, N. A. Cumpsty, J. J. Adamczyk, and F. E. Marble. Endwall Blockage in Axial Compressors. *ASME Journal of Turbomachinery*, 121:499–509, 1999.

B. Lakshminarayana, M. Pouagare, and R. Davino. Three-dimensional flow field in the tip region of a compressor rotor passage - part i: Mean velocity profiles and annulus wall boundary layer. *ASME Journal of Engineering for Power*, 104:760–771, 1982a.

B. Lakshminarayana, M. Pouagare, and R. Davino. Three-dimensional flow field in the tip region of a compressor rotor passage - part ii: Turbulence properties. *ASME Journal of Engineering for Power*, 104:772–781, 1982b.

B. Lakshminarayana, M. Zaccaria, and B. Marathe. The structure of tip clearance flow in axial compressors. *ASME Journal of Turbomachinery*, 117:336–347, 1995.

B. Liu, H. Wang, H. Liu, H. Yu, H. Jiang, and M. Chen. Experimental investigation of unsteady flow field in the tip region of an axial compressor rotor passage at near stall condition with spiv. *ASME Conference Proceedings*, 2003. GT2003-38185.

J. P. Longley, H.-W. Shin, R. E. Plumley, P. D. Silkowski, I. J. Day, E. M. Greitzer, C. S. Tan, and D. C. Wisler. Effects of rotating inlet distortion on multistage compressor stability. *ASME Journal of Turbomachinery*, 118:181–188, 1996.

N. M. McDougall. *Stall Inception in Axial Compressors*. PhD thesis, University of Cambridge, Cambridge, UK, 1988.

N. M. McDougall, N. A. Cumpsty, and T. P. Hynes. Stall Inception in Axial Compressors. *ASME Journal of Turbomachinery*, 112:116–125, 1990.

F. K. Moore and E. M. Greitzer. A Theory of Post-Stall Transients in Axial Compression Systems: Part I - Development of Equations. *ASME Journal of Turbomachinery*, 108:68–76, 1986.

K. N. S. Murthy and B. Lakshminarayana. Laser doppler velocimeter measurement in the tip region of a compressor rotor. *AIAA Journal*, 24:807–814, 1986.

W. M. Osborn, G. W. Lewis, and L. J. Heidelberg. Effect of several porous casing treatments on stall limit and on overall performance of an axial flow compressor rotor. Technical report, NASA TN D-6537, 1971.

J. D. Paduano, A. H. Epstein, L. Valavani, J. P. Longley, E. M. Greitzer, and G. R. Guenette. Active control of rotating stall in a low speed axial compressor rotor. *ASME Journal of Turbomachinery*, 115:48–56, 1993.

R. L. Panton. *Incompressible Flow*. John Wiley & Sons, Inc., 1996.

J. M. M. Place. *Three-Dimensional Flow in Axial Compressors*. PhD thesis, University of Cambridge, Cambridge, UK, 1997.

D. C. Prince, D. C. Wisler, and D. E. Hilvers. Study of casing treatment stall margin improvement phenomena. Technical report, NASA CR-134552, 1974.

A. M. Rolt and K. G. Kyprianidis. Assessment of new aeroengine core concepts and technologies in the eu framework 6 newac programme. *ICAS Conference Proceedings*, 2010.

H. Saathoff, A. Deppe, U. Stark, M. Rohdenburg, H. Rohkamm, D. Wulff, and G. Kosyna. Steady and unsteady casingwall flow phenomena in a single-stage low-speed compressor at part-load conditions. *International Journal of Rotating Machinery*, 9:327–335, 2003.

H. Schrapp. *Experimentelle Untersuchungen zum Aufplatzen des Spaltwirbels in Axialverdichtern*. PhD thesis, Technische Universitaet Carolo-Wilhelmina zu Braunschweig, 2008.

P. A. Seitz. *Casing Treatment for Axial Flow Compressors*. PhD thesis, University of Cambridge, Cambridge, UK, 1999.

A. Shabbir and J. J. Adamczyk. Flow Mechanism for Stall Margin Improvement due to Circumferential Casing Grooves on Axial Compressors. *ASME Journal of Turbomachinery*, 127:708–717, 2005.

A. K. Simpson and J. P. Longley. An experimental study of the inception of rotating stall in a single-stage low-speed axial compressor. *ASME Conference Proceedings*, 2007. GT2007-27181.

G. D. J. Smith and N. A. Cumpsty. Flow Phenomena in Compressor Casing Treatment. *ASME Journal of Turbomachinery*, 106:532–541, 1984.

Z. S. Spakovsky, C. M. van Schalkwyk, H. J. Weigl, J. D. Paduano, K. L. Suder, and M. M. Bright. Rotating stall control in a high-speed stage with inlet distortion: Part i - circumferential distortion. *ASME Journal of Turbomachinery*, 121:517–524, 1999a.

Z. S. Spakovsky, H. J. Weigl, J. D. Paduano, C. M. van Schalkwyk, K. L. Suder, and M. M. Bright. Rotating stall control in a high-speed stage with inlet distortion: Part i - radial distortion. *ASME Journal of Turbomachinery*, 121: 510–516, 1999b.

A. H. Stenning. Rotating Stall and Surge. *ASME Journal of Fluids Engineering*, 102:14–20, 1980. Author deceased prior to publishing.

J. A. Storer. *Tip Clearance Flow in Axial Compressors*. PhD thesis, University of Cambridge, Cambridge, UK, 1991.

J. A. Storer and N. A. Cumpsty. Tip Leakage Flow in Axial Compressors. *ASME Journal of Turbomachinery*, 113:252–259, 1991.

J. A. Storer and N. A. Cumpsty. An approximate analysis and prediction method for tip clearance loss in axial compressors. *ASME Journal of Turbomachinery*, 116:648–656, 1994.

A. J. Strazisar, M. M. Bright, S. Thorp, D. E. Culley, and K. L. Suder. Compressor stall control through endwall recirculation. *ASME Conference Proceedings*, 2004. GT2004-54295.

K. L. Suder and M. L. Celestina. Experimental and Computational Investigation of the Tip Clearance Flow in a Transonic Axial Compressor Rotor. *ASME Journal of Turbomachinery*, 118:218–229, 1996.

K. L. Suder, M. D. Hathaway, S. A. Thorp, A. J. Strazisar, and M. B. Bright. Compressor Stability Enhancement Using Discrete Tip Injection. *ASME Journal of Turbomachinery*, 123:14–23, 2001.

H. Takata and Y. Tsukuda. Stall margin improvement by casing treatment - its mechanism and effectiveness. *ASME Journal of Engineering for Power*, 99: 121–133, 1977.

C. S. Tan. Three-Dimensional and Tip Clearance Flows in Compressors. *Von Karman Institute for Fluid Dynamics Lecture Series 2006-06: Advances in Axial Compressor Aerodynamics*. Belgium, 2006.

D. E. VanZante, A. J. Strazisar, J. R. Wood, M. D. Hathaway, and T. H. Okiishi. Recommendations for achieving accurate numerical simulation of tip clearance flows in transonic compressor rotors. *ASME Journal of Turbomachinery*, 122: 733–742, 2000.

H. D. Vo. *Role of Tip Clearance Flow on Axial Compressor Stability*. PhD thesis, MIT, Cambridge, MA, 2001.

H. D. Vo, C. S. Tan, and E. M. Greitzer. Criteria for Spike Initiated Rotating Stall. *ASME Journal of Turbomachinery*, 130:011023, 2008.

H. J. Weigl. *Active Stabilization of Rotating Stall and Surge in a Transonic Single Stage Axial Compressor*. PhD thesis, MIT, Cambridge, MA, 1997.

H. J. Weigl, J. D. Paduano, L. G. Frechette, A. H. Epstein, E. M. Greitzer, M. M. Bright, and A. J. Strazisar. Active Stabilization of Rotating Stall and Surge in a Transonic Single-Stage Axial Compressor. *ASME Journal of Turbomachinery*, 120:625–636, 1998.

M. P. Wernet, D. V. Zante, T. J. Strazisar, W. T. John, and P. S. Prahst. Characterization of the Tip Clearance Flow in an Axial Compressor using 3-D digital PIV. *Experiments in Fluids*, 39:743–753, 2005.

I. Wilke and H. P. Kau. A numerical investigation of the influence of casing treatments on the tip leakage flow in a hpc front stage. *ASME Conference Proceedings*, 2002. GT2002-30642.

A. G. Wilson and C. Freeman. Stall Inception and Development in an Axial Flow Aero-Engine. *ASME Journal of Turbomachinery*, 116:216–225, 1994.

D. C. Wisler. Loss reduction in axial-flow compressors through low-speed model testing. *ASME Journal of Engineering for Gas Turbines and Power*, 107:354–363, 1985.

A. Young, I. J. Day, and G. Pullan. Stall warning by blade pressure signal analysis. *ASME Conference Proceedings*, 2011. GT2011-45850.